CHEMIA

S T U D I A

UNIVERSITATIS BABEŞ–BOLYAI

CHEMIA

4

CUPRINS – CONTENT – SOMMAIRE – INHALT

Studia Universitatis Babes-Bolyai Chemia has been selected for coverage in Thomson Reuters products and custom information services. Beginning with V. 53 (1) 2008, this publication is indexed and abstracted in the following:

- Science Citation Index Expanded (also known as SciSearch®)
- Chemistry Citation Index®
- Journal Citation Reports/Science Edition

QUANTITATIVE EVALUATION OF SOME VOLATILE AROMATIC HYDROCARBONS FROM WATER USING A THREE PHASE EXTRACTION SYSTEM AND GAS CHROMATOGRAPHY ANALYSIS*

VLAD AGOTICI[a], IONEL CIUCANU [a*]

ABSTRACT. The analysis of benzene, toluene and xylene by microextraction into a three phase extraction system (liquid-liquid-solid) followed by gas chromatography is described. The analytes are extracted very fast into a very small volume of organic solvent and simultaneously into a solid sorbent. The efficiency of different solvents (dichloromethane, chloroform, carbon tetrachloride, *n*-hexane and cyclohexane) added to the sample in different volumes for liquid microextraction was evaluated. The best results were obtained by using dichloromethane. The extracted quantity in the three phase system was significantly higher than the usual two phase liquid-solid microextraction. The RSD was between 11-12%, the linearity was very good (over 1 magnitude order from 5 ng/mL to 6 μg/mL) for all three compounds, the limits of detection (S/N = 3) were in the ppb range and the recoveries between 84-96%. The working conditions (extraction time, temperature, solvent, solvent volume, stirring rate) were optimized. The optimum conditions for the extraction of all three analytes were experimentally established for 200 μL dichloromethane as organic phase, 25°C, at a stirring rate of 400 rpm and 5 minutes extraction time. The developed method was applied for the analysis of purposed compounds in wastewater samples.

Keywords: liquid-solid microextraction, liquid-liquid microextraction, liquid-liquid-solid microextraction, volatile aromatic hydrocarbons, gas chromatography

INTRODUCTION

Benzene, toluene and xylenes are some of the most important and frequent water contaminants. They appear in water due to various causes but especially from industrial wastewaters. These compounds are used in large amounts as precursors in the chemical industry and as solvents. They are also present in fuels [1].

Aromatic hydrocarbons are considered highly toxic, carcinogenic and dangerous for the environment [1-7]. The toxicity of volatile aromatic hydrocarbons is caused mainly by the degradation products, in most cases phenol derivatives which are toxic at the membrane level. The metabolism of benzene, toluene and xylenes is dose-dependent and usually very extensive at dose level that do not saturate the first metabolic step of each compound which includes P450 cytochrome and mixed function oxidases [1, 2].

Benzene affects mainly the hepatic functions and inhibits the activity of dehydrogenase and phosphatase [2]. It is converted mainly to phenol by the mixed-function oxidase system, primarily in the liver, but also in bone marrow [3]. Benzene toxicology differs from that of other solvents because it is a myelotoxin which affects the blood forming organs (e.g. marrow). The hematological effects caused when the person is chronically exposed to benzene and depend mainly upon the sensibility of the exposed person. In general the hemoglobin level is significantly decreased (in some cases 50% from the normal value) and leukocyte counts are modified [1].

The substituted volatile aromatic hydrocarbons are considered less toxic than benzene. Toluene affects the central nervous system causing dizziness, headaches and fatigue even at small concentration (e.g. 200 ppm for 8 hours) [1]. The small quantity of these compounds, often in traces makes their analysis from environmental matrixes very difficult and often losses occur during sample preparation. For this reason sensible methods for the determination of trace levels of benzene, toluene and xylene (BTX) have been developed during the last decades.

Gas chromatography is considered the most sensitive technique for the analysis of the aromatic hydrocarbons. For gas chromatography analysis the separation from sample matrix and concentration of these compounds has to be performed in order to obtain concentrations over the detection limit.

The classical liquid-liquid extraction is not suitable for the extraction of trace levels of aromatic hydrocarbons; it is time consuming, high amounts of toxic solvents have to be used and most of the analytes can be lost during the extraction procedures.

Several extraction techniques have been developed for the separation and concentration of analytes: liquid-liquid microextraction (single drop extraction), liquid-liquid-liquid microextraction (three phase single drop extraction) [8-10], solid phase extraction [11, 12] and solid phase microextraction [13-20]. The liquid-liquid microextraction and the liquid-liquid-liquid microextraction known also as two respectively three phase single drop extraction techniques have very good enrichment factors and were successfully applied for the microanalysis but they have the disadvantage of the possible dispersion of the extraction drop. Also the maximum volume of solvent which can be used is limited (4 µL) [10, 18].

The simple two phase liquid-solid microextraction is a solvent free technique which consists in the extraction of the analytes on a sorbent (usually a polymer coating on a silica rod) and the direct desorption into the gas chromatograph. This technique is also applied in the analysis of trace level compounds but the extracted quantities are very low because of the small quantity of sorbent available on the fiber [13].

Several methods were developed to increase the sorbent layer. One of these methods uses a wall coated needle (with the advantage that there is no fiber which could be broken) but a desorption gas flow is necessary [19]. Another technique is the "stir bar sorptive extraction" which uses a magnetic stirring bar covered with sorbent [20]. This technique has the advantage of high extraction volume because of the high quantity of sorbent available but has the disadvantage that the injection port of the gas chromatograph has to be modified.

In order to increase the extracted quantity of analytes and to overcome the disadvantages of the above mentioned techniques, we developed a liquid-liquid microextraction in small drops simultaneously with a solid-liquid microextraction. Actually we used a three phase liquid-liquid-solid microextraction system.

RESULTS AND DISCUSSION

Influence of the solvent on the extracted quantity

The volume of the organic solvent added to the sample is very important. If the volume of organic solvent added to the water sample is lower than its solubility limit, no extraction improvement was noticed (on the contrary: a competition between the analyte and the added organic solvent for the sorbent will occur and the extracted quantity will decrease significantly). When volume of the solvent added to the water sample is higher than the solubility limit, a three phase system will be formed. The analytes will be concentrated in the organic phase and than transferred to the sorbent. When a high volume of organic solvent is used, the analytes will be diluted in the organic phase and the extraction efficiency will decrease.

Figure 1 shows the influence of the quantity of organic solvent added to the sample.

At high volumes of solvent (over 600 µL in case of dichloromethane and over 200 µL for carbon tetrachloride, *n*-hexane and cyclohexane) the polydimethylsiloxane fiber will be supersaturated with organic solvent, and a significant loss of extraction efficiency will occur. At 12 mL water sample containing the analytes at a concentration of 5 µg/mL each, different solvents were added in different volumes (200 µL dichloromethane, 20 µL chloroform, 20 µL carbon tetrachloride, 20 µL *n*-hexane and 20 µL cyclohexane).
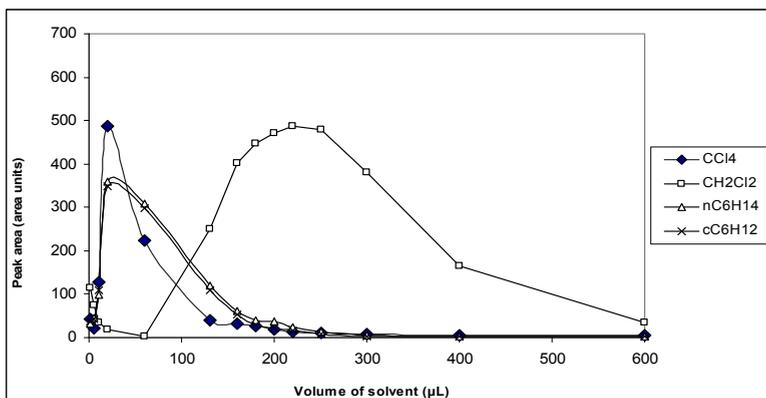
Figure 1. Influence of solvent volume upon extracted quantity of *o*-xylene.
All extractions were performed at 25°C, 500 rpm using 12 mL
of water sample containing 5 µg/mL of *o*-xylene.

Figures 2-4 show the influence of the volume of organic solvent in
the in the liquid-liquid-solid microextraction.
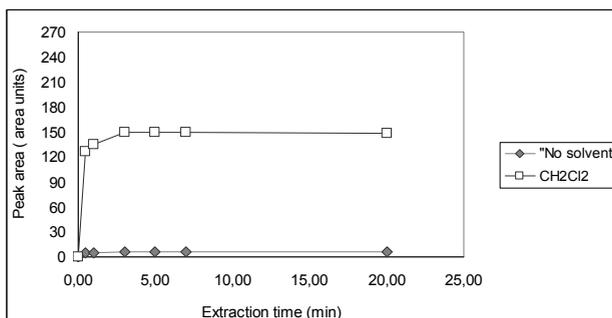
Figure 2. Three phase extraction of benzene (5 µg/mL concentration, 400 rpm, 25°C).
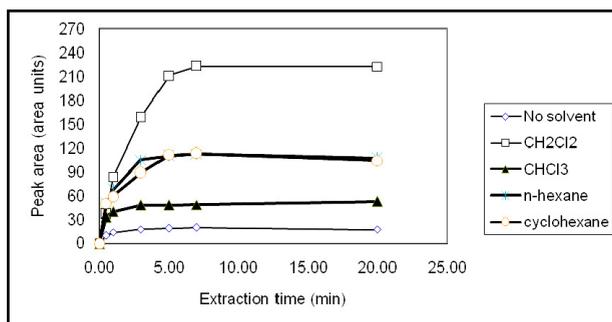
Figure 3. Three phase extraction of toluene (5 µg/mL concentration, 400 rpm, 25°C).

8
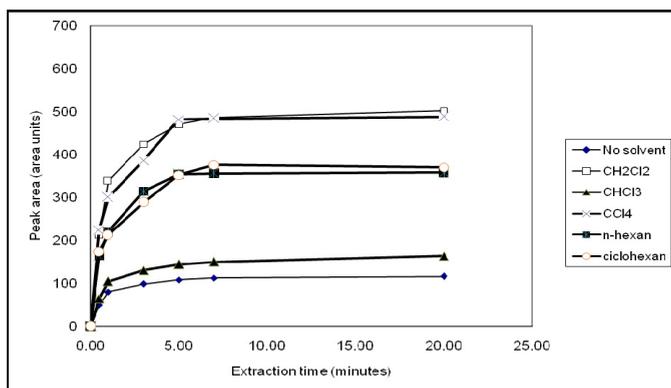
Figure 4. Three phase extraction of *o*-xylene (5 µg/mL concentration, 400 rpm, 25°C).

Table 1. Retention time of analytes and solvents at oven temperature 50°C,
isothermal elution, splitless mode, nitrogen flow rate of 1 mL/min.

No.	Compound	Retention time (min)
1.	Benzene	3.11
2.	Toluene	4.92
3.	*o*-Xylene	9.32
4.	Dichloromethane	2.42
5.	Chloroform	2.66
6.	Carbon Tetrachloride	3.09
7.	*n*-Hexane	3.12
8.	Cyclohexane	3.13

Benzene, carbon tetrachloride and cyclohexane could not be separated in the conditions described above because the solvent peak overlaps the benzene peak. Benzene, carbon tetrachloride, *n*-hexane and cyclohexane have very close retention times, as it is shown in Table 1.

Chlorinated hydrocarbons have higher affinity for lipophilic compounds than aliphatic hydrocarbons like *n*-hexane and cyclohexane [21].

For this reason, the extracted quantity of analyte is higher when using a chlorinated solvent, compared to aliphatic hydrocarbons. In the optimum conditions (200 µL dichloromethane for 12 mL sample volumes, at 25°C, 400 rpm and 5 µg/mL concentration) the extracted quantity for benzene is 6 times higher, for toluene 11 times higher and for *o*-xylene 16 times higher with the three phase liquid-liquid-solid microextraction system compared with the simple two phase liquid-solid microextraction.

The 100 μm non-bonded polydimethylsiloxane fiber is not adequate for this method. In the presence of solvents it swells and there is the possibility that the coating is stripped off when it is retracted into the protection needle. Also the amount of solvent extracted is very high and the desorption process is not constant due to the diffusion of solvent in the polydimethylsiloxane coating and the results are not reproducible.

Influence of the stirring rate, temperature and salt addition

The three phase extraction of benzene and toluene is an equilibrium process and the parameters of this equilibrium depend on the analyte, solvent used as the third phase, type of solid phase (sorbent), amount of solvent, temperature, volatility, agitation. The time needed for the equilibrium to be reached can be determined from the extraction curve.

Before the equilibrium is reached, the extracted quantity increases almost exponentially with the extraction times in case of liquid-liquid-solid microextraction. After the equilibrium is reached, the extracted quantity will not be significantly higher with the increase of the extraction time.

We established experimentally that after 5 minutes the extracted quantity of analytes will not increase significantly (see Figures 1-3). All the extractions were carried out at 5 minutes extraction time.

The stirring of the sample improves the mass transfer from the sample (first liquid phase) into the second phase (organic solvent) and third phase (the sorbent).

When solvents with lower density than water are used (like *n*-hexane and cyclohexane) a higher stirring rate does not lead to a significant increase in extraction efficiency. At a high stirring rate (over 600 rpm) a decrease of extracted quantity can be observed, probably because the dispersion of the solvent in the aqueous sample occurs. As a consequence, the amount of solvent extracted with the fiber is lower and also the extracted quantity of analytes decreases.

For the solvents with higher density than water (like dichloromethane and chloroform) the stirring rate is very important. The increase of stirring rate leads to an increase of extracted quantity of analytes because their mass transfer from water sample into the organic phase is higher. Also the high density solvent is dispersed into the water sample and has easier access to the fiber which is positioned on the upper side of the sample vial.

However the stirring rate cannot be increased over 800 rpm because a turbulent flow occurs in the vial and produces the breaking of the silica fiber which is very sensitive.

The maximum acceptable stirring rate was 400 rpm. Increasing the stirring rate over this value does not significantly increase the extracted quantity of analytes.

Figure 5 shows the influence of the stirring rate upon the extracted quantity of analytes.
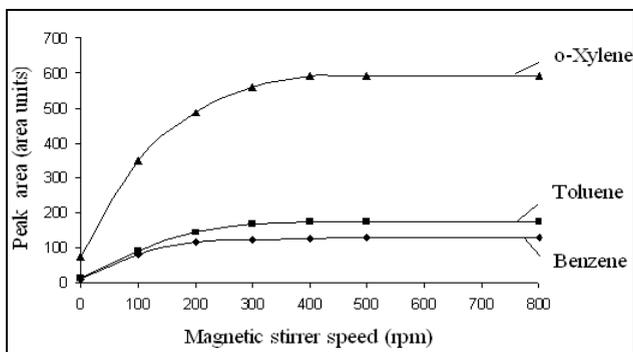
Figure 5. Influence of the stirring rate upon the extracted quantity of benzene, toluene and *o*-xylene extracted with 200 µL of dichloromethane at 25°C, with a cylindrical-shaped stirring bar (1.5 cm x 0.5 cm) in 14 mL sample vials containing 12 mL sample volume and 5 µg/mL concentration for each analyte.

The temperature is very important for the extraction of these volatile analytes and it is important to keep it constant. Increasing the temperature will decrease the extracted volume because of the volatilization of the analytes. The optimum temperature was found to be 25°C.

The addition of NaCl to the samples will decrease the extracted quantity of benzene and increase the one of toluene and *o*-xylene. Addition of all other salts (NaHCO$_3$, FeSO$_4 \cdot$7H$_2$O, CaCO$_3$) will slightly decrease the extracted quantity.

At low concentrations the salt effect can be neglected. The decrease respectively the increase of the extracted quantity of analytes by salt addition in a concentration range from 1-100 mg/mL is not significantly higher than the relative standard deviation of the method.

Calcium carbonate is not soluble in water over 14 mg/L. In this case the saturated solution of calcium carbonate was tested. If solid particles of insoluble salt are present, the extracted quantity of analytes decreases significantly, probably because a part of analytes are adsorbed on the surface of the solid particles.

These results are in accordance with the general observation that the addition of salts enhances the extraction of polar compounds while for the nonpolar compounds the influence is insignificant [18].

Quantitative determination of BTX from wastewater

Quantitative evaluation was performed by calibration curve method. As external standard we used the analyte itself by performing extractions at the optimum conditions at different concentrations. The linearity range of the method was verified by extracting analytes at different concentrations.

For this purpose, a stock solution of 6000 ng/mL was prepared. This stock solution was then diluted to desired concentrations (12 times by adding 1 mL concentrated solution to 11 mL of ultrapure water obtaining a concentration of 500 ng/L of each analyte. The second solution containing 500 ng/L analyte was then diluted 1:10 and 1:100 obtaining solutions of 50 ng/mL and 5 ng/mL for each analyte).

The extractions were performed in 14 mL extraction vials containing 12 mL sample volume. For each extraction the optimum conditions were used, namely: dichloromethane as the second phase, 200 μL solvent volume, 400 rpm, at 25°C and 5 minutes extraction time.

The linearity of the method was very good, from 5 ng/mL to 6 μg/mL (over 1 magnitude order). The linear equation, regression coefficients, relative standard deviations and limit of detections are shown in Table 2.

In order to check the recovery of each analyte, a tap water sample was analyzed. To this sample each analyte was added in a concentration of 1 μg/mL and 5 μg/mL (by adding 0.25 mg and 1.25 mg to 250 mL water corresponding to 0.28 μL and 1.44 μL of each analyte according to their density). The results are presented in the table below.

Table 2. Linearity range, equations, regression coefficients, RSD and detection limits of the liquid-liquid-solid microextraction system.

Compound	Linearity range (ng mL^{-1})	Calibration curve	Correlation coefficient	RSD (%) n = 5	LOD (ng/mL) 3 phase extraction	LOD (ng/mL) 2 phase extraction
Benzene	5-6000	y=225.79x	0.9955	12.09	2.48	17.82
Toluene	5-6000	y=297.05x	0.9920	11.92	0.53	6.21
o-Xylene	5-6000	y=1172.3x	0.9902	12.05	0.08	2.29

Table 3. Recovered quantities of analytes added to tap water using three phase liquid-liquid-solid microextraction.

Sample	Compound	Spiked quantity (μg/mL)	Found quantity (μg/mL)	Recovery (%)
Tap water	Benzene	1.00	0.89	88.89
		5.00	4.22	84.44
	Toluene	1.00	0.98	97.93
		5.00	4.55	90.93
	o-Xylene	1.00	0.93	92.61
		5.00	4.85	97.02

Application of the method

This method can be successfully applied to the analysis of benzene, toluene and *o*-xylene from wastewater. This wastewater was taken from the canalization system before entering the sewage facility.

A sample of wastewater from a petroleum storage facility was analyzed using the two phase extraction system and the three phase extraction system.

Because this sample contains a complex mixture of hydrocarbons the experimental conditions were modified in order to elute also the heavy components. Details about the gas chromatographic conditions are presented below.
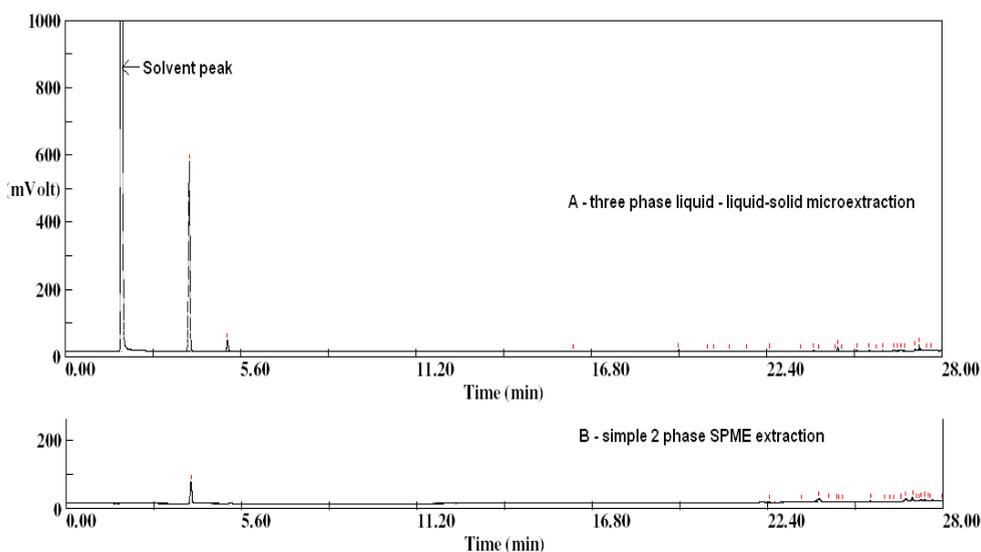
Figure 6. Analysis of a complex sample of hydrocarbons from wastewater from a petroleum storage facility. A: 3 phase liquid-liquid-solid microextraction, B: 2 phase liquid-solid microextraction. Compounds were identified according to the retention time: 1 – benzene, 2- toluene). All the tests were performed at 25°C, at 400 rpm, in 14 mL vials, containing 12 mL sample. Gas chromatographic conditions: injector temperature 220°C, FID detector temperature 250°C, oven temperature 50°C isothermal for 10 minutes followed by temperature gradient of 3°C/min until 250°C, kept 5 minutes at 250°C and then the oven was cooled at 50°C.

Even in case of complex samples, the three phase liquid-liquid-solid microextraction is very efficient compared with the 2 phase liquid-solid microextraction.

Using the three phase extraction system, certain selectivity is achieved for the volatile compounds with low molecular mass, because of the higher affinity of these analytes for the solvent compared with the other, heavier and more polar ones. Choosing the right solvent, the selectivity is achieved.

13

This method will be tested also for other classes of water contaminants with different polarity and also with other type of solvents beside chlorinated ones and hydrocarbons. These studies will be presented in a following paper.

CONCLUSIONS

This study proved that the three phase liquid-liquid-solid microextraction is a reliable method for the quantification of BTX from wastewater. The optimum extractions were performed at 25°C, using dichloromethane as the third phase (optimum volume 200 µL for 12 mL sample volume), at 400 rpm stirring rate and 5 minutes extraction time.

The salt addition does not influence significantly the extraction procedure.

The linearity of the method is very good, over a wide range of concentrations (from 5 ng/mL to 6 µg/mL). All the peaks were narrow, with an asymmetry at 10% in the range 0.95-1.10.

The peaks of solvent (dichloromethane) and of analytes are separated very well.

EXPERIMENTAL SECTION

Chemicals and Materials

Benzene (99% purity), toluene (99.8% purity), o-xylene (reagent grade 97%), calcium carbonate (99% purity), ferrous sulfate heptahydrate (99% purity) and sodium hydrogen carbonate (99.7%) were purchased from Sigma-Aldrich (Steinheim, Germany), dichloromethane (HPLC purity), sodium chloride (analytical grade), n-hexane (HPLC purity) were purchased from Riedel de Haën (Seelze, Germany). Cyclohexane (99.7% purity) was purchased from Merck (Darmstadt, Germany). Ultra pure, deionized water was obtained with a Millipore system at 18.2 MΩ·cm.

The stirring of samples was carried out with a Gerhardt magnetic stirrer (2.5 A, 580 V, 230W) at 25°C, with a 1 cm magnet.

The 7 µm thick bonded polydimethylsiloxane coated silica fiber, the 100 µm non-bonded polydimethylsiloxane coated silica fiber and the manual holder were purchased from Supelco (Bellafonte PA, USA).

Standard solutions of 5 µg/mL were prepared by adding 1.25 mg benzene, toluene and o-xylene to deionized water to fill up 250 mL glass bottles. Because these quantities are difficult to weigh, the adequate volume was added with a Hamilton syringe, according to the density of each analyte (1.42 µL benzene, 1.44 µL toluene and 1.43 µL of o-xylene). The mixture was magnetically stirred at 25°C for quick dissolution for 30 minutes. The concentrated solutions were successively diluted to obtain the desired concentrations.

Dichloromethane (20-800 µL) that was the third phase has been transferred with a micropipette in the 14 mL sample vials containing 12 mL sample volume.

Gas chromatography

All the tests were done on an Ultra Trace Gas Chromatograph from Thermo Finnigan with the following parameters: injection temperature - 220°C, oven temperature - at 50°C isothermal elution, detector temperature - 250°C, hydrogen flow rate - 35 mL/min, air flow rate - 250 mL/min and nitrogen as carrier flow rate - 1 mL/min.

The column used was DB-5 (polydimethylsiloxane with 5% phenyl) having 30 m length, 0.25 mm internal diameter and 0.25 film thickness of the stationary phase.

Quantitative evaluation was done by calibration curve method. The calibration curve was done by plotting the peak area versus concentration of analyte.

ACKNOWLEDGMENTS

REFERENCES

1. P.L. Williams, J.R. James, S.M. Roberts, "Principles of Toxicology: Environmental and Industrial Application", John Willey & Sons, New York, **2000**, chapter 16.

2. L.G. Cockerham, B.S. Shane, "Basic Environmental Toxicology", CRC Press Inc, Boca Raton, **1994**, chapter 6.

3. WHO (World Health Organisation), "Benzene in Drinking Water. Background Document for Preparation of WHO Guidelines for drinking water", **2003**.

4. WHO (World Health Organisation), "Toluene in Drinking Water. Background Document for Preparation of WHO Guidelines for Drinking Water", **2004**.

5. WHO (World Health Organization), "Xylenes in Drinking Water. Background Document for Preparation of WHO Guidelines for Drinking Water Quality", **2003**.

6. G.D. DiVicenzo, W.J. Krasavage, *American Industrial Hygiene Association Journal,* **1974**, *35(1),* 21.

7. A.J. McMichael*, IARC Scientific Publication*, **1988**, *85*, 3.

8. H. Liu, P.K. Dasgupta, *Trends in Analytical Chemistry*, **1996**, *15(9),* 468.

9. E. Psillakis, N. Kalogerakis, *Trends in Analytical Chemistry*, **2003**, *22(10),* 565.

10. T. Ligor, B. Buszewski, *Chromatographia Supplement*, **2000**, *51*, 279.

11. N.J.K. Simpson, "Solid Phase Extraction: Principles, Techniques and Applications", Marcel Dekker Inc, New York, **2000**, chapter 2, 3.

12. K. Kawata, T. Ibaraki, A. Tanabe, H. Yagoh, A. Shinoda, H. Suzuki, Y. Yasuhara, *Journal of Chromatography A*, **2001**, *911(1),* 75.

13. E. Palm, DE Patent 2,139,992, 19971 (b), Palm E., US Patent 3, 797, 318, **1974**.

14. J. Pawliszyn, "Sampling and Sample Preparation for Field and Laboratory", Elsevier Science B.V., Amsterdam, **2002**, chapters 9, 10.

15. C.L. Arthur, J. Pawliszyn, *Journal of Analytical Chemistry,* **1990**, *62*, 2145.

16. I. Ciucanu, K.C. Swallow, R. Caprita, *Analytica Chimica Acta*, **2004**, *519(1),* 93.

17. M. Draga, I. Ciucanu, V. Agotici, A. Fernandez, R. Barna, *Chemosphere,* **2009**, *75*, 1210.

18. L. Xu, C. Basheer, H.K. Lee, *Journal of Chromatography A*, **2007**, *1152*, 184.

19. J. Lipinski, *Fresenius Journal of Analytical Chemistry,* **2001**, *369,* 57.

20. V.M. Leon, B. Alvarez, M.A. Cobollo, S. Munoz, I. Valor, *Journal of Chromatography A*, **2003**, *999(1-2),* 99.

21. J.M. Kokosa, A. Przyjazny, M.A. Jeannot, "Solvent Microextraction: Theory and Practice", John Wiley & Sons, New York, **2009**, chapter 2.

UV-VIS STUDY REGARDING THE INFLUENCE OF TWO POTENTIAL ENVIRONMENTAL POLLUTANTS ON THE TOTAL FLAVONOID CONTENT IN *TRITICUM AESTIVUM* L. AND *SECALE CEREALE* L.*

OCSANA OPRIŞ[a], FLORINA COPACIU[a,*], VIRGINIA COMAN[b], DUMITRU RISTOIU[a]

ABSTRACT. Waste waters produced by the textile industry and the animal wastes from the intensive farming which are generally used for field irrigation are considered pollutant sources for the environment. These pollutants can be taken by soil and then by plants. The flavonoids are secondary metabolites of plants; therefore their determination in plants is necessary because they have different important roles in body of plants. The spectrophotometric determination of the total flavonoid content from *Triticum aestivum* L. (wheat) and *Secale cereale* L. (rye) treated with two potential environmental pollutants (Nylosan Red N-2RBL - textile azo dye and ampicillin - antibiotic) is presented in this paper. The studied plants were periodically watered with solutions of Nylosan Red N-2RBL and ampicillin respectively, prepared at different ($1.5 \cdot 10^{-5}$, $1.5 \cdot 10^{-4}$, $1.5 \cdot 10^{-3}$, 1 mg/L) concentrations. The total flavonoids from plants were extracted by sonication in a solvent mixture of ethanol:water in a ratio of 80:20 (v/v). The quantitative determination of total flavonoids was performed with an UV-Vis 1800 Shimadzu spectrophotometer using aluminium chloride as reagent and rutin as standard. In both treatments, a decrease in total flavonoid content compared to the control (wheat and rye untreated samples) has been observed.

Keywords: *UV-Vis spectroscopy, flavonoids, textile azo dye, antibiotic, Triticum aestivum* L.*, Secale cereale* L.

INTRODUCTION

The environment is contaminated with numerous organic compounds, used extensively in various fields. Two major classes of environmental pollutants, often mentioned in literature are the textile dyes which are considered toxic [1] and the antibiotics which are pseudo-persistent and may play an important role in the development/maintenance/ transfer/spread of their resistance of bacteria [2].

Textile manufacturing is one of the largest industrial sources generating of waste waters because a high quantity of water is used to obtain the textile products (125-150 L water for 1 kg textile product). Thus, the resulted waste waters contain a large number of water-soluble chemical pollutants that is a serious problem for environment [3, 4]. In the textile industry, more than 100.000 different dyes are commercially available and it is estimated that about 15% of the world dye production is lost during the dyeing process [5]. The most common dyes used in the textile industry are the azo dyes [6]. Intensive irrigation of agricultural lands with water polluted with various industrial effluents severally effects soil fertility and plant growth. Carbohydrate, protein and chlorophyll contents are related to plant growth, a decrease of their content is a clear indication of the toxic nature of the dye industry effluents [7]. In a recent study the effects of the toxic dyes on narrow-leaved cattails were expressed in terms of relative plant growth rate and the appearance of symptoms such as necrosis, and chronic or acute wilting [8].

The other class of pollutants included in this study is the antibiotics that have been used for several decades in human medicine for their antibacterial properties [9]. Antibiotics are also extensively used in veterinary medicine as growth promoters or to prevent diseases. The major concern with agricultural antibiotic usage have been their presence in animal-based food products, the development and spread of antibiotic resistant bacteria, and the transport to aquatic environments from lands amended with antibiotic-laden manure [10]. Several studies have been investigated the potential risks for a range of antibiotics to be taken up from soil by plants, and also have been assessed the potential risks of this exposure route in terms of human health [11]. Other major concern surrounding antibiotics uptake by plants is the contamination of food supply that is associated with health risks [10]. Many studies report the impact of antibiotic exposure to plants. For example sulfadimethoxine was found to reduced significantly root, stalk, and leaf growth in millet (*Panicum miliaceum* L.), pea (*Pisum sativum* L.), corn (*Zea mays* L.), and barley (*Hordeum vulgare* L.) [12, 13]. Also, streptomicyn was found to inhibit chlorophylls synthesis in barley [14] and fluoroquinolone antibiotics to inhibit the photosynthesis of plants [15].

Flavonoids are secondary metabolites categorized as phenolic compounds, widely found throughout plants and prokaryotes. More than 6500 flavonoids have been identified. Flavonoids protect plants against various biotic and abiotic stresses, exhibit a diverse spectrum of biological functions and play an important role in the interaction between plants and environment. Flavonoids have roles against frost, drought resistance and may play a functional role in plant, heat acclimation and freezing tolerance. Flavonoids absorb the harmful UV radiation which can induce cellular damage. Another important role of flavonoids is that they are responsible for protecting the plants from microbes and insects [16]. The determination of flavonoids in plants is necessary because they have an important role in plant development.

This study is focused on the spectrophotometric determination of total flavonoid content in *Triticum aestivum* L. (wheat) and *Secale cereale* L. (rye), treated with the textile azo dye Nylosan Red N-2RBL (NR) and the ampicillin (AMP) antibiotic in four ($1.5 \cdot 10^{-5}$, $1.5 \cdot 10^{-4}$, $1.5 \cdot 10^{-3}$, 1 mg/L) concentrations.

RESULTS AND DISCUSSION

The quantitative analysis of total flavonoid content in plants was performed using UV-Vis spectrophotometer. The method is based on the reaction of total flavonoids with aluminum chloride ($AlCl_3$) resulting a yellow compound. Its maximum of absorbance was identified at 420 nm, being characteristic for flavonoids, expressed as rutin. The calibration plot was drawn through seven points, using concentrations ranging between 0.02 - 0.4 mg/mL. A good correlation coefficient of 0.99942 was obtained. In Figure 1 are presented the calibration plot of rutin and its corresponding UV-Vis spectra.
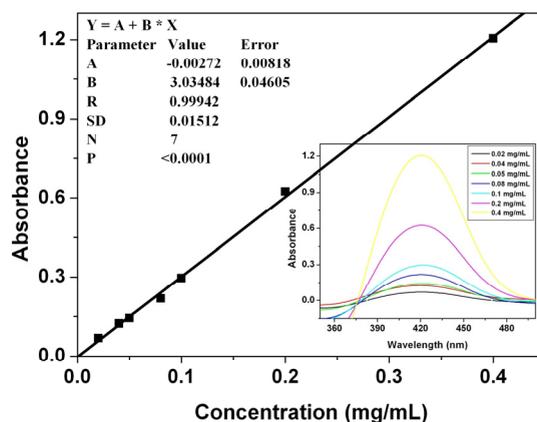
Figure 1. Calibration plot of rutin and its corresponding UV-Vis spectra.

As it was specified in a previous paper [17] for the extraction of total flavonoids from plants, several extraction methods were tested: maceration, microwave assisted solvent and sonication, the last one being the most effective. Some solvent mixtures of ethanol:water in different ratios 100:0, 80:20, 70:30, 60:40, 50:50 and 40:60 (v/v) were tested. The best results were obtained with the ratio 80:20 (v/v) that was used further for the extraction of total flavonoids from wheat and rye treated previously with NR and AMP pollutants.

Further, the extractions of total flavonoids from plants treated with NR and AMP was performed as is described in the experimental section. In both treatments, a decrease of the total flavonoid content compared to control plants (untreated wheat and untreated rye) was observed.

In the case of wheat treated with NR the decrease of total flavonoid content is proportional with the applied concentrations of textile azo dye. The tests on rye do not show so proportional decrease between the concentrations of NR used for watering the plants, compared to wheat tests. In this case it was observed a significant decrease in total flavonoid content for 1 mg/L NR concentration, approximately 65%, and for all other concentrations used the decrease is approximately 50% compared to control (Figure 2).
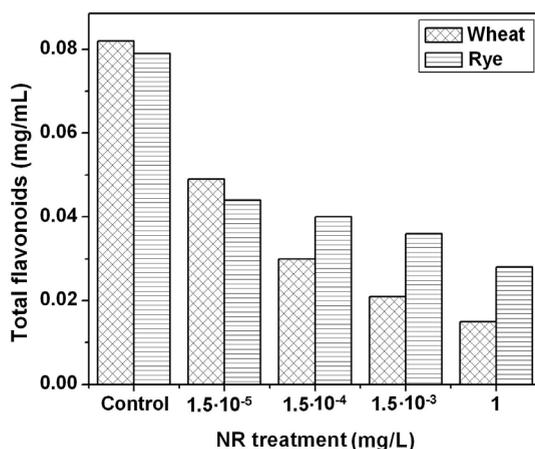
Figure 2. The total flavonoid content in wheat and rye treated with NR in different concentrations.

For AMP treatments on wheat, a decrease of total flavonoid content was observed, approximately 60% compared to control, even at the lowest concentration used for watering the plants ($1.5 \cdot 10^{-5}$ mg/L). The amounts of total flavonoids decrease with increasing the concentration of AMP. The differences between the decreases of total flavonoids are not very significantly influenced by the concentrations of AMP used for plant treatment, especially in the case of rye. This aspect it might be caused by the nature of plant according to that the plants resist differently to these abiotic stress conditions after a certain period of time. In the case of the rye treated with AMP, for all concentrations used in this test, the total flavonoid content decreased with approximately 30% compared to control (Figure 3).

For the identification and quantification of total flavonoids in treated plants, a simple, cheap and easy to use UV-Vis method was used.

The method used was according to Romanian Pharmacopoeia and the quantitative determination was expressed as rutin. For the calibration plot, a correlation coefficient of 0.99942 was obtained.

In both treatments with NR and AMP, a continuous and uniform decrease of total flavonoid content compared to control samples of (untreated wheat and rye) can be observed. The lowest amount of total flavonoids is observed in the case of NR textile azo dye, for both treated plants (wheat and rye). This fact explains that the class of azo dyes is considered more toxic for environment.
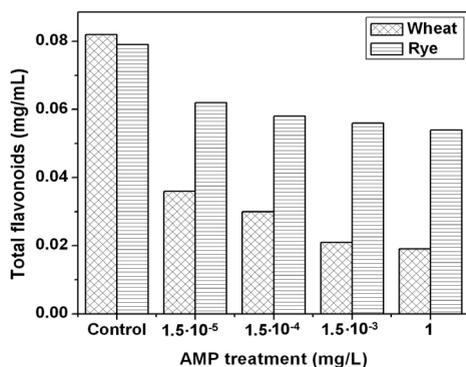
Figure 3. The total flavonoid content in wheat and rye treated with AMP in different concentrations.

The both treatments with NR and AMP reduce more drastically the total flavonoid content in the case of wheat (Figure 4a) in comparison with that of rye (Figure 4b). The two pollutants act practically similar over the wheat (Figure 4a), except for $1.5 \cdot 10^{-5}$ mg/L concentration when ampicillin reduces more total flavonoids than Nylosan Red. In the case of rye (Figure 4b), the azo dye reduces drastically the total flavonoids than the antibiotic. The concentration of total flavonoids decreases slowly according to the increase of NR and AMP concentration respectively.

(a)   (b)
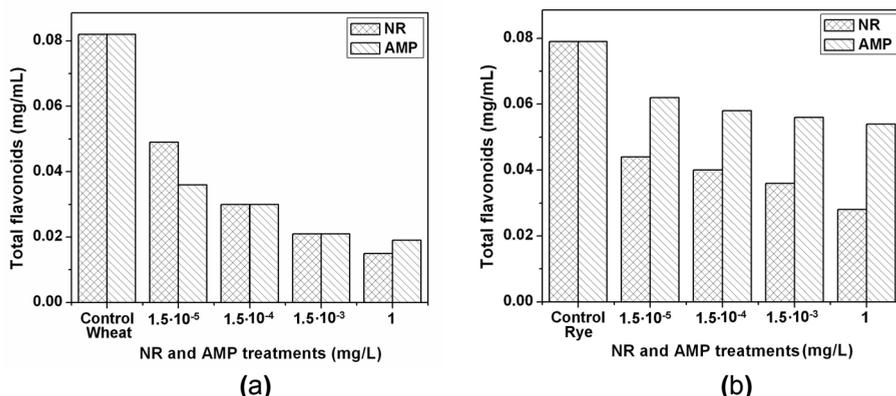
Figure 4. The total flavonoid content in wheat (a) and rye (b) treated with NL and AMP in different concentrations.

CONCLUSIONS

Due to the importance of flavonoids for living organisms, their identification and determination in plant tissue play an important role for plant growth.

The determination of total flavonoid content in wheat and rye, treated with the NR azo-textile dye and the AMP antibiotic at four different concentrations ($1.5 \cdot 10^{-5}$, $1.5 \cdot 10^{-4}$, $1.5 \cdot 10^{-3}$, 1 mg/L) was performed using UV-Vis technique.

UV-Vis spectrophotometric method is a simple, accessible and inexpensive technique, easy to use in order to obtain information concerning the action of studied pollutants over the total flavonoids from plants. The UV-Vis measurements of wheat and rye samples untreated and treated with Nylosan Red N-2RBL (textile azo dye) and ampicillin (beta-lactam antibiotic) give us useful data regarding the possible toxic effects of these two classes of compounds over the plants and by these over the human and animal health. According to our studies, the toxic effects of these compounds depend on the matrix over they have contact and act.

EXPERIMENTAL SECTION

Chemicals: The Nylosan Red N-2RBL textile azo dye [18, 19] and ampicillin sodium salt antibiotic [20] were purchased from Clariant Produkte (Switzerland) AG, respectively from Antibiotice (Romania) (Table 1). Ethanol of 96% was acquired from Nordic Invest (Romania). $AlCl_3$ 99%, sodium acetate (AcNa) used for sample preparation and rutin trihydrate 97% used for quantitative analysis were purchased from Alfa Aesar (Germany). Water purified by a Milli-Q Ultrapure water purification system (Millipore, USA) was used for experiments.

Table 1. Data of selected compounds used for plant treatments.

Common name/ Abbreviation	Nylosan Red N-2RBL/ NR	Ampicillin/ AMP
Class	Azo dye	Antibiotic
Chemical name	Sodium 6-amino-5-[[4-chloro-3-[[(2,4 dimethylphenyl) amino]sulfonyl]phenyl]azo]-4-hydroxynaphthalene-2-sulfonate	Sodium [2S-[2α,5α,6β (S*)]]-6-(aminophenyl-acetamido)-3,3-dimethyl-7-oxo-4-thia-1-azabicyclo[3.2.0]heptane-2-carboxylate
CAS number	71873-39-7	69-52-3
Chemical formula	$C_{24}H_{20}ClN_4O_6S_2Na$	$C_{16}H_{18}N_3O_4SNa$
Molecular weight (g·mol^{-1})	583.01	371.39

Common name/ Abbreviation	Nylosan Red N-2RBL/ NR	Ampicillin/ AMP
Structural formula		
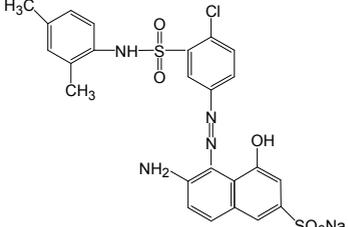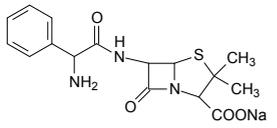
Apparatus: UV-Vis 1800 Shimadzu spectrophotometer with software UV Probe Ver. 2.31.

Plant material: The wheat and rye were the studied plants and they were grown by periodically watering with different solutions of NR and AMP respectively, and monitored during 39 days. Each studied plant was submitted to five different treatments consisting in one for control (untreated) and four treated with pollutant (NR and AMP respectively) at four different concentrations ($1.5 \cdot 10^{-5}$, $1.5 \cdot 10^{-4}$, $1.5 \cdot 10^{-3}$, 1 mg/L). All treatments including controls were carried out in duplicate. The detailed procedure consisted as follows: each test was conducted in aluminum recipients (22×10×6 cm); into each recipient, separately 70 seeds of wheat and rye respectively were sown at a depth of 1 cm; the plants were regularly watered at intervals of 3 days, with 70 mL of NR and AMP solutions of different concentrations. The average temperature of the room where the experiments were done was 22°C. Until the extraction of total flavonoids, the plants were watered 13 times with NR and AMP solutions respectively.

Stock solution: For the quantitative analysis of total flavonoid content in wheat and rye, the calibration plot of rutin was performed. The stock solution of rutin was prepared at 1 mg/mL concentration.

Working solutions: The working solutions of rutin in concentration of 0.02, 0.04, 0.05, 0.08, 0.10, 0.20, 0.40 mg/mL were prepared by diluting the stock solution.

Measuring solutions: The measuring solutions were prepared as follows: 1 mL working solution with 1.5 mL of NaAc 100 g/L, and 2.5 mL AlCl$_3$ 25 g/L, were brought with ethanol to a final volume of 10 mL.

Blank solutions: The blank solutions were consisted in 1 mL working solution, 8 mL water and brought with ethanol to the same final volume of 10 mL.

Sample preparation: The extraction procedure of flavonoids from wheat and rye is presented below. An amount of 0.5 g plant material was powdered with liquid nitrogen and then was added 20 mL of ethanol:water

mixture in ratio of 80:20 (v/v). For maceration, the extracts were kept 10 min in oven at temperature of 35°C, and then were sonicated for 30 minutes at the same temperature. Each extract was filtered through Macherey-Nagel filters (MN 640 d·ø 125 mm) and it was brought to a final volume of 25 mL with the same solvent mixture. The quantitative determination of total flavonoids was done by UV-Vis method using $AlCl_3$ as reagent and rutin as standard [21].

Data handling: All data shown in figures were performed using ORIGIN 8 (OriginLab Corporation, MA, USA) software.

ACKNOWLEDGMENTS

REFERENCES

1. H. Moawad, W.M. Abd El-Rahim, M. Khalafallah, *Journal of Basic Microbiology*, **2003**, *43*, 218.

2. B. Li, T. Zhang, Z. Xu, H.H.P. Fang, *Analytica Chimica Acta*, **2009**, *645*, 64.

3. L. Rafaëlly, S. Héron, W. Nowik, A. Tchapla, *Dyes and Pigments*, **2008**, *77*, 191.

4. L. Wojnárovits, E. Takács, *Radiation Physics and Chemistry*, **2008**, *77*, 225.

5. A.B. Prevot, D. Fabbri, E. Pramauro, C. Baiocchi, C. Medana, *Journal of Chromatography A*, **2008**, *1202*, 145.

6. Y.H. Lee, S.G. Pavlostathis, *Water Research*, **2004**, *38*, 1838.

7. N. Puvaneswari, J. Muthukrishnan, P. Gunasekaran, *Indian Journal of Experimental Biology*, **2006**, *44*, 618.

8. S. Nilratnisakorn, P. Thiravetyan, W. Nakbanpote, *Science of the Total Environment*, **2007**, *384*, 67.

9. F. Tamtam, F. Mercier, B. Le Bot, J. Eurin, Q.T. Dinh, M. Clément, M. Chevreuil, *Science of the Total Environment*, **2008**, *393*, 84.

10. H. Dolliver, K. Kumar, S. Gupta, *Journal of Environmental Quality*, **2007**, *36*, 1224.

11. K. Kümmerer, *Chemosphere*, **2009**, *75*, 417.

12. L. Migliore, G. Brambilla, S. Cozzolino, L. Gaudio, *Agriculture, Ecosystems and Environment*, **1995**, *52*, 103.

13. L. Migliore, G. Brambilla, P. Casoria, C. Civitareale, S. Cozzolino, L. Gaudio, *Agriculture, Ecosystems and Environment*, **1996**, *60*, 121.

14. E.B. Yaronskaya, E.R. Gritskevich, N.L. Trukhanovets, N.G. Averina, *Russian Journal of Plant Physiology*, **2007**, *54*, 388.

15. L. Aristilde, A. Melis, G. Sposito, *Environmental Science & Technology,* **2010**, *44,* 1444.

16. A. Samanta, G. Das, S.K. Das, *International Journal of Pharmaceutical Science and Technology*, **2011**, *6*, 12.

17. M.L. Soran, O. Opriş, F. Copaciu, C. Varodi, *Processes in Isotopes and Molecules (PIM 2011)*, *AIP Conference Proceedings*, **2012**, *1425*, 47, doi 10.1063/1.3681963.

18. A. Reffas, V. Bernadet, B. David, L. Reinert, M. Bencheikh Lehocine, M. Dubois, N. Batisse, L. Duclaux, *Journal of Hazarduos Materials*, **2010**, *175*, 779.

19. www.textile.clariant.com

20. www.sigmaaldrich.com

21. ***, "Romanian Pharmacopoeia", X-th edition, Medical Publishing, Bucharest, **1993**.

GS-MS AND FTIR STUDIES OF THE LIQUID PRODUCTS OBTAINED BY THERMAL AND CATALYTIC DEGRADATION OF POLYSTYRENE WASTE*

MIUŢA RAFILA FILIP[a,b,*], AURELIA POP[b], TIBERIU RUSU[a]

ABSTRACT. In this paper, gas chromatography mass spectrometry (GC-MS) and Fourier-transform infrared spectrometry (FTIR) were used to study the liquid products obtained from the thermal and catalytic degradation of polystyrene waste (PS) in order to establish the conditions for the best conversion degree of polystyrene waste into styrene monomer. The polystyrene waste was submitted to a thermal degradation process at 380°C and 430°C respectively, in absence and in presence of different types of metallic oxides as catalysts in a ratio of 1/10 in mass, catalyst/PS. The used catalysts were: amphoteric solids, two types of alumina; acidic solid, silica gel and basic solids, calcium oxide and copper oxide 13% deposited on alumina. Gas and liquid products and a residue were obtained by the degradation process of polystyrene waste. The yields for all obtained liquid products at both temperatures were between 83 and 89%. The GC-MS results showed that the liquid products contain mainly toluene, ethylbenzene, styrene monomer, (1-methylethyl) benzene and α-methylstyrene. The FTIR spectra of liquid products indicated the specific vibration bands of the functional groups of their compounds. The obtained results showed that the most efficient catalyst used in the thermal degradation of polystyrene waste was silica gel, for which it was obtained the largest amounts of styrene monomer at both temperatures (68.76% at 380°C and 73.16% at 430°C).

Keywords: polystyrene waste, thermal and catalytic degradation, GC-MS, FTIR, styrene monomer

INTRODUCTION

Polystyrene and its related products are not biodegradable in the natural environment and cause serious environmental problems. The polystyrene waste represents 10% of the plastic packaging in the residential waste stream. Therefore their recycling is important for both economical and ecological reasons.

---

* This paper was presented at the "17th International Symposium on Separation Sciences. News and Beauty in Separation Sciences, Cluj-Napoca, Romania, September 5-9, 2011"
[a] Technical University of Cluj-Napoca, Faculty of Materials and Environmental Engineering, 103-105 Muncii Avenue, 400641, Cluj-Napoca, Romania
[b] Babeş-Bolyai University, Raluca Ripan Institute for Research in Chemistry, 30 Fântânele Street, 400294 Cluj-Napoca, Romania, * *filip_miuta@yahoo.com*

Polystyrene is one of the most used materials in the modern plastic industry due to its excellent physical properties and low cost. The recycling of polystyrene can be done using mechanical, chemical and thermal methods. The liquid and gaseous products resulted from the degradation process of polystyrene is highly dependent on the reaction conditions. The catalysts used for the degradation are selective in the production of the liquid and gaseous products. Catalytic cracking has the advantage of leading to the high contents of products having higher commercial value [1, 2].

The polystyrene pyrolysis was investigated at a relative low temperature range of 370 to 400°C using a batch-type stirred vessel. The oil products were identified and determined by gas chromatography mass spectrometry (GC-MS) technique. The main products were single aromatic species (styrene ca. 70 wt.%, α-methylstyrene, toluene) and double aromatic species (1,3-diphenylpropane and 1,3-diphenylbutene) [3]. The study of polystyrene degradation was made by continuous distribution kinetics in a bubbling reactor. Molecular-weight distributions of products were determined by gel permeation chromatography and indicate the random and chain scission mechanism. The applied mathematics model accounts for the mass transfer of vaporized products from polymer melt to gas bubble [4]. The pyrolysis of polystyrene waste in a fluidized-bed reactor generated the residue that is an important factor in the recovery of styrene monomer and oil from polystyrene waste. The optimum temperature was found to be 550°C for the recovery of the maximum oil yields of 19-20%, styrene monomer of 10-11% and gas products by using of two types of ZSM-5 zeolites [5]. The catalytic transformation of polystyrene waste into hydrocarbons with higher commercial value was almost complete between 400-500°C by using H-ZSM-11 and Zn-ZSM-11 modified zeolites. Thus the authors obtained a quantity of liquid hydrocarbons greater than 94.96 wt% and a lower quantity of solid residues (<0.3 wt.%). The main liquid hydrocarbons of polystyrene degradation were 1,5-hexadiene and styrene, and in minor proportion indane and α-methylstyrene, these compounds being very important in the polymer technology and fine chemical field. The reaction products were analyzed by gas chromatography mass spectrometry [6]. The halloysite catalysts presented a good catalytic performance for the degradation of polystyrene. Styrene and ethylbenzene were the main components of liquid products obtained with the selectivity over 99% determined by GC-MS. The high selectivity to styrene was observed at higher temperatures. Acidity of catalysts, reaction temperature and contact time were necessary to control the product distribution between styrene monomer and ethylbenzene [7]. Pyrolysis of high-impact polystyrene over the zeolite Al-MCM-41 showed an important decomposition that depends on polymer/catalyst contact and it is observed by TGA in three steps. The results obtained showed the possibility of using TGA as a fast tool in order to characterize different

styrene-butadiene copolymers [8]. The catalytic pyrolysis of polystyrene over base modified silicon mesoporous molecular sieve (K_2O/Si-MCM-41) was made at 400°C when the conversion of polystyrene was 90.53%, the yield of liquid products was 85% and the yield of styrene reached of 69.02%. The reaction products were analyzed by gas chromatography: GC-MS, GC-FID (flame ionization detector) [9]. The dealuminated HY zeolites were successfully applied for expandable polystyrene waste degradation in a batch operation at 375°C. The HY catalyst showed an increase in oil yield with a concomitant decrease in coke and residual products. The styrene monomer-to-styrene dimer ratio increases notable over steam-treated zeolite HY-700 and the conversion and product distribution depend on acidity of zeolites [10]. Catalytic degradation of polystyrene into liquid fuels has been carried out in a simple experimental set-up using Al_2O_3 supported Sn and Cd catalysts. The major component in liquid product was the aromatic hydrocarbon with at least 80% selectivity to ethylbenzene. The liquid product is suitable to be used as fuel with kerosene [11]. Styrene monomer recovery from polystyrene waste was studied in supercritical solvents by a novel fast process for to avoid coke formation. The highest yield of styrene obtained from polystyrene in supercritical toluene at 360°C for 20 min reached 77 wt.% [12]. Benzene was used as a solvent for the degradation of polystyrene waste in the presence of hydrogen at elevated temperature and pressure and of metal oxide catalysts. The most suitable catalyst for polystyrene degradation in hydrogen environment was found manganese dioxide, a catalyst with higher reactivity. The final product was analyzed by gas chromatography and it contains mainly methanol, benzene, and styrene monomer [13]. The co-pyrolysis of waste polystyrene with coal was investigated at high temperature obtained by microwave copper interaction. The obtained liquid products were the oily fraction and the aqueous fraction containing sulfide. The oily liquid product was analyzed using GC-MS and it was found that it contains mainly aromatic compounds in a narrow range [14].

In order to establish the characteristics of products obtained from plastic waste recycling, various analytical techniques are mentioned in literature, namely: gas chromatography, Fourier transform infrared spectroscopy (FTIR), Raman spectroscopy, size exclusion chromatography, energy-dispersive X-ray fluorescence spectroscopy, thermal analysis, headspace solid-phase microextraction, pyrolysis-GC with mass spectrometry detection (Py-GC-MS) [15-18].

In this work, GC-MS and FTIR techniques have been used to investigate the liquid products obtained from the thermal and catalytic degradation of polystyrene waste (PS) using different types of solid catalysts (amphoteric, acidic, basic). The paper describes the effect of the catalysts with different textural properties and the effect of temperature over the degradation of polystyrene waste and its conversion into styrene monomer.

RESULTS AND DISCUSSION

The textural properties of the calcined catalysts were determined by nitrogen adsorption-desorption isotherms at 77 K. Firstly the catalysts were degassed under vacuum at 160ºC for 5 hours and then their surface area was determined by BET procedure. The external surface area and micropore volume were obtained applying the t-plot (de Boer) method. The total pore volume was measured at relative pressure $P \cdot P_0^{-1} = 0.99$ and it was obtained by the BJH (Barrett, Joyner, Halenda) desorption method.

In Table 1 are presented the structural parameters of the metal oxide catalysts used for thermal degradation of polystyrene waste.

Table 1. The structural parameters of metal oxide catalysts

Catalysts	Specific surface area, BET[a], $m^2 g^{-1}$	Micropore area[b] $m^2 g^{-1}$	Micropore volume[b] $cm^3 g^{-1}$	Total pore area[c] $m^2 g^{-1}$	Total pore volume[c] $cm^3 g^{-1}$	Average pore diameter[c] nm
SiO_2	205.69	57.56	0.00560	301.79	0.535	7.1
CuO/Al_2O_3	158.64	61.18	0.01040	251.77	0.473	7.5
Al_2O_3 a	92.26	12.64	0.00030	48.59	0.063	5.2
Al_2O_3 b	40.70	6.48	0.00020	34.76	0.053	6.1
CaO	4.85	1.46	0.00010	4.56	0.029	25.3

[a] BET method; [b] t-plot method; [c] BJH desorption method

The thermal degradation experiments were conducted at 350°C and 430°C respectively operating temperature in absence and in presence of the metal oxide catalysts. The obtained thermal degradation products were classified in three groups: liquid, gas and residue. As known, the thermal and catalytic degradation yield of polymers depends on many parameters such as: temperature, polymer and catalyst type, experimental reactor, residence time of volatiles in reactor etc. [1, 2]. The temperature and the catalyst play an important role in the distribution of compounds of the liquid products obtained. The temperature is increased gradually to produce a gradual melting of the polymer. The polystyrene bed temperature is considered the degradation temperature of polystyrene waste. In order to compare the effect of catalyst on the yield and distribution of end-products the textural properties of the catalysts were taken into consideration.

The obtained liquid products from the catalytic degradation of the polystyrene waste, at 380ºC and 430ºC respectively, have different colours due to the type of used catalyst and the degradation temperature as it is presented in Figure 1. The code of liquids is according to the used catalyst for PS degradation. For example: PS-SiO_2 is the liquid product obtained at the thermal degradation of polystyrene waste in the presence of silica gel catalyst or PS is the liquid product obtained at the thermal degradation of polystyrene waste in absence of the catalyst.

The yields of the obtained products at thermal and catalytic degradation of polystyrene waste, calculated according to the equation (1-3), are presented comparatively in Figure 2.
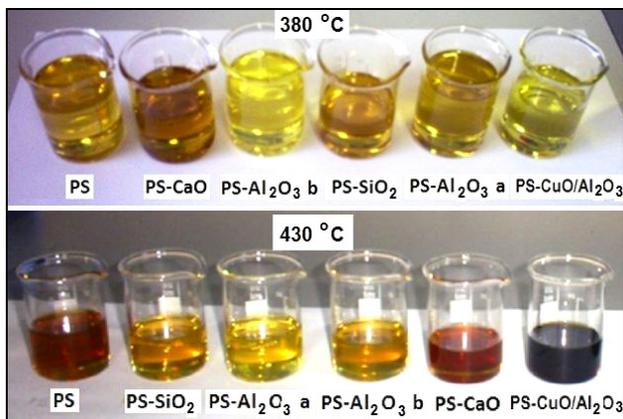
Figure 1. The liquid products obtained at the thermal and catalytic degradation of polystyrene waste.
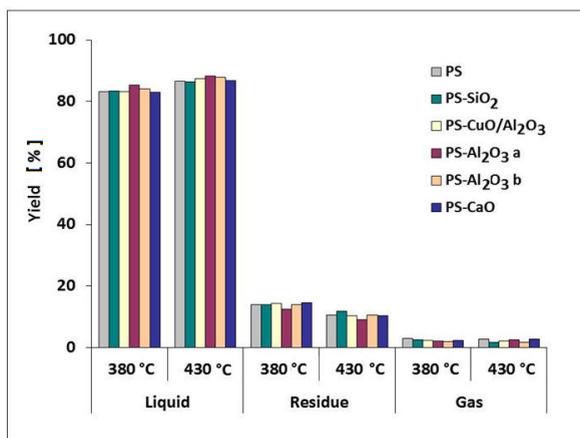
Figure 2. The yields of thermal degradation products of polystyrene waste in absence and in presence of catalysts.

The results presented in Figure 2 show that the yields of liquid products obtained by the thermal and catalytic degradation of the polystyrene waste have high values between 83 and 89%. The yield of liquids increases with increasing degradation temperature while the residue yield decreases with increasing temperature. Also, the yield of the obtained gaseous products has approximately equal values at both studied temperatures.

31

GC-MS Analysis

For the identification and quantification of hydrocarbons, the liquid products have been studied by GC-MS and by area percentage of TIC (total ion chromatogram). In Figure 3 are given the GC-MS chromatograms of all studied liquid products.
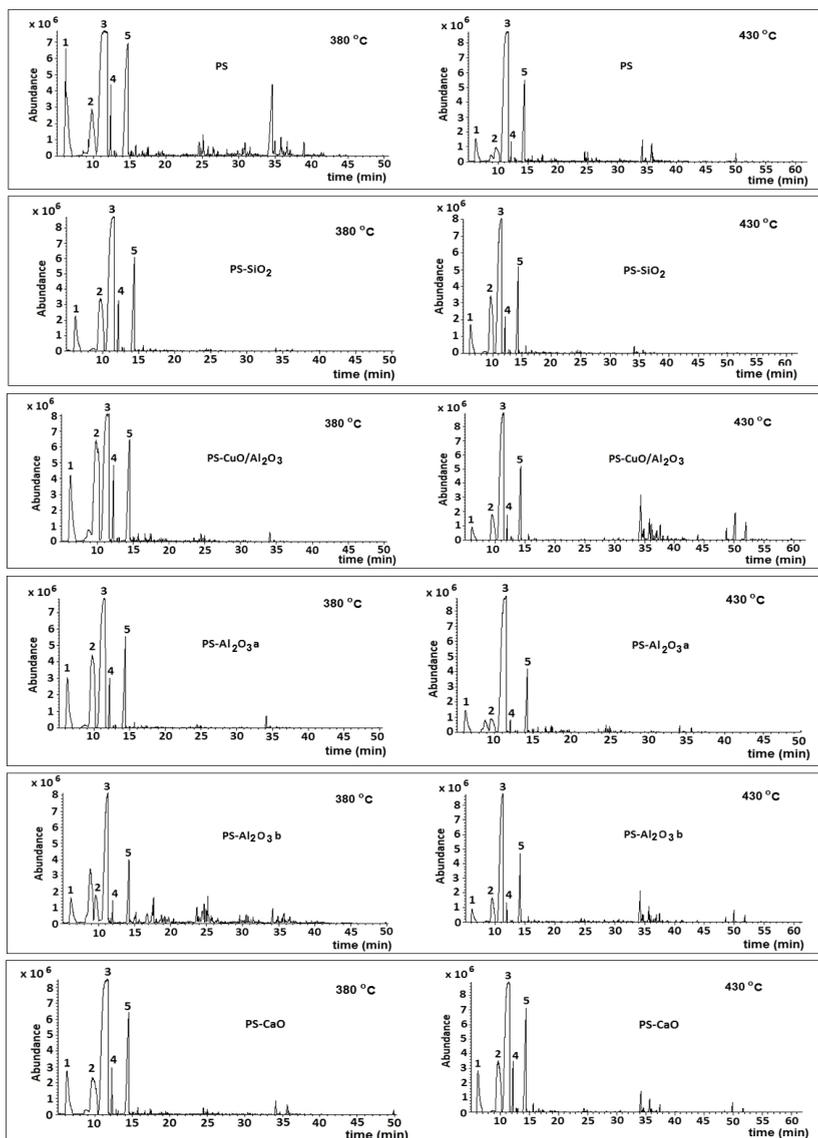
Figure 3. The GC-MS chromatograms of liquid products obtained by thermal and catalytic degradation of polystyrene waste.

The obtained liquids contain mainly the compounds: toluene (**1**, 6.28 min), ethylbenzene (**2**, 9.69 min), styrene monomer (**3**, 11.27 min) (up to 70%), 1-methylethylbenzene (**4**, 12.42 min) and α-methylstyrene (**5**, 14.40 min). In all cases, the styrene monomer is the major degradation product.

The compounds were identified by comparison of their mass spectra with those from the DATABASE/wiley6.1 spectra library. For example, in Figure 4 are shown the recorded mass spectra of the compounds (toluene, ethylbenzene, styrene monomer, α-methylstyrene) from the liquid products obtained from thermal degradation at 380°C of polystyrene waste in presence of alumina catalyst (Al_2O_3 a). For all studied liquids, the mass spectrum of each peak (compound) was compared with the corresponding mass spectrum from data spectra library.
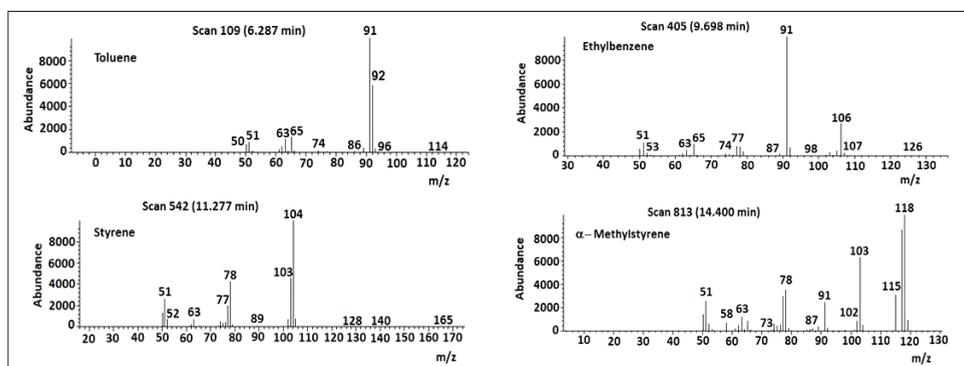
Figure 4. The mass spectra of compounds from liquid product obtained at thermal degradation at 380ºC of polystyrene waste in presence of alumina catalyst (Al_2O_3 a).

In the mass spectra from Figure 4 it can be observed the specific ions of each compound obtained by MS fragmentations: toluene (m/z 91, 92), ethylbenzene (m/z 91, 106), styrene monomer (m/z 78, 104), α-methylstyrene (m/z 78, 103, 118). These data certify the presence of these compounds in the liquid product.

Besides these main compounds of the studied liquid products, the GC-MS chromatograms contain some small peaks of other compounds found in smaller quantities. In some cases (PS at 380ºC, PS-CuO/Al_2O_3 at 430ºC or PS-Al_2O_3 b at 380ºC) the thermal degradation of polystyrene waste produces these secondary compounds like heptylbenzene (25.10 min) and 1,1'-(1,3-propanedil)*bis*-benzene (34.60 min). Their formation is desirable to be minimized by using the catalysts.

The GC-MS results of liquid products obtained from thermal and catalytic degradation of polystyrene waste are presented in Figure 5.

The results show that the temperature and the type of catalyst affect the quantity of the obtained styrene monomer. The largest quantities of the styrene monomer (68.76%, 380°C; 73.16%, 430°C) are obtained from thermal degradation of polystyrene waste in the presence of silica gel catalyst at both degradation temperatures. These results are due to the structural properties of the silica gel that is a solid acidic catalyst with a high BET specific surface area (205.69 m$^2 \cdot$g^{-1}) and a total pore area of 301.79 m$^2 \cdot$g^{-1}, respectively (Table 1).

The thermal degradation at 380°C of polystyrene waste in presence of CuO/Al$_2$O$_3$, a basic catalyst, produces the styrene monomer of 49.63% and a higher quantity of 21.38% ethylbenzene against the other cases. Instead, at 430°C is obtained a larger quantity of 67.68% styrene monomer.
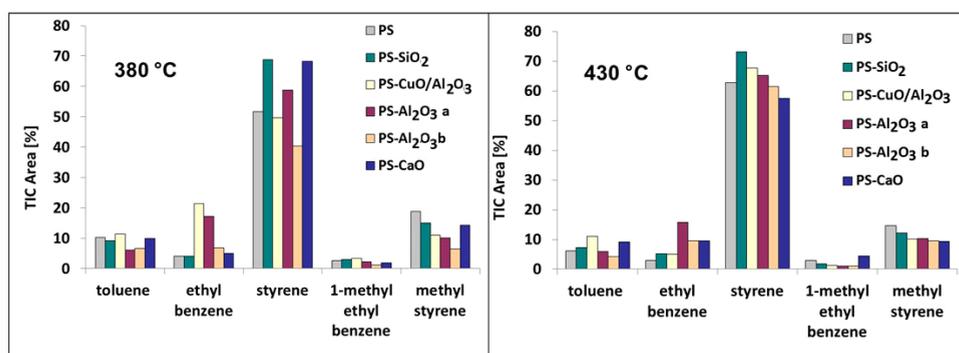
Figure 5. The distribution of compounds (TIC area, %) of liquid products obtained by the thermal and catalytic degradation of polystyrene waste.

The quantity of the styrene monomer obtained by the thermal degradation of polystyrene waste in presence of aluminas, amphoteric catalysts, is influenced by the structural properties and the temperature. The quantity of styrene monomer obtained using (Al$_2$O$_3$ a) catalyst with a higher BET specific surface area is greater than that obtained in the presence of (Al$_2$O$_3$ b) catalyst with a lower BET specific surface area.

The CaO is a basic solid catalyst with a low value for the BET specific surface area and the total pore volume, but with a high average pore diameter (Table 1). This type of catalyst produces a high quantity of styrene monomer at the temperature of 380°C as one can see in Figure 4.

We can conclude that the most efficient catalyst used in this thermal degradation method of polystyrene waste for both degradation temperatures is silica gel, an acid solid catalyst. Also, for the CaO, a basic solid catalyst it was obtained at 380°C a quantity of styrene monomer comparable with that obtained in presence of silica gel catalyst.

FTIR Analysis

Fourier-transform infrared spectrometry (FTIR) is able to quickly discern different bond vibration modes of a molecule. Thus, it is widely used to interpret the molecular characteristics and structure of compounds [20].

In Figure 6 are presented the FTIR spectra of the liquid product resulted from the thermal degradation of polystyrene waste in presence of SiO_2 at both temperatures. In all cases, the FTIR spectra of liquid products contain the same absorption bands. The main absorption bands and the type of the characteristic vibrations (stretching, bending, rocking) of the functional groups of the liquid products obtained from thermal and catalytic degradation of waste polystyrene are presented in Table 2.
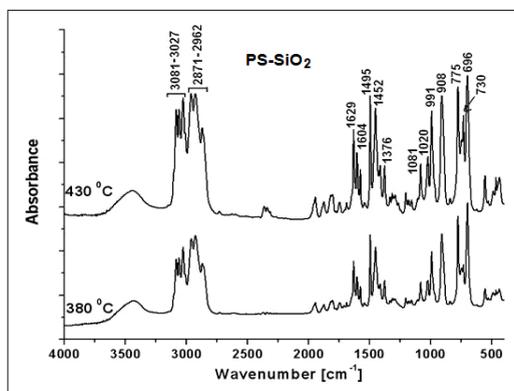
Figure 6. The FTIR spectra of obtained liquid fractions from thermal degradation of polystyrene waste in presence of SiO_2 catalyst.

Table 2. The assignments of absorption bands of studied liquid fractions [20]

Group frequency (cm^{-1})	Functional group	Assignment
3081,3060,3027	C-H aromatic ring	C-H stretching
2962	methyl	ν_{as} (CH_3), C-H asymmetric stretching
2925	methylene	ν_{as} (CH_2), C-H asymmetric stretching
2871	methyl	ν_s (CH_3), C-H symmetric stretching
1629	vinyl	ν (C=C), stretching (origin CH=CH)
1604,1495	aromatic ring	aromatic ring
1452	C-CH_3	δ_{as} C-CH_3 asymmetric bending
1376	methyl	C-H umbrella bending mode
1081, 1020	vinyl	C-H in plane bending
991, 908	vinyl	C-H out-of-plane bending
730	aromatic ring	aromatic ring rocking
775, 696	mono substituted aromatic ring	C-H out-of-plane bending of aromatic ring

In FTIR spectra of liquids products it can be observed three bands at 3081, 3060 and 3027 cm^{-1} that are assigned of the vibration of C-H bond in the aromatic ring. In addition, there are strong bands present in the region of 675–900 cm^{-1} that confirm the presence of aromatic compounds.

The presence of methyl groups are indicated by the bands from 2962 and 2871 cm^{-1} that correspond to the asymmetric and symmetric stretching vibrations of C-H bond. The band from 1376 cm^{-1} is assigned to umbrella bending mode vibration of C-H bond. The asymmetric stretching vibration of C-H bond in methylene group can be observed at 2925 cm^{-1}. The intense absorption band from 1629 cm^{-1} may be assigned to the characteristic vibrational mode of C=C bond (origin CH=CH), and those of 991 and 908 cm^{-1} are attributed to the C-H out-of-plane bending vibrations corresponding to the vinyl group. The bands at 1452 cm^{-1} can be assigned to asymmetric and symmetric bending vibration of C-CH$_3$ group. The aliphatic functional groups observed in the FTIR spectra indicate that these aliphatic groups are probably present as alkyl groups attached to the aromatic rings.

The FTIR results of the liquid product from the thermal and catalytic degradation of polystyrene waste are in good agreement with those obtained by GC-MS analysis of the liquid product.

CONCLUSIONS

Gas chromatography - mass spectrometry (GC-MS) and Fourier transform infrared spectrometry (FTIR) were used in this work to study the selectivity of different catalysts in the conversion of polystyrene waste into styrene monomer.

The thermal and catalytic degradation process of polystyrene waste have been performed at 380°C and 430°C, in absence and presence of five metallic oxide catalysts: amphoteric solids, two types of aluminas (Al$_2$O$_3$); acidic solid, silica gel (SiO$_2$); basic solids, calcium oxide (CaO) and copper oxide 13% deposited on alumina (CuO/Al$_2$O$_3$). The structural parameters of these catalysts influence the thermal degradation process of polystyrene waste by obtained products. Therefore, the yields of obtained liquid products have been calculated between 83.13% and 88.39% and these results depend on the experimental conditions, temperature and the type of catalysts.

The GC-MS results show that the obtained liquid products contain mainly toluene, ethylbenzene, styrene monomer (up to 73.16%), 1-methyl-ethylbenzene and α-methylstyrene. The silica gel, an acid solid catalyst has been founding the most efficient catalyst in this thermal degradation method of polystyrene waste at both degradation temperatures.

The FTIR spectra of liquid products of thermal and catalytic degradation of polystyrene waste show the presence of the functional groups methyl, methylene, aromatic ring and vinyl double bond and C-CH$_3$ bond from branched structure of the compounds from liquid products. All FTIR results are in good correlation with those obtained by GC-MS.

These techniques are very suitable for the characterization of liquid products obtained at the thermal and catalytic degradation of polystyrene waste and for the establishment of its further applications as feed stocks in chemical industry or for the obtaining of styrene monomer.

The results obtained show that the thermal degradation method of polystyrene waste in presence of silica gel catalyst can be used as recycling method of waste polystyrene into styrene monomer.

EXPERIMENTAL SECTION

Materials

For this study, polystyrene waste, namely vessel detergent boxes and disposable glass and plates, were used to study thermal and catalytic degradation into styrene monomer. These wastes were cut into small pieces (approximately 5 x 5 mm) and used as raw materials for the degradation process.

The metal oxide catalysts (Table 1) used for the degradation of polystyrene waste were two amphoteric solids (acidic and basic alumina, Al_2O_3), one acidic (silica gel, SiO_2), and two basic (calcium oxide, CaO; copper oxide 13% deposited on alumina, CuO/Al_2O_3) respectively. The aluminas (acidic alumina pH = 4.2, Al_2O_3 a; basic alumina pH = 9, Al_2O_3 b,) and the silica gel (SiO_2) used in this study are stationary phases for thin layer chromatography and have been produced at the *Raluca Ripan* Institute for Research in Chemistry Cluj-Napoca, Romania. Calcium oxide (CaO) was purchased from Fluka and copper oxide 13% deposited on alumina (CuO/Al_2O_3) as miniballs with a diameter of about 1 mm, from Aldrich.

The studied catalysts were subjected to a heating treatment in an oven in two stages: first at 200°C for 2 hours to remove the adsorbed water from the mesopores, then followed another heat treatment at 500°C for 5 hours to activate the active centres.

After the thermal treatment the initial properties of alumina and silica gel have been modified. The pH values of both aluminas became 8.55. This can be explained by the removing of chlorine from the acidic alumina surface. These calcined aluminas are amphoteric solids with different textural properties and they were used as catalysts. Over 200°C, the thermal treatment of silica gel determine changes on its structure due to the removing of the water entrapped by hydrogen bonds from the hydroxyl groups of the surface [19].

The textural properties of the calcined catalysts were determined by nitrogen adsorption-desorption isotherms at 77 K using a Micromeritics TriStar II 3020 instrument.

Thermal Degradation Procedure

Thermal degradation of the polystyrene waste was performed in a laboratory installation equipped with: glass vessel, heating mantle with thermostat, thermometer with thermocouple, condenser for cooling and condensing of the resulted gases, graduated cylinder to collect the liquid product and a special bag for the collection of the gaseous product. An amount of 30 g from polystyrene waste was subjected to the thermal degradation at operating temperature. The catalyst was added in the vessel in a mass ratio of 1/10 to the polystyrene waste. Before the starting of the polystyrene degradation procedure, the nitrogen was continuously passed through the installation with a flow rate of 30 mL min^{-1} for several minutes to eliminate the air. Then it was followed by the thermal decomposition step by increasing the temperature gradually up to 380°C and 430°C respectively, in order to produce a gradual melting of the polymer. The degradation temperature was considered the temperature of the polystyrene bed. The condensable gases were condensed in a water cooled condenser (4°C) and collected as a liquid product. The incondensable gases were collected in a special bag as a gaseous product. The small quantity of residue and the used catalyst remain in the glass vessel. The liquid product were measured and analysed by GC-MS and FTIR.

Analysis of Products

The yields of obtained products by PS thermal and catalytic degradation (L – liquid products, R – residue and G – gaseous products) were calculated using the equations 1-3. The liquid product and the residue were weighed directly.

$$L(wt.\%) = \frac{m_L}{M_{PS}} \cdot 100 \qquad (1)$$

$$R(wt.\%) = \frac{m_R}{M_{PS}} \cdot 100 \qquad (2)$$

$$G(wt.\%) = 100 - (L + R) \qquad (3)$$

where m_L is the weight of liquid product (g), m_R the weight of residue (g) and M_{PS} the weight of polystyrene waste (g).

The liquid product was subjected to dehydration with $MgSO_4$ in order to remove any traces of water that can affect the GC-MS and FTIR analyses. GC-MS measurements were made using a Hewlett Packard HP 5890 Series II GC gas chromatograph interfaced to a Hewlett Packard 5972 Series mass selective detector with a DB-5MS capillary column (30 m x 0.53 mm ID x 1.50 µm film thickness). Temperature of the injector was 250°C. MS mode was carried out in full scan, with the scan range of 1.6-700 amu and the scan speed up to 1800 amu·s^{-1}. The ionization intensity of 70 eV and the multiplier voltage of

1823.5 V were used. Oven temperature program was as follows: the initial temperature of 40°C was held for 4 min, increased with 5°C min^{-1} at 280°C and maintained at this final temperature for 10 min. The volume of injected sample was 1 μL. The acquisition of chromatographic data was performed by means of the HPchem software. All mass spectra were interpreted using the library spectra (DATABASE/wiley6.1).

The liquid product was measured also by spectrometric infrared technique with a JASCO-FTIR 610 Fourier-transform infrared spectrometer in the 4000-400 cm^{-1} wave number range, using the liquid film technique. The FTIR spectra of all the studied liquid products were registered at room temperature.

REFERENCES

1. K. Pielichowski, J. Njuguna, "Thermal Degradation of Polymeric Materials", Rapra Technology Limited, Shawbury, **2005**.

2. T. Maharana, Y.S. Negi, B. Mohanty, *Polymer-Plastics Technology and Engineering*, **2007**, *46*, 729.

3. Y.S. Kim, G.C. Hwang, S.Y. Bae, S.C. Yi, S.K. Moon, H. Kumazawa, *Korean Journal of Chemical Engineering*, **1999**, *16*, 161.

4. W.S. Cha, S.B. Kim, B.J. McCoy, *Korean Journal of Chemical Engineering*, **2002**, *19*, 239.

5. C.G. Lee, J.S. Kim, P.S. Song, G.S. Choi, Y. Kang, M.J. Choi, *Korean Journal of Chemical Engineering*, **2003**, *20*, 133.

6. L.B. Pierella, S. Renzini, D. Cayuela, O.A. Anunziata, *2nd Mercosur Congress on Chemical Engineering; 4th Mercosur Congress on Process Systems Engineering*, **2005**, http://www.enpromer2005.eq.ufrj.br/lng/en.

7. J.W. Tae, B.S. Jang, J.R. Kim, I. Kim, D.W. Park, *Solid State Ionics*, **2004**, *172*, 129.

8. A. Marcilla, A. Gémez-Siurana, J.C. García Quesada, D. Berenguer, *Polymer Degradation and Stability,* **2007**, *92*, 1867.

9. C. Xie, F. Liu, S. Yu, F. Xie, L. Li, S. Zhang, J. Yang, *Catalysis Communications*, **2008**, *9*, 1132.

10. V.R. Chumbhale, J.S. Kim, W.Y. Lee, S.H. Song, S.B. Lee, M.J. Choi, *Journal of Industrial and Engineering Chemistry,* **2005**, *11*, 253.

11. A. Ramli, D.R. Abu Bakar, *Journal of Applied Sciences*, **2011**, *11*, 1346.

12. K. Huang, L. Tang, Z. Zhu, C. Zhang, *Polymer Degradation and Stability,* **2005**, *89*, 312.

13. P. Tivary, C. Guria, *Journal of Polymer and the Environment*, **2010**, *18*, 298.

14. Z. Hussain, K.M. Khan, N. Basheer, K. Hussain, *Journal of Analytical and Applied Pyrolysis,* **2011**, *90*, 53.

15. F. Vilaplana, A. Ribes-Greus, S. Karlsson, *Analytica Chimica Acta*, **2007**, *604*, 18.

16. N. Miskolczi, L. Bartha, *Journal of Biochemical and Biophysical Methods,* **2008**, *70*, 1247.

17. P. Kusch, G. Knupp, *Journal of Polymer and the Environment,* **2004**, *12*, 83-87.

18. R. Rial-Otero, M. Galesio, J.L. Capelo, J. Simal-Gándara, *Chromatographia*, **2009**, *70*, 339.

19. Y. Sander González, C. Costa, C.M. Márquez, P. Ramos, *Journal of Hazardous Materials,* **2011**, *187*, 101.

20. B.C. Smith, "Infrared Spectral Interpretation. A Systematic Approach", CRC Press, Boca Raton, **1999**.

RADIOCHEMICAL DETERMINATION OF URANIUM FOR ENVIRONMENTAL SAMPLES BY OPEN TUBULAR LIQUID CHROMATOGRAPHY AND ALPHA SPECTROMETRY*

DAN CONSTANTIN NIŢĂ[a,*], OANA ALEXANDRA RUSU[a], LIVIU DOREL BOBOŞ[b], CONSTANTIN COSMA[a]

ABSTRACT. Uranium-series analyses are an essential component of many research projects in Earth and environmental science and also for the protection of public health. In this work a simple and fast method for the determination of uranium isotopes using open tubular liquid chromatography and alpha spectrometry is described. The uranium standard solution was acidified at pH 1 with hydrochloric acid before separation. A strong base anion resin Dowex AG 1X8 was used for the separation of target compounds. The elution of uranium at different concentrations of hydrochloric acid (0.05; 0.10 and 0.15 M) was tested. After its separation from thorium, the uranium is electrodeposited onto stainless steel discs and then measured by alpha spectrometry. The measurements were performed using an ORTEC SOLOIST alpha spectrometer with PIPS (Passivated Implanted Planar Silicon) detector and the data acquisition was made by ASPEC-927 Dual Multichannel. The results of performed experiments showed that Dowex AG 1X8 resin is a selective sorbent for uranium and it can be used for the preconcentration of uranium isotopes from different aquatic samples.

Keywords: uranium, separation, open tubular liquid chromatography, alpha spectrometry

INTRODUCTION

The identification and determination of uranium isotopes is an important tool for the environmental studies and for the protection of public health [1-3]. Radium and uranium from soil and building materials are the main sources for indoor radon, a radioactive gas considered at this time as the second cause of the lung cancer risk [4-7]. The identification and the quantification of uranium isotopes require a proper separation of each isotope and high purification of them in order to obtain highly accurate results. Alpha-particle

---

* This paper was presented at the "17th International Symposium on Separation Sciences. News and Beauty in Separation Sciences, Cluj-Napoca, Romania, September 5-9, 2011"

[a] Babeş-Bolyai University, Faculty of Environmental Sciences and Engineering, 30 Fântânele Street, RO-400294 Cluj-Napoca, Romania, * *dan.nita@ubbcluj.ro*

[b] Babeş-Bolyai University, Faculty of Chemistry and Chemical Engineering, 11 Arany Janos Street, RO-400028 Cluj-Napoca, Romania

spectrometry is one of the measurement technique used for the determination of uranium isotopes [8-10]. The main advantages of this method are the low background and the good resolution. The current techniques for the uranium separation and purification require sample dissolution with strong acids, precipitation and ion exchange [11, 12]. A proper combination of some of these techniques allows obtaining a very good separation of uranium.

Ion exchange is successfully applied to the separation and determination of radionuclides in the pure form of complex mixtures. In the recent years this method has found wide application due to its simplicity, speed and high degree of purity obtained.

The aim of this work is to develop a selective radiochemical separation method of uranium from thorium using Dowex AG 1X8 resin and to quantify it by alpha spectrometry after electrodeposition onto stainless-steel discs.

RESULTS AND DISCUSSION

The tests were carried out on simulated waste samples containing a known activity of uranium isotope, in order to check the efficiency of the separations. The resin used in this work was Dowex AG 1X8 (100-200 mesh) that is a Type I strong base anion resin containing 4% divinylbenzene (DVB). Its structure is based on a microporous copolymer of styrene and DVB that results in maximum resistance to oxidation, reduction, mechanical wear and breakage. The resin active principle consists in the quaternary ammonium $(-NR_3^+)$ groups which are capable of binding chloride complexes of UO_2^{2+} (e.g. $UO_2Cl_4^{2-}$). Uranium may be separated with an anion exchanger, since in 9M HCl uranium forms a negatively charged complex $[UO_2Cl_4]^-$ that may be trapped on the anion exchanger, while the other elements pass through the column.

The uranium recovery was calculated after its passing through the home made columns. In order to evaluate the efficiency of the separation method by alpha spectrometry, alpha sources were prepared by electrodeposition. In Table 1 are presented the recoveries obtained for samples 1-12 which are the samples obtained using the pretreatments of column filled with Dowex resin described in Table 2.

As it could be observed from Figure 1, for the first separation column, the higher uranium recovery (98.3%) was obtained for the sample 5 by eluting with 0.10M HCl at room temperature, while the lowest recovery (62.0%) was obtained for sample 1 by eluting with 0.05M HCl heated. The other values are inside of this range.

The results from Figure 1 prove that the eluent HCl concentration is an important recovery parameter. The best results were obtained for tests at room temperature. The increase of eluent temperature encourages the recovery process for around 0.10M HCl concentration of eluent.

Table 1. The uranium recoveries obtained for samples 1-12.

Sample no	Amount added (Bq/sample)	Amount found (Bq/sample)	Recovery (%)
1	5.6	3.5	62.0
2	4.5	3.9	87.0
3	9.6	6.5	68.0
4	11.9	11.4	95.9
5	11.9	11.7	98.3
6	11.9	10.0	84.4
7	11.8	8.5	72.4
8	8.0	6.8	85.3
9	9.4	6.9	73.7
10	14.7	14.3	97.4
11	7.5	7.5	99.7
12	9.6	8.5	88.8
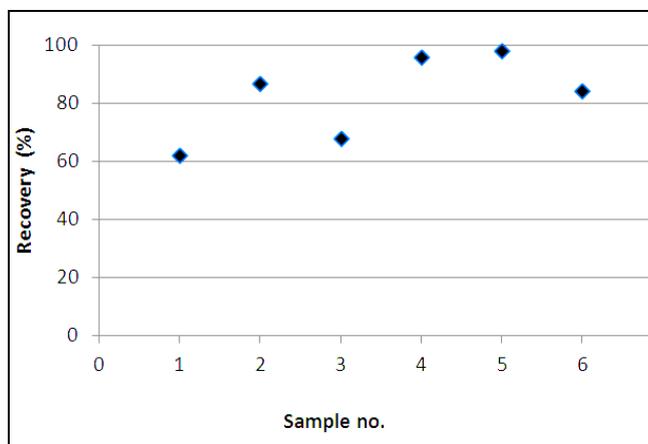
Figure 1. The recovery obtained for the first column conditioning
(washed with 0.10M HCl and 9M HCl). Samples 1-6.

The second column recovery offers us interesting results which are represented in the chart of Figure 2. We could observe a generally good positioning of the achieved values ranged around of 90% recovery for tests at room temperature.

The highest recovery value (99.71%) was achieved for the sample 11 obtained by eluting with 0.10M HCl at room temperature meanwhile the lowest recovery (72.40%) was obtained for sample 7 by eluting with 0.05M HCl heated. It can be observed the same situation as in the case of first column conditioning: the HCl concentration of eluent influences the recovery process. The best results were obtained for 0.10M HCl concentration of eluent at room temperature.
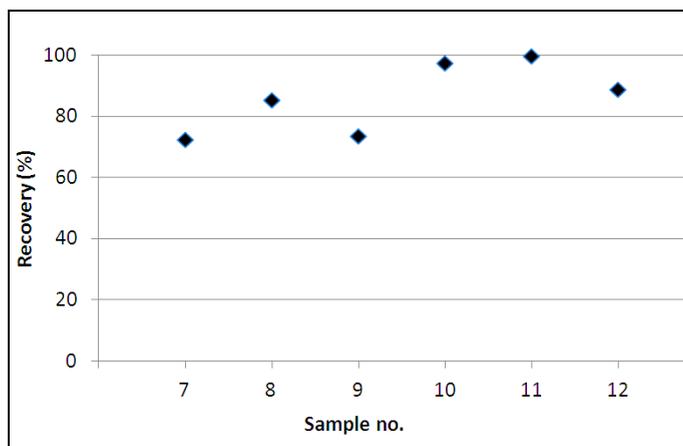
Figure 2. The recovery obtained for the second column conditioning
(the resin kept 12 hours in 9M HCl). Samples 7-12.

The main energies of U isotopes are: [238]U - 4196 KeV, [234]U - 4777 KeV, and [235]U - 4679 KeV. The Figure 3 illustrates the [238]U, [234]U and [235]U activities (counts). Also it can be observed that the two peaks representing the [238]U and [234]U are not equal as they should be (secular equilibrium), so we can conclude that the used U is depleted uranium.
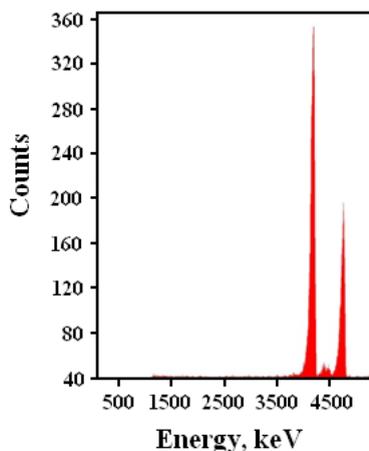
Figure 3. The obtained uranium alpha spectrum.

No thorium could be found in any of the final solutions; the main energies of thorium isotopes are: [232]Th – 4007 KeV, 3952 KeV and [230]Th – 4682 KeV, 4615 KeV [13]. Therefore we can conclude that a very good separation of uranium from thorium have been obtained.

This investigation proves that the recovered U isotopes feature a high purity related to a high uranium recovery. This fact demonstrates that the performed analysis method is suitable for the environmental U determinations.

CONCLUSIONS

The uranium separation and determination from samples is a very important tool in environmental studies. A very good uranium recovery in the separation process is required due to its low concentration in environmental samples.

The highest recovery obtained for uranium separation by open tubular liquid chromatography was 99.71% by conditioning the resin 12 hours in 9M HCl and then eluting with 0.10M HCl at room temperature. The lowest recovery obtained was 62% by conditioning the column with 0.10M HCl and 9M HCl and then eluting with heated 0.05M HCl. The recovery percent increases significantly with the increasing of the eluent HCl concentration around 0.10M. The alpha spectrum do not show any traces of added thorium, we can state that a very good separation of uranium from thorium have been done.

Our future work will be focused on applying this method on real samples and also testing other resins for uranium separation by open tubular liquid chromatography.

EXPERIMENTAL SECTION

In this work we used a strong basic anion exchange resin, Dowex AG 1X8 (100-200 mesh) purchased from Sigma-Aldrich. All chemicals were analytical grade.

The performance of methodology was checked by using uranium standard solutions. The solutions were prepared by dissolution of uranyl nitrate $UO_2(NO_3)_2 \cdot 6H_2O$ (99.99%, purchased from Merck Company) in 9M HCl solution. In this way the uranyl nitrate was converted to chloride form.

A very good separation between uranium and thorium is required taking into account the environmental applications. We prepared a low activity mixed solution of these two radionuclides. Therefore, a known quantity of thorium (1 Bq/sample) obtained from a $Th(NO_3)_4 \cdot 5H_2O$ salt was added to uranium solutions from Table 1 in order to check the selectivity of the performed separation protocol for uranium.

The standard solution was acidified at pH 1 with hydrochloric acid before the uranium separation. The resin is completely hydrated prior to column packing and then it is washed using a mobile phase that will cause the greatest swelling.

In this paper two different ways for resin conditioning were used. The first one, the conditioning was accomplished by washing the column loaded with Dowex 1X8 resin with 0.10M HCl and then with 9M HCl. The second

conditioning was made by washing the same type of resin with pure H_2O and after, keeping the resin for about 12 hours in 9M HCl. In Table 2 are presented the two column conditionings and the eluents of different HCl concentrations at different temperatures used for uranium and thorium elution process. The columns used in this work are 7 cm length and 1 cm internal diameter. The same volume of standard solutions was used for every uranium and thorium separation. The uranium anionic complexes should be retained on the resin and thorium should pass through the column. A solution of 9M HCl was passed through the column for washing any traces of other possible elements retained on the column, including thorium.

For the elution of uranium through columns, different temperatures for eluents were tested using different aqueous solutions of hydrochloric acid (0.05; 0.10 and 0.15 M) (Table 2). The same volume of eluent (20 mL in two stages) was used for all separations. The elution was performed at a rate of 5-6 drops per minute. The room temperature was about 22°C.

The samples obtained after elution were electrodeposition onto stainless steel discs. The measurements of uranium isotopes were performed with alpha spectrometer with an ORTEC SOLOIST alpha spectrometer with PIPS (Passivated Implanted Planar Silicon) detector (1200 mm^2 size).

Table 2. The column conditioning and the used eluents.

Sample No	Dowex 1X8 Column Conditioning	Eluent
1		0.05 M HCl heated to boiling point
2		0.10 M HCl heated to boiling point
3	Washed with 0.1M HCl and then with 9M HCl	0.15 M HCl heated to boiling point
3		0.05 M HCl at room temperature
5		0.10 M HCl at room temperature
6		0.15 M HCl at room temperature
7		0.05 M HCl heated to boiling point
8		0.10 M HCl heated to boiling point
9	Kept 12 hours in 9M HCl and then loaded into the column.	0.15 M HCl heated to boiling point
10		0.05 M HCl at room temperature
11		0.10 M HCl at room temperature
12		0.15 M HCl at room temperature

The resolution of the detector is 19 KeV and the data acquisition was made by ASPEC-927 Dual Multichannel.

REFERENCES

1. M. Surić, D.A. Richards, D.L. Hoffmann, D. Tibljaš, M. Juračić, *Marine Geology*, **2009**, *262*, 62.

2. A. Tanaka, T. Doi, T. Uehiro, *Journal of Environmental Radioactivity*, **2000**, *50*, 151.

3. M. Kalina, W.N. Wheelerb, G. Meinrath, *Journal of Environmental Radioactivity,* **2005**, *78*, 151.

4. C. Cosma, D. Ristoiu, A. Poffijn, G. Meesen, *Environment International,* **1997**, *22*, 383.

5. C. Cosma, M. Moldovan, T. Dicu, T. Kovacs, *Radiation Measurements*, **2008**, *43*, 1423.

6. C. Sainz, A. Dinu, T. Dicu, K. Szacsvai, C. Cosma, L.S. Quindós, *Science of the Total Environment,* **2009**, *407*, 4452.

7. P.F. Baias, W. Hofmann, R. Winkler-Heil, C. Cosma, O.G. Duliu, *Radiation Protection Dosimetry,* **2010**, 1*38*, 111.

8. F.B. Saidou, J.-P. Laedermanna, M.G. Kwato Njockb, P. Froidevaux, *Applied Radiation and Isotopes,* **2008**, *66*, 215.

9. E. Garcia-Torano*, Applied Radiation and Isotopes,* **2006**, *64*, 1273.

10. R.K. Singhal, U. Narayanan, R. Karpe, A. Kumar, A Ranade, V. Ramachandran, *Applied Radiation and Isotopes,* **2009**, *67*, 501.

11. F.V. Tomea, M.P. Blanco Rodriguez, J.C. Lozano, *Applied Radiation and Isotopes,* **2002**, *56*, 393-398.

12. S.-E. Lauritzen and J.E. Mylroie, *Journal of Cave and Karst Studies,* **2000**, *62*(1), 20.

13. M. Ivanovich and R.S. Harmon (Eds.), "Uranium-Series Disequilibrium: Applications to Earth, Marine, and Environmental Sciences", Oxford University, Press, **1982**, 21.

A COMPUTATIONAL INVESTIGATION OF THE DECAY MECHANISM OF THE REACTION PRODUCT OF ANTHRANILATE DIOXYGENASE (ANTHRANILIC ACID DIOL)

RADU SILAGHI-DUMITRESCU[a,*], RADU GHINGA[b]

ABSTRACT. Anthranilate diol is a non-aromatic dihydrodiol produced during the enzymatic degradation of anthranilate by anthranilate dioxygenase. The anthranilate diol is generally accepted to decompose spontaneously to catechol, thus regaining aromaticity. The present study employs density functional (DFT), Hartree-Fock (HF) and AM1 calculations to examine the mechanism of anthranilate diol decomposition.

Keywords: anthranilate, anthranilate diol, Rieske dioxygenase, catechol, DFT

INTRODUCTION

Rieske dioxygenases (RDO) are non-heme iron enzymes catalyzing the cis-1,2 di-hydroxylation of aromatic substrates, producing non-aromatic dihydrodiols. Within this family of enzymes, anthranilate dioxygenase catalyzes the transformation of anthranilate (2-aminobenzoate) to the corresponding diol, which then further decomposes to catechol and regains its aromaticity as shown in *Figure* 1.
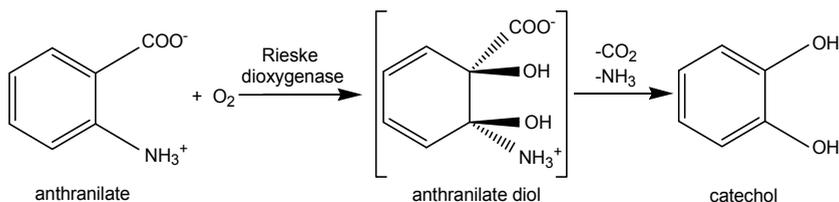
Figure 1. The reaction catalyzed by anthranilate dioxygenase, followed by decomposition of the diol.

[a] Universitatea Babeş-Bolyai, Facultatea de Chimie şi Inginerie Chimică, Str. Kogălniceanu, Nr. 1, RO-400084 Cluj-Napoca, Romania, * *rsilaghi@chem.ubbcluj.ro*
[b] Grup Şcolar de Transporturi Auto "Henri Coandă", Str. Mărăşeşti, Nr. 34, RO-310332 Arad, Romania, radughinga@gmail.com

One currently assumes that this latter decomposition occurs spontaneously; it is, however, not known precisely whether this requires assistance from the enzyme or if it occurs after liberation of the diol from the active site. The atomic-level details of this process are, likewise, not known. The present paper reports a computational investigation aiming to evaluate the stability and decomposition pathway of the anthranilate diol.

RESULTS AND DISCUTIONS

Equilibrium geometries

Figure 2 shows optimized geometries for the anthranilic acid diol - neutral and zwitterions, and Table 1 shows key bond lengths and distances in anthranilate and anthranilate diol, as computed with HF/6-31G**, BP86/6-31G**, and AM1.
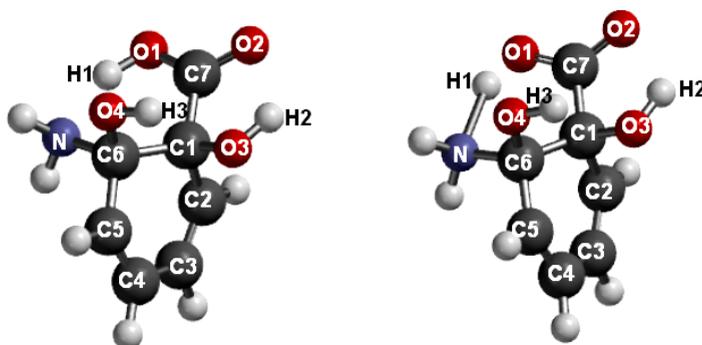
Figure 2. BP86-optimized geometry for the anthranilate diol –
neutral vs. zwitterion.

For the diol, the BP86 and the HF methods (but not AM1) failed to locate a minimum on the potential energy surface; instead, upon geometry optimization one of the NH_3 protons migrated to the nearby carboxylate oxygen. However, for the anthranilic acid even the AM1 failed in producing a zwitterionic geometry. Table 1 shows that the C-C bonds within the phenyl ring in anthranilic acid range within 0.03-0.04 Å of each other as expected for an aromatic compound, whereas again as expected in the corresponding diol (based on AM1 results) the C-C bonds range from 1.34 Å (typical for a double bond) to 1.57 Å for the C1-C6 bond involving the substituted carbon atoms (slightly longer than a typical single bond).

Table 1. Key bond lengths and distances in the anthranilate diol and anthranilic acid (in Å), as computed with HF/6-31G**, BP86/6-31G**, and AM1 (cf. Figure 1).

| | Anthranilate diol | | | | Anthranilate | | |
| | Neutral | | | Zwitterion | Neutral | | |
bond	BP86	HF	AM1	AM1	BP86	HF	AM1
C6-N	1.51	1.47	1.46	1.54	1.37	1.37	1.38
C6-O4	1.41	1.39	1.44	1.41	-	-	-
C1-O3	1.44	1.40	1.42	1.42	-	-	-
C1 -C7	1.57	1.55	1.53	1.59	1.49	1.49	1.47
C1-C2	1.52	1.52	1.50	1.50	1.42	1.40	1.40
C2-C3	1.35	1.32	1.34	1.34	1.39	1.37	1.39
C3-C4	1.47	1.48	1.45	1.45	1.41	1.39	1.40
C4-C5	1.35	1.32	1.34	1.34	1.39	1.37	1.38
C5-C6	1.52	1.52	1.52	1.51	1.42	1.40	1.43
C1-C6	1.57	1.55	1.59	1.57	1.44	1.41	1.42
C7-O1	1.32	1.30	1.36	1.26	1.37	1.33	1.39
C7-O2	1.23	1.19	1.23	1.25	1.23	1.19	1.24
N-H1	1.56	1.80	2.69	1.04	4.56	4.46	4.44
O1-H1	1.05	0.96	0.97	2.01	0.98	0.94	0.97
O3---H3	1.94	2.13	2.24	2.04	-	-	-
O2---H2	1.86	2.01	2.27	2.01	-	-	-
O4-H3	0.99	0.95	0.97	0.97	-	-	-
O3-H2	1.00	0.95	0.97	0.98	-	-	-

Decomposition pathways

Figure 3 shows the decomposition pathways computed for the anthranilic acid diol, with HF/6-31G** and BP86/6-31G** following the C---N coordinate (i.e., cleavage of the C-NH2 bond). Figure 4 shows the decomposition pathways following the C---CO2 coordinate.
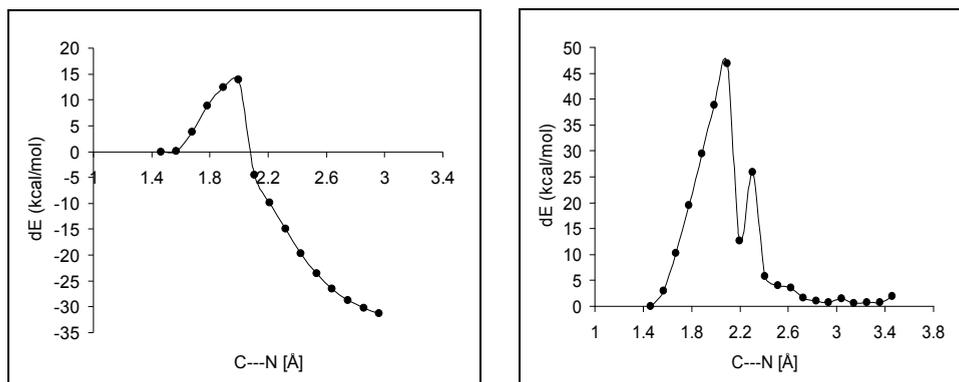
Figure 3. DFT and HF energy profiles assuming a reaction coordinate where the C---N distance is elongated. Relative energies are given.

51

The ~30 kcal/mol difference seen in Figure 3 in apparent activation energies computed with HF and DFT following the C---N coordinate can be explained by the fact that in the DFT calculations a proton transfer occurs early on the potential energy surface, transforming the NH_2 substituent into NH_3, which then facilitates liberation of ammonia almost concerted with liberation of CO_2.
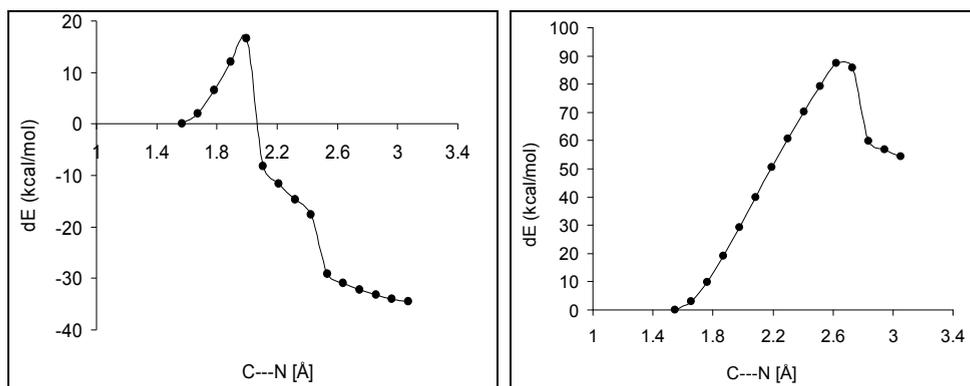
Figure 4. DFT and HF energy profiles assuming a reaction coordinate where the C---CO2 distance is elongated. Relative energies are given.

By contrast, in the HF-computed potential energy surface the CO_2 remains bonded to the molecule. A similar result is obtained in Figure 4, where the apparent activation energies computed by the two methods differ by ~70 kcal/mol; here, following the C---CO_2 coordinate the NH_3 remains bonded to the benzene ring with HF throughout the calculations, whereas it spontaneously dissociates from the benzene ring, almost concerted with dissociation of CO_2, in the DFT calculations. Thus, DFT appears to have located, in both cases, lower-energy pathways than HF. Importantly, these lower-energy pathways involve concerted breaking of two bonds as opposed to one. This fact, together with the asymetry in the DFT-derived potential energy curves in Figures 3 and 4 (with much steeper slopes to the right of the transition state), as well as the fact that HF predicts prohibitevly high energy barriers, all suggest the need for examining the reaction barrier along more than one coordinate. Therefore, Figure 5 shows potential energy surfaces where the two reaction coordinates are monitored concomitantly. It may be seen that the lowest-energy pathway connecting the reactant with the product does involve elongation along both coordinates, with the C-N bond elongated more than the C-C bond (at the saddle point, the C-C bond is 1,77 Å and the C-N bond is 1,94 Å with DFT and, for HF, the C-C bond is 1,86 Å and the C-N bond is 1,99 Å).

Figure 6 shows a two-dimensional representation of the lowest-energy pathways from Figure 5, illustrating how the asymmetry initially noted for the single-coordinate curves of Figures 3 and 4 has now disappeared, and showing

52

how the computed activation energies are now reasonable with DFT as well as with HF. Nevertheless, it is particularly important to note that the values predicted by the two methods differ by ~25 kcal/mol, which, considering that one of the values is 15 kcal/mol, represents a very large difference. Indeed, based on the DFT data the anthranilic acid diol should be disappearing within a millisecond timescale, whereas the HF data suggests that the diol should be detectable on a longer time-scale.
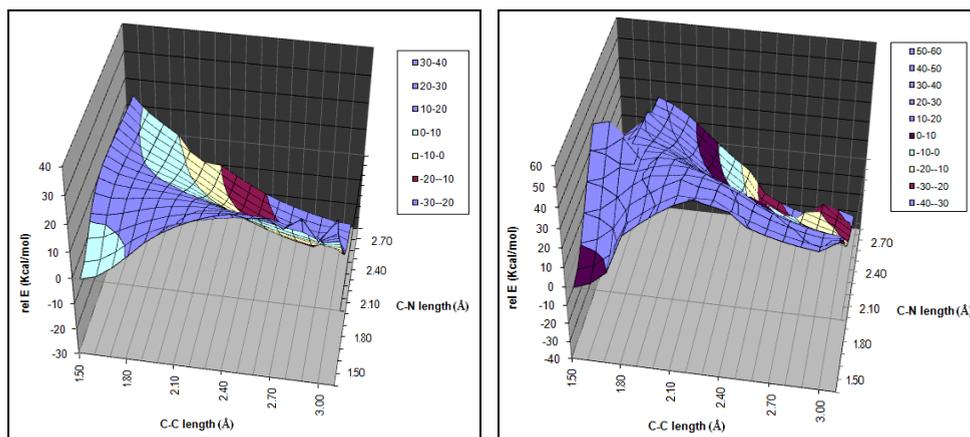
Figure 5. 3-D charts for the anthranilate diol decomposition as computed with BP86/6-31G** and HF/6-31G**following C---N and C---CO$_2$ coordinates simultaneously.
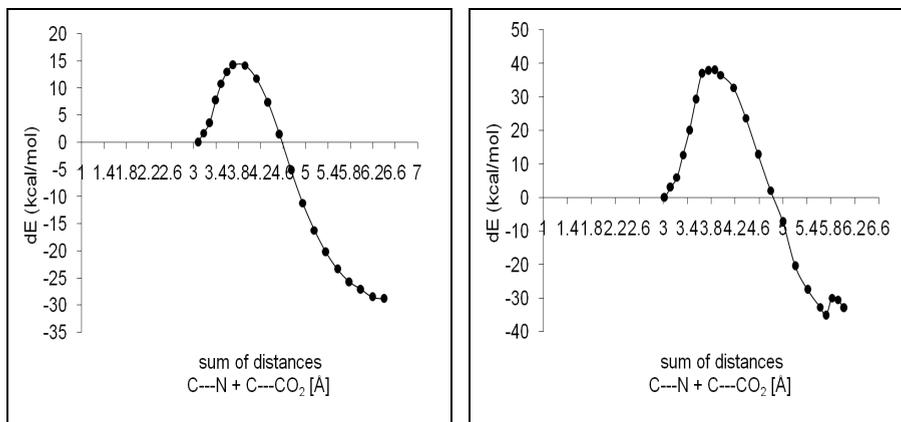
Figure 6. Section of the 3-D chart (see fig.6) for the anthranilate diol decomposition as computed with BP86/6-31G** and HF/6-31G** following C---N and C---CO2 coordinates simultaneously (data extracted from Figure 5).

To conclude, the decomposition pathway for decomposition of the anthranilic acid diol has been identified in detail, and shown to involve quasi-simultaneous elongation of the carbon-ammonia and carbon-CO_2 bond lengths. On the methodological side, a failure of the computational methods in yielding optimized geometries for the amfionic structures is noted, as is the unacceptably large difference in activation energies computed by DFT vs HF – a difference which has qualitative and not only quantitative consequences on the predictions made by the two methods.

METHODS

The present study employs three calculation methods: the BP86 density functional method using the 6-31G** basis set, Hartree-Fock with the 6-31G** basis set, and the semi-empirical method AM1, as implemented in the Spartan software package.[12]

ACKNOWLEDGEMENT

REFERENCES

1. L.P. Wackett, *Enzyme and Microbial Technology*, **2002**, *31*, 577.

2. B.M. Bundy, A.L. Campbell, E.L. Neidle, *J Bacteriology,* **1998**, *180*(17), 4466.

3. A. Ichihara, K. Adachi, K. Hosokawa, Y. Takeda, *The Journal Of Biological Chemistry,* **1962**, *237*, 2296.

4. R. Silaghi-Dumitrescu, *Studia UBB Chemia*, **2007**, *2*, 103.

5. H.K. Chang, P. Mohseni, G.J. Zylstra, *J Bacteriology,* **2003**, *185*(19), 5871.

6. P.D. Oldenburg, Y Feng, I. Pryjomska-Ray, *Journal of The American Chemical Society*, *132*, 17713.

7. D.M. Kurtz, Z.M. Beharry, D.M. Eby et al., *Journal Of Inorganic Biochemistry,* **2001**, *86*, 304.

8. L.P. Wackett, *Enzyme and Microbial Technology,* **2002**, *31*, 577.

9. D.M. Eby, Z.M. Beharry, E.D. Coulter, *Journal of Bacteriology,* **2001**, *183*, 109.

10. P.D. Oldenburg, C.Y. Ke, L. Que, *Abstracts of Papers of the American Chemical Society*, **2007**, *233*, 173.

11. Z.M. Beharry, D.M. Eby, E.D. Coulter, R. Viswanathan, E.L. Neidle, R.S. Phillips, D.M. Kurtz Jr., *Biochemistry,* **2003**, 2542(46), 13625.

12. Spartan 5.0, Wavefunction, Inc., 18401 Von Karman Avenue Suite 370, Irvine, CA 92612 U.S.A.

ANTIOXIDANT ACTIVITY AND TOTAL PHENOLIC CONTENT OF SOME ROMANIAN RED WINES

ANAMARIA HOSU[a,*], CLAUDIA CIMPOIU[a], VASILE MICLAUS[a], VIRGIL DANCIU[a], MIHAI INCEU[a]

ABSTRACT. The positive health effects of the consumption of wines are due to their phenolic constituents with significant antioxidant activity. The antioxidant activity evaluation of is of major interest to compare the potential antioxidant value of different food, to evaluate their antioxidant intake. The aims of this study were to evaluate the influence of wine variety, vintage year and winery on the atioxidant characteristics of some Romanian red wines. "Fetească Neagră", "Cabernet Sauvignon" and "Merlot" varieties of red wines, produced in three different vintage year by different Romanian wineries were investigated in terms of antioxidant activity and total phenolic content, by UV-VIS spectrophotometry. The results of this study showed that the wine variety, the vintage year and the winerie affected the antioxidant activity and the phenolic content of wines. Also, linear correlations were found between the antioxidant activity of wines determined by DPPH and ABTS assays, and the antioxidant activity and the total phenolic content of wines.

Keywords: red wine, antioxidant activity, phenolic content, spectrophotometry

INTRODUCTION

The positive health effects of the consumption of wines are due to their phenolic constituents with significant antioxidant activity [1]. Moreover, phenolic compounds are one of the most important quality parameters of wine, since they contribute to their organoleptic characteristics, particulary color, astringency and bitterness [2,3]. Phenolic compounds present different antioxidant activities, so their presence or absence and their concentration variations will influence the antioxidant activity of wines. Studies have shown that the polyphenol content and the antioxidant activity of wines depend on many factors, such as: grape varieties, soil, climatic conditions, [4], oenological techniques, ageing process etc. [5].

---

[a] Babes-Bolyai University Cluj-Napoca, Faculty of Chemistry and Chemical Engineering, 11 Arany Janos St. 400028, Cluj-Napoca, Romania

[*] Corresponding author: *ahosu@chem.ubbcluj.ro*

There are many analytical methods for assessing the antioxidant activity of foodstuffs but unfortunately, none of these is a standardized one. The most frequently used methods are spectrophotometric that employ chromogenic compounds of radical nature [6-8]. They are mostly based on oxidizing-reducing reactions, phenolic compounds functioning as reduction agents, being able to donate hydrogen radical or electron [9]. In these assays, free radicals react with antioxidant compounds leading to the decrease of radical concentration, and then absorbance measurements are performed. Folin-Ciocalteu method is commonly used only for assessment of the total phenolic content (the sum of phenolic compounds) of wines [10].

The aims of this study were to evaluate the influence of wine variety, vintage year and winery on the antioxidant characteristics and total phenolic content of some Romanian red wines, produced in three different vintage years by different Romanian wineries. Moreover, the correlation between these characteristic was done.

RESULTS AND DISCUSSION

The antioxidant activities of the analyzed wines, expressed as mg vit C/mL of wine (in case of DPPH assay) and µmol Trolox/mL of wine (when ABTS assay was used) and the total phenolic content (mg of gallic acid/mL of wine) were calculated according the calibration curves equations (Table 1) and were presented in Table 2.

Table 1. Calibration curves equations

Assay	Equation	r^2
DPPH	$A_0 - A_s = 8.121 \times$ vit C (mg/mL) $- 0.123$	0.9920
ABTS	$A_0 - A_s = 4.290 \times$ Trolox (µmol/mL) $- 2.890$	0.9702
TPC	$A_s = 0.009 \times$ gallic acid (µg/mL) $+ 0.125$	0.9841

A_0 - absorbance of the bank sample
A_s - absorbance of the analyzed wine

Table 2. The antioxidant activities and the total phenolic content of the analyzed red wines

Wine	Antioxidant activity		TPC (mg gallic acid/mL wine)
	mg vit C/mL wine	µmol Trolox/mL wine	
MPM2006	2.839±0.002	1.302±0.001	3.533±0.022
MPM2007	2.779±0.001	1.277±0.001	3.048±0.003
MPM2008	2.741±0.002	1.338±0.001	3.789±0.078
MR2006	2.039±0.001	1.080±0.001	2.850±0.003
MR2007	2.453±0.001	1.179±0.003	2.050±0.012

Wine	Antioxidant activity		TPC (mg gallic acid/mL wine)
	mg vit C/mL wine	μmol Trolox/mL wine	
MR2008	2.338±0.001	1.188±0.001	2.250±0.078
MSC2006	1.850±0.009	1.024±0.001	1.939±0.032
MSC2007	2.135±0.020	1.225±0.001	3.091±0.087
MSC2008	1.886±0.003	1.120±0.001	1.933±0.012
CSO2006	2.102±0.001	1.155±0.001	2.315±0.045
CSO2007	1.894±0.001	1.123±0.002	2.105±0.012
CSO2008	2.033±0.004	1.159±0.001	2.176±0.034
CSURL2006	2.407±0.009	1.238±0.001	2.478±0.101
CSURL2007	2.051±0.006	1.082±0.001	1.904±0.008
CSURL2008	2.213±0.007	1.245±0.001	2.309±0.036
CSVM2006	2.713±0.003	1.330±0.001	4.220±0.038
CSVM2007	2.724±0.002	1.344±0.001	4.029±0.093
CSVM2008	2.522±0.004	1.301±0.001	2.909±0.103
FNDM2006	1.905±0.004	1.169±0.003	1.796±0.006
FNDM2007	1.816±0.001	1.114±0.002	1.781±0.059
FNDM2008	2.455±0.002	1.276±0.001	2.676±0.056
FNSC2006	1.626±0.007	1.057±0.001	1.220±0.014
FNSC2007	2.104±0.015	1.207±0.003	1.989±0.033
FNSC2008	1.985±0.004	1.162±0.001	1.948±0.008
FNURL2006	1.705±0.001	1.070±0.001	1.454±0.008
FNURL2007	2.094±0.002	1.194±0.001	2.018±0.006
FNURL2008	2.016±0.001	1.202±0.002	2.504±0.064

Data expressed as mean ± standard deviation
M-Merlot, CS-Cabernet Sauvignon, FN-Fetească Neagră
PM-Prince Mircea, R-Recaş, SC-SERVE Ceptura, O-Oprişor, URL-Urlaţi, VM-Vânju-Mare, DM-Dealu Mare

The antioxidant activity of wines, determined using DPPH free radical varies between 1.626 mg vit C/mL wine for FNSC2006 and 2.839 mg vit C/mL wine for MPM 2006. Comparing the antioxidant activity of wines from different grape varieties, determined by DPPH method, the results show that, regardless of vintage year and wineries, wines FN have the lowest antioxidant activity ranging from 1.626 mg vit C/mL wine (FNSC2006) to 2.455 mg vit C/mL wine (FNDM2008). Results also show that the antioxidant activities of the same variety of wines are usually influenced by vineyard and the vintage year:

- for M variety, regardless vintage year, wines from PM vineyard have the highest antioxidant activity, followed by wines from R and SC vineyards. Also, MPM wines possess the highest antioxidant activities among all analyzed wines;

- for CS variety, the antioxidant activities of VM wines > URL wines > O wines;
- among the wines of the FN variety, the antioxidant activities of FN wines variety do not differ significantly from one vineyard to another and from one year to another. FNSC2006 wine possesses the lowest antioxidant activity (1.626 mg vit C/mL wine), and FNDM2008 wine has the highest antioxidant activity (2.455 mg vit C/mL wine).

When $ABTS^{•+}$ free radical was used, the antioxidant activity of wines ranged between 1.024 µmol Trolox/mL wine (MSC2006) and 1.344 µmol Trolox/mL wine (CSVM2007).

The antioxidant activities evaluated by DPPH and ABTS assays were correlated. Good correlation coefficient were found between the antioxidant activities of M wines (r^2 = 0.8089, y=0.6216 + 0.224 x), CS wines (r^2 = 0.8853, y=0.5557 + 0.289 x) and FN wines (r^2 = 0.9399, y=0.6185 + 0.2276 x), determined by DPPH and ABTS assays. Also, a good correlation between the antioxidant content determined with DPPH and $ABTS^{•+}$ was obtained when all wines were considered (Figure 1).
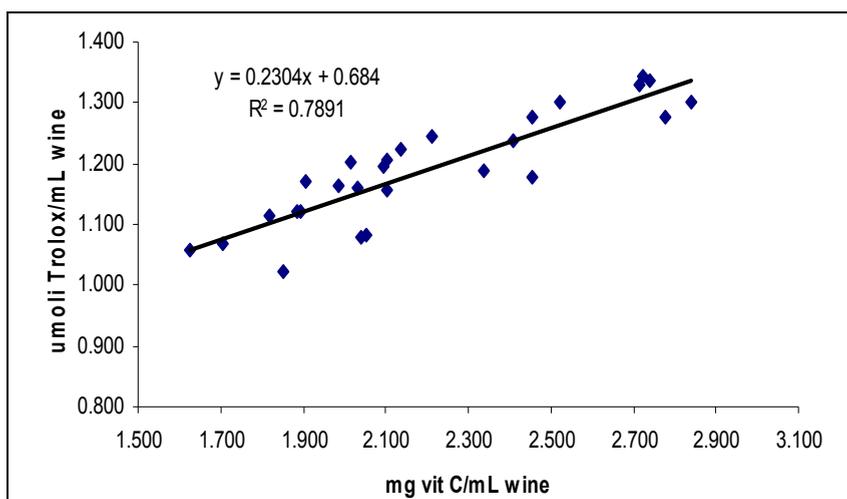
Figure 1. The correlation between the antioxidant activities of wines evaluated by DPPH and ABTS assays

As literature shows [7, 11, 12], differences between the antioxidant activities of wines evaluated with DPPH and ABTS assays may be attributable to the fact that every individual phenolic compound contained in wine causes a different response to each specific radical used in the assay.

DPPH and ABTS[•+] radicals have different stereochemical structures and different paths of genesis and thus they give, after the reaction with the antioxidants, qualitatively different responses to the inactivation of each radical [12]. The obtained results support the finding of Prior and Cao [13], that different methods should be used in parallel for the estimation of the antioxidant activity of samples.

Polyphenols are important constituents of wines, significantly contributing to their antioxidant activity. The results presented in Table 1 show that the phenolic content of the analyzed wines widely vary, ranging between 1.220-4.220 mg gallic acid/mL wine. The total phenolic content was correlated with the antioxidant activity determined both by DPPH and ABTS assays, considering each sort of wine as well as all wines (Table 3).

Table 3. Correlation coefficients between the TPC and the antioxidant activity determined by DPPH and ABTS assays

	r^2	
	DPPH assay	ABTS assay
M wines (n=9)	0.4935	0.7653
CS wines (n=9)	0.8370	0.6327
FN wines (n=9)	0.8061	0.8609
Total of wines (n=27)	0.7245	0.6773

The results show that when the sorts of wines are considered, the TPC of M wines are better correlated with the antioxidant activities determined by the ABTS assay. In case of FN wines, the TPC are almost similarly correlated with their antioxidant content investigated by both ABTS and DPPH assays. The TPC of CS wines are better correlated with the antioxidant activity evaluated with DPPH; phenolic compounds contribute with 83.70% to the antioxidant activity of CS wines. Results also show that, when all wines are considered, a moderate correlation between the TPC values and the antioxidant activities determined by DPPH and ABTS assays is obtained. However, the lack of strong correlation between these assays support the idea that different sorts of wines contain different classes of phenolic compounds with different behavior against DPPH and ABTS[•+] radicals.

CONCLUSIONS

DPPH and ABTS assays can be applied for the determination of the antioxidant activity of red wines. Differences between the antioxidant activities of wines evaluated with DPPH and ABTS assays may be due to the different behavior of every individual phenolic compound from wine against

different radicals used in the assays. MPM wines and CSVM wines present high antioxidant activities and total phenolic contents. The antioxidant activity and the phenolic content of the analyzed wines depend on the wine variety, the vintage year.

EXPERIMENTAL PART

Material and methods

Chemicals and reagents
1,1-Diphenyl-2-picrylhydrazyl (DPPH), 2,2-azinobis (3-ethylbenzthiazolin-6-sulfonic acid) diammonium salt (ABTS), 6-hydroxy-2,5,7,8-tetramethylchroman-2-carboxylic acid (Trolox), ascorbic acid (vit C), gallic acid Folin-Ciocalteu's reagent and $K_2S_2O_8$ were purchased from Merck (Darmstadt, Germany). Na_2CO_3 and methanol were obtained from Reactivul Bucureşti (Bucharest, Romania) and Chimopar (Bucharest, Romania), respectively. All chemicals and solvent were analytical grade.

Sample collection
Twenty-seven Romanian red wines of "Fetească Neagră" (FN), "Cabernet Sauvignon" (CS) and "Merlot" (M) varieties, produced in 2006, 2007 and 2008 vintage years were chosen from commercial wineries: Oprişor – O, Urlaţi –URL, Vânju Mare – VM, Prince Mircea – PM, Recaş – R, SERVE Ceptura – SC, Dealu Mare – DM. They were used directly, without any treatment.

Instrumental
The absorbance measurements were performed with T80+ UV/VIS Spectrophotometer (PG-Instruments).

Free radical scavenging assays

DPPH assay
0.25 mL of wine appropriately diluted with distilled water were added to 3.0 mL of 0.09 mg/mL methanolic solution of DPPH. After 20 min, the absorbance of the reaction mixture was measured at 517 nm. Each wine was analyzed triplicate. Calibration was performed in the 0.150 - 0.275 mg vit C/mL concentration range, following the same procedure. The obtained calibration curve was used for antioxidant activity calculation.

ABTS assay
The first step in ABTS assay was the generation of the ABTS$^{\bullet+}$ cationic radical. The ABTS$^{\bullet+}$ was obtained from the reaction of 7 mmol/L ABTS diammonium salt solution with 2.45 mmol/L $K_2S_2O_8$ solution added 1:1 (v/v). The reaction mixture was incubated for 24 h at room temperature, in dark place. Then, 0.5 mL of wine were added to 3 mL ABTS$^{\bullet+}$ solution. Absorbance measurements

were done after 20 min, at 734 nm. Calibration was performed in the 1.10 - 1.35 µmol of Trolox/ mL concentration range, following the same procedure. The obtained calibration curve was used for antioxidant activity calculation.

Total phenolic content

Total phenolic content (TPC) of wine samples were determined according to Folin-Ciocalteu method, using gallic acid as standard. 1.5mL of Folin-Ciocalteu reagent (0.2 mol/L) was added at 0.3 mL of wine appropriately diluted with distilled water. The reaction mixture was allowed to react for 5 min and then, 1.2 mL of 0.7mol/L Na_2CO_3 solution were added. Sample was incubated at room temperature, in dark place for 120 min, and its absorbance was measured at 760 nm. The experiment was performed three times for each wine. Calibration was performed in the 0 - 100 µg gallic acid/ mL concentration range, following the same procedure. The obtained calibration curve was used for antioxidant activity calculation.

ACKNOWLEDGMENTS

REFERENCES

1. V. Vrček, M. Bojić, I. Žuntar, G. Mendaš, M. Medić-Šarić, *Food Chemistry*, **2011**, *124*, 354

2. N. Landrault, P. Poucheret, P. Ravel, F. Gasc, G. Cros, P-L. Teissedre, *Journal of Agricultural and Food Chemistry*, **2001**, *49*, 3341

3. T. Okuda, T. Takayanagi, M. Sato, K. Yokotsuka, *Journal of Wine Research*, **2002**, *13*, 93

4. V. Katalini, M. Milos, D. Modun, I. Musi, M. Boban, *Food Chemistry*, **2004**, *86*, 593

5. J.M. Ubalde, X. Sort, A. Zayas, R.M. Poch, *Journal of Wine Research*, **2010**, *21*, 1

6. D. Villaño, M.S. Fernández-Pachón, A.M. Troncoso, M.C. Garcia-Parrilla, *Talanta*, **2004**, *64*, 501

7. D. Villaño, M.S. Fernández-Pachón, A.M. Troncoso, M.C. Garcia-Parrilla, *Analytica Chimica Acta*, **2005**, *538*, 391

8. M. Locatelli, R. Gindro, F. Travaglia, J-D. Coïsson, M. Rinaldi, M. Arlorio, *Food Chemistry*, **2009**, *114*, 889

9. D. Huang, B. Ou, R.L. Prior, *Journal of Agricultural and Food Chemistry*, **2005**, *53*, 1841

10. H.N. Budak, Z.B. Guzel-Seydim, *Journal of the Science of Food and Agriculture*, **2010**, *90*, 2021

11. M.S. Fernández-Pachón, D. Villaño, M.C. Garcia-Parrilla, A.M. Troncoso, *Analytica Chimica Acta*, **2004**, *513*, 113

12. J. Lachman, M. Šulc, M. Schilla, *Food Chemistry*, **2007**, *103*, 802

13. R.L. Prior, G. Cao, *Free Radical Biology and Medicine*, **1999**, *27*, 1173

ASYMMETRIC BENT-CORE LIQUID CRYSTALS BASED ON 1,3-BIS-(4`-HYDROXYPHENYLAZO)BENZENE CENTRAL CORE

**DRAGOŞ IUGANU[a], IRINA CÂRLESCU[a],
GABRIELA LISA[a], DAN SCUTARU[a,*]**

ABSTRACT. The paper presents the synthesis and liquid-crystalline properties of some new asymmetric *bent-core* compounds based on a 1,3-bis-(4`-hydroxyphenylazo)benzene central core. The first class of asymmetric derivates were obtained by esterification of some hockey-stick derivates with 4-methoxybenzoic acid and the second one by estherification with 3-bromo-4-methoxybenzoic acid, in the presence of 4-dimethylaminopyridine (**DMAP**) and N,N'-d**icyclohexyl-carbodiimide (DCC). The** liquid crystalline properties were investigated by differential scanning calorimetry (DSC) and polarizing optical microscopy (POM). The first class evidenced enantiotropic liquid crystalline properties, while the second one presented monotropic liquid crystalline behavior.

Keywords: liquid crystals, asymmetric bent-core compounds

INTRODUCTION

Liquid crystals (LCs) have been intensively investigated for about half a century and numerous important applications have been developed for them in modern technologies. For example, LC display panels and LC-based organic light emitters are widely used in the information display industry. Being a new member in the LC family, banana-shaped LCs have attracted intense attention because of their electro-optically switchable ferro- and antiferroelectricity although the individual molecules are achiral [1–5]. The relationship between the molecular structures and their mesomorphic properties is one of the most intensively studied topic for banana-shaped LCs. To study the influence of structural variations on mesomorphic properties and transition temperatures, different parts of the banana-shaped molecules have been varied and more than 1000 banana-shaped mesogens have been synthesized in the last years [6–10]. Since then, hundreds of *bent-core* compounds were synthesized and

---

[a] Gheorghe Asachi Technical University of Iaşi, Faculty of Chemical Engineering and Environmental Protection, 73 D. Mangeron St., Iaşi, Romania
* *dscutaru@ch.tuiasi.ro*

the structures of the banana phases were characterized with numerous analyzing techniques. A brief review of the literature reveals that most of the synthesized banana shaped LCs contain five benzene rings in their bent cores and the remaining banana-shaped LCs are composed of either four, six or seven benzene rings in their bent cores [11].

This paper presents the synthesis, structural characterization and mesomorphic behavior of two new asymmetric classes of bent core type compounds, which have as central core 1,3-bis-(4`-hydroxyphenylazo)benzene. The new compounds consist of six aromatic rings, connected *via* azo groups and esteric units of identical orientation. The asymmetry of molecules is caused by uneven distribution of the aromatic rings. For one series of the *bent-core* compounds one terminal aromatic ring presents a bromine atom as lateral substituent. The longer arm of the asymmetric compounds is ended with an alkoxy tail while the shorter arm ends with a methoxy group. Nine of the reported compounds present liquid crystalline properties under polarized optical microscopy (POM) and DSC investigation.

RESULTS AND DISCUSSION

Scheme 1 presents the total synthesis of the new asymmetric *bent-core* liquid crystals **4a-e** and **5a-e**. The first part of the synthesis depicts the synthesis of the phenolic intermediates **3a-e** which were obtained in our group for a previous work.

The central core, 1,3-bis-(4`-hydroxyphenylazo)benzene (**2**) was synthesized using diazotization and coupling reactions [12]. The azo aromatic acid chlorides (**1a-e**) were obtained by reacting the 4-(4-alkoxyphenylazo)-benzoic acids [15] with thionyl chloride [13].

The hockey-stick like compounds **3a-e** were obtained by reacting the 4-(4-alkoxyphenylazo)-benzoyl chlorides **1a-e** with 1,3-bis-(4`-hydroxyphenylazo) benzene (**2**) in a two-phase system dichloromethane / aqueous potassium carbonate and in the presence of tetrabutylammonium hydrogensulfate as phase transfer catalyst, at room temperature [14].

Finally, the esterification of **3a-e** compounds with 4-methoxybenzoic acid or 3-bromo-4-methoxybenzoic acid in the presence of DCC and DMAP, in anhydrous methylene chloride afforded the final *bent-core* compounds **4a-e** (in 35–73% yields) and, respectively, **5a-e** (in 37–60% yields).

Liquid-crystalline properties

Investigation by POM and DSC techniques of the mesomorphic properties of the asymmetric derivatives **4a-e** evidenced enantiotropic liquid-crystalline properties while for **5a-d** compounds the behavior was of monotropic type (compound **5e** did not present liquid crystalline properties). For the *bent-core* compounds **5a-d** the mesomorphic behavior is quite different, due to the presence of the bromo substituent on the aromatic ring. Thus, the stability

of mesophases for compounds **4a-e** on cooling is superior if compared with compounds **5a-e**, which exhibited only monotropic mesophases. The types of mesophases were assigned by visual comparison with known phase standards. According to the literature data, the first series of banana-shaped compounds showed a B_6 mesophase [16].

1a - e

$R = - C_nH_{2n+1}, n = 6 \div 10)$

2

1,3-bis(4`-hydroxyphenylazo)benzene

TBAHS
K_2CO_3, aq
CH_2Cl_2

3a - e

$R = - C_nH_{2n+1}, (n = 6 \div 10)$

CH_3O , $COOH$, X

DCCI
DMAP
CH_2Cl_2

4a - e
$R = - C_nH_{2n+1}, (n = 6 \div 10), X = -H$

5a - e
$R = - C_nH_{2n+1}, (n = 6 \div 10), X = -Br$

Scheme 1

65
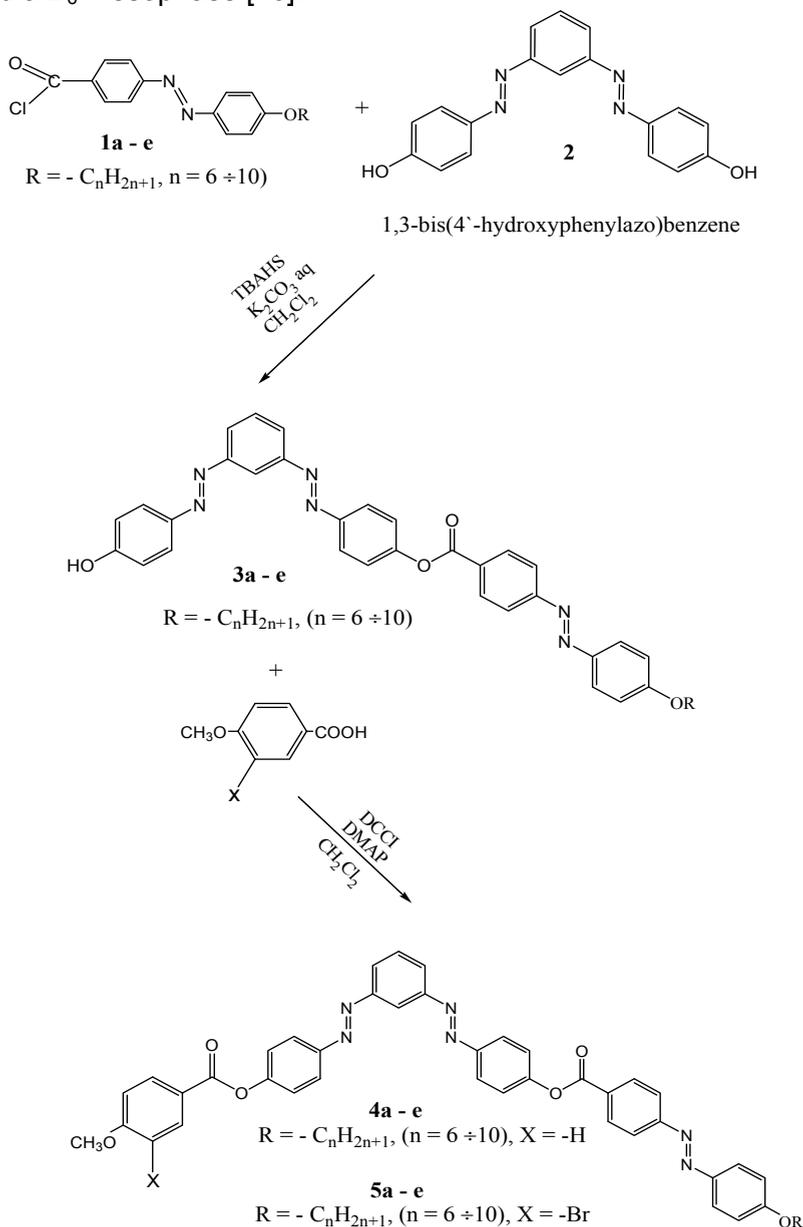
Table 1 presents the ranges of the stability of mesophases corresponding to compounds **4a-e** and **5a-e**.

Table 1. Range of mesophases for the asymmetric compounds **4a–e** / **5a-e**

Compounds		Range of mesophases (^{0}C)	
		On heating	On cooling
4a /5a	n=6	156-183^{0}C / -	169-105^{0}C / 166-151^{0}C
4b /5b	n=7	146-205^{0}C / -	200-132^{0}C / 179-156^{0}C
4c /5c	n=8	159-181^{0}C / -	177-112^{0}C / 166-152^{0}C
4d /5d	n=9	133-159^{0}C / -	138-67^{0}C / 159-150^{0}C
4e /5e	n=10	128-142^{0}C / -	137-122^{0}C / -

The results highlight the range of mesophase that is wider on cooling. The presence of the 4-methoxybenzoic acid as terminal unit have a positive influence, causing the increasing of the mesophase range (on heating from 14-59^{0}C and on cooling from 15-64^{0}C for compounds **4a-e**), but the introduction of a bromine atom as lateral substituent on the aromatic ring as in **5a-d** compounds cause the decreasing of mesophase stability between 9-23^{0}C, on cooling.

Both **4a-e** and **5a-e** derivatives showed a very good thermal stability, evidenced by thermal analysis studies, the T_{onset} values being situated with around 100^{0}C higher than the isotropisation temperatures. Generally, the thermal degradation of the asymmetric *bent-core* compounds of **4** and **5** type takes place in two stages, with the exception of **4a** or **5a** and **4d** compounds when the degradations occurs in one and three stages, respectively.

Tables 2 and 3 give the temperatures of the phase transitions determined by using differential scanning calorimetry and/or POM.

Table 2. Transition temperatures (°C) and transition enthalpies (ΔH / Jg^{-1}) for the bent-core compounds **4a-e**

Compounds		T / °C (ΔH / Jg^{-1})							T_{onset} (°C)
		Heating (°C)			Cooling (°C)				
		K_1 / K_2	K_2/LC	LC / I	I /LC	LC/LC	LC/ K_2	K_2 / K_1	
4a	n=6	113 [0.70]	156 [-23.68]	183 [-0.36]	169 [1.83]	-	105 [23.97]	-	330
4b	n=7	125 [-15.92]	146 [-24.81]	205 [-2.41]	200 [6.22]	-	132 [31.85]	-	345
4c	n=8	131 [4.10]	158 [-31.82]	181 [-3.50]	177 [1.77]	-	112 [23.63]	-	341
4d	n=9	133*	-	159*	138*	124*	67*	48*	202
4e	n=10	-	128 [-13.92]	142 [-0.32]	137 [1.51]	-	122 [-1.76]	117 [3.99]	325

On the heating cycle, three endothermic peaks are present. The first one, at 125°C, is determined by the phenomenon of polymorphism and describes a crystalline-crystalline transition. The B_6 mesophase starts at 146°C, which is accompanied by a relatively large thermal effect (-24.81 J/g), and ends with the peak at 205°C. At this point the isotropisation occurred, and the peak is accompanied by a small thermal effect. On the cooling cycle it can be observed the presence of two exothermic peaks. One at 200^0C, caused by the isotropic-liquid crystalline transition, and the prominent peak at 132^0C which corresponds to the liquid crystal-crystalline transition.

The presence of bromine atom in the structure of **5a-e** compounds does not favorable influence the liquid crystalline behavior. Compounds **5a-e** evidenced only a monotropic behavior, with narrow intervals of stabilities of the mesophases (Table 1).

Table 3. Transition temperatures (°C) and transition enthalpies
(ΔH / Jg^{-1}) for the bent-core compounds **5a-e**

Compounds		Heating (°C)		Cooling (°C)				T_{onset} (°C)
		K_1/K_2	K_2/I	I /LC	LC/ K_3	K_3 / K_2	K_2 / K_1	
5a	n=6	-	175 [-33.45]	166 [0.38]	151 [3.59]	147 [4.63]	-	333
5b	n=7	133 [-8.52]	172*	179 [1.60]	156 [5.75]	119 [6.68]	80 [2.09]	304
5c	n=8	-	176*	166*	152*	-	-	337
5d	n=9	158 [-25.91]	166 [-0.29]	159 [0.47]	150 [-26.07]	65 [0.34]	-	337
5e	n=10	-	168*	-	-	154 [28.45]	121 [0.41]	336

Abbreviations: K – crystalline; LC – liquid crystal; I – isotropic; T_{onset} – the initial temperature of thermal degradation; * Data obtained from POM investigations

Figure 1 presents, as an example, the DSC curves of compound **4b**.
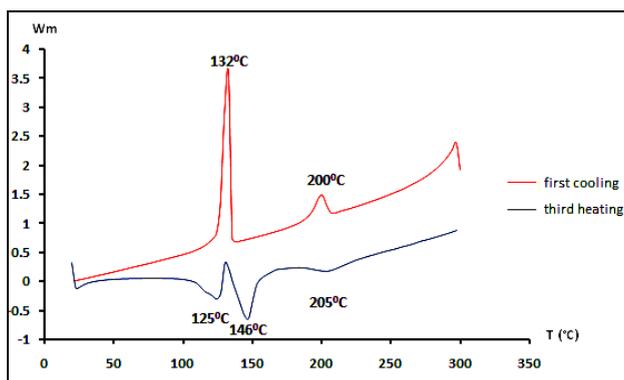
Figure 1. The DSC curves of compound **4b**

As an example, according to POM data, the mesophase for compound **5c** begins, on cooling, at 166°C and ends at 152°C when the crystallization occurred.

Figure 2 presents the textures observed by polarized optical microscopy upon heating and cooling cycles for compound **4b**.

Figure 3 depicts, as an example, the DSC curves of compound **5c** and Figure 4 presents the textures observed by polarized optical microscopy upon cooling for compounds **5a** and **5c**.

(a)   (b)   (c)
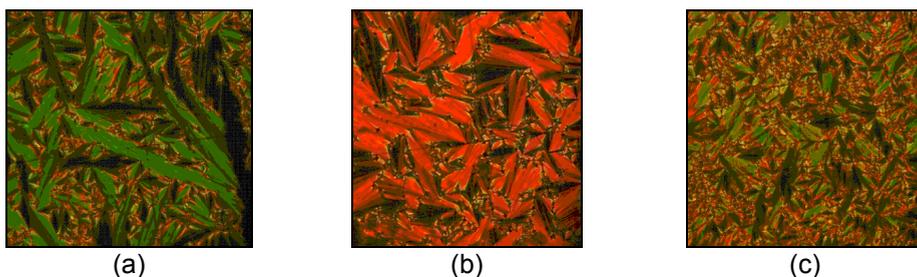
Figure 2. Thermal optical micrographs of the texture displayed by compound 4b: (a) 171^0C, first cooling; (b) 167^0C, second cooling; (d) 196^0C, third heating.
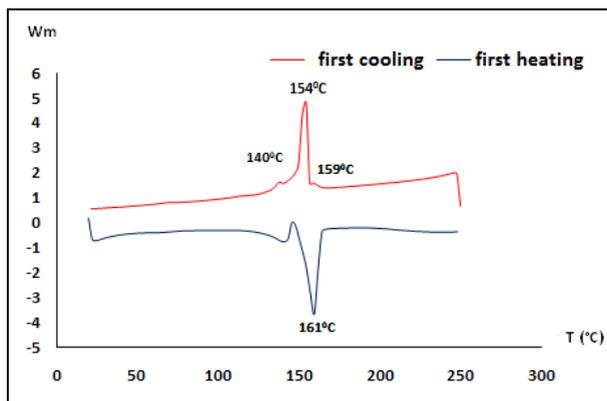
Figure 3. The DSC curves of compound **5c**

(a)   (b)
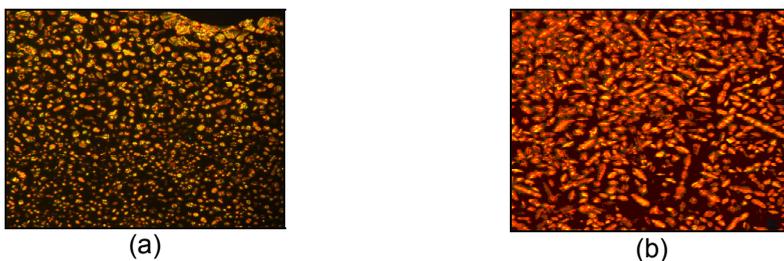
Figure 4. Thermal optical micrographs of the textures displayed by compounds **5a** and **5c** on first cooling: a) **5a**, 157^0C and b) **5c**, 157^0C.

CONCLUSIONS

Two new series of *bent-core* liquid crystals based on a 1,3-disubstituted core have been synthesized and their mesomorphic properties have been investigated. ^{1}H-NMR and ^{13}C-NMR were used for structural characterization while the liquid crystalline behavior was confirmed by differential scanning calorimetry and optical polarizing microscopy. The liquid crystalline behavior was of enantiotropic or monotropic type, depending on the structure of the asymmetric compounds. The assigned mesophases were of smectic type. The obtained compounds showed a very good thermal stability in the mesophase domain.

EXPERIMENTAL SECTION

MATERIALS

Analytical reagents and solvents were provided either by Aldrich (Germany), or by Merck (Germany), and were used without further purification. Silica gel 60 (Merck) was used for column chromatography (CC). Thin-layer chromatography (TLC) was performed on silica gel plates (Merck, silica gel F_{254}). 4-((3-((4-Hydroxyphenyl)azo)phenyl)azo)phenyl 4-((4-alkyloxyphenyl) azo) benzoates were synthesized in our laboratory for a previous work [12-15].

INSTRUMENTATION

Confirmation of the structures of the intermediates and final products was obtained by ^{1}H-NMR and ^{13}C-NMR, using a Bruker Avance DRX 400 MHz spectrometer (Rheinstein, Germany) with tetramethylsilane as internal standard. Chemical shifts were reported in ppm relative to tetramethylsilane (TMS) as internal standard.

Transition temperatures were determined using a Linkam heating stage and Linksys 32 temperature control unit (Surrey, BC, Canada) in conjunction with a Axioscop 40 Zeiss polarizing optical microscope (Jena, Germany) and Qimaging/Retiga-1000R camera for image capture (Surrey, BC, Canada), the transitions being confirmed by DSC analysis (Mettler Toledo DSC1). Heating and cooling cycles were run at rates of 10^0C/min under nitrogen atmosphere, with sample measured in closed lid aluminum pans. Mesophase type was assigned by visual comparison (under the microscope) with known phase standards.

All thermal analyses were performed on a Mettler-Toledo TGA SDTA851[e] derivatograph in an N_2 atmosphere, with a flow rate of 20mL/min and a heating rate of 10^0C/min from 25^0C to 900^0C. In order to obtain comparable data, constant operational parameters were kept for all samples.

SYNTHESIS

General method for the synthesis of the asymmetric bent-core liquid crystals 4a-e

A mixture of 1 equiv. of asymmetric compounds **(3a-e)**, 1.1 equiv. of 4-methoxybenzoic acid, and 1.5 equiv. of DMAP, dissolved in dry CH_2Cl_2, was stirred for a few minutes and then 1.8 equiv. of DCC dissolved in dry dichloromethane was added dropwise. The reaction mixture was stirred for 72 h at room temperature and then the precipitated N,N`-dicyclohexylurea (DCCU) was filtered off. The solvent was evaporated in vacuum and the solid was chromatographed on silicagel using a 20/1 mixture of dichloromethane/ ethyl acetate as eluent.

4-((3-((4-(4-((4-hexyloxyphenyl)azo)benzoyloxy)phenyl)azo)phenyl)-azo) phenyl 4-methoxybenzoate (4a): Quantities: compound **(3a)** (0.190 g; 0.30 mmol), 4-methoxybenzoic acid (0.05 g; 0.33 mmol), DCC (0.112g; 0.54 mmol), DMAP (0.055 g; 0.45 mmol), 100 ml dry dichloromethane. Orange product, η = 47.82 % (0.110 g), liquid crystal: 113^0C (K/K), 156^0C (K/CL), 183^0C (CL/I), 169^0C (I/CL), 105^0C (CL/K) .^1H-RMN δ_H ppm ($CDCl_3$): 8.45 (m, 1H, Ar), 8.35 (d, 2H, Ar, J=8.33 Hz), 8.18 (d, 2H, Ar, J=8.55 Hz), 8.05 (m, 6H, Ar), 7.96 (m, 4H, Ar), 7.65 (m, 1H, Ar), 7.44 (d, 2H, Ar, J=8.55 Hz), 7.40 (d, 2H, Ar, J=8.55 Hz), 7.00 (m, 4H, Ar), 4.05 (t, 2H, -O-CH_2), 3.89 (s, 3H, -OCH_3), 1.82 (cv, 2H, -CH_2), 1.49 (cv, 2H, -CH_2), 1.34 (m, 4H, -CH_2), 0.92 (t, 3H, -CH_3). ^{13}C-RMN δ_C ppm ($CDCl_3$): 164.53, 164.38, 164.11, 162.55, 155.96, 153.45, 153.37, 153.35, 153.22, 150.27, 150.10, 146.88, 132.41, 131.30, 130.09, 129.68, 125.43, 125.39, 125.35, 124.39, 124.33, 122.60, 122.53, 122.44, 121.54, 116.52, 114.86, 113.95 (2* >C=O esteric + 26C, aromatic); 68.61 (-O-CH_2), 55.55 (OCH_3), 31.59, 29.21, 25.72, 22.59, 13.97 (5C, aliphatic).

4-((3-((4-(4-((4-heptyloxyphenyl)azo)benzoyloxy)phenyl)azo)phenyl)-azo) phenyl 4-methoxybenzoate (4b): Quantities: compound **(3b)** (0.200 g; 0.31 mmol), 4-methoxybenzoic acid (0.052 g; 0.34 mmol), DCC (0.116g; 0.56 mmol), DMAP (0.057 g; 0.46 mmol), 100 ml dry dichloromethane. Orange product, η = 41.49 % (0,100 g), liquid crystal: 125^0C (K/K), 146^0C (K/CL), 205^0C (CL/I), 200^0C (I/CL), 132^0C (CL/K). ^1H-RMN δ_H ppm ($CDCl_3$): 8.45 (m, 1H, Ar), 8.34 (d, 2H, Ar, J=8.55 Hz), 8.17 (d, 2H, Ar, J=8.55 Hz), 8.06 (m, 6H, Ar), 7.96 (m, 4H, Ar), 7.66 (m, 1H, Ar), 7.44 (d, 2H, Ar, J=8.77 Hz), 7.40 (d, 2H, Ar, J=8.77 Hz), 7.00 (m, 4H, Ar), 4.05 (t, 2H, -O-CH_2), 3.89 (s, 3H, -OCH_3), 1.82 (cv, 2H, -CH_2), 1.48 (cv, 2H, -CH_2), 1.34 (m, 6H, -CH_2), 0.91 (t, 3H, -CH_3). ^{13}C-RMN δ_C ppm ($CDCl_3$): 164.52, 164.37, 164.20, 162.63, 156.09, 153.57, 153.51, 153.48, 153.34, 150.38, 150.22, 147.04, 132.43, 131.30, 130.21, 130.07, 129.67, 125.36, 125.22, 124.40, 124.33, 122.63, 122.51, 122.44, 121.70, 116.66, 114.95, 114.02 (2* >C=O esteric + 26C, aromatic); 68.57 (-O-CH_2), 55.55 (OCH_3), 31.79, 29.23, 29.05, 26.01, 22.61, 14.04 (6C, aliphatic).

4-((3-((4-(4-((4-octyloxyphenyl)azo)benzoyloxy)phenyl)azo)phenyl)-azo) phenyl 4-methoxybenzoate (4c): Quantities: compound **(3c)** (0.160 g; 0.24 mmol), 4-methoxybenzoic acid (0.04 g; 0.26 mmol), DCC (0.09g; 0.44 mmol), DMAP (0.044 g; 0.36 mmol), 100 ml dry dichloromethane. Orange product, η = 72.91 % (0.140 g), liquid crystal: 131^0C (K/K), 158^0C (K/CL), 181^0C (CL/I), 177^0C (I/CL), 112^0C (CL/K).^{1}H-RMN δ_H ppm (CDCl$_3$): 8.46 (m, 1H, Ar), 8.35 (d, 2H, Ar, J=8.55 Hz), 8.18 (d, 2H, Ar, J=8.77 Hz), 8.07 (m, 6H, Ar), 7.97 (m, 4H, Ar), 7.67 (m, 1H, Ar), 7.44 (d, 2H, Ar, J=8.77 Hz), 7.40 (d, 2H, Ar, J=8.76 Hz), 7.01 (m, 4H, Ar), 4.05 (t, 2H, -O-CH$_2$), 3.90 (s, 3H, -OCH$_3$), 1.82 (cv, 2H, -CH$_2$), 1.48 (cv, 2H, -CH$_2$), 1.30 (m, 10H, -CH$_2$), 0.90 (t, 3H, -CH$_3$). ^{13}C-RMN δ_C ppm (CDCl$_3$): 164.53, 164.38, 164.10, 162.55, 155.95, 153.45, 153.36, 153.34, 153.22, 150.25, 150.10, 146.88, 132.41, 131.30, 130.08, 129.68, 125.43, 129.39, 125.35, 124.38, 124.33, 122.60, 122.53, 122.44, 121.52, 116.52, 114.85, 113.95 (2* >C=O esteric + 26C, aromatic), 68.48 (-O-CH$_2$-), 55.54 (OCH$_3$), 31.81, 29.35, 29.23, 29.17, 26.01, 22.66, 14.10 (7C, aliphatic).

4-((3-((4-(4-((4-nonyloxyphenyl)azo)benzoyloxy)phenyl)azo)phenyl)-azo) phenyl 4-methoxybenzoate (4d): Quantities: compound **(3d)** (0.200 g; 0.30 mmol), 4-methoxybenzoic acid (0.05 g; 0.33 mmol), DCC (0.111g; 0.54 mmol), DMAP (0.054 g; 0.45 mmol), 100 ml dry dichloromethane. Orange product, η = 35.41 % (0.085 g), liquid crystal: 133^0C (K/K), 159^0C (CL/I), 138^0C (I/CL), 124^0C (CL/CL), 67^0C (CL/K), 48^0C (K/K) .^{1}H-RMN δ_H ppm (CDCl$_3$): 8.46 (m, 1H, Ar), 8.35 (d, 2H, Ar, J=8.55 Hz), 8.17 (d, 2H, Ar, J=8.77 Hz), 8.07 (m, 6H, Ar), 7.97 (m, 4H, Ar), 7.67 (m, 1H, Ar), 7.44 (d, 2H, Ar, J=8.55 Hz), 7.40 (d, 2H, Ar, J=8.55 Hz), 7.01 (m, 4H, Ar), 4.05 (t, 2H, -O-CH$_2$), 3.90 (s, 3H, -OCH$_3$), 1.82 (cv, 2H, -CH$_2$), 1.48 (cv, 2H, -CH$_2$), 1.28 (m, 10H, -CH$_2$), 0.89 (t, 3H, -CH$_3$). ^{13}C-RMN δ_C ppm (CDCl$_3$): 164.54, 164.39, 164.11, 162.54, 155.95, 153.44, 153.34, 153.22, 150.25, 150.10, 146.86, 132.41, 131.30, 130.53, 130.07, 129.68, 125.35, 125.19, 124.38, 124.33, 122.60, 122.53, 122.44, 122.30, 121.52, 116.52, 114.85, 113.95 (2 * >C=O esteric + 26C, aromatic); 68.48 (-O-CH$_2$), 55.54 (OCH$_3$), 31.88, 29.52, 29.39, 29.26, 29.18, 26.01, 22.67, 14.12 (8C, aliphatic).

4-((3-((4-(4-((4-decyloxyphenyl)azo)benzoyloxy)phenyl)azo)phenyl)-azo) phenyl 4-methoxybenzoate (4e): Quantities: compound **(3e)** (0.200 g; 0.29 mmol), 4-methoxybenzoic acid (0.049 g; 0.32 mmol), DCC (0.109 g; 0.53 mmol), DMAP (0.051 g; 0.42 mmol), 100 ml dry dichloromethane. Orange product, η = 37.65 % (0,09 g), liquid crystal: 128^0C (K/CL), 142^0C (CL/I), 137^0C (I/CL), 122^0C (CL/K), 117^0C (K/K). ^{1}H-RMN δ_H ppm (CDCl$_3$): 8.46 (m, 1H, Ar), 8.36 (d, 2H, Ar, J=8.55 Hz), 8.18 (d, 2H, Ar, J=8.77 Hz), 8.07 (m, 6H, Ar), 7.98 (m, 4H, Ar), 7.68 (m, 1H, Ar), 7.445 (d, 2H, Ar, J=8.77 Hz), 7.40 (d, 2H, Ar, J=8.55 Hz), 7.02 (m, 4H, Ar), 4.06 (t, 2H, -O-CH$_2$), 3.91 (s, 3H, -OCH$_3$), 1.83 (cv, 2H, -CH$_2$), 1.48 (cv, 2H, -CH$_2$), 1.28 (m, 12H, -CH$_2$), 0.89 (t, 3H, -CH$_3$). ^{13}C-RMN δ_C ppm (CDCl$_3$): 164.55, 164.39, 164.09, 162.54, 155,96, 153.44, 153.36, 153.34, 153,20, 150.26, 150.09, 146.88, 132.41, 131.30, 130.08, 129.68, 125.44, 125.41, 125.34, 124.59, 124.32, 122.59, 122.52, 122.45, 121.51, 116.49, 114.85, 113.95 (2 * >C=O esteric + 26C, aromatic); 68.48 (-O-CH$_2$), 55.54 (OCH$_3$), 31.89, 29.70, 29.56, 29.37, 29.31, 29.16, 26.00, 22.68, 14.11 (9C, aliphatic).

71

General method for the synthesis of the asymmetric bent-core liquid crystals 5a-e

A mixture of 1 equiv. compounds **(3a-e)**, 1.1 equiv. of 3-bromo-4-methoxybenzoic acid, and 1.5 equiv. of DMAP, dissolved in dry CH_2Cl_2, was stirred for a few minutes and then 1.8 equiv. of DCC dissolved in dry dichloromethane was added dropwise. The reaction mixture was stirred for 48 h at room temperature and then the precipitated N,N`- dicyclohexylurea (DCCU) was filtered off. The solvent was evaporated in vacuum and the solid chromatographed on silicagel using a 20/1 mixture of dichloromethane/ethyl acetate as eluent.

4-((3-((4-(4-((4-hexyloxyphenyl)azo)benzoyloxy)phenyl)azo)phenyl)-azo) phenyl 3-bromo-4-methoxybenzoate (5a): Quantities: compound **(3a)** (0.175 g, 0.28 mmoli), 3-bromo-4-methoxybenzoic acid (0.071 g, 0.30 mmoli), DCC (0.103 g, 0.5 mmoli), DMAP (0.051g, 0.42 mmoli), 100 ml dry dichloromethane. Orange product, η = 42.73 % (0.100 g), liquid crystal: 175^0C (K/I), 166^0C (I/CL), 151^0C (CL/K), 147^0C (K/K). ^1H-RMN δ_H ppm $(CDCl_3)$: 8.45 (m, 1H, Ar), 8.40 (d, 1H, Ar, J=1.97 Hz), 8.35 (d, 2H, Ar, J=8.55 Hz), 8.16 (dd, 1H, Ar, J_1=8.55 Hz, J_2=1.97 Hz), 8.06 (m, 6H, Ar), 7.97 (m, 4H, Ar), 7.68 (m, 1H, Ar), 7.44 (d, 2H, Ar, J=8.77 Hz), 7.39 (d, 2H, Ar, J=8.77 Hz), 7.02 (d, 2H, Ar, J=8.99 Hz), 6.985 (d, 1H, Ar, J=8.99 Hz), 4.05 (t, 2H, -O-CH_2), 3.99 (s, 3H, -OCH_3), 1.82 (cv, 2H, -CH_2), 1.49 (cv, 2H, -CH_2), 1.35 (m, 4H, -CH_2), 0.92 (t, 3H, -CH_3). ^{13}C-RMN δ_C ppm $(CDCl_3)$: 164.36, 163.41, 162.51, 160.20, 155.92, 153.36, 153.30, 153.19, 153.10, 150.21, 150.18, 146.84, 135.39, 131.42, 131.27, 130.04, 129.67, 125.44, 125.32, 124.36, 124.32, 122.69, 122.58, 122.42, 122.39, 116.48, 114.82, 111.22 (2*>C=O esteric + 26C, aromatic); 68.48 (-O-CH_2), 56.56 (OCH_3), 31.57, 29.13, 25.69, 22.59, 14.04 (5C, aliphatic).

4-((3-((4-(4-((4-heptyloxyphenyl)azo)benzoyloxy)phenyl)azo)phenyl)-azo) phenyl 3-bromo-4-methoxybenzoate (5b): Quantities: compound **(3b)** (0.170 g, 0.27 mmoli), 3-bromo-4-methoxybenzoic acid (0.067 g, 0.29 mmoli), DCC (0.098 g, 0.47 mmoli), DMAP (0.048 g, 0.39 mmoli), 100 ml dry dichloromethane. Orange product, η = 59.73 % (0.135 g), liquid crystal: 133^0C (K/K), 172^0C (K/I), 179^0C (I/CL), 156^0C (CL/K), 119^0C (K/K), 80^0C (K/K). ^1H-RMN δ_H ppm $(CDCl_3)$: 8.46 (m, 1H, Ar), 8.40 (d, 1H, Ar, J=8.55 Hz), 8.35 (d, 2H, Ar, J=8.55 Hz), 8.17 (dd, 1H, Ar, J_1=8.55 Hz, J_2=1.97 Hz), 8.12 (m, 6H, Ar), 8.00 (m, 4H, Ar), 7.70 (m, 1H, Ar), 7.49 (d, 2H, Ar, J=8.77 Hz), 7.43 (d, 2H, Ar, J=8.77 Hz), 7.02 (d, 2H, Ar, J=8.99 Hz), 6.98 (d, 1H, Ar, J=8.99 Hz), 4.06 (t, 2H, -O-CH_2), 3.95 (s, 3H, -OCH_3), 1.83 (cv, 2H, -CH_2), 1.53 (cv, 2H, -CH_2), 1.38 (m, 6H, -CH_2), 0.95 (t, 3H, -CH_3). ^{13}C-RMN δ_C ppm $(CDCl_3)$: 164.39, 163.44, 162.53, 160.23, 155.94, 153.43, 153.32, 153.20, 153.12, 150.24, 150.20, 150.09, 146.86, 135.40, 131.43, 131.29, 130.05, 129.68, 125.45, 125.34, 124.37, 124.31, 122.58, 122.52, 122.44, 116.47, 114.84, 113.93 (2 * >C=O esteric + 26C, aromatic); 68.47 (-O-CH_2), 56.56 (OCH_3), 31.75, 29.15, 29.04, 25.95, 22.59, 14.07 (6C, aliphatic).

4-((3-((4-(4-((4-octyloxyphenyl)azo)benzoyloxy)phenyl)azo)phenyl)-azo) phenyl 3-bromo-4-methoxybenzoate (5c): Quantities: compound **(3c)** (0.200 g, 0.30 mmoli), 3-bromo-4-methoxybenzoic acid (0.077 g, 0.33 mmoli), DCC

(0.113 g, 0.55 mmoli), DMAP (0.056 g, 0.46 mmoli), 100 ml dry dichloromethane. Orange product, η = 45.45 % (0.120 g), liquid crystal: 176^0C (CL/I), 166^0C (I/CL), 152^0C (CL/K). ^{1}H-RMN δ_H ppm (CDCl$_3$): 8.46 (m, 1H, Ar), 8.42 (d, 1H, Ar, J=1.97 Hz), 8.35 (d, 2H, Ar, J=8.55 Hz), 8.16 (dd, 1H, Ar, J$_1$=8.55, J$_2$=1.97), 8.07 (m, 6H, Ar), 7.98 (m, 4H, Ar), 7.68 (m, 1H, Ar), 7.44 (d, 2H, Ar, J=8.77 Hz), 7.39 (d, 2H, Ar, J=8.77 Hz), 7.02 (d, 2H, Ar, J=8.55 Hz), 6.99 (d, 1H, Ar, J=8.55 Hz), 4.05 (t, 2H, -O-CH$_2$), 3.99 (s, 3H, -OCH$_3$), 1.83 (cv, 2H, -CH$_2$), 1.48 (cv, 2H, -CH$_2$), 1.34 (m, 8H, -CH$_2$), 0.90 (t, 3H, -CH$_3$). ^{13}C-RMN δ_C ppm (CDCl$_3$): 164.37, 163.42, 162.53, 160.23, 155.95, 153.43, 153.32, 153.21, 153.13, 150.24, 150.20, 150.09, 146.87, 135.40, 132.40, 131.42, 131.29, 130.06, 129.68, 125.43, 125.34, 124.37, 122.58, 122.52, 122.43, 116.50, 114.84, 113.94 (2 * >C=O esteric + 26C, aromatic); 68.47 (-O-CH$_2$), 55.53 (OCH$_3$), 31.80, 29.34, 29.22, 29.15, 26.00, 22.64, 14.09 (7C, aliphatic).

4-((3-((4-(4-((4-nonyloxyphenyl)azo)benzoyloxy)phenyl)azo)phenyl)-azo)phenyl 3-bromo-4-methoxybenzoate (5d): Quantities: compound **(3d)** (0.240 g, 0.36 mmoli), 3-bromo-4-methoxybenzoic acid (0.091 g, 0.39 mmoli), DCC (0.133 g, 0.64 mmoli), DMAP (0.058 g, 0.47 mmoli), 100 ml dry dichloromethane. Orange product, η = 41.13 % (0.130 g), liquid crystal: 158^0C (K/K), 166^0C (K/I), 159^0C (I/CL), 150^0C (CL/K), 65^0C (K/K). ^{1}H-RMN δ_H ppm (CDCl$_3$): 8.46 (m, 1H, Ar), 8.42 (d, 1H, Ar, J=1.97 Hz), 8.355 (d, 2H, Ar, J=8.34 Hz), 8.16 (dd, 1H, Ar, J$_1$=8.55 Hz, J$_2$=1.97 Hz), 8.07 (m, 6H, Ar), 7.98 (m, 4H, Ar), 7.68 (m, 1H, Ar), 7.44 (d, 2H, Ar, J=8.56 Hz), 7.40 (d, 2H, Ar, J=8.56 Hz), 7.02 (d, 2H, Ar, J=8.55 Hz), 6.99 (d, 1H, Ar, J=8.55 Hz), 4.05 (t, 2H, -O-CH$_2$), 4.00 (s, 3H, -OCH$_3$), 1.83 (cv, 2H, -CH$_2$), 1.48 (cv, 2H, -CH$_2$), 1.28 (m, 10H, -CH$_2$), 0.89 (t, 3H, -CH$_3$). ^{13}C-RMN δ_C ppm (CDCl$_3$): 164.38, 163.43, 162.53, 160.23, 155.94, 153.43, 153.32, 153.21, 153.13, 150.20, 150.09, 146.87, 135.40, 132.40, 131.42, 131.29, 130.06, 129.68, 125.49, 125.34, 124.37, 124.31, 122.58, 122.52, 122.43, 116.50, 114.84, 113.94 (2 * >C=O esteric + 26C, aromatic); 68.47 (-O-CH$_2$), 55.53 (OCH$_3$), 31.87, 29.52, 29.37, 29.25, 29.15, 25.99, 22.66, 14.10 (8C, aliphatic).

4-((3-((4-(4-((4-decyloxyphenyl)azo)benzoyloxy)phenyl)azo)phenyl)-azo) phenyl 3-bromo-4-methoxybenzoate (5e): Quantities: compound **(3e)** (0.33 g, 0.48 mmoli), 3-bromo-4-methoxybenzoic acid (0.122 g, 0.53 mmoli), DCC (0.179 g, 0.87 mmoli), DMAP (0.088 g, 0.72 mmoli), 100 ml dry dichloromethane. Orange product, η = 37.03 % (0.160 g), m.p=168^0C. ^{1}H-RMN δ_H ppm (CDCl$_3$): 8.46 (m, 1H, Ar), 8.40 (m, 1H, Ar, J=1.97 Hz), 8.35 (d, 2H, Ar, J=8.55 Hz), 8.17 (dd, 1H, Ar, J$_1$=8.77 Hz, J$_2$=1.97 Hz), 8.07 (m, 6H, Ar), 7.97 (m, 4H, Ar), 7.68 (m, 1H, Ar), 7.44 (d, 2H, Ar, J=8,77 Hz), 7.395 (d, 2H, Ar, J=8.77 Hz), 7.02 (m, 2H, Ar, J=8.77 Hz), 6.98 (d, 1H, Ar, J=8.55 Hz), 4.05 (t, 2H, -O-CH$_2$), 3.99 (s, 3H, -OCH$_3$), 1.82 (cv, 2H, -CH$_2$), 1.48 (cv, 2H, -CH$_2$), 1.28 (m, 12H, -CH$_2$), 0.89 (t, 3H, -CH$_3$). ^{13}C-RMN δ_C ppm (CDCl$_3$): 164.38, 163.43, 162.53, 160.23, 155.94, 153.42, 153.33, 153.30, 153.21, 153.12, 150.20, 150.07, 146.86, 135.41, 132.40, 131.41, 131.29, 130,06, 129.68, 125.49, 125.34, 124.37, 122.58, 122.52, 122.44, 116.49, 114.84, 113.93 (2 * >C=O esteric + 26C, aromatic); 68.46 (-O-CH$_2$), 55.52 (OCH$_3$), 31.88, 29.67, 29.54, 29,36, 29.31, 29.15, 25.99, 22.66, 14.10 (9C, aliphatic).

REFERENCES

1. T. Niori, T. Sekine, J. Watanabe, T. Furukawa, H.J. Takezoe, *Materials Chemistry,* **1996**, *6*, 1231.
2. D.R. Link, G. Natale, R. Shao, J.E. Maclennan, N.A. Clark, E. Korblova, D.M. Walba, *Science*,**1997**, *278*, 1924.
3. G. Heppke, D. Moro, *Science*, **1998**, *279*, 1872.
4. D.M. Walba, E. Korblova, R. Shao, J.M. Maclennan, D.R. Link, M.A. Glaser, N.A. Clark, *Science*, **2000**, *288*, 2181.
5. D.A. Coleman, J. Fernsler, N. Chattham, M. Nakata, Y. Takanishi, E. Körblova, D.R. Link, R.-F. Shao, W.G. Jang, J.E. Maclennan, O. Mondainn-Monval, C. Boyer, W. Weissflog, G. Pelzl, L.-C. Chien, J. Zasadzinski, J. Watanabe, D.M. Walba, H. Takezoe, N.A. Clark, *Science*, **2003**, *301*, 1204.
6. G. Pelzl, S. Diele, W. Weissflog, *Advanced Matererials*, **1999**, *11*, 707.
7. C.-K. Lee, J.-H. Kim, E.J. Choi, W.-C. Zin, L.-C. Chien, *Liquid Crystals*, **2001**, *28*, 1749.
8. C.-K. Lee, S.-S. Kwon, S.-T. Shin, E.-J. Choi, S. Lee, L.-C. Chien, *Liquid Crystals*, **2002**, *29*, 1007.
9. C.-K. Lee, S.-S. Kwon, T.-S. Kim, E.-J. Choi, S.-T. Shin, W.-C. Zin, D.-C. Kim, H. Kim, L.-C. Chien, *Liquid Crystals*, **2003**, *30*, 1401.
10. S.-T. Shin, H. Choi, C.-K. Lee, S.-S. Kwon, T.-S. Kim, E.J. Choi, S.-Y. Kim, W.-C. Zin, D.-C. Kim, L.-C. Chien, *Liquid Crystals*, **2004**, *31*, 935.
11. Y. Huang Ming, Yuan and Ma, Qing-Lan, **2010**, *Liquid Crystals*, *37*:9, 1119.
12. H. Sanielevici, F. Urseanu, „*Synthesis of azo dyes", Vol.1.*, Technical Publishing House, Bucharest, **1987**, chapter 1, 61, chapter 2, 196.
13. Gh. Simion, D. Iuganu, I. Cârlescu, D. Scutaru, *Bulletin of the Polytechnic Institute of Iaşi, Section Chemistry and Chemical Engineering*, **2011**, *57* (3), 213.
14. D. Iuganu, I. Cârlescu, G. Lisa, G.H. Mehl, D. Scutaru, *unpublished results from our laboratory.*
15. E.-R. Cioancă, G. Lisa, D. Scutaru, *Analele Universităţii din Bucureşti – Chimie (serie nouă)*, **2010**, *19*(2), 39.
16. I. Dierking, "*Textures of liquid crystals"*, WILEY-VCH Verlag, GmbH & Co. KGaA, Weinheim, **2003**.

ASYMMETRIC BENT-CORE LIQUID CRYSTALS BASED ON A 2,7-DIHYDROXYNAPHTALENE CORE WITH AZO AND ESTERIC CONNECTING GROUPS

GHEORGHE SIMION[a], IRINA CARLESCU[a], GABRIELA LISA[a], DAN SCUTARU[a,*]

ABSTRACT. Two series of asymmetric bent-core type derivatives containing 2,7-dihydroxynaphtalene as central unit and 4-(4-alkyloxyfenilazo)-benzoyl and 4-methoxy-benzoyl or 3-bromo-4-methoxy-benzoyl side arms as mesogenic groups have been synthesized. The liquid crystalline properties have been investigated by differential scanning calorimetry (DSC) and polarized optical microscopy (POM). All the synthesized compounds presented liquid crystalline properties, mainly monotropic, with smectic or nematic textures.

Keywords: bent-core compounds, 2,7-dihydroxynaphtalene azo aromatic mesogens

INTRODUCTION

In the last period, an outstanding development occurs in the field of unconventional liquid crystals¸ which present very different molecular shapes if compared with the so-called "classic liquid crystals" and that are capable to generate atypical mesophases, with specific textures. Unconventional liquid crystals are organic derivatives with liquid crystalline properties and unusual molecular shape such as: *banana* type mesogens, *bent-core*, *bow shaped* or *boomerang* structures [1-5], *disc-rod* systems [6-9], *butterfly* mesogens [10], dendrimers up to supermolecules [11] and complex supramolecular structures [12]. New types of mesophases were discovered and physical forces permitting the self-assembling of such systems in ordered structured were investigated.

Among the unconventional liquid crystals, the bent core compounds represent a very promising field. Although biaxial nematic phase was predicted by Freiser forty years ago, it remained a hot subject in the literature in the effort to prove the existence of this new mesophase as a physical reality by using the known experimental methods [13]. Now, it is considered that the use of biaxial nematic liquid crystals for LCD will ensure much faster response times at lower costs. In the case of bent core compounds, the reorientation of the molecules does not require much energy when compared to nematics.

---

[a] Gheorghe Asachi Technical University of Iaşi, Faculty of Chemical Engineering and Environmental Protection, 73 D. Mangeron St., Iaşi, Romania
* *dscutaru@ch.tuiasi.ro*

Structure property relations in bent core mesogens are less predictable than those of calamitics. The only criterion need to be applied is that two mesogenic groups should be connected non-linearly. The connection is made through a central unit, which plays a key role in inducing the bent shape of molecules. If the connection between the mesogenic lateral groups is not in tight angle, there is no chance to obtain banana mesogens even if the construction of the molecule in all other buildings stones corresponds to the structure of bananas [14]. The most calamitic molecules can play the mesogenic groups role in *bent core* systems, being constituted from two aromatic rings connected through different connection groups and a terminal chain, linked in *para* position of the aromatic rings. These calamitic molecules are preferentially connected to an aromatic rigid core of five or six atoms, in the way that the angle between the two wings (bending angle) to be between 120 and 140°. Generally, the majority of bent core compounds are 1,3-disubstituted benzenes, 2,7-disubstituted naphthalene ring [15-17], 1,3,4-oxadiazol or 2,5-disubstituted-tiophene [18], 2,6-disubstituted pyridine [19] etc.

An important role on transition temperature controlling, interval and type of forming mesophase has the length, rigidity and the polarity of lateral structures and the length and the chemical nature of terminal chains. The nature, position and direction of connecting groups between rings play an important role on banana mesophases.

The most successful bent core mesogenic materials exhibiting several (switchable) mesophases contain the sensitive azomethine group. But this group is thermally instable and sensitive to proton and metal surfaces. The *bent-core* molecules containing azo linkage have been little studied, although there are numerous examples for other classes of liquid crystalline compounds in which the presence of this connecting group offered very interesting properties to the synthesized structures [20].

Study of *bent-core* units based on biaxial liquid crystals represents a very actual subject not only from theoretically point of view but practically too. The existence of a stable biaxial nematic mesophase might produce a whole class of liquid crystals based on devices that will considerably improve the switching properties or as optical compensation films etc [21].

This paper presents the synthesis, structural characterization and mesomorphic properties of two new series of asymmetric bent core compounds, containing azo-aromatic and esteric linkages as connecting groups, based on a 2,7-dihydroxynaphthalene core and 4-(4-alcoxifenilazo)-benzoyl and 4-methoxy-benzoyl or 3-bromo-4-methoxy-benzoyl units as mesogenic groups. The liquid crystalline properties were evaluated by means of polarized optical microscopy and differential scanning calorimetry. All the synthesized compounds presented liquid crystalline properties, mainly of monotropic type, with nematic or smectic textures.

RESULTS AND DISCUSSION

The synthesis of the target compounds is depicted in **Scheme 1**. The final compounds were obtained in a two step reaction. In the first step, 2,7-dihydroxynaftalene was reacted with 4-methoxy- or 3-bromo-4-methoxy benzoylchlorides [22] in the presence of pyridine, in anhydrous dichloromethane to form the monoesters **3a**, **3b**. In the second step, monoesters **3a**, **3b** were reacted with 4-(4-alkyloxyphenylazo)-benzoyl chloride, in aqueous K_2CO_3 / dichloromethane, using tetrabutylammonium hydrogen sulfate (*TBAHS*) as phase transfer catalyst. All the obtained compounds were purified by column chromatography (silicagel, methylene chloride : ethyl acetate = 20:1) and characterized by ^{1}H- and ^{13}C-NMR and mass spectrometry. Yields were between 39.4-82.3%.
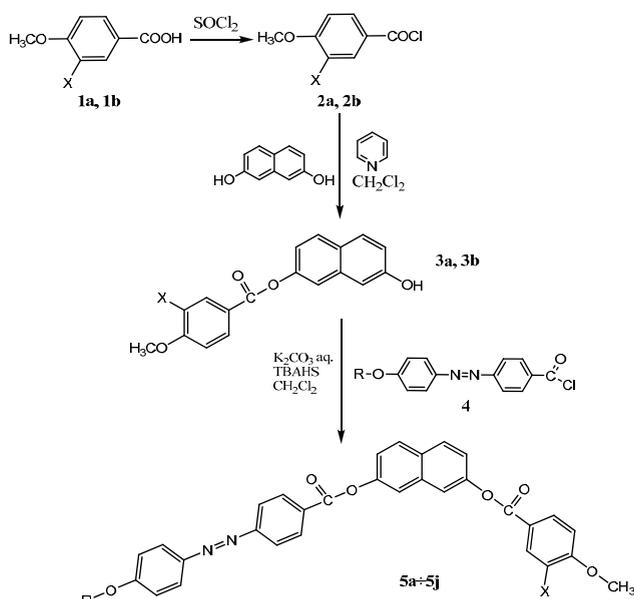
Scheme 1.

The presence of liquid crystalline properties was investigated by means of differential scanning calorimetry (DSC) and polarized light optical microscopy (POM). All the synthesized **5a ÷ 5j** compounds presented liquid crystalline properties, mainly of monotropic type (only compound **5j** presented enantiotropic liquid crystalline properties).

For a better confirmation of the intervals of mesophases, the DSC runs for compounds **5i** and **5j** were repeated several times with heating-cooling cycles of 10, 20 and 40^{0}C per minute but no significant changes could be observed. The observed textures were assigned by visual comparison (under the microscope) with literature data [23].

Table 1. Transition temperatures [°C] and transition enthalpies [J·g^{-1}]
of compounds **5a÷5j**

Comp.	n	$T / \,^{\circ}C$ [$\Delta H / Jg^{-1}$]						T_{onset}
		Heating (°C)		*Cooling (°C)*				
		Cr/N	N/I	I/Sch.	I/Sm$_x$	N	Cr	
5a	6	-	140 [-48.72]	137*	-	130 [0.24]	96 [46.29]	349
5b	7	-	133 [-36.87]	130*	-	124 [0.22]	104 [42.56]	350
5c	8	-	140 [-47.85]	135*	-	127 [0.20]	108 [29.37]	353
5d	9	-	150 [-59.04]	146*	-	131 [8.47]	107 [2.81]	339
5e	10	-	146 [-55.36]	142*	-	112 [0.21]	92 [39.33]	337
5f	6	-	149 [-48,27]	-	-	99*	86 [21,85]	295
5g	7	-	159 [-45,83]	-	-	108*	103 [19,32]	329
5h	8	-	147 [-45,25]	-	-	109*	98 [27,35]	333
5i	9	-	129 [-32,03]	-	106 [0,35]	-	91 [11,72]	323
5j	10	130 [0,28]	146 [-0,28]	-	135 [0,94]	-	107 [32,51]	319

Abbreviation: Cr-crystalline, Sm$_x$-smectic, I-isotropic, N-nematic, Sch. – Schlieren * Data obtained from POM investigations T$_{onset}$ - the initial temperature at which the degradations processes begin

For all the investigated compounds, the isotropisation temperatures and the isotropic – liquid crystal transitions are relatively low (between 129 – 159^{0}C on heating and 106 – 146^{0}C on cooling).

For the **5a ÷ 5e** compounds, the stability range of the mesophases on cooling is reasonable large (between 26 – 50^{0}C) while for **5f÷5j** brominated compounds is relatively small (between 5 – 28^{0}C). In the case of compound **5j**, when heated, the stability range of the mesophase is only 16^{0}C. Taking into consideration the structural differences between the two series of compounds, it may be concluded that the presence of bromine atom in the structure of **5f÷5j** compounds has a negative influence upon the stability of the mesophases.

Due to the very small transition enthalpies, the temperatures of entering into mesophase for **5a÷5h** compounds could be evidenced only by means of polarized optical microscopy.

As examples, Figure 1 exemplifies the DSC curves for compounds **5a** and **5j**.
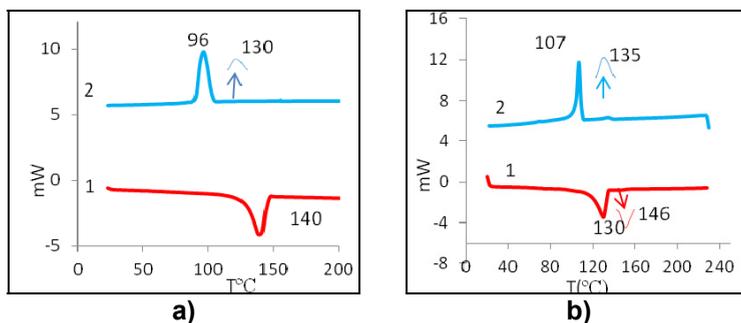
Figure 1. DSC curves: (a) **5a**: 1 – second heating, 2 – first cooling,
(b) **5j**: 1 – second heating, 2 – first cooling

According to POM, on cooling, compound **5a** presents two liquid crystalline transitions: the first one, with Schlieren textures, begins at 137 ^{0}C and ends at 130^{0}C (Figure 2a and 2b); the second one, of nematic type, starts at 130^{0}C and holds until crystallization (96^{0}C) (Figure 2c).
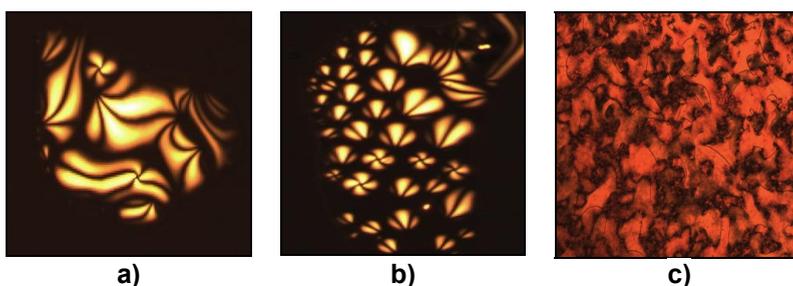
Figure. 2. Optical textures for compound **5a**: Schlieren textures, a) 135^{0}C and b) 131^{0}C; nematic texture, c) 127^{0}C

Figure 3 presents some other example of nematic textures of compounds 5b ÷ 5d.
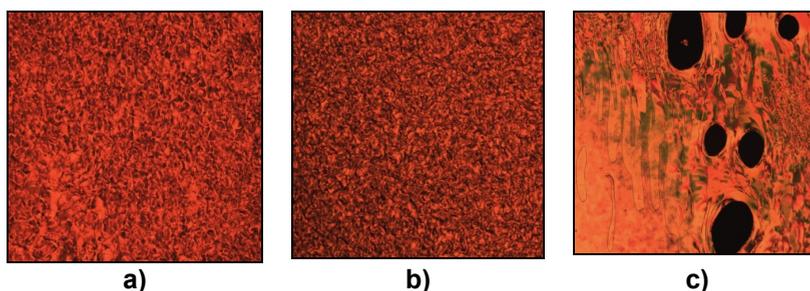
Figure 3. Nematic optical textures (cooling): a) **5b**, 118^{0}C, b) **5c**, 115^{0}C, c) **5d**, 120^{0}C.

In the case of brominated compounds **5f÷5j** polarized optical microscopy evidenced both nematic and smectic textures.

Compounds **5f÷5h** have a monotropic behavior, with nematic textures when cooling, while compound **5i** revealed a smectic one (Figure 4).

For compound **5j**, during the heating process polarized optical microscopy showed a nematic texture between 130 – 146^{0}C (Figure 5a). On cooling, between 135 – 107, SmA *bâtonnets* texture appeared (Figure 5b).
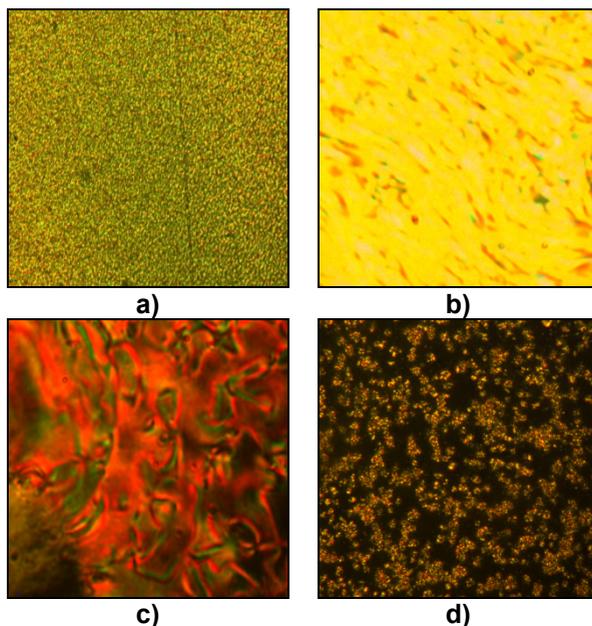
Figure 4. Optical textures, second cooling: nematic:
a) **5f**, 90^{0}C, b) **5g**, 104^{0}C, c) **5h**, 97^{0}C; smectic: d) **5i**, 98^{0}C.
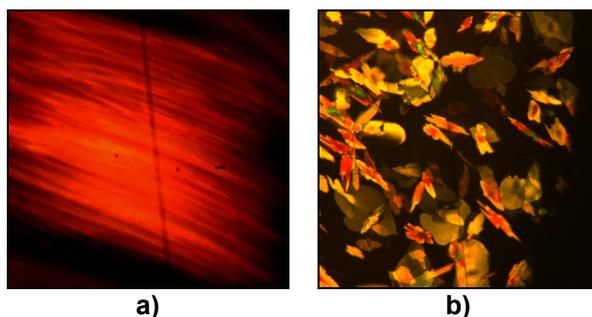
Figure 5. Optical textures for compound **5j**:
a) second heating, 135^{0}C, nematic; b) second cooling, 120^{0}C, smectic A, bâtonnets

The thermogravimetric data evidenced a very good thermal stability for all the investigated compounds, the temperatures at which degradation processes begun (T_{onset}) being situated with around 200^0C higher than the isotropisation temperatures (**Table 1**). For all **5a ÷ 5j** compounds, thermal degradation took place in only one stage, with a weight loss of about 70%. In all the cases, a residue of about 30% has been left. Such a thermal behavior, with T_{onset} values between 300 and 350^0 is similar with other classes of bent core compounds containing azo-aromatic and esteric linking groups [24,25].

CONCLUSIONS

Two series of asymmetric bent-core derivatives based on 2,7-dihydroxynaphtalene core and with 4-(4-alcoxifenilazo)-benzoyl and 4-methoxy-benzoyl or 3-bromo-4-methoxy-benzoyl wings as mesogenic groups have been synthesized and investigated by DSC and POM from the point of view of liquid crystalline properties. All the synthesized compounds presented liquid crystalline properties, mainly monotropic, with nematic or smectic textures. Thermogravimetric studies evidenced a very good thermal stability for all the investigated compounds.

EXPERIMENTAL SECTION

MATERIALS

3-Bromo-4-metoxy-benzoic acid (**1b**), 4-metoxy-benzoyl chloride (**2a**), 3-bromo-4-metoxy-benzoyl chloride (**2b**) and 4-(4-alkoxyphenylazo)-benzoyl chloride (**4**) have been prepared accordingly to literature data [22, 26]. All other materials used in the present work have been purchased from Sigma Aldrich and used as received. For column chromatography Silica gel 60 (Merck) was used, while for thin layer chromatography Silica gel plates (Merck Silica gel F254) were used.

TECHNIQUES

Nuclear magnetic resonance (NMR) spectra were recorded on a Bruker® Avance DRX 400 MHz spectrometer. Chemical shifts were reported in ppm relative to tetramethylsilane (TMS) as internal standard. Mass spectra were recorded on a quadrupole-time of flight mass spectrometer equipped with an electrospray ion source (Agilent® 6520 Accurate Mass Q-ToF LC/MS). The FTIR spectra were recorded on a Nicolet Magna 550 spectrometer (NaCl crystal window). Transition temperatures were determined using a Linkam heating stage connected with a Linksys 32 temperature control unit in conjunction with a Axioscop 40 Zeiss polarizing optical microscope and Qimaging/Retiga-1000R camera for image capture, the transitions being confirmed by DSC analysis (Mettler Toledo DSC1). Heating and cooling cycles

were run at rates of 10^0C/min under nitrogen atmosphere, with sample measured in closed lid aluminum pans. All the thermal analysis were run in the same conditions, on 2.8 - 4.3 mg samples on a Mettler-Toledo® TGA SDTA851® derivatograph in N_2 atmosphere, with a flow rate of 20 ml/min and a heating rate of 10 ^{0}C/min from 25 to 900°C.

SYNTHESIS

General method for the preparation of 2-(4- methoxyphenylcarbonyloxy) -2-hydroxynaphtalene (3a) and 2-(3-bromo-4-methoxyphenylcarbonyloxy)- 2-hydroxynaphtalene (3b). Compounds were prepared by adapting literature data [27]. To a mixture of 2,7-dihydroxynaphtalene (14.18 mmol) and pyridine (86,77 mmol) in dry dichloromethane (80 ml), a solution of acyl chloride **2** (3.53 mmol) in dichloromethane (10 ml) was added dropwise at 0^0C. The solution was stirred at 0^0C for 24 h, diluted with water (100 ml), extracted with dichloromethane, dried over $MgSO_4$ and evaporated. A viscous residue was obtained which was purified by column chromatography on Silica Gel using a mixture of methylene chloride: ethyl acetate 20:1 as eluent and giving the purified products as white powder.

2-(4-Methoxyphenylcarbonyloxy)-2-hydroxynaphtalene (3a). Quantities: 2.27 g (14.18 mmol) 2,7-dihydroxynaphtalene, 7 ml (86.77 mmol) pyridine, 0.60 g (3.53 mmol) 4-methoxybenzoyl chloride. Yield 40.76 % (1.7 g), m.p.= 203^0C. ^{1}H-NMR δ_C ppm (DMSO-d6): 9.86 (s, 1H, -OH), 8.13 (d, 2H, Ar, J= 8.8 Hz), 7.83 (dd, 2H, Ar, J_1= 8.8 Hz, J_2= 15.3 Hz), 7.57 (d, 1H, Ar, J= 2.0 Hz), 7.16 (m, 4H, Ar), 7.10 (dd, 1H, Ar, J_1= 2.3 Hz, J_2= 8.8 Hz), 3.89 (s, 3H, -O-CH_3). ^{13}C-NMR δ_C ppm (DMSO-d6): 164.40, 163.71, 155.95, 148.82, 135.13, 131.97, 129.29, 129.01, 125.66, 121.05, 118.42, 118.22, 116.96, 114.26, 108.48 (1 * >C=O esteric + 14 C, aromatic), 55.61(-O-CH_3). *FT-IR* (KBr, cm^{-1}): 3435.21 (vOH, aromatic), 3068.74 (vCH, aromatic), 2929.86, 2858.5 (vCH, aliphatic), 1718.57 (v O-C=O); m/z (DMSO): 317.16 $[M+Na]^+$.

2-(3-Bromo-4-methoxyphenylcarbonyloxy)-2-hydroxynaphtalene (3b). Quantities: 2.27 g (14.18 mmol) 2,7-dihydroxynaphtalene, 7 mL (86.77 mmol) pyridine, 0.87 g (3.53 mmol) 3-bromo-4-methoxybenzoyl chloride. Yield 31.25 % (1.65 g), m.p.= 185^0C. ^{1}H-NMR δ_C ppm (DMSO-d6): 9.98 (s, 1H, -OH), 8.55 (dd, 1H, Ar, J_1= 2.19, Hz, J_2= 8.55 Hz), 8.295 (d, 1H, Ar, J= 2.19 Hz), 7.86 (1H, d, Ar, J= 8.98 Hz), 7.82 (1H, d, Ar, J= 8.77 Hz), 7.585 (1 H, d, Ar, J= 1.97 Hz), 7.33 (1 H, d, Ar, J= 8.77 Hz), 7.18 (1 H, dd, Ar, J_1= 2.19 Hz, J_2= 8.77 Hz), 7.14 (1H, d, Ar, J= 2.19), 7.10 (1 H, dd, Ar, J_1= 2.41 Hz, J_2= 8.77 Hz), 3.99 (s, 3H, -CH_3). ^{13}C-NMR δ_C ppm (DMSO-d6): 163.27, 159.68, 155.92, 148.60, 135.02, 134.12, 131.36, 129.25, 128.99, 125.66, 122.33, 118.43, 118.00, 116.87, 112.58, 110.71, 108.42 (1 * >C=O esteric + 16 C, aromatic), 56.77 (-O-CH_3). *FT-IR* (KBr, cm^{-1}): 3431.36 (v OH, aromatic), 3058.09 (vCH, aromatic), 2962.65, 2941.44 (vCH, aliphatic), 1712.78 (v O-C=O); m/z (DMSO): 395.08 $[M+Na]^+$.

General method for the preparation of 2-((4-alkyloxyphenyl)-4-azophenylcarbonyloxy)-7-(4-methoxyphenylcarbonyloxy)naphtalen (5a÷5e) and 2-((4-alkyloxyphenyl)-4-azophenylcarbonyloxy)-7-(3-bromo-4-methoxy-phenylcarbonyloxy)naphtalen (5f÷5j). Compounds were prepared by adapting literature data [28]. Acyl chlorides were prepared and introduced immediately into synthesis. A mixture of compound **3**, 4-(4-alkyloxyphenylazo)-benzoyl chloride **4**, potassium carbonate, tetrabutylammonium hydrogensulfate (TBAHS) in dichloromethane (150 mL) and water (40 mL) were vigorously stirred for 24 h at room temperature. For a good solubility of the compound **3** in methylene chloride a few drops of tetrahydrofuran (THF) were added. The organic layer was separated, washed several times with distilled water, dried on anhydrous magnesium sulfate and concentrated on rotary evaporator. Compounds (**5a÷5j**) were purified by column chromatography on Silica Gel using a mixture of methylene chloride: ethyl acetate 20:1 as eluent. Orange products were obtained.

2-((4-Hexyloxyphenyl)-4-azophenylcarbonyloxy)-7-(4-methoxyphenyl-carbonyloxy)naphtalen (5a). Quantities: 0.22 g (0.8297 mmol) 2-(4-methoxyphenylcarbonyloxy)-2-hydroxynaphtalene, 0.28 g (0.8297 mmol) 4-(4-hexyloxyphenylazo)-benzoyl chloride, 0.14 g (1.005 mmol) K_2CO_3, 6.4 mg (0.019 mmol) TBAHS. Yield 70.48 % (0.32 g), orange product, liquid crystal: 140^0C (K/I), 137^0C (I/CL), 130^0C (CL/CL), 96^0C (CL/K). ^{1}H-NMR δ_C ppm (CDCl$_3$): 8.37 (d, 2H, Ar, J= 8.4 Hz), 8.20 (d, 2H, Ar, J= 8.8 Hz), 7.99 (d, 2H, J= 7.4 Hz), 7.97(d, 2H, Ar, J= 8.6 Hz), 7.93(dd, 2H, Ar, J_1= 3.7 Hz, J_2=8.9 Hz), 7.69 (dd, 2H, Ar, J_1= 1.7 Hz, J_2= 9.9 Hz), 7.39 (dd, 1H, Ar, J_1= 2.2 Hz, J_2= 6.8 Hz), 7.36 (dd, 1H, Ar, J_1= 2.2 Hz, J_2= 6.58 Hz), 7.01 (m, 4H, Ar), 4.05 (t, 2H, -O-CH$_2$-), 3.90 (s, 3H, -O-CH$_3$), 1.83 (qv, 2H, -CH$_2$-), 1.49 (qv, 2H, -CH$_2$-), 1.32 (m, 4H, -CH$_2$-), 0.92 (t, 3H, -CH$_3$).^{13}C-NMR δ_C ppm (CDCl$_3$): 164.95, 164.79, 163.99, 162.49, 155.86, 149.48, 149.24, 146.86, 134.43, 132.38, 131.28, 130.34, 129.54, 129.42, 129.32, 125.33, 122.56, 121.73, 121.44, 121.06, 118.62, 118.54, 114.83, 113.89 (2*>C=O esteric + 22 C, aromatic), 68.46, 55.53, 31.56, 29.13, 25.68, 22.60, 14.04 (1*-O-CH$_2$- + 1*-O-CH$_3$ + 5 C, aliphatic); m/z(CHCl$_3$): 603.36 [M+1].

2-((4-Heptyloxyphenyl)-4-azophenylcarbonyloxy)-7-(4-methoxy-phenyl- carbonyloxy)naphtalen (5b). Quantities: 0.22 g (0.8297 mmol) 2-(4-methoxyphenylcarbonyloxy)-2-hydroxynaphtalene, 0.29 g (0.8297 mmol) 4-(4-heptyloxyphenylazo)-benzoyl chloride, 0.14 g (1.005 mmol) K_2CO_3, 6.4 mg (0.019 mmol) TBAHS. Yield 68.81 % (0.32 g), orange product, liquid crystal: 133^0C (K/I), 130^0C (I/CL), 124^0C (CL/CL), 104^0C (CL/K). ^{1}H-NMR δ_C ppm (CDCl$_3$): 8.37 (d, 2H, Ar, J= 8.5 Hz), 8.20 (d, 2H, Ar, J= 8.9 Hz), 7.99 (d, 2H, Ar, J= 7.24 Hz), 7.965 (d, 2H, Ar, J= 7.46 Hz), 7.925 (dd, 2H, Ar, J_1= 3.6 Hz, J_2= 8.99 Hz), 7.69 (dd, 2H, Ar, J_1= 2.0 Hz, J_2= 9.86 Hz), 7.385 (dd, 1H, Ar, J_1= 2.2 Hz, J_2= 6.8 Hz), 7.365 (dd, 1H, Ar, J_1= 2.2 Hz, J_2= 6.58 Hz), 7.01 (m, 4H, Ar), 4.05 (t, 2H, -O-CH$_2$-), 3.89 (s, 3H, -O-CH$_3$), 1.83 (qv, 2H, -CH$_2$-), 1.48 (qv, 2H, -CH$_2$-), 1.32 (m,

6H, -CH$_2$-), 0.91 (t, 3H, -CH$_3$). ^{13}C-NMR δ$_C$ ppm (CDCl$_3$): 164.94, 164.79, 163.98, 162.48, 155.84, 149.46, 149.23, 146.85, 134.42, 132.38, 131.27, 130.32, 129.53, 129.42, 129.33, 125.32, 122.55, 121.71, 121.44, 121.05, 118.62, 118.53, 114.82, 113.88 (2*>C=O esteric + 22 C, aromatic), 68.45, 55.52, 31.77, 29.16, 29.04, 25.96, 22.61, 14.10 (1*-O-CH$_2$- + 1*-O-CH$_3$ + 6 C, aliphatic); m/z(CHCl$_3$): 617.38 [M+1].

2-((4-Octyloxyphenyl)-4-azophenylcarbonyloxy)-7-(4-methoxyphenyl-carbonyloxy)naphtalen (5c). Quantities: 0.22 g (0.8297 mmol) 2-(4-methoxy-phenylcarbonyloxy)-2-hydroxynaphtalene, 0.31 g (0.8297 mmol) 4-(4-octyloxy-phenylazo)-benzoyl chloride, 0.14 g (1.005 mmol) K$_2$CO$_3$, 6.4 mg (0.019 mmol) TBAHS. Yield 42.10 % (0.20 g), orange product, liquid crystal: 140^{0}C (K/I), 135^{0}C (I/CL), 127^{0}C (CL/CL), 108^{0}C (CL/K). ^{1}H-NMR δ$_C$ ppm (CDCl$_3$): 8.38 (d, 2H, Ar, J= 8.5 Hz), 8.21 (d, 2H, Ar, J= 8.7 Hz), 7.99 (d, 2H, Ar, J= 7.7 Hz), 7.97 (d, 2H, Ar, J= 8.7 Hz), 7.93 (dd, 2H, Ar, J$_1$= 4.0 Hz, J$_2$= 8.9 Hz), 7.69 (dd, 2H, Ar, J$_1$= 2.0 Hz, J$_2$= 10.1 Hz), 7.39 (dd, 1H, Ar, J$_1$= 2.0 Hz, J$_2$= 7.1 Hz), 7.37 (dd, 1H, Ar, J$_1$= 2.0 Hz, J$_2$= 7.1 Hz), 7.02 (m, 4H, Ar), 4.06 (t, 2H, -O-CH$_2$-), 3.90 (s, 3H, -O-CH$_3$), 1.83 (qv, 2H, -CH$_2$-), 1.49 (qv, 2H, -CH$_2$-), 1.33 (m, 8H, -CH$_2$-), 0.90 (t, 3H, -CH$_3$). ^{13}C-NMR δ$_C$ ppm (CDCl$_3$): 164.96, 164.81, 164.00, 162.50, 155.87, 149.48, 149.24, 146.87, 134.44, 132.39, 131.29, 130.34, 129.55, 129.43, 129.34, 125.33, 122.56, 121.74, 121.45, 121.07, 118.63, 118.55, 114.84, 113.90 (2*>C=O esteric + 22 C, aromatic), 68.47, 55.54, 31.82, 29.35, 29.24, 29.17, 26.01, 22.67, 14.12 (1*-O-CH$_2$- + 1*-O-CH$_3$ + 7 C, aliphatic); m/z(CHCl$_3$): 631.39 [M+1].

2-((4-Nonyloxyphenyl)-4-azophenylcarbonyloxy)-7-(4-methoxyphenyl-carbonyloxy)naphtalen (5d). Quantities: 0.22 g (0.8297 mmol) 2-(4-methoxyphenylcarbonyloxy)-2-hydroxynaphtalene, 0.32 g (0.8297 mmol) 4-(4-nonyloxyphenylazo)-benzoyl chloride, 0.14 g (1.005 mmol) K$_2$CO$_3$, 6.4 mg (0.019 mmol) TBAHS, yield 82.30 % (0.32 g), orange product, liquid crystal: 150^{0}C (K/I), 146^{0}C (I/CL), 131^{0}C (CL/CL), 107^{0}C (CL/K) ^{1}H-NMR δ$_C$ ppm (CDCl$_3$): 8.36 (d, 2H, Ar, J= 8.4 Hz), 8.20 (d, 2H, Ar, J= 8.7 Hz), 7.98 (d, 2H, Ar, J= 7.0 Hz), 7.96 (d, 2H, Ar, J= 8.5Hz), 7.92 (dd, 2H, Ar, J$_1$= 3.4 Hz, J$_2$= 8.8 Hz), 7.68 (dd, 2H, Ar, J$_1$= 1.4 Hz, J$_2$= 9.6 Hz), 7.38 (dd, 1H, Ar, J$_1$= 2.1 Hz, J$_2$= 7.3 Hz), 7.36 (dd, 1H, Ar, J$_1$= 2.2 Hz, J$_2$= 7.3 Hz), 7.00 (m, 4H, Ar), 4.04 (t, 2H, -O-CH$_2$-), 3.88 (s, 3H, -CH$_3$), 1.82 (qv, 2H, -CH$_2$-), 1.47 (qv, 2H, -CH$_2$-), 1.29 (m, 10 H, -CH$_2$-), 0.89 (t, 3H, -CH$_3$). ^{13}C-NMR δ$_C$ ppm (CDCl$_3$): 164.93, 164.77, 163.98, 162.49, 155.84, 149.47, 149.23, 146.85, 134.43, 132.37, 131.27, 130.33, 129.52, 129.41, 129.31, 125.33, 122.55, 121.72, 121.43, 121.05, 118.61, 118.53, 114.82, 113.89 (2*>C=O esteric + 22 C, aromatic), 68.45, 55.51, 31.87, 29.53, 29.38, 29.26, 29.16, 26.00, 22.68, 14.12 (1*-O-CH$_2$- + 1*-O-CH$_3$ + 8 C, aliphatic); m/z(CHCl$_3$): 645.41 [M+1].

2-((4-Decyloxyphenyl)-4-azophenylcarbonyloxy)-7-(4-methoxy phenyl- carbonyloxy)naphtalen (5e). Quantities: 0.22 g (0.8297 mmol) 2-(4-methoxyphenylcarbonyloxy)-2-hydroxynaphtalene, 0.33 g (0.8297 mmol) 4-(4-decyloxyphenylazo)-benzoyl chloride, 0.14 g (1.005 mmol) K$_2$CO$_3$, 6.4 mg (0.019 mmol) TBAHS. Yield 44.33 % (0.32 g), orange product, liquid crystal: 146^{0}C (K/I), 142^{0}C (I/CL), 112^{0}C (CL/CL), 92^{0}C (CL/K). ^{1}H-NMR δ$_C$ ppm (CDCl$_3$): 8.37 (d, 2H, Ar, J=8.1 Hz), 8.20 (d, 2H, Ar, J= 8.5 Hz), 7.97 (d, 2H, Ar, J= 7.1 Hz), 7.96 (d, 2H, Ar, J= 8.4 Hz), 7.93 (dd, 2H, Ar, J$_1$= 3.3 Hz, J$_2$= 8.7 Hz), 7.67 (dd, 2H, Ar, J$_1$= 1.3 Hz, J$_2$= 9.5 Hz), 7.38 (dd, 1H, Ar, J$_1$= 2.1 Hz, J$_2$= 7.3 Hz), 7.35 (dd, 1H, Ar, J$_1$= 2.3 Hz, J$_2$= 7.4 Hz), 7.01 (m, 4H, Ar), 4.04 (t, 2H, -O-CH$_2$-), 3.89 (s, 3H, -CH$_3$), 1.82 (qv, 2H, -CH$_2$-), 1.47 (qv, 2H, -CH$_2$-), 1.32 (m, 12H, -CH$_2$-), 0.89 (t, 3H, -CH$_3$). ^{13}C-NMR δ$_C$ ppm (CDCl$_3$): 164.94, 164.78, 163.98, 162.48, 155.84, 149.47, 149.23, 146.85, 134.42, 132.38, 131.27, 130.32, 129.53, 129.42, 129.31, 125.33, 122.55, 121.71, 121.44, 121.05, 118.62, 118.53, 114.82, 113.88 (2*>C=O esteric + 22 C, aromatic), 68.45, 55.52, 31.89, 29.56, 29.56, 29.38, 29.32, 29.16, 26.00, 22.69, 14.13 (1*-O-CH$_2$- + 1*-O-CH$_3$ + 9 C, aliphatic); m/z(CHCl$_3$): 659.43 [M+1].

2-((4-Hexyloxyphenyl)-4-azophenylcarbonyloxy)-7-(3-bromo-4-meth-oxyphenylcarbonyloxy)naphtalen (5f). Quantities: 0.20 g (0.5373 mmol) 2-(3-bromo-4-methoxyphenyl-carbonyloxy)-2-hydroxynaphtalene 0.20 g (0.591 mmol) 4-(4-hexyloxyphenylazo)-benzoyl chloride, 0.10 g (0.7163 mmol) K$_2$CO$_3$, 4.52 mg (0.013 mmol) TBAHS. Yield 50 % (0.18 g), orange product, liquid crystal: 149^{0}C (K/I), 99^{0}C (I/CL), 86^{0}C (CL/K). ^{1}H-NMR δ$_C$ ppm (CDCl$_3$): 8.45 (d, 1H, Ar, J= 2.1 Hz), 8.38 (d, 2H, Ar, J= 8.6 Hz), 8.19 (dd, 1H, Ar, J$_1$= 2.1 Hz, J$_2$= 8.6 Hz), 7.96 (m, 6H, Ar), 7.71 (d, 1H, Ar, J= 2.0 Hz), 7.68 (d, 1H, Ar, J= 2.0 Hz), 7.40 (dd, 1H, Ar, J$_1$= 2.3 Hz, J$_2$= 8.9 Hz), 7.36 (dd, 1H, Ar, J$_1$= 2.2 Hz, J$_2$= 8.9 Hz), 7.02 (m, 3H, Ar), 4.06 (t, 2H, -O-CH$_2$-), 4.01 (s, 3H, -O-CH$_3$), 1.83 (qv, 2H, -CH$_2$-), 1.50 (qv, 2H, -CH$_2$-), 1.37 (m, 4H, -CH$_2$-), 0.93 (t, 3H, -CH$_3$). ^{13}C-NMR δ$_C$ ppm (CDCl$_3$): 164.81, 163.85, 162.54, 160.18, 155.94, 149.37, 149.28, 146.93, 135.44, 134.44, 131.43, 131.31, 130.36, 129.64, 129.46, 125.35, 123.03, 122.58, 121.22, 118.60, 114.87, 111.60, 111.25 (2*>C=O esteric + 21 C, aromatic), 68.51, 56.57, 31.58, 29.15, 25.70, 22.61, 14.03 (1*-O-CH$_2$- + 1*-O-CH$_3$ + 5 C, aliphatic). m/z(CHCl$_3$): 681.32 [M+1].

2-((4-Heptyloxyphenyl)-4-azophenylcarbonyloxy)-7-(3-bromo-4-meth-oxyphenylcarbonyloxy)naphtalen (5g). Quantities: 0.20 g (0.5373 mmol) 2-(3-bromo-4-methoxyphenyl-carbonyloxy)-2-hydroxynaphtalene 0.21 g (0.591 mmol) 4-(4-heptyloxyphenylazo)-benzoyl chloride, 0.10 g (0.7163 mmol) K$_2$CO$_3$, 4.52 mg (0.013 mmol) TBAHS. Yield 40.54 % (0.15 g), orange product, liquid crystal: 159^{0}C (K/I), 108^{0}C (I/CL), 103^{0}C (CL/K). ^{1}H-NMR δ$_C$ ppm (CDCl$_3$): 8.45 (d, 1H, Ar, J= 1.9 Hz), 8.38 (d, 2H, Ar, J= 8.5 Hz), 8.19 (dd, 1H, Ar, J$_1$= 1.9 Hz, J$_2$= 8.6 Hz), 7.96 (m, 6H, Ar), 7.71 (d, 1H, Ar, J= 1.6 Hz), 7.68 (d, 1H, Ar, J= 1.6 Hz), 7.40 (dd, 1H, Ar, J$_1$= 2.1 Hz, J$_2$= 8.9 Hz), 7.36 (dd, 1H, Ar, J$_1$= 2.1 Hz, J$_2$= 8.9 Hz), 7.02 (m, 3H, Ar), 4.06 (t, 2H, -O-CH$_2$-), 4.00 (s, 3H, -O-CH$_3$), 1.83

(qv, 2H,-CH$_2$-), 1.49 (qv, 2H, -CH$_2$-), 1.36 (m, 6H, -CH$_2$-), 0.91 (t, 3H, -CH$_3$). ^{13}C-NMR δ$_C$ ppm (CDCl$_3$): 164.79, 163.83, 162.53, 160.17, 155.93, 149.36, 149.27, 146.92, 135.43, 134.43, 131.41, 131.29, 130.35, 129.63, 129.44, 125.34, 123.02, 122.58, 121.21, 118.58, 114.86, 111.80, 111.24 (2*>C=O esteric + 21 C, aromatic), 68.50, 56.56, 31.78, 29.19, 29.05, 25.98, 22.61, 14.08 (1*-O-CH$_2$- + 1*-O-CH$_3$ + 6 C, aliphatic). m/z(CHCl$_3$): 695.19 [M+1].

2-((4-Octyloxyphenyl)-4-azophenylcarbonyloxy)-7-(3-bromo-4-methoxyphenylcarbonyloxy)naphtalen (5h). Quantities: 0.20 g (0.5373 mmol) 2-(3-bromo-4-methoxyphenyl-carbonyloxy)-2-hydroxynaphtalene, 0.22 g (0.591 mmol) 4-(4-octyloxyphenylazo)-benzoyl chloride, 0.10 g (0.7163 mmol) K$_2$CO$_3$, 4.52 mg (0.013 mmol) TBAHS. Yield 39.47 % (0.15 g), orange product, liquid crystal: 147^{0}C (K/I), 109^{0}C (I/CL), 98^{0}C (CL/K). ^{1}H-NMR δ$_C$ ppm (CDCl$_3$): 8.45 (d, 1H, Ar, J= 2.1 Hz), 8.37 (d, 2H, Ar, J= 8.3 Hz), 8.19 (dd, 1H, Ar, J$_1$= 2.1 Hz, J$_2$= 8.6 Hz), 7.96 (m, 6H, Ar), 7.71 (d, 1H, Ar, J= 2.1 Hz), 7.68 (d, 1H, Ar, J= 2.1Hz), 7.40 (dd, 1H, Ar, J$_1$= 2.3 Hz, J$_2$= 8.9 Hz), 7.36 (dd, 1H, Ar, J$_1$= 2.2 Hz, J$_2$= 8.8 Hz), 7.02 (m, 3H, Ar), 4.06 (t, 2H, -O-CH$_2$-), 4.00 (s, 3H, -O-CH$_3$), 1.83 (qv, 2H, -CH$_2$-), 1.49 (qv, 2H, -CH$_2$-), 1.35 (m, 8H, -CH$_2$-), 0.90 (t, 3H, -CH$_3$). ^{13}C-NMR δ$_C$ ppm (CDCl$_3$): 164.80, 163.85, 162.51, 160.13, 155.88, 149.31, 149.23, 146.87, 135.41, 134.39, 131.42, 131.28, 130.31, 129.61, 129.44, 125.32, 122.96, 122.57, 121.21, 118.59, 114.83, 111.75, 111.21 (2*>C=O esteric + 21 C, aromatic), 68.47, 56.55, 31.81, 29.34, 29.24, 29.17, 26.01, 22.67, 14.12 (1*-O-CH$_2$- + 1*-O-CH$_3$ + 7 C, aliphatic). m/z(CHCl$_3$): 708.14 [M+1].

2-((4-Nonyloxyphenyl)-4-azophenylcarbonyloxy)-7-(3-bromo-4-methoxyphenylcarbonyloxy)naphtalene (5i). Quantities: 0.20 g (0.5373 mmol) 2-(3-bromo-4-methoxyphenyl-carbonyloxy)-2-hydroxynaphtalene, 0.23 g (0.591 mmol) 4-(4-nonyloxyphenylazo)-benzoyl chloride, 0.10 g (0.7163 mmol) K$_2$CO$_3$, 4.52 mg (0.013 mmol) TBAHS, yield 78.32 % (0.11 g), orange product, liquid crystal: 129^{0}C (K/I), 106^{0}C (I/CL), 91^{0}C (CL/K). ^{1}H-NMR δ$_C$ ppm (CDCl$_3$): 8.44 (d, 1H, Ar, J= 1.6 Hz), 8.37 (d, 2H, Ar, J= 8.4 Hz), 8.18 (dd, 1H, Ar, J$_1$= 5.7 Hz, J$_2$= 7.2 Hz), 7.94 (m, 6H, Ar), 7.69 (d, 1H, Ar, J= 2.4 Hz), 7.68 (d, 1H, Ar, J= 2.3Hz), 7.39 (dd, 1H, Ar, J$_1$=1.7 Hz, J$_2$=8.9 Hz), 7.36 (dd, 1H, Ar, J$_1$= 2.2 Hz, J$_2$= 8.8 Hz), 7.01 (m, 3H, Ar), 4.05 (t, 2H, -O-CH$_2$-), 3.99 (s, 3H, -O-CH$_3$), 1.84 (qv, 2H,-CH$_2$-), 1.47 (qv, 2H, -CH$_2$-), 1.29 (m, 10H, -CH$_2$-), 0.88 (t, 3H, -CH$_3$).^{13}C-NMR δ$_C$ ppm (CDCl$_3$): 164.78, 163.83, 162.50, 160.12, 155.87, 149.31, 149.25, 146.86, 135.39, 134.39, 131.43, 131.29, 130.28, 129.60, 129.43, 125.44, 122.94, 122.56, 121.20, 118.57, 114.83, 111.75, 111.21 (2*>C=O esteric + 21 C, aromatic), 68.46, 56.54, 31.88, 29.53, 29.38, 29.26, 29.16, 26.00, 22.67, 14.12 (1*-O-CH$_2$- + 1*-O-CH$_3$ + 8 C, aliphatic). m/z(CHCl$_3$): 723.15 [M+1].

2-((4-Decyloxyphenyl)-4-azophenylcarbonyloxy)-7-(3-bromo-4-methoxyphenylcarbonyloxy)naphtalen (5j). Quantities: 0.20 g (0.5373 mmol) 2-(3-bromo-4-methoxyphenyl-carbonyloxy)-2-hydroxynaphtalene, 0.236 g (0.591 mmol) 4-(4-decyloxyphenylazo)-benzoyl chloride, 0.10 g (0.7163 mmol) K$_2$CO$_3$,

4.52 mg (0.013 mmol) TBAHS. Yield 70.88 % (0.28 g), orange product, liquid crystal: 130^0C (K/K), 146^0C (CL/I), 135^0C (I/CL), 107^0C (CL/K). ^{1}H-NMR δ_C ppm (CDCl$_3$): 8.44 (d, 1H, Ar, J= 1.5 Hz), 8.37 (d, 2H, Ar, J= 8.3 Hz), 8.18 (dd, 1H, Ar, J$_1$= 5.6 Hz, J$_2$= 7.4 Hz), 7.95 (m, 6H, Ar), 7.70 (d, 1H, Ar, J= 2.3 Hz), 7.67 (d, 1H, Ar, J= 2.3Hz), 7.39 (dd, 1H, Ar, J$_1$= 1.7 Hz, J$_2$=8.9 Hz), 7.35 (dd, 1H, Ar, J$_1$= 2.3 Hz, J$_2$= 8.6 Hz), 7.00 (m, 3H, Ar), 4.05 (t, 2H, -O-CH$_2$-), 3.99 (s, 3H, -O-CH$_3$), 1.82 (qv, 2H,-CH$_2$-), 1.46 (qv, 2H, -CH$_2$-), 1.31 (m, 12H, -CH$_2$-), 0.88 (t, 3H, -CH$_3$). ^{13}C-NMR δ_C ppm (CDCl$_3$): 164.78, 163.83, 162.50, 160.12, 155.86, 149.30, 149.23, 146.86, 135.39, 134.39, 131.41, 131.28, 130.29, 129.60, 129.44, 125.45, 122.94, 122.56, 121.20, 118.58, 114.84, 111.74, 111.20 (2*>C=O esteric + 21 C, aromatic), 68.47, 56.55, 31.89, 29.58, 29.56, 29.38, 29.32, 29.16, 26.00, 22.69, 14.13 (1*-O-CH$_2$- + 1*-O-CH$_3$ + 8 C, aliphatic). m/z(CHCl$_3$): 736.21 [M+1].

ACKNOWLEDGEMENTS

REFERENCES

1. a) G. Pelzl, S. Diele, W. Weissflog, *Advanved Materials* **1999**, *11*, 707; b) W. Wiessflog et al., *Liquid Crystals*, **2001**, *11*, 1603.

2. T. Niori, T. Sekine, J. Watanabe, T. Furukawa, H. Takezoe, *Journal of Materials Chemistry*, **1996**, *6*, 1231.

3. T.J. Dingemans, E.T. Samulski, *Liquid Crystals*, **2000**, *27*, 131.

4. Ch.K. Lai, Y.-Ch. Ke, J.-Ch. SU, Ch.-Shen, W.-R. Li, *Liquid Crystals*, **2002**, *29* (7), 915.

5. V. Görtz, J.W. Goodby, Chemical Communications, **2005**, 3262.

6. (a) T. Hegmann, F. Peidis, S. Diele, C. Tschierske, *Liquid Crystals*, **2000**, *27* (10), 1261; (b) T. Hegmann, J. Kain, S. Diele, B. Schubert, H. Bogel, C. Tschierske, *Journal of Materials Chemistry*, **2003**, *13*, 991; (c) Y. Shimizu, A. Kurobe, H. Monobe, N. Terasawa, K. Kiyohara, K. Uchido, *Chemical Communications*, **2003**, 1676.

7. R.W. Date, D.W. Bruce, *Journal of American Chemical Society*, **2003**, *125* (30), 9012.

8. P.H.J. Kouwer, G.H. Mehl, *Journal of American Chemical Society*, **2003**, *125* (37), 11172.

9. P.H.J. Kouwer, C.J. Welch, G. McRobbie, L. Priest, B.J. Dodds, G.H. Mehl, *Journal of Materials Chemistry*, **2004**, *14*, 1798.

10. a) T. Hegmann, B. Neumann, J. Kain, S. Diele, C. Tschierske, *Journal of Materials Chemistry*, **2000**, *10*, 2244; b) T. Hegmann, J. Kain, S. Diele, B. Schubert, H. Bogela, C. Tschierske, *Journal of Materials Chemistry*, **2003**, *13*, 991.

11. I.M. Saez, J.W. Goodby, *Journal of Materials Chemistry*, **2005**, *15*, 26.

12. a) C. Tschierske, *Journal of Materials Chemistry*, **1998**, *8* (7), 1485; b) C. Tschierske, *Journal of Materials Chemistry*, **2001**, *11*, 2647; c) C. Tschierske, *Current Opinion Colloid and Interface Science*, **2002**, *7*, 69; d) B. Chen, X.B. Zeng, U. Baumeister, S. Diele, G. Ungar, C. Tschierske, *Angewandte Chemie International Edition*, **2004**, *43*, 4621; e) A. Kraft, A. Reichert, R. Kleppinger, *Chemical Communications*, **2000**, 1015.

13. M.J. Freiser, *Physical Review Letters*, **1970**, *24*, 1041.

14. V. Prasad, *Liquid Crystals*, **2001**, *28*, 145.

15. J. Thisayukta, H. Niwano, H. Takezoe and J. Watanabe, *Journal of Materials Chemistry*, **2001**, *11*, 2717.

16. R. Amaranatha Reddy, B.K. Sadashiva and S. Dhara, *Chemical Communications*, **2001**, 1972.

17. J. Svoboda, V. Novotna, V. Kozmik, M. Glogarova, W. Weissflog, S. Diele and G. Pelzl, *Journal of Materials Chemistry*, **2003**, *13*, 2104.

18. T.J. Dingemans, E.T. Samulski, *Liquid Crystals*, **2000**, *27*, 131.

19. J. Matraszek, J. Mieczkowski, J. Szydowska, E. Gørecka, *Liquid Crystals*, **2000**, *27*, 429.

20. V. Prasad, D.S.S. Rao, and S.K. Prasad, *Liquid Crystals*, **2001**, *28*, 643.

21. V. Prasad, S.-W. Kang, K.A. Suresh, L. Joshi, Q. Wang, S. Kumar, *Journal of American Chemical Society*, **2005**, *127* (49), 17224.

22. Beilstein Handbuch der Organischen Chemie II, X, 103, Springer-Verlag, Berlin **1949**.

23. I. Dierking, ”*Textures of liquid crystals*”, WILEY-VCH Verlag, GmbH & Co. KGaA, Weinheim, **2003**.

24. E.R. Cioanca, E.L. Epure, I. Carlescu, G. Lisa, D. Wilson, N. Hurduc, D. Scutaru, *Molecular Crystals and Liquid Crystals*, **2011**, *537*, 51.

25. G. Lisa, E.R. Cioanca, N. Tudorachi, I. Carlescu, D. Scutaru, *Thermochimica Acta*, **2011**, *524*(1-2), 179.

26. G. Simion, D.F. Iuganu, I. Cârlescu, D. Scutaru, *Bulletin of the Polytechnic Institute of Iaşi, Section Chemistry and Chemical Engineering*, **2011**, *57*(3), 213.

27. V. Kozmik, A. Kovarova, M. Kuchar, J. Svoboda, V. Novotna, M. Glogarova, J. Kroupa, *Liquid Crystals*, **2006**, *33*(1), 41.

28. J. Svaboda, V. Novotna, V. Kozmik, M. Glagorova, W. Weissflog, S. Diele, G. Pelzl, *Journal of Materials Chemistry,* **2003**, *13*, 2104.

RAMAN AND SERS CHARACTERIZATION
OF NORMAL PATHOLOGICAL SKIN

ALEXANDRA FĂLĂMAŞ[a,*], CRISTINA DEHELEAN[b],
SIMONA CÎNTĂ PÎNZARU[a]

ABSTRACT. This study presents a Raman characterization of normal pathological mice skin both *in vivo* and *ex vivo*. Good correlation between the *in vivo* acquired spectra from the back of the mice specimens and the *ex vivo* formalin fixed skin samples was observed, although the *in vivo* spectra presented better resolved Raman bands. Additionally, using near-infrared laser excitation SERS spectra were acquired from the *ex vivo* skin samples immersed in Ag nanoparticles. The NIR-SERS spectra revealed main vibrational modes at 1573, 1327, 1227 and 227 cm^{-1} preponderantly characteristic to nucleic acids, which bring additional contribution to the chemical composition of the Raman investigated tissue.

Keywords: Raman, SERS, mice skin, in vivo

INTRODUCTION

Human and animal skin has been the subject of numerous spectroscopic investigations in the last years. Raman spectroscopy implies the detection of the inelastically scattered photons by the irradiated sample. Although the Raman signal is extremely weak, the main advantages of the technique rely on the fact that the sample requires minimal or no preparation and that the interface from water absorption is almost absent from the Raman spectra. The intensity of the active Raman bands is dependent on the concentration of the scattering species and independent on the sample thickness. Since the introduction of Raman spectroscopy for skin research [1], the technique has gained increasing popularity for both *in vivo* and *ex vivo* applications. Gniadecka et al. reported the in vitro Raman spectra of human skin, hair and nail [2], Caspers et al. investigated the properties of different skin layers using *in vivo* confocal Raman micro spectroscopy [3]. Additionally, the technique was used for the *in vivo* and *ex vivo* diagnosis of a variety of skin cancers [4-8].

[a] Babeş-Bolyai University, Faculty of Physics, 1 Kogălniceanu str., 400084 Cluj-Napoca, România
[b] Victor Babeş University of Medicine and Pharmacy, Faculty of Pharmacy, Eftimie Murgu Square 2, 300041 Timişoara, România
* alexandra.falamas@ubbcluj.ro

Regardless of the multitude applications of Raman spectroscopy, the technique has some disadvantages, as well. Firstly, of all the photons scattered by the sample only one in 10^6-10^8 represent the Raman signal. This inherently weak process can not be usually amplified by increasing the laser power because of the risk of damaging the sample. Another disadvantage of Raman spectroscopy is that fluorescence usually interferes with the Raman signal. Surface enhanced Raman signal (SERS) [9-11] can help overcome both problems, because of the amplification of the scattering efficiency per molecule and the adsorption process of the investigated sample to the metal surface which promotes fluorescence quenching. SERS at extremely high enhancement levels may transform Raman spectroscopy from a structural analytical tool to a sensitive single-molecule and nanoscale probe [12, 13] due to the favorable optical properties of the metallic nanostructures.

SERS has been lately used for a multitude of medical applications ranging from probing and imaging live cells [14], to developing SERS gene probes which can be used to detect DNA biotargets [15], to *ex vivo* diagnosing of normal and cancerous samples [16] and *in vivo* tumor targeting in live animals [17].

Other studies [18] have proved that the colloidal silver nanoparticles are able to penetrate the skin tissues and they were detected in the stratum corneum and the outermost surface of the epidermis. Our group has evidence before the possibility of acquiring SERS spectra from tissue samples [19, 20] and concluded that the Ag colloidal nanoparticles that can be incorporated into the interstitial space in the tissues allowed high quality SERS signal. Tissue differentiation based on the chemical composition changes would be suitable for surface enhanced Raman scattering since the ability to nanoparticles uptake has been proved. Different tissue structures have characteristic features in the SERS spectra and thus, SERS diagnosis of the samples is possible [16].

In this study we employed Raman and SERS spectroscopies for the characterization of mice skin, both *in vivo* and *ex vivo*. The aim of the research was to probe the molecular components from the skin tissues when investigating *in vivo* mice specimens versus *ex vivo* formalin fixed samples and to enhance the Raman signal of the autopsy tissue samples by employing the SERS effect.

RESULTS AND DISCUSSION

The *in vivo* Raman spectra acquired from the skin on the back of the healthy specimens (Fig.1 A) presented contributions from the main components of biological tissues: proteins, lipids, nucleic acids, carbohydrates and especially collagen. The main bands observed in the *in vivo* Raman spectra were assigned to proteins and lipids. These are the 1654 cm^{-1} (amide I band of proteins), 1445 cm^{-1} (CH$_2$ bending mode of lipids and proteins), 1003 cm^{-1} (phenylalanine) and 937 and 855 cm^{-1} (collagen). The Raman spectra acquired from the healthy mice skin were similar to those reported by other research groups obtained from

human and animal skin using near infrared and infrared excitation radiation for both *in vivo* or *ex vivo* measurements [2, 4, 21]. According to the current literature [2], the positions of the amide I and III bands at 1654 and 1269 cm^{-1}, as well as the presence of the well developed band at 937 cm^{-1} suggested a helical protein structure.

The 1200-1340 cm^{-1} spectral range presents mainly amide III bands of proteins and nucleic acids characteristic vibrational modes. These are the 1250 and 1269 cm^{-1} (amide III), the latter having the highest relative intensity in this region, the 1314 and 1338 cm^{-1} bands of guanine and CH_3CH_2 wagging of nucleic acids and collagen and adenine and guanine modes of DNA/RNA, respectively.

The 1030-1130 cm^{-1} spectral range presents useful information about the nature of the stratum corneum lipid bilayer packing [22]. C-C stretching modes of lipids are observed at 1127, 1087 and 1061 cm^{-1}. Additionally, these bands give information about the proteins as well, such as the 1127 cm^{-1} band assigned to C-N stretching modes of proteins and 1033 cm^{-1} band characteristic to C-H bending vibrations of phenylalanine of collagen [23].

Following the *in vivo* Raman measurements, autopsy samples were collected from the skin on the back of the rodents and further used for *ex vivo* Raman and SERS investigations. Fig.1 B) presents typical Raman spectra acquired from the formalin immersed skin sample. The spectra usually present the same fluorescent background as the *in vivo* Raman spectra and show the same main vibrations. Although, slight differences between the *in vivo* and the *ex vivo* Raman spectra can be observed. The 1200-1340 cm^{-1} spectral interval shows the same main components of tissues such as proteins, lipids and nucleic acids and the most intense peak is assigned to the amide III band of proteins as in the *in vivo* Raman spectra. In the 1030-1130 cm^{-1} range, the observed peaks are not as well resolved, although the Raman modes assigned to phenylalanine, the C-O stretching mode of carbohydrates, the C-C stretching vibrations of lipids as well as the C-N stretching mode of proteins can still be seen, usually slightly shifted when compared to the *in vivo* observed ones. Going towards lower wavenumbers, the main discrepancy is given by the absence of the proline band characteristic to collagen at 937 cm^{-1}. However, the main peak observed in this region is located at 919 cm^{-1} and is assigned to proline, as well [24]. On the other hand, the 853 cm^{-1} band is still present and shows the same band profile as seen in the *in vivo* spectra.

When passing from one spectrum to another the *ex vivo* Raman spectra showed basically the same profile and main bands, although some differences regarding the relative intensity of the bands or slight shiftings of the wavenumbers could be noticed. One explanation for this could be the inhomogenity of the skin tissues. Overall, the *ex vivo* Raman spectra matched well the *in vivo* ones and basing our assumptions on the above interpretations, we can conclude that the formalin fixation of tissues, did not affect significantly the acquisition of the spectral information.

Further aim of this research was to probe the Raman enhancement using Ag colloidal nanoparticles uptaken by the skin tissues along the formalin fixation. The autopsy skin samples collected from the mice specimens were immersed in 10% formalin solution mixed with colloidal silver.

A   B
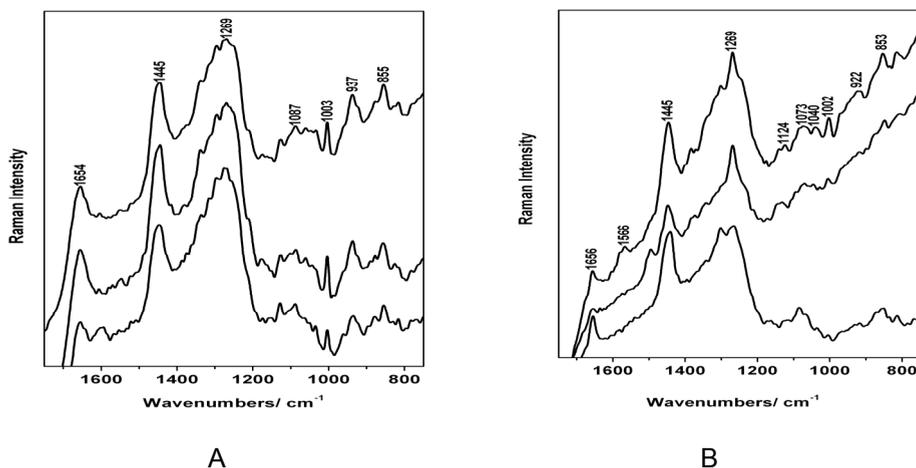
Figure 1. A) *In vivo* and B) *ex vivo* Raman spectra of healthy mice skin

Figure 2 presents several SERS spectra acquired from the healthy skin sample incubated with colloidal nanoparticles. The spectra were recorded using short acquisition times (3 to 5 seconds) and a strong tissue signaling with high specificity was obtained. The insertion in the figure shows the upper spectrum after background subtraction and zoom offset.

The most intense bands seen in the SERS spectra are located at 1573, 1443, 1327, 1227, 721, 652, 418 and 229 cm^{-1} (Figure 2). Other bands are observed as well, although having weaker relative intensity. The relative intensities in the SERS spectra are expected to differ significantly from the Raman ones, due to the adsorption behavior of certain molecules to the silver nanosurface. The SERS signal is expected from the molecular species located in the close vicinity of the uptaken nanoparticles, superimposed with the normal Raman scattering of the species from the laser focus area (< 1 μm). Due to the inherent inhomogenity of the tissue, the nanoparticles distribution is not uniform. Assuming that the Raman scattering effect is accompanied by the absorption, transmission as well as the elastic scattering, the rather low Raman efficiency would be much lower than the local SERS enhancement. Therefore, we assume the assignment of the recorded signal as being preponderantly SERS signal. According to the surface selection rules, the out of plane bending modes of a molecule adsorbed flat on the silver surface will be enhanced in the SERS spectra, while the in plane bending modes will be enhanced when the molecule is adsorbed perpendicular to the surface [25, 26].

92
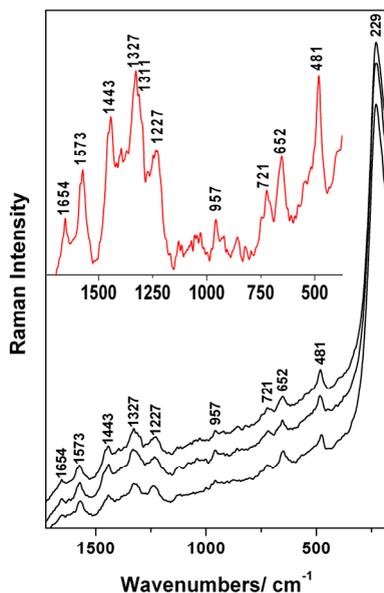
Figure 2. Typical SERS spectra acquired from the healthy mice skin tissue. The insertion shows a detailed SERS spectrum after background subtraction.

The main bands reported here were observed in our previous SERS studies as well, although at that time the main problem was the reproducibility of the spectra. It was surprising to observe in this study that the SERS spectra acquired from different points on the skin sample showed good reproducibility. Some of the vibrational modes observed here were reported by other research groups investigating the SERS effect in cells using gold or silver nanoparticles [27, 28]. Thus, the observed bands in our spectra can be assigned to the molecules or the molecular groups adsorbed to or in the close vicinity of the silver nanoparticles. The vibrational modes seen in the high wavenumber region of the spectra like the 1573 and 1443 cm^{-1} are assigned to nucleic acids constituents and proteins CH$_2$ and CH$_3$ bending vibrations, respectively. The 1380-1280 cm^{-1} spectral range exhibits an intense broad band centered at 1327 cm^{-1}. This Raman mode is assigned to phospholipids. This broad band contains other contributions as well, located at 1313 cm^{-1} assigned to nucleic acids and collagen and 1340 cm^{-1} assigned to bending mode of collagen and lipids [14, 29].

The same situation is seen for the 1280-1180 cm^{-1} spectral range which exhibits several contributions, as well. The most intense broad band observed here is centered at 1227 cm^{-1} and was assigned in the literature to the amide III band of proteins [30].

93

In the low wavenumber region of the spectra more nucleic acids bands can be observed, such as the 652 cm^{-1} band which may be assigned to a superposition of a tyrosine vibration and the guanine SERS fingerprint, or the 721 cm^{-1} assigned to adenine. The strongly enhanced sharp band seen at 229 cm^{-1} may indicate the formation of a metal-adsorbate bond, proving the interaction between the metal colloids and certain molecular species inside the skin tissue [31, 32].

Summarizing these findings, one could tentatively conclude that the silver nanoparticles penetrated the tissues along with the formalin in the fixation process.

CONCLUSIONS

This study presented a Raman and SERS characterization of healthy mice skin, serving as reference for further Raman skin diagnostic purpose. *In vivo* Raman investigations of the mice specimens were possible proving the efficiency of the technique for nondestructive and noninvasive studies. The interpretation of both *in vivo* and *ex vivo* Raman spectra revealed vibrational modes characteristic to proteins, lipids, nucleic acids and collagen. These findings prove that the formalin fixation of the autopsy collected skin samples did not affect significantly the acquisition of the Raman spectra.

By inoculating the samples with silver colloidal solution, it was possible to enhance the Raman signal characteristic to the skin tissues. The most intense vibrations were assigned to nucleic acids, although signal from proteins and lipids could be observed as well. These findings, as well as the intense band at 229 cm^{-1}, demonstrate the interaction between the metallic nanosurface and the adsorbate molecules in the tissues. The metal nanoparticles based SERS technique was applied here successfully as a sensitive, nondestructive spectroscopic method for the molecular structural probing in skin tissues.

EXPERIMENTAL PART

The Lee Meisel silver colloid was prepared through the standard method [33]. Briefly, 100 ml of a 1 mM $AgNO_3$ aqueous solution was heated to 93-100°C and then 2 ml of a 1% trisodium citrate solution was added. The mixture was kept in constant (previously achieved) temperature for about 1 hour and then was allowed to cool down to the room temperature. The resultant colloidal mixture was of dark grey color. Finally, the colloidal solution was centrifuged at 5500 rotations/min, for 5 min, resulting colloidal nanoparticles with extinction maximum at 420 nm and band half width of 50 nm. For the preparation of the solutions three distilled water was used.

Materials and methods

For this experiment BALB/c mice specimens were employed which were obtained from Charles River, Germany. The work protocol followed all NIAH-National Institute of Animal Health rules and the animals' regulations at the University of Medicine and Pharmacy Biobase, Timisoara, Romania. The animals were maintained during the experiment in standard conditions: 12h light-dark cycle, food and water ad libidum, temperature 24º C, humidity above 55%. At the time of the measurements, the mice specimens were 18 weeks old. After the *in vivo* Raman measurements, autopsy samples were collected from the skin on the back of the mice and immersed in formalin solution for further Raman investigations or formalin solution mixed with Lee Meisel silver colloid for the SERS measurements.

For the *in vivo* measurements, the mice were completely anesthesized with ketamine. The increased heart rate and breathing was monitored using the Raman microscope video-camera for defocussing reasons.

Instrumentation

For the Raman and SERS measurements a dispersive high performance micro-Raman spectrometer, Bruker Senterra with high spatial and spectral resolution was employed. The spectra were acquired using the 785 nm laser line and the exposure time for each spectrum was 3 to 5 s. The output laser power was set to 100 mW. The spectral resolution was 9 cm^{-1}.

REFERENCES

1. A. Williams, H. Edwards, B. Barry, *Int. J. Pharm.*, **1992**, *81*(2-3), 11

2. M. Gniadecka, P. Alshede Philipsen, S. Sigurdsson, S. Wessel, O. Faurskov Nielsen, D. HØjgaard Christensen, J. Hercogova, K. Rossen, H. Klem Thomsen, R. Gniadecki, L. Kai Hansen, H. Ch. Wulf, *J Invest Dermatol*., **2004**, *122*, 443

3. P. Caspers, G. Lucassen, G. Puppels, *Biophys. J.,* **2003**, *85*(1), 572

4. H. Wang, N. Huang, J. Zhao, H. Lui, M. Korbelika, H. Zeng, *J. Raman Spectrosc.,* **2011**, *42*(2), 160

5. Z. Huang, H. Zeng, I. Hamzavi, D. McLean, H. Lui, *Opt. Lett*, **2001**, *26*, 1782

6. N. Skrebova Eikje, K. Aizawa, T. Sota, Y. Ozaki, S. Arase, *The Open Medicinal Chemistry Journal*, **2008**, *2*, 38

7. M. Larraona-Puy, A. Ghita, A. Zoladek, W. Perkins, S. Varma, I.H. Leach, A.A. Koloydenko, H. Williams, I. Notingher, *J. Mol. Struct.,* **2010**, *993*(1-3), 57

8. S.B. Cartaxo, I.D. de Abranches Oliveira Santos, R. Bitar, A. Fernandes Oliveira, L. Masako Ferreira, H. Silva Martinho, A. Abrahão Martin, *Acta Cirúrgica Brasileira,* **2010**, *25*(4), 351

9. D.L. Jeanmarie, R.P. Van Duyne, *J. Electroanal. Chem.,* **1977**, *84*, 1

10. M.G. Albrecht, J.A. Creighton, J. *Electroanal. Chem.,* **1977**, *99*(15), 5215

11. M. Moskovits, *Reviews of Modern Physics*, **1987**, *57*(3), 783

12. K. Kneipp, H. Kneipp, J. Kneipp, *Acc. Chem. Res.*, **2006**, *39*(7), 443

13. M.K. Gregas, F. Yan, J. Scaffidi, H.N. Wang, T. Vo-Dinh, *Nanomedicine: Nanotechnology, Biology and Medicine,* **2001**, *7*, 115

14. J. Kneipp, H. Kneipp, B. Witting, K. Kneipp, Nanomedicine: Nanotechnology, *Biology and Medicine*, **2010**, *6*, 214

15. T. Vo-Dinh, F. Yan, M.B. Wabuyele, *J. Raman Spectroscopy*, **2005**, *36*, 640

16. S. Cinta Pinzaru, L.M. Andronie, I. Domsa, O. Cozar, S. Astilean, *J. Raman Spectroscopy,* **2008**, *39*, 331

17. X. Qian, X.H. Peng, D.O. Ansari, Q.Y. Goen, G. Z. Chen, D.M. Shin, L. Yang, A.N. Young, M.D. Wang, S. Nie, *Nature Biotechnology*, **2008**, *26*(1), 83

18. F. Filon Laresea, F. D'Agostin, M. Crosera, G. Adami, N. Renzi, M. Bovenzi, G. Main, *Toxicology,* **2009**, *255*, 33

19. A. Falamas, S. Cinta Pinzaru, C.A. Dehelean, M.M. Venter, *Studia UBB Chemia*, **2010**, *2,* tom II, 273

20. A. Falamas, S. Cinta Pinzaru, C. Dehelean, Ch. Krafft, J. Popp, *Romanian Journal of Biophysics*, **2010**, *20*(1), 1

21. J. Zhao, H. Lui, D. McLean, H. Zeng, *Recent Advances in Biomedical Engineering*, **2010**, 455

22. B.W. Barry, H.G.M. Edwards, A.C. Williams, *J. Raman Spectroscopy*, **1992**, *23*, 641

23. S. Fendel, B. Schrader, *Fresenius' J Anal Chem*, **1998**, *360*(5), 609

24. Z. Movasaghi; S. Rehman; I.U. Rehman, *Applied Spectroscopy Reviews*, **2007**, *42*, 493

25. J.A. Creighton, "Spectroscopy of Surfaces - Advances in Spectroscopy", Wiley: New York, **1988**, vol. 16, p. 37 (Chapter 2)

26. X. Gao, J.P. Davies, M.J. Weaver, *J. Phys. Chem. A,* **1990**, *94*, 6858

27. K. Kneipp, A.S. Haka, H. Kneipp, K. Badizadegab, N. Yoshizawa, C. Boone, K.E. Shafer-Peltier, J.T. Motz, R.R. Dasari, M.S. Feld, *Appl. Spectr.*, **2002**, *56*(2), 150

28. W.A. El-Saida, T.H. Kim, H. Kim, J.W. Choi, *Biosensors and Bioelectronics*, **2010**, *26*, 1486

29. O. Aydin, M. Kahraman, E. Kilic, M. Culha, *Appl. Spectr.,* **2009**, *63*(6), 662

30. H.W. Tang, X.B. Yang, J. Kirkham, D. Alastair Smith, *Appl. Spectr.*, **2008**, *62*(10), 1060

31. A. Raj, K. Raju, H. Tresa Varghese, C.M. Granadeiro, H.I.S. Nogueirad, C.Y. Panicker, *J. Braz. Chem. Soc.,* **2009**, *20*(3), 549

32. T. Itoh, K. Hashimoto, V. Biju, M. Ishikawa, B.R. Wood, Y. Ozaki*, J. Phys. Chem. B,* **2006**, *110*, 9579

33. P.C. Lee, D. Meisel, *J. Phys. Chem.,* **1982**, *86*, 3391

MICROSTRUCTURE AND PROPERTIES OF ELECTROTECHNICAL PORCELAIN

MARIA GOREA[a,*], RODICA CREŢ[b], FERENC KRISTALY[c]

ABSTRACT. We have investigated the microstructure of an industrial porcelain for medium voltage electrical insulators by the means of X-ray diffraction (XRD), as well as optical and electron (SEM) microscopy. Syn–orthorhombic mullite ($Al_{4.54}Si_{1.46}O_{9.73}$), hexagonal quartz ($SiO_2$), syn–rhombohedral corundum (Al_2O_3) and tetragonal silica (SiO_2) are the crystalline components, as determined by XRD. Electron microscopy (SEM) coupled with energy-dispersive spectroscopy (EDS) evidenced the presence of mullite crystals with variable Si:Al ratios, from 1:1, 1:2 to 1:3 or even 1:4 in the areas where K^+ is present. Small prismatic crystals were observed on the corundum grains; their composition resembles Al-rich mullite. Locally, the glass phase is highly enriched in K^+ as a result of orthoclase melt. The large quartz grains show marginal reaction rims related to the chemical attack of the feldspar melt. The physical, electric and mechanic characteristics of the porcelain vary in broad limits in direct connection with the compositional heterogeneity.

Keywords: microstructure, porcelain, characteristics

INTRODUCTION

Traditional vitreous ceramics such as porcelains, some refractory material and structural clay products in which significant fluid phase (30-70 %) forms during firing is obtained from a mix of kaolin, flux and filler. They were studied in detail by many authors [1-4]. Clays (usually kaolin) represent about 50 % from the mix; in the raw state they build a matrix for the other components, while during forming they confer plasticity to the ceramic body. The flux (feldspar) is included in amounts of about 25 % of the mix. It provides fluid phase at relatively low temperatures that interact with other components, leading to the formation of a melt which vitrifies the body. The filler (sand, or alumina), representing 25 %, is a stable component at high temperatures that

---

[a] Babeş-Bolyai University, Faculty of Chemistry and Chemical Engineering, 11 Arany Janos Str, RO-400084, Cluj-Napoca, Romania, * *mgorea@chem.ubbcluj.ro*
[b] Technical University, Faculty of Electrical Engineering, 26-28 G. Bariţiu Str. RO-400027, Cluj Napoca, Romania, rodica_cret@yahoo.fr
[c] University of Miskolc, Faculty of Earth Science and Engineering, 3515 Miskolc-Egyetemváros, Miskolc, Hungary, kristalyf81@yahoo.com

helps minimising deformation and shrinkage during firing. The last stages of the evolution of the porcelain microstructure are known only in basic lines. Mullite represents the only stable component in the Al_2O_3–SiO_2 system under normal temperatures and pressures. Pure mullite is a solid solution with Al_2 [Al_{2+2x} Si $_{2-2x}$] O_{10-x} compositions, where $0.17 \le x \le 0.5$ [5, 6]. Mullite formation is determined by the nature of the raw materials, processing method, temperature but also the additional ingredients used for enhancing specific properties. Based on the crystallization pattern and the crystal size, two types of mullite crystals were identified in porcelains. The small mullite aggregates (< 0.5 µm) of cubic symmetry resulted from the transformation of clay minerals are called "*primary mullite*", while the long, acicular mullite (> 1 µm) noticed in the feldspar melt are called "*secondary mullite*". The Al_2O_3/SiO_2 ratio for the primary mullite is close to 2:1 (Al_2O_3-rich), while the value reaches 3:2 for secondary mullite; the Al_2O_3 content varies from the areas with clay relics to that with feldspar relics [7-11]. In the first stages of sintering the tri-component porcelains kaolin clay shrinks and cracks. Subsequently, at 500–600 ˚C, the kaolinite dehydroxylates to form metakaolinite. At around 900 ˚C it transforms into spinel, while at 1000 ˚C the fine primary mullite crystals form. Primary mullite turns into secondary mullite at high temperatures, of about 1400 ˚C. The liquid phase obtained from the melting of the feldspars at low temperatures (1100 ˚C) reacts with the components of the ceramic body, thus leading to the crystallization of the acicular secondary mullite. The latter cross-cuts the microstructure and creates a more dense body. The feldspar melting process starts at the contact areas between feldspar crystals and clay relics, the amorphous silica resulted from kaolinite decomposition being easily mobilized in the melt, at around 985 ˚C. Potential extraneous phases contained by kaolin and feldspar (Na_2O, CaO, MgO, TiO_2 or Fe_2O_3) may influence the mullite crystallization, the porcelain's vitrification temperature, and the viscosity of the melt. Quartz or alumina are refractory materials that are added into the ceramic composition for minimising the ceramic body's deformation and shrinkage, in the case of formation of significant amounts of melted phase. Quartz is structurally transformed at 573 ˚C and is considered relatively insoluble in the feldspar melt under 1250 ˚C. Above this temperature, solubilisation of quartz is evidenced by the presence of reaction rims at the contact of quartz grains with the embedding Si-rich melt. Solubilisation is controlled by the size of the grains: below 20 µm, a complete solubilisation is registered at temperatures above 1350 ˚C. The final microstructure of porcelain is built by mullite crystals, vitreous phase and small amounts of quartz surrounded by fine cracks that will define the porcelain's properties [12].

The increase in density, homogeneity degree of the ceramic body and the shrinkage mechanisms during firing are revealed when studying microstructure evolution. Such studies are of high interest for commercial porcelain industry.

Our study aims is characterizing and quantifying the mineral and amorphous phases in a particular, "aluminous"-rich electrotechnical porcelain, as well as its physical-chemical, electrical and mechanical characterization. Finally, we have correlated the material's composition with its properties.

REZULTS AND DISCUSSIONS

Porcelain microstructure

The tested ceramic bodies are samples of commercial porcelain obtained from a mix of 50 % kaolin, 28 % feldspars and 22 % alumina processed by the wet method and submitted to thermal treatment at 1300 ˚C.

The chemical composition of the fired porcelain (Table1) is characterised by a high content of Al_2O_3 that is typical for this type of material. Also, the dominance of K_2O over Na_2O favours the formation of a viscous melt and prevents deformations upon firing; last but not least, this feature confers a higher dielectric rigidity.

Table 1. Chemical composition of the studied porcelain

Oxide	SiO_2	Al_2O_3	CaO	MgO	Na_2O	K_2O	Fe_2O_3	LOI
[%]	44.17	43.60	1.23	0.24	1.46	2.32	1.30	5.68

The phase composition of the fired porcelain was investigated by the means of XRD (figure 1), optical and electron (SEM) microscopy. The qualitative and semi-quantitative data point to the presence of about 50 to 60 % vitreous phases, which embeds the crystalline phases.

The crystalline phases mainly consist of orthorhombic synthetic mullite ($Al_{4.54}Si_{1.46}O_{9.73}$) – 54.60 %; rhombohedral synthetic corundum (Al_2O_3) – 16.60 %; hexagonal quartz (SiO_2) ~ 18.18 % and tetragonal silica dioxide (SiO_2) – 10.80 %. The unit cell parameters of these mineral components are presented in Table 2.

Table 2. The unit cell parameters of the crystalline phases

	a	b	c
Mullite (orthorhombic)	7.5421	7.6957	2.88362
Quartz (hexagonal)	4.9	4.9	5.4
Corundum (rhombohedral)	4.7607	4.7607	12.995
Silica dioxide (tetragonal)	4.978	4.978	6.9321

Mullite is an X-ray discernible crystalline compound resulted by the transformation of clayey raw materials (primary mullite), or by crystallization from feldspar melts (secondary mullite), respectively. Corundum, the high temperature Al_2O_3 phase originates from the raw materials, *i.e.* technical alumina that is not structurally transformed in the range of the firing temperature.
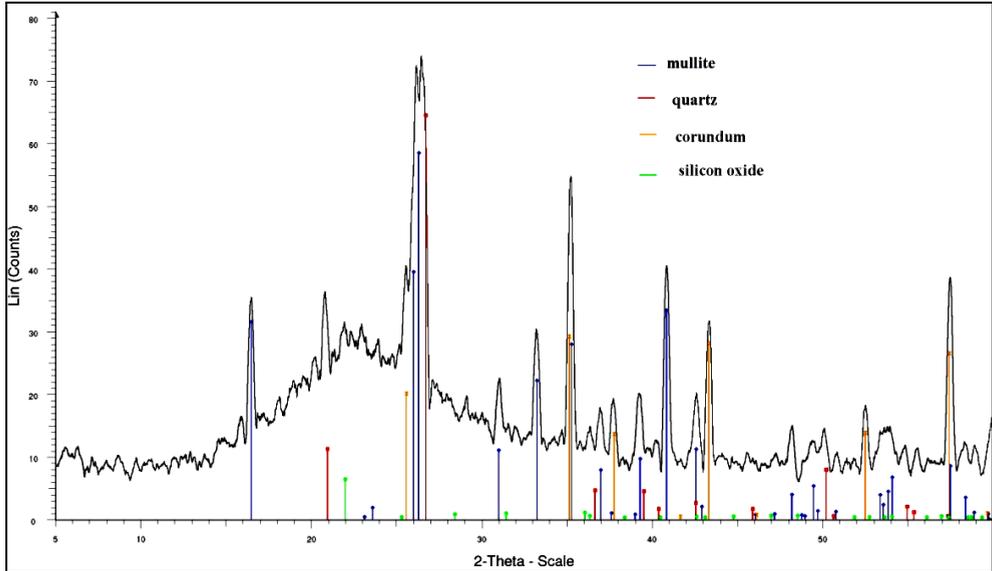
Figure 1. X-ray pattern of the electrotechnical porcelain

Hexagonal quartz, the undesirable form in electrotechnical porcelain given its volume variation during the polymorphous transition at 573 °C is the result of using SiO_2-rich (quartzitic) feldspar as flux raw material. Tetragonal silica dioxide represents the low temperature polymorph of cristobalite formed by clay minerals' transformations under thermal treatment (high cristobalite has cubic symmetry).

The fine texture of the porcelain is illustrated in polarizing optical microscopy images (figure 2). A high amount of quartz and closed pores within a relatively homogeneous vitreous matrix can be noticed.
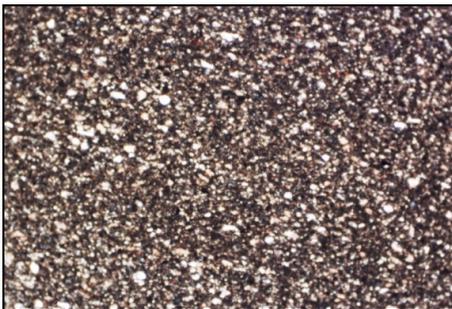
Figure 2. Electrotechnical porcelain with fine texture consisting of one vitreous and one crystalline phase; quartz is the dominant phase (1N)
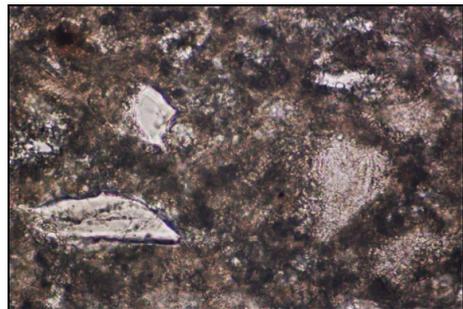
Figure 3. Quartz grains with reaction rim Fine from the interaction with the feldspar melt (1N)

The smaller quartz grains are turned into solution, while the larger ones are only partly solubilised, with the formation of a reaction rim around these particles (figure 3). The melt is rich in SiO_2, thus favouring the crystallization of the acicular secondary mullite. In some areas the melt still preserved the shape of the solubilised feldspar grain; the framework of acicular secondary mullite is well-defined, with largely crystallized outlines.

The SEM image (figure 4) of the feldspar melt evidences corundum segregations; they are probably due to an incomplete homogenization. Also only partly solubilised large quartz grains, as well as a large, unmelted orthoclase grain are also visible.
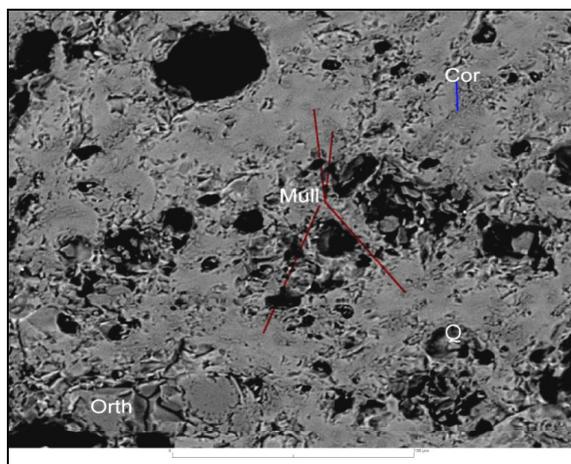
Figure 4. SEM image of the studied porcelain showing regions of mullite (Mull), corundum (cor), quartz grain (Q) and unmelted feldspar (Orth)

The transformations under firing of the clay minerals with the formation of primary mullite are documented by the SEM+EDS analyses (figure 5). The light grey areas with a 2:1 Si:Al ratio are typical for the incipient stage of transformation (and represent relics of the clay minerals). Subsequently, in the darker areas, K^+ ion is depleted, while the Si:Al ratio increases from 1:1 to 1:2, with the formation of γ-Al_2O_3 spinel. The detailed image on the right shows small crystals embedded in the vitreous matrix. In these areas, alumina is the dominant component, the Si:Al ratio varying from ~ 1:3 to 1:4. Thus, three distinctive types of mullite-containing compositions are evidenced by the SEM images: clay minerals relics with aggregates of primary mullite; clay relics cross-cut by the feldspar melt, with secondary mullite; and, an alumina-rich composition with the so-called tertiary mullite, a typical phase for Al-rich porcelains. The vitreous matrix shows a similar composition in all these investigated areas.

To summarize, electron microscopy (SEM+EDS) evidences areas with distinctive chemical compositions, starting with SiO_2-rich ones containing also alkalis (K^+) and evolving into alumina-rich ones containing To summarize, electron microscopy (SEM+EDS) evidences areas with distinctive chemical compositions, starting with SiO_2-rich ones containing also alkalis (K^+) and evolving into alumina-rich ones containing secondary mullite. In the corundum-rich areas, small prismatic crystals are assigned to the Al_2O_3-rich tertiary mullite.
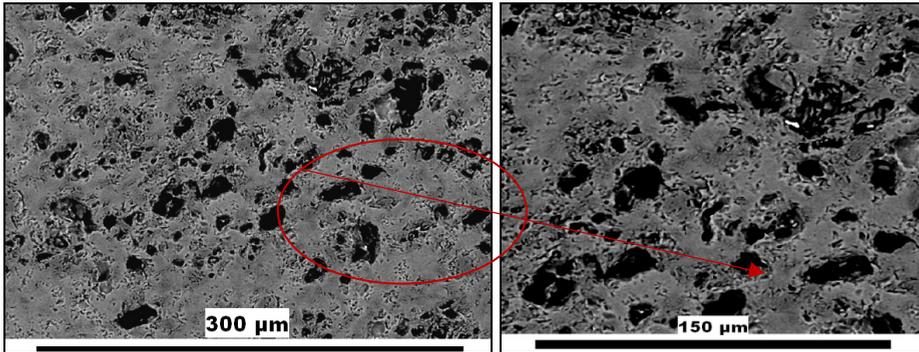
Figure 5. Microstructure of the porcelain. SEM+EDS images document areas with distinctive Al:Si compositions.

Density and apparent porosity

Compactness characteristics, as well as bending resistance are the significant physical characteristics that correlate with the microstructure of ceramics. Thus, in the case of the studied porcelain, we measured the average apparent density (ρ_a) by using the Archimedes method. The obtained value, 2.52276 g/cm^3, falls within the requested interval. On the other hand, the apparent porosity (P_a) is slightly higher, 0.11823 %, as compared to the standard value, *i.e.*, 0.0 %. Porosity – especially the one of the closed pores was also evaluated by microscopic methods; as expected, the values are relatively higher.

Electrical characterisation

The relative permittivity, the dielectric loss factor - measured at 20 °C and 100 Hz, and the volume resistivity - measured under direct current, show values within the required intervals (Table 3). Samples 1 and 3 represent exceptions; their permittivity values are slightly above the upper limit (6-7); the same is true for the loss factor of sample 4 that is somewhat higher than the standard. On the contrary, the dielectric rigidity shows lower values than the requested ones: from $E_{str} > 20$ MV/m they decrease even to 15-16 MV/m. This fact can be explained by the presence of some extraneous ions, as well as by the large volume of closed pores and some local compositional heterogeneities in the ceramic body.

The variation of the permittivity coefficient with temperature, $\alpha_\varepsilon(T) = 1/\varepsilon_{ri} \cdot \Delta\varepsilon/\Delta T$ [K^{-1}], are presented in table 4, while the variation plot in figure 6. The slope of the curve defines an experimental value $\alpha_\varepsilon(T) = 1.45 \times 10^{-3}$ [K^{-1}] that is much higher than the required one, $\alpha_\varepsilon(T) = 0.5 - 0.6 \times 10^{-3}$ [K^{-1}]. The high permittivity values can be also correlated with the high internal porosity and the presence of some impurities.

Table 3. Electrical characteristics of the studied porcelain

Sample	Relative permittivity (ε_r)	Dielectric loss factor, at 20 °C (tg δ)	Volume resistivity [Ωcm]
1.	7.17	0.023	
2.	6.33	0.019	
3.	7.10	0.022	5.8×10^{13}
4.	6.61	0.029	4.4×10^{14}
5.	6.99	0.023	
6.	6.90	0.014	
7.	6.45	0.021	8.88×10^{13}
8.	6.98	0.020	6.67×10^{13}
9.	6.80	0.014	2.2×10^{14}
standard	6-7	0.025	$> 10^{11}$
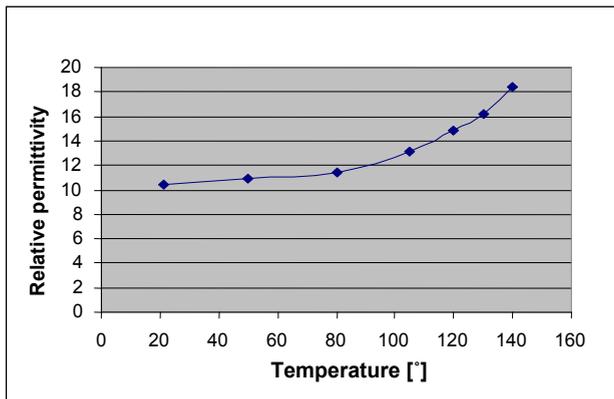
Figure 6. Variation of relative permittivity with temperature

Table 4. ε_r and $\alpha_\varepsilon(T)$ values measured at various temperatures

T [°C]	ε_r	$\alpha_\varepsilon 10^3$ [K^{-1}]
21	ε_{ri} = 10.48	
50	10.92	1.45
80	11.35	1.42
105	13.10	2.98
120	14.88	4.79
130	16.16	4.85
140	18.35	6.28

Mechanical characterisation

The bending resistance of the glazed porcelain, τ_g, is 147.103 MPa while that of the non-glazed one is 108.988 MPa. Both values are much higher than the standard limits, *i.e.* minimum 60 MPa and respectively minimum 50 MPa. The explanation is related to the absence of fine fissures in the ceramic body.

The mechanical compression strength was measured on 10 mm diameter cylindrical test samples of variable length by using an up-to-date universal equipment with automatic data processing and display (including $\sigma \rightarrow \varepsilon$ diagrams). The curves plotted for samples 3 and 4 are presented in figure 7.
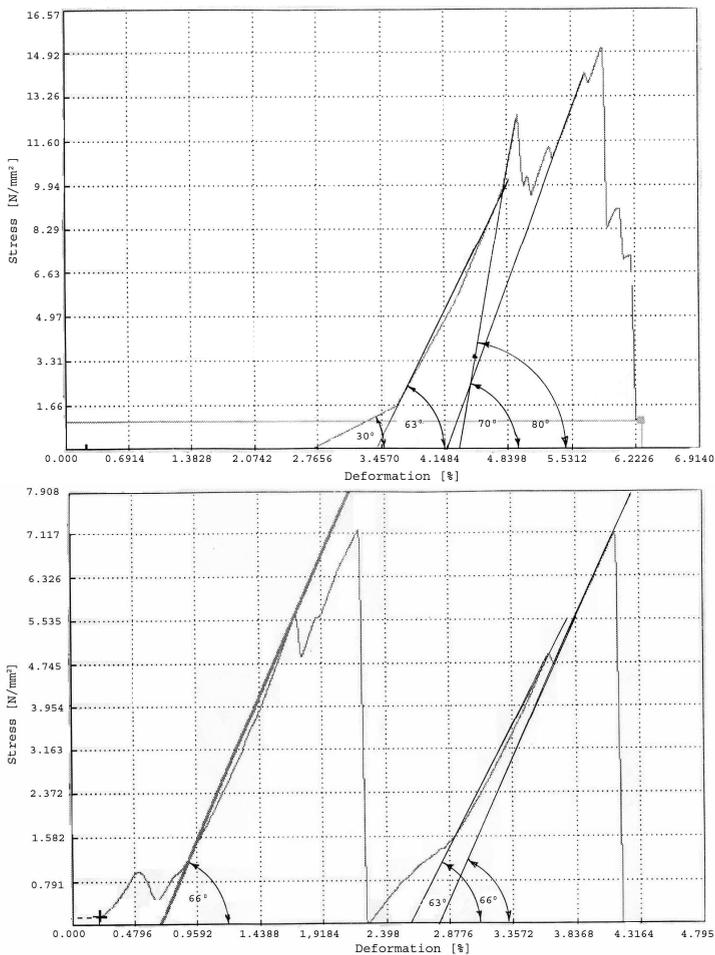
Figura 7. Tension, σ – specific linear deformation, ε diagram for tester no. 3 (left) and 4 (right) obtained by using the "Gabaldini-Sun5" equipment with automatic data processing and display

It is remarkable that the ceramic samples do not collapse in a single step; in the case of sample 3 there are four steps, while for sample 4 there are three. From the plots one can calculate β angle, which is used to determine the elasticity modulus, E. Table 5 shows the mechanical compression strength values for the porcelain test samples.

Table 5. Mechanical resistance values for the tested porcelain samples

Sample	D [mm]	A = πd²/4 [mm]	L [mm]	Fmax [N]	σ_r = Fmax/A [N/mm²]	E = tgβ = σ/ε [N/mm²]	Obs. β [°]
3	9.5	70.882	9.4	1068	15.07	1.66/0.00864 = 192	30
						9.9/0.018398= 538	63
						12.43/0.00691 = 1798.8	70
						15.07/0.0167 = 902.39	80
4	9.5	70.882	11.6	509.55	7.19	5.6/0.01059 = 528.8	66
						4.82/0.01 = 482	63
						7.117/0.0138 = 515.8	66

The breaking compression strength and the elasticity modulus values cover a wide interval for samples formed from the same material. This confirms the compositional heterogeneity of the studied porcelain.

CONCLUSIONS

The microstructural investigation of the porcelain ceramic body has evidenced the presence of heterogeneous mixtures consisting of feldspar, quartz and alumina, accompanied by insulated or aggregated particles of totally or partly transformed kaolinite. Hexagonal quartz is related to the quartzitic (SiO_2-rich) feldspar used as flux material. Feldspars are partly solubilised, as indicated by the reaction rims surrounding the grains. Tetragonal SiO_2 represents the low temperature polymorph of cristobalite resulted by thermally-induced transformations of clay minerals. Electron microscopy (SEM+EDS) evidenced the presence of areas with distinctive chemical composition, starting from SiO_2-rich ones, also containing K^+ (feldspar melt), varying to alumina-rich ones including small secondary mullite crystals. The electrical characteristics (dielectric permittivity, loss factor, volume resistivity, rigidity) vary in a large range (some beyond the acceptable limits). This can be explained by the large compositional and structural heterogeneity of the material, as well as by the presence of closed and open pores. The degree of loss is high, and it increases with increasing temperature (permittivity variation coefficient is about three times higher than the standard accepted one). The test samples show large limits of variation for the breaking compression strength and the elasticity module. These represent consequences of the compositional heterogeneity evidenced by microscopic investigation.

EXPERIMENTAL SECTION

The industrial electrotechnical porcelain samples thermally treated at 1300 ˚C have been obtained in the laboratory and then investigated by specific methods. The composition was determined by wet chemical analysis in solution. The phase composition was investigated by X-ray diffraction by using a Bruker D8 diffractometer with Cu anticathode, in the 5–64 2θ˚ interval. Optical microscopic study in polarised light was carried out on thin sections (25-30 microns) using a Nikon Eclipse E 2000 microscope, while electron microscopy (SEM+EDS) on a JEOL JXA-8600 Superprobe micro-beam electron microscope. The compaction measurements were acquired by weighting in air and water, based on the Archimedes principle. The electrical and mechanical characteristics were obtained according to the current standard procedures.

REFERENCES

1. Y. Iqbal, W.E. Lee, *J. Am. Ceram. Soc.*, **1999**, *82*[12], 3584.
2. Sujeong Lee, Youn Yoong Kim, Hi-Soo Moon*, J. Am. Ceram. Soc.,* **1999**, *82*[10], 2841.
3. H. Schneider, J. Schreuer, B. Hildman, *Journal of the European Ceramic Society*, **2008**, *28*, 329.
4. W.E. Lee, G.P. Souza, C.J. McConville, T. Tarvornpanich, Y. Iqbal, *Journal of the European Ceramic Society*, **2008**, *28*, 2, 465.
5. B.R. Johnson, W.M. Kriven, J. Schneider, *Journal of the European Ceramic Society,* **2001**, *21*, 2541.
6. S. Freimann, S. Rahman, *Journal of the European Ceramic Society,* **2001**, *21*, 2453.
7. W.E. Lee, Y. Iqbal, *Journal of the European Ceramic Society,* **2001**, *21*, 2583.
8. M.A. Sainz, F.J. Serrano, J.M. Amigo, J. Bastida, A. Caballero, *Journal of the European Ceramic Society,* **2000**, *20*, 403.
9. N. Montoya, F.J. Serrano, M.M. Reventos, J.M. Amigo, J. Alarcon, *Journal of the European Ceramic Society,* **2010**, *30*, 839.
10. Yamuna, S. Devanarayanan, M. Lalithambika, *J. Am. Ceram. Soc.*, **2002**, *85*[6], 1409.
11. S. Lee, Y.J. Kim, H.J. Lee, H.S. Moon, *J. Am. Ceram. Soc.*, **1999**, *82*[10], 2841.
12. Y. Iqbal, W.E. Lee, *J. Am. Ceram. Soc.,* **2000**, *83*[12], 3121.

THE RELATION BETWEEN THE ELECTRIC RESPECTIVE MAGNETIC ENERGIES BY WHICH THE DRUGS OPERATE

NICOLAE BONCIOCAT[a], ADINA COTARTA[a]

ABSTRACT. In a recent communication we have shown a new method for classifying the drugs. There are three classes of drugs, corresponding to three electric schemas: (1), (1*) and (1**). As criteria of classifying we have proposed the Thomson radial frequency of the series(1*), respective parallel(1**) circuit [1]. Consider a drug $D \in \left(1^{**}\right)$. The relation between the electric and magnetic energies is: $(E_D)_E, \max = R^2 (E_D)_B, \max \frac{C_p}{L_p}(\omega_1)$.

Similar, for a drug $D \in \left(1^*\right)$ results: $(E_D)_E, \max = R^2 (E_D)_B, \max \frac{C_s}{L_s}(\omega)$ By ω_1 is denoted the resonance radial frequency. The *indexes p, s* indicate that the pseudo-capacitance, respective the pseudo-inductance are arranged in parallel, respective in series. The electric, respective magnetic energies take the maximum values. The drugs belonging to the class $\left(1^{**}\right)$, act both by magnetic and electric energy, i.e., they are superior as compared with those belonging to the class(1*). This conclusion remains valid for the *antioxidant(A.O.)* respective *pro-oxidant(P.O.) drugs*, because the A.O-drugs $\in$ [$J_{A,O}^{**}$ drugs] $\in \left(1^{**}\right)$ and P.O-drugs $\in$ [$J_{P,O}^{*}$ drugs] $\in \left(1^*\right)$ belong to sub-classes of the classes(1*), (1**).

Keywords: drug, multi-electrode, Thomson radial frequencies, antioxidant, pro-oxidant capacity

INTRODUCTION

Bonciocat et al., have shown, in a series of papers, the faradaic current density of an electrode redox reaction occurring with combined limitations of charge transfer and non-stationary linear semi-infinite diffusion, is the solution of an integral equation of Volterra type [2-6]. By solving this equation, new methods of direct and cyclic voltammetry have been developed [7-17]. Very recently has been shown that the Electrochemical Impedance Spectroscopy method may have important applications in the drug research [18-23].

[a] University "Politehnica" of Bucharest, Faculty of Applied Chemistry and Materials Science, Department of Applied Physical Chemistry and Electrochemistry, Computer Added Electrochemistry Laboratory, UPB- CAEL Bucharest, Romania

Let's consider a drug $D \in (I^*)$. From the significance of the radial Thomson frequency $\omega_{Th,p} = \left[L_p(\omega_1) C_p(\omega_1) \right]^{-1/2}$ it results:

$$L_p(\omega_1) C_p(\omega_1) = \frac{1}{\omega_{Th,p}^2} \qquad (1)$$

and from the physical significance of the criterion:

$$J^{**} = \frac{\left[\omega_{Th,p} \right]_0^2}{\left[\omega_{Th,p} \right]_0^2 - \omega_1^2} \qquad \text{results:}$$

$$L_p(\omega_1) C_p(\omega_1) = \frac{1}{\left[\omega_{Th,p} \right]_0^2} = \frac{1 - J^{**}}{\omega_1^2 J^{**}} \qquad (2)$$

We shall use the notations:

$$a = \frac{1}{\left[\omega_{Th,p} \right]_0^2}; \qquad b = \frac{1 - J^{**}}{\omega_1^2 J^{**}} \qquad (3)$$

as well as:

$\quad E_D \quad = \quad$ energy contained in a drug D

$\quad (E_D)_E =\quad$ electric energy contained in a drug D

$\quad (E_D)_B =\quad$ magnetic energy contained in a drug D

Then:

$$(E_D)_E = \frac{1}{2} C_p V^2 = \frac{1}{2} C_p (RI)^2 = \frac{1}{2} R^2 C_p I^2 = \frac{1}{2} R^2 \frac{a}{L_p} I^2 =$$

$$= \frac{1}{2} R^2 \frac{b}{L_p} I^2 = \frac{R^2}{2} \frac{C_p}{L_p} \frac{b}{C_p} I^2 \qquad (4)$$

respective:

$$(E_D)_B = \frac{1}{2} L_p I^2 = \frac{1}{2} \frac{a}{C_p} I^2 = \frac{1}{2} \frac{b}{C_p} I^2 \qquad (5)$$

and thus:

$$E_D = \frac{1}{2} \frac{b}{C_p} I^2 \left(1 + C_p \frac{R^2}{L_p} \right) \qquad (E_D)_E / (E_D)_B = R^2 \frac{C_p}{L_p} \qquad (6)$$

Equations(6) lead to the following conclusions:

$$\frac{C_p}{L_p} R^2 \langle 1 \qquad \rightarrow (E_D)_E \langle (E_D)_B \text{ i.e., the drug acts firstly by magnetic field}$$

$$\frac{C_p}{L_p} R^2 = 1 \qquad \rightarrow (E_D)_E = (E_D)_B \text{ i.e., the drug acts equally by electric and}$$

magnetic fields

$$\frac{C_p}{L_p} R^2 \rangle 1 \qquad \rightarrow (E_D)_E \rangle (E_D)_B \text{ i.e., the drug acts firstly by electric field}$$

$$R^2 \rightarrow 0 \qquad \rightarrow (E_D)_E = 0 \text{ i.e., the drug acts by magnetic field}$$

$$R^2 \rightarrow \infty \qquad \rightarrow (E_D)_B = 0 \text{ i.e., the drug acts by electric field}$$

The last two conclusions of eqs.(6) show that these two classes of electrochemical cells needed to obtain the Nyquist diagrams. In the class(A) enter the cells adequate to analyze the drugs effects which act by their magnetic fields, while in the class(B) enter the cells adequate to analyze the drugs effects which act by their electric fields.

Therefore:

A) Pt | $K_3Fe(CN)_6$ / $K_4Fe(CN)_6$, (10^{-3}M), Drug, O_2 physically dissolved, KCl (in excess)

The presence of KCl (in excess) assures a value R_{sol} very small.

B) Pt | $K_3Fe(CN)_6$ / $K_4Fe(CN)_6$, (10^{-3}M), Drug, O_2 physically dissolved, KCl (absent)

Absence of KCl assures a value R_{sol} very great. It is very important to mention that the researches made with the 6 drugs and two mixtures of drugs have used cells of type (A) in order to obtain the Nyquist diagrams.

Therefore, the six drugs and two mixtures of drugs investigated, have proved to be antioxidant drugs and the criterion J^{**} have served to estimate their efficiency.

THEORETICAL SECTION

Further let's establish the relation between the quantities **a** and **b**.

For this, we shall elucidate the quantity **b,** by explaining the criterion J^{**} (see eq.(7) below).

It thus results:

$$\frac{1}{J^{**}} = 1 - \frac{\omega_1^2}{[\omega_{Th,p}]_0^2} \tag{7}$$

109

i.e.,

$$-\frac{1-J^{**}}{J^{**}} = \frac{\omega_1^2}{[\omega_{Th,p}]_0^2} \tag{7'}$$

from where:

$$b = \frac{1-J^{**}}{\omega_1^2\, J^{**}} = -\frac{\omega_1^2}{\omega_1^2\,[\omega_{Th,p}]_0^2} = -\frac{1}{[\omega_{Th,p}]_0^2} \tag{8}$$

Therefore the two quantities **a** and **b** are the one the opposite of the other.

Further using eqs.(4), (5), (6) one gets the conclusions:

$$(E_D)_B = \frac{1}{2}\frac{b}{C_p}\, I^2; \quad (E_D)_E = \frac{1}{2}R^2\frac{C_p}{L_p}\frac{b}{C_p}\, I^2 = 0 \;\text{(because R = 0)}$$

$$E_D = \frac{1}{2}\frac{b}{C_p}\, I^2\left(1 + R^2\frac{C_p}{I_p}\right) = (E_D)_B \;\text{(because R = 0)}$$

From eq.(8) results:

$$\lim b = -\frac{1}{\omega_1^2} \tag{8'}$$

$$J^{**} \to -\infty$$

and from the expression (3) of **a**:

$$\lim a \;=\; \frac{1}{\omega_1^2} \;=\; -\;\lim b \tag{8''}$$

$$[\omega_{Th,p}]_0 \to \omega_1 \qquad\qquad J^{**} \to -\infty$$

i.e., the relation $b = -a$ remains for the limiting values to which the quantities **a** and **b** tend corresponding to the resonance Thomson radial frequency:

$$\omega_1 = res\, \omega_{Th,s}\,[\alpha_{D_i}^{*}(\omega_1)=0] = res\, \omega_{Th,p}\,[\alpha_{D_i}^{**}(\omega_1)=0]$$

when the two drugs $D_i \in (1^*)$ respective $D_i \in (1^{**})$ have maximum therapeutic effects.

Using the relation (8) results:

$$\frac{b}{a} = \frac{1-J^{**}}{\omega_1^2\, J^{**}}\cdot[\omega_{Th,p}]_0^2 = \frac{1-J^{**}}{\omega_1^2\, J^{**}}\,\omega_1^2\,[1-\alpha_D^{**}(\omega_1)] =$$

110

$$\frac{1-J^{**}}{J^{**}}\left[1-\alpha_D^{**}(\omega_1)\right] \tag{9}$$

i.e.,

$$\frac{b}{a}\left[\alpha_D^{**}(\omega_1)=0\right]=\frac{1-J^{**}}{J^{**}}=-1$$

i.e., for :

$$J^{**}=-\infty \qquad \rightarrow \qquad J^{**}[\ \alpha_D^{**}(\omega_1)=0]=-\infty \tag{9'}$$

but also:

$$J^{**}[\ \alpha_D^{**}(\omega_1)=0]=\infty \tag{9''}$$

i.e.,

$$|J^{**}[\ \alpha_D^{**}(\omega_1)=0\ ]|=\infty \tag{9'''}$$

The relation (9''') is general, i.e., it is valid irrespective of the values that quantities **a** and **b** may have.

The magnetic energy content in a drug $D \in (1^{**})$

We shall use the eqs.(8') and (8'') to express the magnetic energy content in a drug $D \in (1^{**})$ corresponding to resonance Thomson radial frequency.

It thus results:

$$\lim_{[\omega_{Th,p}]_0\rightarrow\omega_1}(E_D)_B \ = \ \lim_{[\omega_{Th,p}]_0\rightarrow\omega_1}\left(\frac{1}{2}\cdot\frac{a}{C_p}I^2\right)= \ \frac{1}{2}\cdot\frac{I^2}{C_p}\lim_{[\omega_{Th,p}]_0\rightarrow\omega_1} a = \ \frac{1}{2\omega_1^2}\cdot\frac{1}{C_p}I^2 \tag{10}$$

or:

$$\lim_{\substack{J^{**}\rightarrow-\infty}}(E_D)_B = \lim_{J^{**}\rightarrow-\infty}\left(\frac{1}{2}\cdot\frac{b}{C_p}I^2\right)= \frac{1}{2}\cdot\frac{I^2}{C_p}\lim_{J^{**}\rightarrow-\infty} b = \ -\frac{1}{2}\cdot\frac{I^2}{C_p}\cdot\frac{1}{\omega_1^2} = -\frac{1}{2\omega_1^2}\frac{I^2}{C_p} \tag{10'}$$

the two limiting values being one the opposite of the other, i.e.,

$$\lim_{\substack{[\omega_{Th,p}]_0\rightarrow\omega_1 \quad J^{**}\rightarrow-\infty}}(E_D)_B = \ -\lim(E_D)_B \tag{10''}$$

Therefore one may write:

$$\left|\lim(E_D)_B\right| \ = \ \left|\lim(E_D)_B\right|=\frac{1}{2\omega_1^2\ C_p}I^2 \tag{11}$$

$$[\omega_{Th,p}]_0 \to \omega_1 \qquad J^{**} \to -\infty$$

and afterwards, expressing the pseudo-capacity $C_p(\omega_1)$ in function of the Warburg pseudo-capacity $C_W(\omega_1)$.

$$\left| \lim(E_D)_B \right| = \left| \lim(E_D)_B \right| = \frac{1}{2\omega_1^2 \cdot \dfrac{C_w(\omega_1)}{\alpha_D^{**}(\omega_1)}} I^2 = \frac{\alpha_D^{**}(\omega_1)}{2\omega_1^2 C_W(\omega_1)} I^2$$

$$[\omega_{Th,p}]_0 \to \omega_1 \qquad J^{**} \to -\infty$$

$$\alpha_D^{**}(\omega_1) \langle 1 \tag{11'}$$

It remains to establish the values which must be putted in eq.(11') instead of the quantities $\alpha_D^{**}(\omega_1)$ and $C_w(\omega_1)$.

For this purpose we shall use the relation :

$$1 - \frac{1}{\alpha_D^{**}(\omega_1)} = m = \frac{R_{sol} + A_{ct} - \left(R_{sol} + A_{ct}^{**}\right)}{R_W^{**}(\omega_1)} = \frac{R_{sol} + A_{ct} - \left(R_{sol} + A_{ct}^{**}\right)}{0.446\, B_d^{**}} \tag{12}$$

where by B_d^{**} we have noted the ω independent part of a Warburg diffusion resistance $R_w^{**}(\omega_1)$ given by the relation [18, 19] :

$$R_W^{**}(\omega_1) = \frac{B_d^{**}}{2\omega_1^{1/2}} = 0.446\, B_d^{**} \qquad \text{(because } \omega_1 = 1.256 \text{ s}^{-1}\text{).}$$

The expressions of the three quantities which enter in the last part of eq.(12) are:

$$R_{sol} + A_{ct} = \left[\, \text{Re}(\omega_2) - \frac{\text{Re}(\omega_1) - \text{Re}(\omega_2)}{0.122}\, \right] \tag{13}$$

$$R_{sol} + A_{ct}^{**} = \left[\, \text{Re}^{**}(\omega_2) - \frac{\text{Re}^{**}(\omega_1) - \text{Re}^{**}(\omega_2)}{0.122}\, \right] \tag{13'}$$

$$B_d^{**} = 20.6 \left[\text{Re}^{**}(\omega_1) - \text{Re}^{**}(\omega_2)\right] \tag{13''}$$

where $\text{Re}(\omega_1)$, $\text{Re}(\omega_2)$ respective $\text{Re}^{**}(\omega_1)$, $\text{Re}^{**}(\omega_2)$ represent the *mean values* of the abscissa of the first two points:

$$P_1(\omega_1) = P_1\left(1.256 \text{ s}^{-1}\right) \qquad P_2(\omega_2) = P_2\left(1.582 \text{ s}^{-1}\right)$$

respective,

$$P_1^{**}(\omega_1) = P_1^{**}\left(1.256 \text{ s}^{-1}\right) \qquad P_2^{**}(\omega_2) = P_2^{**}\left(1.582 \text{ s}^{-1}\right)$$

of the Nyquist diagrams: $-\mathrm{Im}(\omega)$ vs $\mathrm{Re}(\omega)$, respective $-\mathrm{Im}^{**}(\omega)$ vs $\mathrm{Re}^{**}(\omega)$ made for the reference dielectrode (DRR), respective multi-electrode $(ME)_D^{**} = (DRR)$ containing the drug $D \in (1^{**})$.

Once **the value m** estimated, using eq.(13), the first part of eq.(12) leads to the estimation of $\alpha_D^{**}(\omega_1)$ by equation:

$$\alpha_D^{**}(\omega_1) = \frac{1}{1-m} \tag{14}$$

It remains to estimate the Warburg pseudo-capacity $C_W(\omega_1)$.

As one knows, for very small radial frequencies (as it is the case of the radial frequency $\omega_1 = 1.256\mathrm{s}^{-1}$) the Faraday impedance Z_F becomes the Warburg impedance Z_W, which in the complex plane makes an angle of 45^0 with both the real and imaginary axes. The Warburg pseudo-capacity $C_W(\omega_1)$ introduces a capacity reactance $X_{C_w(\omega_1)}$ situated in the long of imaginary axes and having the expression:

$$X_{C_w(\omega_1)} = -R_w(\omega_1) \cdot j$$

It thus results:

$$tg\left(45^0\right) = 1 = R_w(\omega_1) / X_{C_w(\omega_1)}$$

Taking into account the relation between a capacity C and her capacity reactance X_C, i.e., $C = \dfrac{1}{\omega |X_C|}$ it follows:

$$C_W(\omega_1) = \frac{1}{\omega_1 R_w^{**}(\omega_1)} = \frac{1}{\omega_1 \cdot 0.446 \, B_d^{**}} = \frac{3.571}{B_d^{**}} \tag{15}$$

Further, introducing in eq.(11') the expressions obtained for $\alpha_D^{**}(\omega_1)$ and $C_W(\omega_1)$ results:

$$\left| \lim (E_D)_B \right| = \left| \lim (E_D)_B \right| =$$
$$\left[\omega_{Th,p}\right]_0 \rightarrow \omega_1 \qquad J^{**} \rightarrow -\infty$$

$$= \frac{\alpha_D^{**}(\omega_1)}{2\omega_1^2 \, C_W(\omega_1)} I^2 = \frac{\frac{1}{1-m}}{2\omega_1^2 \cdot 3.571} \cdot B_d^{**} I^2 \cong 0.18 \frac{B_d^{**}}{(1-m)} I^2 \tag{16}$$

In The International System (S I) the magnetic energies of drugs must be expressed in J (Joule). To verify this let's fix to the first expression from eq.(16).

$\alpha_D^{**}(\omega_1)$ is a number; ω_1^2 expresses in s^{-2}; $C_W(\omega_1)$ being a capacity expresses in C/V (i.e., coulomb/ volt); I in C/s (i.e., coulomb/ second). It thus results that the quotients from eq.(16) express in $\dfrac{C^2/s^2}{s^{-2} \cdot C/V} = C \cdot V$ (i.e., coulomb volt), i.e., in J (Joule).

[referring to the expression: $[\dfrac{\alpha_D^{**}(\omega_1)}{2\omega_1^2 C_W(\omega_1)} \cdot I^2]$].

EXPERIMENTAL SECTION

From eqs.(16) results that a drug which acts by magnetic energy will have a greater therapeutic effect if its magnetic energy will be closer to the its maximum magnetic energy, corresponding to the resonance radial frequency ω_1, when:

$[\omega_{Th,\,p}] \rightarrow \omega_1$, respective the criterion $J^{**} \rightarrow -\infty$, i.e.,

$$\left| \lim (E_D)_B \right| = \left| \lim (E_D)_B \right| \cong 0.18 \frac{B_d^{**}}{(1-m)} I^2 \qquad (17)$$

$[\omega_{Th,p}]_0 \rightarrow \omega_1 \qquad J^{**} \rightarrow -\infty$

where the quantities **m** and B_d^{**} are obtained by eqs.(13) and I is given in: coulomb /s = Ampere(A).

The conclusions of the experiences made with the all 6 drugs and 2 mixtures of drugs are:

- all drugs investigated belong to the class (1^{**}), more exactly to the sub-class of the antioxidant drugs $J_{A-D} \subset (1^{**})$ in accord with J^{**} criterion;

- all drugs investigated act by their magnetic energies;

- the obtained values of J^{**} criterion lead to the following sequence of their therapeutic effects, in accord with the sequence given by relation(17):

$|J_{Am}^{**}| < |J_B^{**}| < |J_{Cf2}^{**}| < |J_{Uh+Am}^{**}| < |J_{Uh1}^{**}| < |J_{B+Am+Cf+Uh}^{**}| < |J_{Uh2}^{**}| < |J_{Cf1}^{**}|$ (18)

where:

B	=	Sweedish Bitter
Am	=	Achillea millefolium
Cf	=	Calendulae flos
Uh	=	Urticae herbe
M$_1$	=	Uh +Am
M$_2$	=	B + Am + Cf + Uh

Comparison between the electric, respective magnetic energies by which the drugs belonging to the classes $\left(1^{**}\right)$ respective $\left(1^{*}\right)$ operate.

Consider a drug: $D \in \left(1^{**}\right)$. Then:

$$\left(E_D\right)_E = \frac{1}{2} C_p V^2 = \frac{1}{2} C_p R^2 I^2 \quad \text{respective:} \quad \left(E_D\right)_B = \frac{1}{2} L_p I^2 \qquad (19)$$

Thus:

$$\left(E_D\right)_E = R^2 \left(E_D\right)_B \cdot \frac{C_p}{L_p}(\omega) \qquad (19')$$

equation valid for $\omega = \omega_1$ too, i.e.,

$$\left(E_D\right)_E, \max = R^2 \left(E_D\right)_B, \max \frac{C_p}{L_p}(\omega_1) \qquad (20)$$

For a drug $D \in \left(1^{*}\right)$ the equations are:

$$\left(E_D\right)_E = \frac{1}{2} C_s V^2 = \frac{1}{2} C_s R^2 I^2 \quad \text{respective} \quad \left(E_D\right)_B = \frac{1}{2} L_s I^2 \qquad (21)$$

Thus :

$$\left(E_D\right)_E = R^2 \left(E_D\right)_B \cdot \frac{C_s}{L_s}(\omega) \qquad (21')$$

equation valid for $\omega = \omega_1$ too, i.e.,

$$\left(E_D\right)_E, \max = R^2 \left(E_D\right)_B, \max \frac{C_s}{L_s}(\omega_1) \qquad (22)$$

The indexes **p, s** indicate that the Warburg pseudo-capacity is replaced by a pseudo-inductance, respective pseudo-capacity arranged in parallel, respective in series.

Further, using the expressions obtained for $C_p(\omega)$, $L_p(\omega)$ respective $C_s(\omega)$, $L_s(\omega)$, where $C_p(\omega) = C_W^{**}(\omega)$, $L_p(\omega) = L^{**}(\omega)$, respective $C_s(\omega) = C_W^{*}(\omega)$, $L_s(\omega) = L^{*}(\omega)$, one gets:

$$\frac{C_p}{L_p}(\omega) = \omega \left\{\frac{C_W(\omega)}{\alpha_D^{**}(\omega)}\right\}^2 \cdot \left[1 - \alpha_D^{**}(\omega)\right] \qquad (23)$$

respective:

$$\frac{C_s}{L_s}(\omega) = \omega C_W^2(\omega) \left[\alpha_D^{*}(\omega)\right]^2 \cdot \frac{1}{1 - \alpha_D^{*}(\omega)} \qquad (23')$$

equations which for the resonance radial frequency ω_1 (when $\alpha_D^*(\omega_1) = \alpha_D^{**}(\omega_1) = 0$) become:

$$\frac{C_p}{L_p}(\omega_1) \cong \omega_1 \left\{ \frac{C_W(\omega_1)}{\alpha_D^{**}(\omega_1)} \right\}^2 \qquad \text{respective}$$

$$\frac{C_s}{L_s}(\omega_1) = \omega_1 \, C_W^2(\omega_1)\left[\alpha_D^*(\omega_1)\right]^2 \tag{24}$$

and replacing in eq.(20), respective eq.(22) results:

$$(E_D)_E, \max = R^2 (E_D)_B, \max \, \omega_1 \, [\frac{C_W(\omega_1)}{\alpha_D^{**}(\omega_1)}]^2; \qquad D \in \left(1^{**}\right) \tag{25}$$

respective:

$$(E_D)_E, \max = R^2 (E_D)_B, \max \, \omega_1 \, [\, C_W(\omega_1) \alpha_D^*(\omega_1)]^2 ; \qquad D \in \left(1^*\right) \tag{25'}$$

Because $\alpha_D^*(\omega_1) = \alpha_D^{**}(\omega_1)$ tend to zero, eqs. (25), (25') lead to the conclusions:

$$(E_D)_E, \max \, \rangle\rangle \, \omega_1 \, R^2 (E_D)_B, \max \qquad \text{for} \quad D \in \left(1^{**}\right) \tag{26}$$

$$(E_D)_E, \max \, \langle\langle \, \omega_1 \, R^2 (E_D)_B, \max \qquad \text{for} \quad D \in \left(1^*\right) \tag{26'}$$

The inequalities (26), (26') show the superiority of the drugs belonging to the class $\left(1^{**}\right)$ because these drugs act both by magnetic and electric energies while those belonging to the class $\left(1^*\right)$ act very few by electric energy. At resonance (i.e., for $\omega = \omega_1$) these energies take the maximum values $(E_D)_B, \max$, respective $(E_D)_E, \max$, the energy $(E_D)_E, \max$ being very small as compared with $(E_D)_B, \max$ (see eq.(26')) for drug $D \in \left(1^*\right)$, respective very great as compared to $(E_D)_B, \max$ (see eq.(26)) for drug $D \in \left(1^{**}\right)$.

Finally, it has been shown that the antioxidant drugs belong to a sub-class $J_{A.O.}^{**}$ of the class $\left(1^{**}\right)$ while the pro-oxidant drugs belong to a sub-class $J_{P.O.}^{*}$ of the class $\left(1^*\right)$. It follows that the inequalities (26), (26') hold true for these drugs, i.e.,

$$(E_D)_E, \max \, \rangle\rangle \, \omega_1 \, R^2 (E_D)_B, \max ; \qquad D \in J_{A.O.}^{**} \subset \left(1^{**}\right) \tag{27}$$

$$(E_D)_E, \max \, \langle\langle \, \omega_1 \, R^2 (E_D)_B, \max ; \qquad D \in J_{P.O.}^{*} \subset \left(1^*\right) \tag{27'}$$

CONCLUSIONS

Equations(27), (27') *lead to the following very important conclusions concerning the anti-oxidant and pro-oxidant drugs.*

- An antioxidant drug acts both by magnetic and electric energies; $(E_D)_B$, $(E_D)_E$

- At resonance (i.e., at the radial frequency $\omega_1 = 2\pi\nu_1$, where $\nu_1 = 0,2s^{-1}$ represents the smallest frequency used by the electronic instrument in getting the Nyquist plots, and thus $\omega_1 = 1,256s^{-1}$. These energies take the maximum values: $(E_D)_B$, max, $(E_D)_E$, max.

- The pro-oxidant drugs act very few by electric energy, because $(E_D)_E$, max is very small as compared with $(E_D)_B$, max.
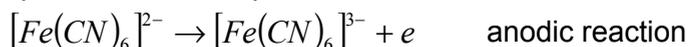
- The antioxidant drugs act both by electric and magnetic energies, *the contribution of electric energy being very important,* because $(E_D)_E$, max is very great as compared with $(E_D)_B$, max.

The last two conclusions explain the superiority of the anti-oxidant drugs.

Another advantage of an antioxidant drug, comes from the fact that when an electric field disappears (i.e., the intensity of the electric field goes to zero), a magnetic field appears, and similarly when the magnetic field disappears, an electric field appears.

In this way, an oscillation of the two energies appears: electric energy→magnetic energy→ electric energy→. During this oscillation, the antioxidant drugs act permanently, while the pro-oxidant drugs, only when the energy is magnetic.

To explain how an antioxidant(A.O.) drug acts, let's start by remembering the reactions of the RRD-dielectrode. They are:

$$\frac{1}{4}O_2 + H^+ + e \rightarrow \frac{1}{4}H_2O \qquad \text{cathodic reaction}$$

$$[Fe(CN)_6]^{2-} \rightarrow [Fe(CN)_6]^{3-} + e \qquad \text{anodic reaction}$$

The electrons resulted by the oxidation of $[Fe(CN)_6]^{4-}$ are consumed by the reduction of $\frac{1}{4}O_2 + H^+$ to $\frac{1}{2}H_2O$. Therefore $\frac{1}{4}O_2 + H^+$ acts as an oxidizer of $[Fe(CN)_6]^{4-}$. It thus results that an A.O.-drug reduces the oxidation effect of $\frac{1}{4}O_2 + H^+$ by consuming a part of the electrons resulted by the oxidation of $[Fe(CN)_6]^{4-}$ to $[Fe(CN)_6]^{3-}$.

Thus, the important effect of an A.O-drug is the reduction of the intensity of the important oxidation reaction.

As for the P.O-drug, *the important effect is the increase of the intensity of the important oxidation reaction.*

Finally, it is very important to underline that, presently are known many oxidation reactions, occurring in biological systems, about which one supposes that are at the origin of many illnesses, and for this reason, the development of experimental methods for estimating the therapeutic efficiencies of the A.O.drugs, represents the most important aim of the future researchers in the domain of biological and pharmaceutical sciences.

From this point of view, one may conclude that the two EIS methods presented at Journees d'Electrochimie 2009 [1] and RICCCE 2009 [23] have the necessary conditions for playing a very important role for a scientific classifications of drugs produced by the chemical industry, or taken from the God Pharmacy(i.e., by an adequate transforming of the medicinal plants).

Unfortunately, such an action necessitates 4-5 years and a team of researchers in which must enter electrochemists, biochemists, physicists and specialists in medicinal plants. Although such an action implies so many difficulties, it must be done, because the results that will be obtained, will justify the efforts, and what it is much more important will decide the directions in which the future developments of the medicinal sciences in Romania must be done.

This also explains the importance of the criteria:

$$[\omega_{Th,p}]_0 = \omega_1 \sqrt{1 - \alpha_D^{**}(\omega_1)} \; ; \qquad [\omega_{Th,s}]_0 = \omega / \sqrt{1 - \alpha_D^{*}(\omega_1)}$$

$$0 \leq \alpha_D^{**}(\omega_1) \leq 1 \; ; \; 0 \leq \alpha_D^{*}(\omega_1) \leq 1$$

for the classification of drugs belonging to the classes (1**) respective (1*) and of the criteria:

$$J^{**} = \frac{[\omega_{Th,p}]_0^2}{[\omega_{Th,p}]_0^2 - \omega_1^2} \; ; \quad J^{*} = \frac{\omega_1}{[\omega_{Th,s}]_0} \qquad -\infty \leq J^{**} \leq 0 \; ; \qquad 0 \langle J^{*} \langle 1$$

for the classification of A.O-drugs, respective P.O-drugs.

These four criteria will be necessary for the future development of drug-sciences not only in Romania, but also in the world.

REFERENCES

1. N. Bonciocat, A. Cotarta, *Studia UBB Chemia*, **2009**, *LIV*, 55.

2. N. Bonciocat, *Electrokhimiya*, **1993**, *29*, 97.

3. N. Bonciocat, "Electrochimie si Aplicatii", Dacia Europa - Nova, Timisoara, **1996**, chapter 5, 262-267.

4. N. Bonciocat, "Alternativa Fredholm in Electrochimie", Editura MEDIAMIRA, Cluj-Napoca, **2005**, chapter 2.

5. N. Bonciocat and A. Cotarta, *Revue Roumaine de Chimie*, **1998**, *43*, 925.

6. N. Bonciocat and A. Cotarta, *Revue Roumaine de Chimie*, **1998**, *43*, 1027.

7. N. Bonciocat, ″Electrochimie si Aplicatii″, Dacia Europa-Nova, Timisoara, **1996**, chapter 6.

8. N. Bonciocat and A. Cotarta, "A new approach based on the theory of variational calculus in studying the electrodepositing process of chromium in the system $Cr^0/CrCl_2$, LiCl-KCl", *Contract Copernicus 1177-2* "Utilisation de sels fondus en metallurgie", *Final Report of European Community*, July **1998.**

9. I.O. Marian, E. Papadopol, S. Borca and N. Bonciocat*, Studia UBB Chemia*, **1998**, *43*, 91.

10. N. Bonciocat, *Scientific Bulletin Chemistry Series Polytechnic University Timisoara*, **1998**, *43* (57), 5.

11. N. Bonciocat, "Alternativa Fredholm in Electrochimie", Editura MEDIAMIRA, Cluj-Napoca, vol.I, **2005**, chapter 5.

12. N. Bonciocat, E. Papadopol, S. Borca and I.O. Marian, *Revue Roumaine de Chim*ie, **2000**, *45*, 981.

13. N. Bonciocat, E. Papadopol, S. Borca and I.O. Marian, *Revue Roumaine de Chim*ie, **2000**, *45*, 1057.

14. I.O. Marian, R. Sandulescu and N. Bonciocat, *Journal of Pharmaceutical and Biomedical Analy*sis, **2000**, *23*, 227.

15. I.O. Marian, N. Bonciocat, R. Sandulescu and C. Filip, *Journal of Pharmaceutical and Biomedical Analy*sis, **2001**, *24*, 1175.

16. N. Bonciocat, A. Cotarta, J. Bouteillon and J.C. Poignet, *Journal of High Temperature Material Processes*, **2002**, *6*, 283.

17. N. Bonciocat, I.O. Marian, R. Sandulescu, C. Filip and S. Lotrean, *Journal of Pharmaceutical and Biomedical Analysis*, **2003**, *32*, 1093.

18. N. Bonciocat and A. Cotarta, *"*Spectroscopia de Impedanta Electrochimica in cazul Limitarilor de Transfer de Sarcina si Difuziune*"*, Editura Printech, Bucuresti, **2005**.

19. N. Bonciocat and I.O. Marian, *"*Metoda Impedantei Faraday si Variantele sale*"*, Editura Presa Universitara Clujeana, **2006**, chapter 5.

20. N. Bonciocat and A. Cotarta, *Annals of West University of Timisoara, Series Chemistry,* **2006**, *15*(2), 137.

21. N. Bonciocat and A. Cotarta, *Scientific Bulletin Chemistry Series Politehnica University Timisoara*, **2007**, *52*(66), 1-2, 90.

22. N. Bonciocat, *Studia UBB Chemia*, **2008**, *LIII*, 1, 31.

23. N. Bonciocat and A. Cotarta, *Studia UBB Chemia*, **2009**, *LIV,* 211.

NICKEL RECOVERY FROM ELECTRONIC WASTE
I. NICKEL RECOVERY FROM CATHODE RAY TUBES

BIANCA ROBOTIN[a], VASILE COMAN[a], PETRU ILEA[a, *]

ABSTRACT. The aim of the present study was the recovery of nickel from waste electrical and electronic equipment and particularly, from cathode ray tubes. The major nickel sources in cathode ray tubes are the electron gun and the nickel containing shadow mask. For the nickel recovery tests, the metallic components were chemically (H_2SO_4, HCl, $FeCl_3$ aqueous solutions) and electrochemically (H_2SO_4, HCl, $NaCl$ aqueous solutions) solubilised. The obtained solutions were treated for selective nickel/iron separation. The resulted solutions were used for the electrowinning of nickel or nickel-iron alloys.

Keywords: electronic waste, cathode ray tube waste, nickel recovery

INTRODUCTION

Nowadays, resource recycling and environmental protection are central topics worldwide. Fast and continuous technological development in different areas leads to a massive accumulation of waste materials. Among these, an important class are the waste electrical and electronic equipments (WEEEs) [1-5]. WEEEs contain valuable materials, such as precious metals (Au, Ag, Pd, Pt), different useful metals (Cu, Ni, Zn, etc.), and a significant amount of chemical elements (Pb, Hg, Cr, Sn, Cd), which are hazardous for the environment and human health. Recycling of these materials is therefore an attractive alternative which aims at both recovering and reusing the metal values and avoiding the environmental risks [6].

Among WEEEs, cathode ray tubes (CRTs) recycling represents a major concern, mainly due to their large volume, toxicity of their material content, legislation (disposal restrictions) and recycling costs [7]. Moreover, the recent tendency of replacing CRT technology with liquid crystal, plasma, and light-emitting diode (LED) displays generates a massive accumulation of CRT waste. From the total weight of a TV set/computer screen, the CRT constitutes two thirds. The CRT components vary as a function of producer, model and fabrication year. The main materials used for CRT fabrication are glass and metal. Glass represents approximately 85 % of the total weight [8]

---

[a] Babes-Bolyai University, Faculty of Chemistry and Chemical Engineering, 11 Arany Janos Street RO-400028, Cluj-Napoca, Romania
* *pilea@chem.ubbcluj.ro*

and it has a negative impact on the environment when disposed improperly, due to its high content of heavy metals, especially Pb. Although numerous studies on glass recycling exist, an ultimate solution is still not obvious [8, 9]. Metals such as Fe, Ni, Co, Cr, Mn are found in the electron gun (EG) and in the shadow mask / aperture grill, depending on the used technology. In a CRT, the metallic components of an EG contain various amounts of nickel. On top of that, in some CRTs, there is another source of nickel, i.e. the shadow mask made of a nickel steel alloy (INVAR) with a low thermal expansion coefficient. To our knowledge, until now, there aren't any literature studies concerning the metal recovery and/or separation from CRTs, the main focus being on the recycling of the CRT glass [8, 9].

The current study focuses on nickel recovery from electronic waste, especially from CRTs. Nickel is an important metal, heavily utilized in industry mainly due to its anticorrosion properties [10]. At the same time, nickel could have a negative impact on the environment and human health if it contaminates the soil due to an improper disposal [11]. The recovery of nickel from WEEEs is therefore necessary for environmental reasons and, at the same time, could be economically feasible since nickel has an elevated price (18000 USD/tonne, October 2011, see: *http://www.metalprices.com*).

The extractive metallurgy of nickel can be the first place to look for technologies with direct application in the field of nickel recovery from electronic waste. The major nickel source on Earth is represented by the nickel ores (laterites and sulphides), which are extracted all over the world. The hydrometallurgical processes of obtaining the pure metal from its ores involve various leaching procedures. In the case of nickel, when using acid leaching, the main acids used are concentrated sulphuric and hydrochloric acid [10]. In the case of HCl, oxidizing agents, such as $FeCl_3$, are added to the mix [12], in order to facilitate the leaching process.

In our studies, the metallic composition of the EGs was determined, followed by a chemical and electrochemical solubilisation of the metallic components using different acid leaching agents and finally, nickel and iron were separated from the resulted solutions**.** The electrodeposition of nickel and nickel-iron alloys from the resulted solutions is currently under investigation.

RESULTS AND DISCUSSION

In our case, the first operation of the metal recycling process from electronic waste consisted of the manual dismantling of the monitors, when the plastic parts were separated from the cathode ray tube, the electrical wiring and the printed circuit boards contained within. In the next step, the CRT was broken down into pieces and the metallic parts were separated from the glass and ceramic components. The electron gun and shadow mask found inside the CRTs were further used for the solubilisation experiments.

Elemental composition determination of electron guns and shadow masks from CRTs

In order to perform an initial qualitative analysis of the elemental composition of an EG, the sample was investigated using X-ray diffraction (XRD). The XRD analysis result of a typical EG from a colour computer monitor is depicted in Figure 1. The results indicated the presence of Ni, Fe, Co and Cr.
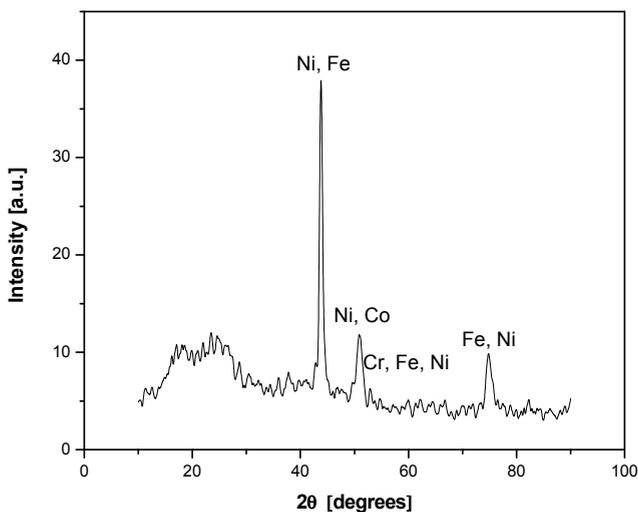

Figure 1. The XRD analysis of a typical EG from a colour monitor

The next stage was the quantitative elemental analysis of the EGs and shadow masks. For that purpose the EG was preliminarily subjected to a mechanical separation process into metallic, glass, and ceramic components, and the metallic parts were separated into magnetic (EGM) and non-magnetic (EGN) fractions. On average, an EG weighs around 18 g, out of which the EGM parts consist of approximately 45 %. In the case of shadow masks, it was noticed that the INVAR alloy was magnetic. The metallic parts from EG and shadow mask were solubilised in *aqua regia* and the resulted solutions were analysed by atomic absorption spectrometry (AAS). The elemental composition of the EG was estimated using five different samples, in order to establish an average composition. The tests were performed both on magnetically separated parts and non-separated ones. As mentioned before, the EG elemental composition is variable depending on the producer, model and manufacturing year. Therefore, the metal concentration varies as it is shown in Table 1.

As it can be seen in Table 1, a magnetic separation of the EG components generates two fractions with different concentration ratios Ni:Fe. The Ni content was higher in EGM (40 to 45 %), counting for 75 % of all Ni content in an EG. Moreover, the solubilisation of the EGN parts brings a high content of Cr in the solution, which is not the case with EGM.

Table 1. Typical elemental composition of the metallic parts of EGs and shadow masks from CRTs

CRT waste type	Ni	Fe	Cr	Mn	Co
	[%]				
EG	25-30	50-60	10-11	1.0-1.5	1-2
EGM	40-45	50-55	ND*	0.3-0.35	3-3.5
EGN	10-15	60-70	17-19	1.0-1.5	ND*
Shadow mask	36-40	60-64	ND*	ND*	ND*

*Not detected

These findings suggest different approaches for the Ni recovery from the magnetic and non-magnetic metallic parts of the EGs. As expected, the INVAR shadow mask has a content of Ni between 36 and 40 %. The experiments concerning the EG and INVAR solubilisation are presented below.

Metallic waste solubilisation
Chemical solubilisation

The EG waste chemical solubilisation was performed in sulphuric and hydrochloric acid respectively. Both acid solutions are used frequently in classical extraction methods of Ni from Ni containing ores [10]. Moreover, Ni electrowinning and electrorefining are performed using sulphate and chloride solutions, and even a mixture of the two. The solubilisation tests were performed using concentrated and diluted acid solutions.

Solubilisation tests in concentrated H_2SO_4 (approx. 18 M) revealed the inefficiency of using this strong acid solution as solubilisation medium due, most probably to, the formation of a passive layer on the metallic surface. A more diluted solution (2 M) of H_2SO_4 proved to be more efficient in dissolving the metallic waste. The results showed that after 12 days, 44.3 % (4.7 g) of the 10.6 g of EG waste were dissolved in 100 ml of 2 M H_2SO_4 solution. If we consider a linear evolution of the solubilisation process, this result translates in a solubilisation rate of 16.3 mg of waste per hour. The same leaching agent (2 M H_2SO_4) was used for comparison in the electrochemical solubilisation tests, described in the next section.

The next approach was to use different concentrations of HCl: 1, 2, 4, 6 and 12 M. When using concentrated HCl (above 6 M) the EG waste can be totally dissolved in a reasonable time period, but toxicity and handling issues arise. The diluted HCl solutions were much less efficient as leaching agents for this type of metallic waste (results not shown).

The low solubilisation efficiencies in mineral acids (H_2SO_4 and HCl) lead to the use of an oxidising agent in acidic media, more precisely $FeCl_3$ in HCl. The solubilisation tests were carried out using both the separated metallic waste (EGM and EGN) and the non-separated waste. In this case small quantities of

waste were used (approximately 1 g) and, for quantification reasons, the tests were stopped after 11 days, before the end of the process. The amount of oxidant needed was stoichiometrically calculated and added in 100 % excess in the 1 M HCl solution. The obtained results are depicted in Figure 2.
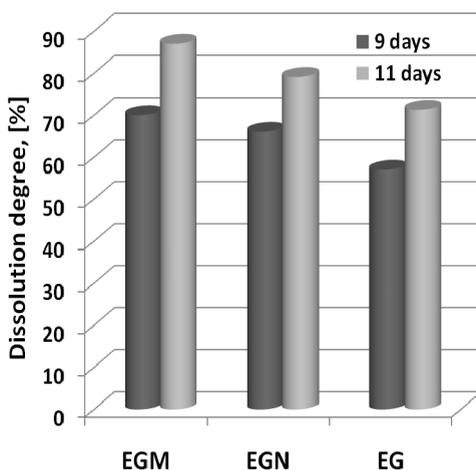

Figure 2. Solubilisation degree of the EGs metallic parts at two different times, by using 0.04 M FeCl$_3$ containing 1 M HCl.

As can be seen from Figure 2, after 9 days approximately 60 % of the non-separated waste was dissolved while, apparently, the magnetic separation produced an increase of the dissolved quantity percentage (approximately 10 %) for both EGM and EGN. At the end of the test, after 11 days, it was found that 87 % of EGM, 79.1 % of EGN and 71.3 % of EG were dissolved, keeping the trend observed after 9 days. Considering the duration and the experimental conditions, the differences between the three cases can be considered within the limits of acceptable experimental errors and they cannot be assigned to a positive effect of magnetic separation. The calculated solubilisation rate in this case is several times lower than for 2 M H$_2$SO$_4$, being situated between 2.7 and 3.3 mg of EG waste per hour.

The results of the chemical solubilisation tests show that, although some approaches are very efficient in dissolving the waste, the procedure takes a very long time and consumes large quantities of concentrated mineral acids. Moreover, handling and toxicity issues arise. In order to partially eliminate the handling concerns, a more diluted acidic media or an oxidizing agent present (e.g. FeCl$_3$) can be used successfully.

In order to improve the solubilisation degree of these wastes and to shorten the time spent for this operation, the next experiments were performed in an electrochemical reactor, using the metallic waste as anode.

Electrochemical solubilisation

The electrochemical solubilisation (ECS) tests were performed on the INVAR shadow mask and on the magnetic parts (EGM) of the EG respectively. The magnetic parts were used due to the high concentration of Ni and the possibility to avoid the contamination with Cr of the resulted solutions. In the next sections the focus will be only on the solutions resulted from the solubilisation of EGM and/or INVAR shadow mask.

The solubilisation of the metallic waste was carried out in three different acidic solutions: 2 M H_2SO_4, 1 M HCl and 0.1 M NaCl (pH = 1) respectively. The tests were carried out in an electrochemical cell with an electrolyte volume of 500 cm^3. The electrodes consisted of two graphite plates (1 cm thickness and 70 cm^2 surface area), with parallel horizontal placement inside the cell. The upper electrode was used as cathode and the metallic waste was placed on the bottom plate, in electrical contact with the anode. The cell was placed on a magnetic stirrer which proved to be very useful for maintaining the electrical contact between the magnetic metallic parts and the graphite anode and at the same time for providing a controlled stirring of the metallic pieces. All ECS experiments were performed at room temperature, under galvanostatic conditions (applied current values between 0.5 and 2 A).

In order to compare the three leaching media, identical quantities of INVAR (around 5 g), were dissolved under galvanostatic conditions (2 A) for the same period of time (2.5 h). The calculated current efficiency was higher than 90 % in all cases. The main differences between the three acidic solutions are detailed below.

In the case of 1 M HCl, a thin green coloured deposit with low adherence was observed on the cathode surface at the end of the experiment. When working under galvanostatic conditions, the reaction taking place at the cathode is hydrogen evolution. If the dissolved metals reach a certain concentration and the potential of the cathode allows for it, the hydrogen evolution is partially replaced by the electrodeposition of the metals (in our case Ni and Fe). Moreover, in an unbuffered medium, the hydrogen evolution reaction changes the local pH at the cathode surface especially, and it can induce the precipitation of Fe and Ni hydroxides, hence the appearance of a coloured precipitate/deposit.

In 0.1 M NaCl (pH = 1) the local pH change effect resulted very soon in a large quantity of precipitate around the cathode. The experiment was stopped after approximately 2 hours and the solution and precipitate were analysed by AAS. The final pH of the solution reached a value around 4, where all Fe(III) should precipitate as $Fe(OH)_3$. The analysis of the precipitate (washed and dried) showed a surprisingly high amount of Ni (45 % of the total Ni-Fe content), although the Ni percentage in INVAR is 36 % and Ni precipitation should occur at higher pH values. The explanation could be the fast precipitation due to high local pH changes. The amount of metal left in the solution was less than half (45 %) of the whole dissolved quantity with a Ni/Fe ratio of 1/2.5. In our opinion this medium can be used for ECS only with a strict control of pH, e.g. by addition of concentrated HCl.

126

The best results from our perspective were those obtained for 2 M H_2SO_4 solution. In this case no deposit or precipitate was observed at the cathode. This fact suggests us to use the same solution for more successive solubilisation tests (e.g. 3), the final concentration of metal in the solution arriving at ~30 g/L. Even at this concentration the cathodic deposition of Ni/Fe didn't occur. The current efficiency was higher compared to HCl and NaCl, reaching approximately 95 %. A parallel test was run, under identical experimental conditions but in absence of electrolysis current, in order to evaluate the contribution of the chemical solubilisation. The result showed that in the same period of time, 2.5 hours, in 2 M H_2SO_4, less than 0.5 % of the total metallic waste was solubilised. The chemical solubilisation rate for pure INVAR in 2 M H_2SO_4 was lower (9 mg/hour) than that for EG wastes (see Section 2.1).

In the case of EGM waste, the results in 2 M H_2SO_4 and 1 M HCl were similar to those for INVAR, with a high current efficiency in both cases (higher than 90 %). Some ECS tests were performed at lower current values (e.g. 0.5 A) when, for a similar amount of used total charge (10 hours), the current efficiency was higher, reaching 99 % in the case of HCl.

Compared with the chemical solubilisation, a higher efficiency of the ECS of the metallic waste in diluted acidic solutions (e.g. 2 M H_2SO_4, 1 M HCl and even 0.1 M HCl) was clearly noticed (hours *vs.* days). In the case of HCl, the chemical solubilisation was efficient only when the concentration of the acid was above 6 M. It was also demonstrated that the ECS is feasible in 0.1 M NaCl (pH = 1), when the pH is maintained at low values by adding acid or by buffering the acidic solution.

Fe-Ni separation from solutions / Iron precipitation

The solution resulted from the solubilisation of the EG waste contains a large amount of Fe ions. If the final purpose is to obtain a relatively pure deposit of Ni, Fe must be separated from the solution before any electrowinning experiments. Another alternative would be the tuning of the experimental parameters (solution composition, pH, temperature, current density) in order to obtained Ni-Fe alloys with a useful composition (e.g. INVAR).

Various studies offer multiple alternatives for Fe removal, the simplest being the precipitation of Fe^{3+} by controlling the temperature and pH of the solution [13-15]. In the case of low concentrations of Fe ions, an extraction using specific solvents could be employed [16, 17], too. Unfortunately, these agents are usually very costly and couldn't justify economically their employment for our purposes (considering Ni and Fe prices), except for low (traces) Fe amounts in the solution.

Our initial approach aimed at a selective precipitation of iron from the solution. The solution used for this purpose was that resulted from the ECS of an EGM sample under galvanostatic conditions (0.5 A) in 1 M HCl, as described above (see Section 2.2). A complete solubilisation of approximately 5.3 g of waste was finished in 10 hours. The resulted solution had the composition shown in

Table 2, with a Ni to Fe ratio in the solution of 1 to 1.2 and traces of Co and Mn. Iron could be partially separated by precipitating Fe^{3+} by raising the solution pH, stepwise, from 2 to 4 (adding NaOH). It was observed that the ratio Ni to Fe was changed to 2:1 with small losses of Ni in the precipitate (Table 2). The results show that by this simple approach a percentage of approximately 55 % of Fe was removed from the solution. The resulted solution could be used for Ni-Fe alloys electrodeposition, with high Ni content [18].

Table 2. Metal concentrations of the samples resulted by
selective precipitation of iron (NaOH addition)

Sample	Ni		Fe		Co		Mn	
	[g/L]	[%]	[g/L]	[%]	[g/L]	[%]	[g/L]	[%]
Solution	9.02	44.40	11.00	51.30	0.39	1.90	0.19	0.90
Precipitate	-	4.50	-	94.10	-	0.05	-	0.04
Filtrate	8.60	64.70	4.20	33.40	0.38	0.80	0.18	0.70

In order to separate more iron from the solution, Fe^{2+} needs to be oxidised to Fe^{3+}. This can be accomplished either chemically (by using oxygen, chlorine or an oxidiser such as sodium persulphate) or electrochemically (by anodic oxidation at a convenient electrode material). Our first approach was the oxidation with air at high temperature. The temperature of the solution was kept constant at 85 ^{0}C for four hours at a pH value around 3.5 and the aeration was performed using a peristaltic pump. The results in this case have shown a removal efficiency of Fe of about 85 %.

The complete removal of Fe^{3+} from a synthetic sulphate based solution containing 1:1 Ni and Fe (~ 10 g/L each) was obtained by precipitating Fe^{3+} at pH 3.5 and 80 ^{0}C. The pH was controlled by adding a solution of 10 % Na_2CO_3. The reaction time was four hours and the analysis of the filtrate showed that there was virtually no Fe left in the solution. The nickel loss in the precipitate was estimated to be around 4.4 % of the initial dissolved quantity.

Nickel and nickel-iron alloys can be electrodeposited on different materials (steel, copper, nickel, carbon) using conventional methods both from sulphate and chloride media in a relatively broad range of acidic solutions (pH between 2 and 4); the influence of different parameters (solution composition, pH, temperature, and current density) on the Ni and Ni-Fe alloys electrowinning is under current study and the results will be presented in future publications.

CONCLUSIONS

Nickel recovery from electronic waste is important both economically and for environmental reasons. The current research aimed at a concrete aspect of WEEE recycling, i.e. the solubilisation of the Ni containing metallic parts of CRTs (EG and shadow mask) and the purification of the obtained aqueous solutions.

The results of our current studies lead us to the following conclusions:

Chemical solubilisation of the metallic EG wastes from CRTs takes a very long time (solubilisation rates in the mg/hour range) and sometimes consumes large quantities of concentrated mineral acids;

The chemical solubilisation can be improved when an oxidizing agent such as $FeCl_3$ is used (see for example the case of diluted HCl);

Electrochemical solubilisation is much faster (hours *vs.* days) and can be performed in less acidic conditions with high efficiencies. Current efficiencies over 90% were obtained in all experimental conditions, even for the highest applied current value (2 A);

Iron can be partially or totally separated from the resulted solutions *via* the oxidation of Fe^{2+} to Fe^{3+}, followed by Fe^{3+} precipitation at controlled pH and temperature;

The resulted solutions, depending on the residual Fe concentration, can be used for the electrodeposition of nickel and/or nickel-iron alloys. The composition of the alloys can be controlled by tuning the experimental electroextraction conditions.

EXPERIMENTAL SECTION

Reagents

The main leaching media used for experiments were 2 M H_2SO_4, 1 M HCl, 0.1 M NaCl in HCl (pH = 1) and 0.04 M $FeCl_3$ in 1 M HCl. All chemicals were of analytical grade and were used as received. All solutions were prepared with double distilled water (Double D Still, JENCONS, England).

Experimental setups

The composition of EGs was established by XRD on a Shimadzu diffractometer XRD-6000 assembled in Bragg-Brentano θ/2θ with a goniometer which operates at atmospheric pressure with Ni filters using $CuK_α$ radiation (λ = 1.5418 Å). The standard calibration was made with quartz powder. Data acquisition conditions were: 40 KV operating potential at a 30 mA current. The peaks qualitative identification was realized using the JCPDS (Joint Committee on Powder Diffraction Standards) database.

The EGs elemental composition was determined by solubilisation in *aqua regia* and Atomic Absorbtion Spectrometry (AAS) measurements using an Atomic Absorption Spectrometer (AAS) Avanta 9500 (GBC, Australia).

For electrochemical solubilisation tests, an electrochemical reactor (electrolyte volume of 500 cm^3) with plane parallel graphite electrodes was used. Saturated Ag|AgCl$_{KCl}$ reference electrodes were used for all experiments.

A PC equipped with a PCI 6221 E data acquisition board (National Instruments, USA) was used to drive a DXC236 potentiostat/galvanostat (Wenking, Germany). The LabView 6.1 software (National Instruments, USA) was used for the process control and data acquisition.

ACKNOWLEDGMENTS

REFERENCES

1. R. Widmer, H. Oswald-Krapf, D. Sinha-Khetriwal, M. Schnellmann, H. Böni, *Environmental Impact Assessment Review,* **2005**, *25*, 436.
2. B.R. Babu, A.K. Parande, C.A. Basha, *Waste Management & Research,* **2007**, *25*, 307.
3. B.H. Robinson, *Science of the Total Environment*, **2009**, *408*, 183.
4. F.O. Ongondo, I.D. Williams, T.J. Cherrett, *Waste Management,* **2011**, *31*, 714.
5. M. Bigum, T.H. Christensen, in *Solid Waste Technology & Management, Vol. 1 & 2* (Ed.: T.H. Christensen), John Wiley & Sons, Ltd, Chichester, UK, **2010**.
6. L.E. Macaskie, I.P. Mikheenko, P. Yong, K. Deplanche, A.J. Murray, M. Paterson-Beedle, V.S. Coker, C.I. Pearce, R. Cutting, R.A.D. Pattrick, D. Vaughan, G. van der Laan, J.R. Lloyd, *Hydrometallurgy,* **2010**, *104*, 483.
7. C. Nnorom, O. Osibanjo, M.O.C. Ogwuegbu, *Resources, Conservation and Recycling,* **2011**, *55*, 275.
8. F. Andreola, L. Barbieri, A. Corradi, I. Lancellotti, *Waste Management and Research,* **2005**, *23*, 314.
9. S. Herat, *CLEAN - Soil, Air, Water,* **2008**, *36*, 19.
10. D.E.G. Kerfoot, in *Ullmann's Encyclopedia of Industrial Chemistry*, Wiley-VCH Verlag GmbH & Co. KGaA, **2000**.
11. E. Denkhaus, K. Salnikow, *Critical Reviews in Oncology/Hematology,* **2002**, *42*, 35.
12. K.H. Park, D. Mohapatra, B.R. Reddy, *Separation and Purification Technology,* **2006**, *51*, 332.
13. K. Wang, J. Li, R.G. McDonald, R.E. Browner, *Hydrometallurgy,* **2011**, *109*, 140.
14. Y. Chang, X. Zhai, B. Li, Y. Fu, *Hydrometallurgy,* **2010**, *101*, 84.
15. S. Agatzini-Leonardou, P.E. Tsakiridis, P. Oustadakis, T. Karidakis, A. Katsiapi, *Minerals Engineering,* **2009**, *22*, 1181.
16. R.K. Mishra, P.C. Rout, K. Sarangi, K.C. Nathsarma, *Hydrometallurgy,* **2011**, *108*, 93.
17. M.-S. Lee, K.-J. Lee, *Hydrometallurgy,* **2005**, *80*, 163.
18. I. Tabakovic, V. Inturi, J. Thurn, M. Kief, *Electrochimica Acta*, **2010**, 55, 6749.

THEORETICAL STUDY OF P(III)=C-P(V) TYPE DIPHOSPHAPROPENES COORDINATED TO TRANSITION METALS

RALUCA SEPTELEAN[a], PETRONELA MARIA PETRAR[a], GABRIELA NEMEŞ[a,*]

ABSTRACT. DFT calculations at BP86/6-311G*(d,p) level of theory were performed RP(Cl)=C-P(=E)MeCl (R=H, Me or Ph and E=O, S) units, in order to realized a energetic and geometric analysis. The coordination modes of diphosphapropenic systems to transition metals were also investigated in the case of $W(CO)_5$, $PtCOCl_2$ and $PdCOCl_2$ organometallic fragment.

Keywords: DFT calculations, diphosphapropene, coordination models

INTRODUCTION

Heteropropene compounds of the X=C-X' type (X, X' being p-block elements) have been intensively studied in the last three decades due to the presence in the system of multiple reactive sites such as the X=C double bond or the X, X' atoms. On the other hand, heteropropenes (especially the ones bearing one or two halogen atoms) are precursors in the synthesis of unsaturated X=C=X' heteroallene compounds. The presence of one or multiple unsaturations in heteropropenic and heteroallenic systems created serious problems in the stabilization of these compounds. Two methods are currently known for solving this problem: the use of bulky groups to thermodynamically stabilize these compounds and the coordination to ML_n fragments that can increase the stability of the X=C=X' moiety by kinetic effects. The literature offers many information on stabilizing the heteropropenes and heteroallenes by connecting the bulky organic groups to the X=C=X' or X=C-X' moieties.

Multiple experimental studies were reported [1-10] regarding the synthesis pathways of this type of compounds and their physico-chemical characterization. Computational studies were performed in order to determine the factors leading to the stabilization of such systems [11-13]. Most of these studies refer to the stabilizing effect of different organic groups with different electronic and steric properties.

---

[a] Babes-Bolyai University, Faculty of Chemistry and Chemical Engineering, Department of Inorganic Chemistry, M. Kogălniceanu No. 1, RO-400082 Cluj-Napoca
 * *sgabi@chem.ubbcluj.ro*

Our group is particularly interested in the field of heterophosphaallenic and heterophosphapropenic compounds [14], their synthesis, physico-chemical characterization and computational studies. Regarding the theoretical investigation, *ab initio* calculations have previously been reported for heterophosphaallenes like RP=C=PR (R = H, F, Cl) [15, 16], HP=C=NH [16, 17] HP=C=O [18], RP=C=AsR or R_3P=C=AsR$_3$ [19, 20] or in cumullenic systems of the type RP=C=P(=O)R' [12, 13]. All these studies take into account the thermodynamic stabilizing effect induced by the groups attached to the X=C=X' fragment. No extensive computational studies that discuss the effects induced by the presence of one or more MLn organometalic fragments attached to the X, X' atoms or the X=C moiety were reported.

This work presents a theoretical study on the coordination ability of diphosphapropenic systems RP(Cl)=C-P(E)(Cl)Me (E = O, S) towards organometallic fragments ML_n (W(CO)$_5$, PtCOCl$_2$, PdCOCl$_2$). Several substituents (R= H, Me, Ph) were taken into account in order to asses a possible influence on the coordination. DFT calculations were carried out on the model compounds to determine the optimized geometries and energies. For the tungsten derivatives, a clear predilection towards coordination though the phosphorus atom involved in the P=C bond was evidenced. Calculations suggest that in the case of palladium or platinum, diphosphapropenes would act as bidentate ligands. The Wiberg bond orders for the M-E bond (E = the donor atom of the diphosphapropenic unit) were also calculated.

RESULTS AND DISCUSSIONS

All starting structures were built with Gaussview 4.1[21]; the geometries were optimized with Gaussian 09[22] package of programs at the DFT BP86/6-311++G(d,p) level of theory for the C, H, Cl, P, O and S atoms and using the LANL2TZ [23] basis set for the metallic atoms. Vibrational analyses were carried out in order to ensure that all structures represent true energy minima.

The most stable geometries as well as the coordination possibilities of diphosphapropenic systems of RP(Cl)=C-P(=E)MeCl (R= H, Me, Ph and E=O, S) to transition metal fragments such as W(CO)$_5$, PdCOCl$_2$ and PtCOCl$_2$ have been studied.

In each of the investigated phosphapropenic system, the geometry of the diphosphapropene system was optimized and the energy minima of the potential surface were used as starting structures for the modeling of the derivatives coordinated to the transition metal.

The optimized geometries for the MePCl=C-P(Me)ClE (E=O, S) systems are presented in Figure 1. The considered ligands present several possibilities of coordinating to transition metals: through the λ^3P atom, the P=C moiety or one of the O or S atoms, as depicted in Figure 2. The coordination

modes taken into account for this study represent the most common behavior towards transition metals of phosphapropenes functionalized with group 16 elements as monodentate ligands.
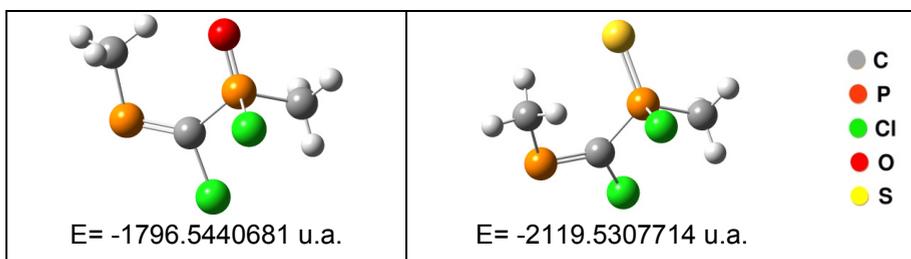

| E= -1796.5440681 u.a. | E= -2119.5307714 u.a. |

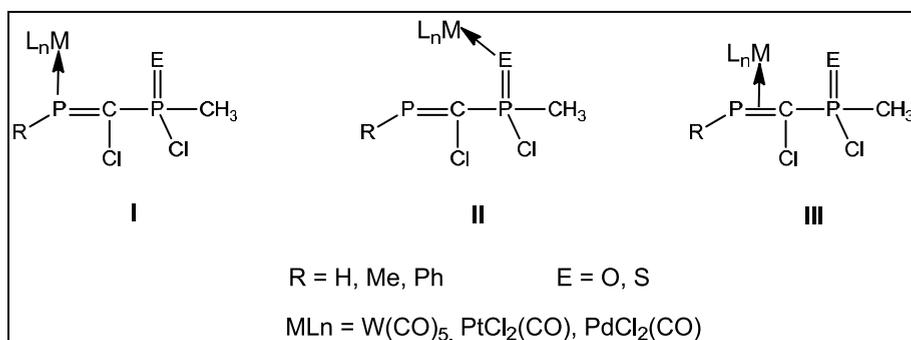**Figure 1.** Optimized structures for MePCl=C-P(=E)ClMe, E=O (a), S (b)

Figure 2. Considered types of PCP(E) systems coordination to organometallic fragments.

Tungsten coordination compounds

The optimization of the three tungsten complexes with diphosphapropenic ligands, corresponding to the considered coordination modes, was followed by a vibrational analysis to ensure that the structures represent true minima. The calculated geometrical parameters are presented in Table 1, along with the relative energies compared to the coordination isomer with the lowest energy of the series.

The metal-diphosphapropenic bond lengths are estimated between 2.372 Å and 2.623 Å for PCPS systems, and 2.269 Å -2.471 Å for the PCPO systems.

The coordination of a sulfur-containing ligand to a metal atom generally leads to an increase in the length of the P=C double bond by up to 0.1 Å. The most dramatic shift was observed (as expected) in type III coordination, together with the lowering of P=C bond order. For instance for MeP=C(Cl)-P(=S)MeCl→W(CO)$_5$ coordination isomers, the calculated Wiberg [24] bond

order estimated through the NBO [25] analysis, decreases from 1.66 for the free ligand to 1.52 for the P-coordinated isomer and 1.12 for type III complexes, losing entirely the double bond character. The NBO analysis suggests in this case a type IIIb structure (see Scheme 1), and not a direct electron donation from the P=C bond to the metal atom. This can be credited to the different electronegativity of the atoms involved in the double bond, allowing an uneven distribution of the electronic charge. A coordination through the sulfur atom does not affect in a significant manner the P=C bond, with an estimated Wiberg bond order of 1.65.
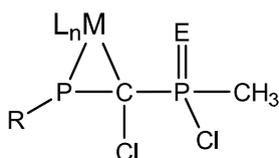
IIIb

Scheme 1.

The calculated P-C single bond lengths range between 1.820 Å and 1.882 Å, in good agreement with reported experimental data [2]. The presence of various atoms on the P(V) atom does not have a strong influence on the bond lengths of the considered compounds.

Figure 3 represents the optimized geometries of the complexes resulted by the coordination of PhP=C(Cl)-P(=O)MeCl to the W(CO)$_5$ organometallic fragment. When the coordination takes place through the P atom or the double bond, the ligand adopts a *cis* configuration, relative to the P=C bond, allowing for a less sterically hindered derivative. If the donor atom is the oxygen, the coordination can occur in a *trans* configuration as well. The geometry around the tungsten atom is that of distorted octahedron.
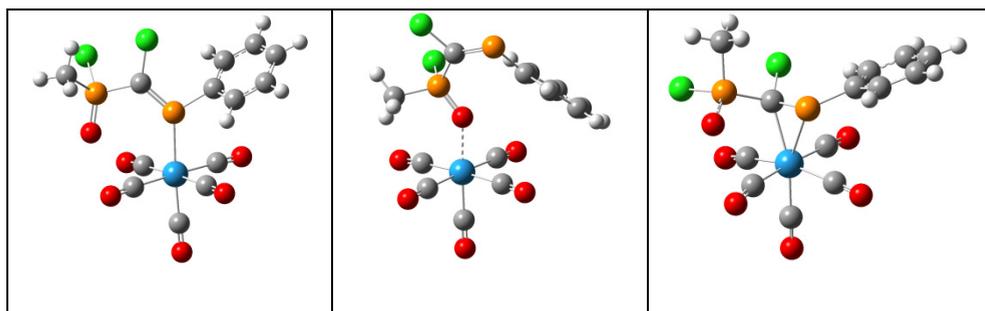

Figure 3. Calculated geometries of PhP=C(Cl)-P(=O)MeCl→W(CO)$_5$

Based on the relative energies presented in Table 1 (as compared to the energy minima of the series of isomers) a general preference for the coordination of the phosphapropenic system to the tungsten atom through the double bonded phosphorus atom is evidenced. There are no noticeable differences in energy between complexes of this type and the ones having a type III coordination, but in all cases the coordination through oxygen and sulfur atoms are disfavored - with an energy higher by more than 10 kcal/mol when compared to their isomers. The only observed exception was for HPCPS systems, where the least favored structure is the one with the coordination of the metal fragment through the double bond.

Table 1. Calculated relative energies and geometric parameters of
PCP(E)→W(CO)$_5$ structures.

	R	E rel (kcal/mol)	M-lig*	λ^3P -C (Å)	λ^5P -C(Å)	E= λ^5P(Å)
PCPO	H			1.699	1.845	1.498
PCPO_W-P	H	0	2.451	1.697	1.843	1.496
PCPO_W-O	H	10.35	2.269	1.702	1.832	1.515
PCPO_W-leg	H	1.06	2.338	1.813	1.847	1.501
PCPO	Me			1.703	1.834	1.500
PCPO_W-P	Me	0	2.463	1.705	1.827	1.501
PCPO_W-O	Me	14	2.292	1.704	1.818	1.519
PCPO_W-leg	Me	7.15	2.323	1.809	1.844	1.502
PCPO	Ph			1.691	1.826	1.483
PCPO_W-P	Ph	0	2.471	1.712	1.820	1.500
PCPO_W-O	Ph	12.25	2.285	1.710	1.817	1.516
PCPO_W-leg	Ph	5.41	2.35	1.815	1.852	1.501
PCPS	H			1.699	1.861	1.946
PCPS_W-P	H	0	2.458	1.709	1.827	1.946
PCPS_W-S	H	6.14	2.623	1.701	1.844	2.000
PCPS_W-leg	H	10.85	2.372	1.794	1.869	1.943
PCPS	Me			1.704	1.844	1.950
PCPS_W-P	Me	0	2.465	1.704	1.838	1.952
PCPS_W-S	Me	14.34	2.617	1.707	1.848	2.003
PCPS_W-leg	Me	9.89	2.393	1.796	1.882	1.950
PCPS	Ph			1.705	1.850	1.946
PCPS_W-P	Ph	0	2.485	1.709	1.842	1.947
PCPS_W-S	Ph	6.36	2.616	1.712	1.834	2.003
PCPS_W-leg	Ph	4.91	2.393	1.802	1.882	1.948

* for systems in which the coordination occurs through the double bond, this value corresponds to the distance between the transition metal and an imaginary point situated at the middle of P-C distance.

Platinum complexes

For the platinum complexes, the metallic fragment considered for the study is $PtCOCl_2$, starting from the optimized geometry of the ligand and a surrounding close to the ideal plan-squared geometry of the metallic atom. The calculated geometrical parameters are presented in Table 2, along with the relative energies, compared to the coordination isomer with the lowest energy of the series.

The metal-phosphapropenic system bond lengths calculated at the BP86/6-311G*(d,p)//LANLTZ level of theory range from 2.100 to 2.342 Å for PCPO derivatives and 2.330 Å and 2.412 Å for the PCPS systems. The P=C double bond length in the coordinative systems increases in general, disregarding the type of coordination. It is worth noticing that the single P-C bond (ranging from 1.811 Å to 1.905 Å, in good agreement with experimental data) is influenced by the type of coordination; in the cases in which the coordination occurs through the group 16 element, the λ^5P –C distance is shortened by around 0.2 Å.

Table 2. Calculated relative energies and geometrical parameters of PCP(E) systems coordinated to $PtCOCl_2$.

	R	E rel (kcal/mol)	M-lig*	λ^3P -C (Å)	λ^5P –C (Å)	E= λ^5P (Å)
PCPO	H			1.699	1.845	1.498
PCPO_Pt-P	H	0.39	2.331	1.689	1.851	1.498
PCPO_Pt-O	H	0.00	2.100	1.700	1.828	1.528
PCPO_Pt-leg	H	10.94	2.188	1.791	1.885	1.497
PCPO	Me			1.703	1.834	1.500
PCPO_Pt-P	Me	0.00	2.333	1.687	1.847	1.496
PCPO_Pt-O	Me	3.42	2.104	1.704	1.813	1.532
PCPO_Pt-leg	Me	11.98	2.173	1.807	1.872	1.498
PCPO	Ph			1.691	1.826	1.483
PCPO_Pt-P	Ph	0.00	2.342	1.694	1.835	1.497
PCPO_Pt-O	Ph	3.92	2.103	1.711	1.811	1.528
PCPO_Pt-leg	Ph	14.91	2.216	1.800	1.899	1.493
PCPS	H			1.699	1.861	1.946
PCPS_Pt-P	H	1.68	2.333	1.689	1.866	1.945
PCPS_Pt-S	H	0.00	2.334	1.690	1.866	1.946
PCPS_Pt-leg	H	13.45	2.233	1.784	1.905	1.945
PCPS	Me			1.704	1.844	1.950
PCPS_Pt-P	Me	0.00	2.332	1.688	1.851	1.946
PCPS_Pt-S	Me	0.33	2.412	1.704	1.827	2.028
PCPS_Pt-leg	Me	15.70	2.186	1.805	1.881	1.946
PCPS	Ph			1.705	1.850	1.946
PCPS_Pt-P	Ph	0.00	2.342	1.697	1.866	1.939
PCPS_Pt-S	Ph	1.26	2.392	1.710	1.853	2.036
PCPS_Pt-leg	Ph	13.37	2.222	1.829	1.898	1.940

Figure 4 represents the BP86 optimized geometries of platinum complexes and HP=C(Cl)-P(=S)MeCl through the phosphorus or sulfur atoms. In the second case it can be noted that the optimization converges to a geometry in which the phosphapropenic system tends to behave as a bidentate ligand, the λ^3P-Pt distance being 2.68 Å.

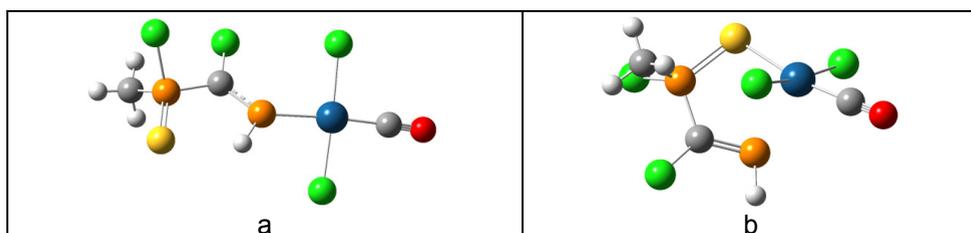**Figure 4.** Optimized geometries of P=C(Cl)-P(=S)MeCl→PtCl$_2$CO

For the systems with H as substituent on the phosphorus atom, the lowest calculated energies are for the isomers with the diphosphapropenic unit coordinated through the E atom (E=O, S), with no significant energy differences between them and type II isomers. The structures in which the coordination of the metallic fragment occurs through the P=C double bond are the least favored in this case, with relative energies higher by more than 10 Kcal/mol.

The same behavior was noted for alkyl and aryl substituted derivatives, so that based on our theoretical result one can expect these systems to coordinate through either P(III) or E atoms. However, if the reaction takes place under the proper conditions (e.g., an appropriate stoichiometric ratio or irradiation) P=C-P(=E) diphosphapropenic derivatives can behave as bidentate ligands towards platinum.

Paladium complexes

Similar to the above mentioned complexes, geometric parameters and relative energies of some palladium complexes were calculated, using model molecules in which the diphosphapropenic systems coordinate to a PdCl$_2$(CO) organometallic fragment. The computed P=C bond lengths range from 1.699 and 1.891 Å, denoting a lowering of the double bond character. The P-C single bond lengths range between 1.814 and 1.8876 Å. Figure 5 presents the optimized geometries of MeP=C(Cl)-P(=S)MeCl→PdCl$_2$(CO) complexes for the first two types of investigated coordination modes.

All three investigated coordination modes lead to palladium complexes with similar energies; thus, the BP86 method cannot estimate a certain preference for coordination to the transition metal. The only exception was noted for HPCPO and PhPCPO, where the coordination through the double bond is clearly energetically disfavored (by 11.29 kcal/mol and 10.90 kcal/mol).
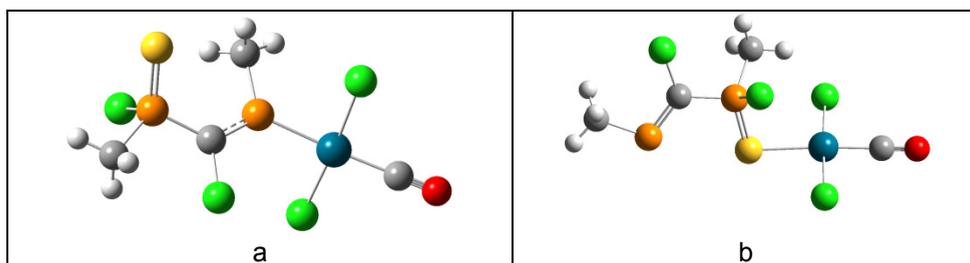
| a | b |

Figure 5. Optimized geometries of MeP=C(Cl)-P(=S)MeCl→PdCl$_2$CO

Bond orders

The Wiberg bond orders for the M-E bond corresponding to the first and second coordination modes considered were evaluated through NBO analysis. The calculated values are presented in Table 4.

The highest bond order was noted for tungsten derivatives for all considered substituents on the λ^3P atom. As reflected by the relative energies, the coordination to the tungsten atom will more preferably take place through the double bonded phosphorus atom for P=C-P=O systems. The W-E bond order is of about 0.3 for E=O and much higher for E=S, indicating higher preference to coordination of the sulfur atom to the metal, accordingly to the HSAB theory.

For platinum and palladium, the lower differences between Pt-P and Pt-E bond orders suggest the possibility of coordination through both atoms, especially for the sulfur derivatives. These findings confirm reported experimental data [10] as well as the analysis of the electronic energies presented above, according to which diphosphapropenic derivatives can act as bidentate ligands in presence of transition metals.

Table 3. Calculated relative energies and geometrical parameters for PCP(E) systems coordinated to PdCOCl$_2$

	R	E rel (kcal/mol)	M-lig*	λ^3P -C (Å)	λ^5P –C (Å)	E= λ^5P (Å)
PCPO	H			1.699	1.845	1.498
PCPO_Pd-P	H	0.36	2.324	1.689	1.850	1.498
PCPO_Pd-O	H	0	2.097	1.700	1.830	1.525
PCPO_Pd-leg	H	11.29	2.254	1.769	1.885	1.498
PCPO	Me			1.703	1.834	1.500
PCPO_Pd-P	Me	0	2.317	1.686	1.842	1.498
PCPO_Pd-O	Me	4.33	2.107	1.704	1.815	1.528
PCPO_Pd-leg	Me	2.89	2.173	1.885	1.856	1.496
PCPO	Ph			1.691	1.826	1.483
PCPO_Pd-P	Ph	0	2.328	1.693	1.846	1.500

	R	E rel (kcal/mol)	M-lig*	λ^3P -C (Å)	λ^5P –C (Å)	E= λ^5P (Å)
PCPO_Pd-O	Ph	3.39	2.108	1.710	1.814	1.526
PCPO_Pd-leg	Ph	10.90	2.485	1.786	1.873	1.495
PCPS	H			1.699	1.861	1.946
PCPS_Pd-P	H	2.18	2.327	1.689	1.862	1.947
PCPS_Pd-S	H	0.00	2.414	1.701	1.827	2.027
PCPS_Pd-leg	H	4.48	2.971	1.691	1.866	1.938
PCPS	Me			1.704	1.844	1.950
PCPS_Pd-P	Me	0.94	2.327	1.691	1.853	1.946
PCPS_Pd-S	Me	0.00	2.424	1.702	1.831	2.009
PCPS_Pd-leg	Me	1.64	2.629	1.888	1.873	1.950
PCPS	Ph			1.705	1.850	1.946
PCPS_Pd-P	Ph	0	2.327	1.693	1.851	1.948
PCPS_Pd-S	Ph	1.36	2.406	1.710	1.840	2.024
PCPS_Pd-leg	Ph	0.8	2.497	1.891	1.876	1.939

Table 4. Wiberg bond orders for M-E (E= O, S) bond.

		PCPO		PCPS	
M	R	M-P	M-O	M-P	M-S
W	H	0.93	0.39	0.94	0.63
W	Me	0.92	0.38	0.91	0.64
W	Ph	0.91	0.39	0.88	0.66
Pt	H	0.72	0.34	0.72	0.65
Pt	Me	0.70	0.35	0.71	0.62
Pt	Ph	0.70	0.35	0.70	0.64
Pd	H	0.64	0.31	0.63	0.5
Pd	Me	0.63	0.31	0.63	0.53
Pd	Ph	0.63	0.31	0.63	0.56

CONCLUSIONS

Calculations performed at the BP86/6-311G*(d,p) level of theory allowed the energetic and geometric analysis of possible coordination modes of diphosphapropenic systems to transition metals. Several RP(Cl)=C-P(=E)MeCl (R=H, Me or Ph and E=O, S) were investigated and their coordination to organometallic fragments of $W(CO)_5$, $PtCOCl_2$ and $PdCOCl_2$ type were evaluated.

Theoretical calculations reveal a general preference for coordination of diphosphapropenic systems to tungsten through the double bonded phosphorus atom.

The coordination to platinum occurs through either the double bonded phosphorus atom or the E atom (E=S, O) of the diphosphapropenic system, without any apparent energetic preference. The least favorable coordination is through the double bond.

For the palladium complexes, no preference for either coordination mode was evidenced, when varying the diphosphapropenic system or the substituents on the phosphorus atom. An exception was observed for systems with R=H, Ph and E=O, for which the coordination is through the P=C moiety.

ACKNOWLEDGEMENT

REFERENCES

[1] J. Escudié, H. Ranaivonjatovo, L. Rigon, *Chemical Reviews*, **2000**, *100*, 3639.

[2] J. Escudié, H. Ranaivonjatovo, *Organometallics*, **2007**, *26*, 1542.

[3] R. Appel, *Multiple Bonds and Low Coordination in Phosphorus Chemistry* in M. Regitz, O. J. Scherer, *Methoden der Organischen Chemie*, **1990**, Thieme:Stuttgart, 157.

[4] M. Yoshifuji, *Journal of Chemical Society, Dalton Transactions*, **1998**, *20*, 3343.

[5] M. Karni, Y. Apeloig, J. Kapp, P. vR. Schleyer, *Theoretical Aspects of Compounds Containing Si, Ge, Sn and Pb*. In: Z. Rappoport, Y. Apeloig, *The Chemistry of Organic Silicon Compounds, Vol. 3*, **2003**, John Wiley & Sons Ltd: Chichester, UK, 1.

[6] S. Ito, M. Yoshifuji, *Chemical Communications,* **2001**, 1208.

[7] H. Liang, K. Nishide, S. Ito, M. Yoshifuji, *Tetrahedron Letters,* **2003**, *44*, 8297.

[8] H. Liang, S. Ito, M. Yoshifuji*, Zeitschrift für anorganische und allgemeine Chemie,* **2004**, *630*, 1177.

[9] S. Ito, K. Nishide, M. Yoshifuji, *Organometallics,* **2006**, *25,* 1424.

[10] R. Septelean, G. Nemes, J Escudie, I. Silaghi-Dumitrescu, H. Ranaivonjatovo, P.M. Petrar, H. Gornitzka, L. Silaghi-Dumitrescu, N. Saffon, *European Journal of Inorganic Chemistry*, **2009**, *5*, 628.

[11] R. Septelean, P.M. Petrar, I. Coman, G. Nemes, *Studia UBB Chemia*, **2010**, *55(3),* 223.

[12] R. Septelean, P.M. Petrar, G. Nemes, J. Escudie, *Journal of Molecular Modeling*, **2011**, *17(7)*, 1719.

[13] R. Septelean, P.M. Petrar, G. Nemes, J. Escudié, I. Silaghi-Dumitrescu, *Phosphorus Sulfur, Silicon and related elements,* **2011**, *186*(12), 2321.

[14] J. Escudié, G. Nemeş, *Comptes Rendus Chimie*, **2010**, *13*, Issues 8-9, 954.

[15] M.T. Nguyen, A.F. Hegarty, *Journal of Chemical Society, Dalton Transactions*, **1985**, *2,* 2005.

[16] N.J. Fitzpatrick, D.F. Brougham, P.J. Groarke, M.T. Nguyen, *Chemische Berichte,* **1994**, *127*, 969.

[17] M. Yoshifuji, T. Niitsu, K. Toyota, N. Inamoto, K. Hirotsu, Y. Odagaki, T. Higuchi, S. Nagase, *Polyhedron* **1988**, *7*, 2213.

[18] M.T. Nguyen, A.F. Hegarty, M.A. McGinn, F. Ruelle, *Journal of Chemical Society, Dalton Transactions*, **1985**, *2*, 1991.

[19] P.M. Petrar, G. Nemes, L. Silaghi-Dumitrescu, J. Escudie*, Revue Roumaine de Chimie*, **2010**, *55(11),* 1061.

[20] P.M. Petrar, G. Nemes, L. Silaghi-Dumitrescu, *Studia UBB Chemia*, **2010**, *55, 4(2),* 25.

[21] I.I.R. Dennington, T. Keith, J. Millam, K. Eppinnett, W.L. Hovell, R. Gilliland, *GaussView, Version 4.1.* Semichem Inc, Shawnee Mission, KS, **2003**.

[22] Frisch MJ, Trucks GW, Schlegel HB, Scuseria GE, Robb MA,Cheeseman JR, Scalmani G, Barone V, Mennucci B, PeterssonGA, Nakatsuji H, Caricato M, Li X, Hratchian HP, Izmaylov AF,Bloino J, Zheng G, Sonnenberg JL, Hada M, Ehara M, Toyota K,Fukuda R, Hasegawa J, Ishida M, Nakajima T, Honda Y, Kitao O,Nakai H, Vreven T, Montgomery JA Jr, Peralta JE, Ogliaro F,Bearpark M, Heyd JJ, Brothers E, Kudin KN, Staroverov VN,Kobayashi R, Normand J, Raghavachari K, Rendell A, Burant JC,Iyengar SS, Tomasi J, Cossi M, Rega N, Millam JM, Klene M,Knox JE, Cross JB, Bakken V, Adamo C, Jaramillo J, GompertsR, Stratmann RE,Yazyev O, Austin AJ, Cammi R, Pomelli C,Ochterski JW, Martin RL, Morokuma K, Zakrzewski VG, VothGA, Salvador P, Dannenberg JJ, Dapprich S, Daniels AD, Farkas O, Foresman JB, Ortiz JV, Cioslowski J, Fox DJ, **2009**, Gaussian09, Revision A.1. Gaussian Inc, Wallingford.

[23] a) D. Feller, *Journal of Computational Chemistry*, **1996**, *17,* 1571; b) K.L. Schuchardt, B.T. Didier, T. Elsethagen, L. Sun, V. Gurumoorthi, J. Chase, J. Li, T.L. Windus, *Journal of Chemical Information and Modeling*, **2007**, *47(3)*, 1045.

[24] K.B. Wiberg, *Tetrahedron*, **1968**, *24*, 1083.

[25] E.D. Glendening; J.K. Badenhoop, A.E. Reed, J.E. Carpenter, J.A. Bohmann, C.M. Morales, F. Weinhold, Theoretical Chemistry Institute, University of Wisconsin, *NBO 5.0*, **2001**.

EXPERIMENTAL STUDY OF SULFUR DIOXIDE ABSORPTION INTO CALCIUM CARBONATE SUSPENSIONS

SIMION DRĂGAN[a,*], ADINA GHIRIŞAN[a]

ABSTRACT. This paper presents the experimental data obtained in absorption process of SO_2 into limestone suspensions. The absorption experiments have been performed in a 0.75 L reactor, fitted with mechanical stirring, at temperature of 293, 303 and 313 K. The consistency of limestone slurry expressed as solid-liquid ratio was: R1=1/30; R2= 1/15; R3=1/10 and R4= 1/7.5. The influence of the limestone content in the initial slurry and the operating temperatures on the total absorption capacity were determined and analyzed. The obtained results, absorption capacity between 0.49 - 2.14 mol SO_2/L slurry, are comparable with those reported by other authors*.

Keywords: absorption, wet desulphurization, calcium carbonate slurry

INTRODUCTION

Atmospheric contamination with high quantities of noxes (CO_2, SO_2, SO_3, NO_x, HF, HCl, etc.) from the coal-fired power plants is a significant problem. This can lead to negative environmental impacts such as acidification of soil and global warming. Particularly notable are the programs on flue gas desulphurization (FGD) technologies that have been ongoing in a number of countries for several years [1-4].

Emissions of sulfur dioxide into the atmosphere have increased with industrial development and many countries have therefore adopted strict regulations regarding SO_2 emissions from fossil fired boilers which are one of the important sources of SO_2 emissions. The removal of SO_2 for various industrial sources has gained a considerable attention in the last years. Many processes for flue gas desulphurization (FGD) have been developed for reducing SO_2 emissions and were grouped into the following three major categories: wet, dry and semi-dry processes [1].

The dominating procedures employed to desulphurization for exhaust gases is based on wet scrubbing, especially slurry scrubbing [1,2]. In the last few decades, wet scrubbing with lime, limestone or dolomite slurry is the most applied method due to its high degree of SO_2 removal, low cost and widespread availability [3-7].

---

[a] "Babeş-Bolyai" University, Faculty of Chemistry and Chemical Engineering, Arany Janos 11, 400028 Cluj-Napoca

* sdragan@chem.ubbcluj.ro

The main factors that favor the use of limestone and dolomite slurry in the FGD processes are:

- limestone and dolomite are abundant minerals;
- the specific properties of the aqueous slurries facilitate an increase the absorption rate;
- the product of SO_2 removal is gypsum that is stable and reusable.

The major disadvantage of this limestone-gyp desulphurization process is the problem concerning the big amount of calcium sulfate obtained.

The aim of the present study is to investigate the absorption process of SO_2 into the natural limestone slurries containing calcium carbonate from Săndulești-Turda. The effect of temperature and the sorbets content of slurry on the total absorption capacities were determined.

RESULTS AND DISCUSSIONS

The overall reaction for FGD process can be written as:

$$SO_{2[g]} + CaCO_{3[s]} + 2H_2O_{[l]} + 0.5O_2 \rightarrow CaSO_4 \cdot 2H_2O_{[s]} + CO_{2[g]} \quad (1)$$
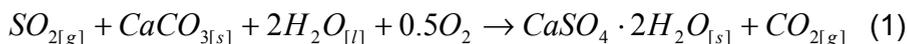
A simplified representation of mass transfer and reaction steps model for the absorption process of sulfur dioxide in calcium carbonate slurry is shown in figure 1.
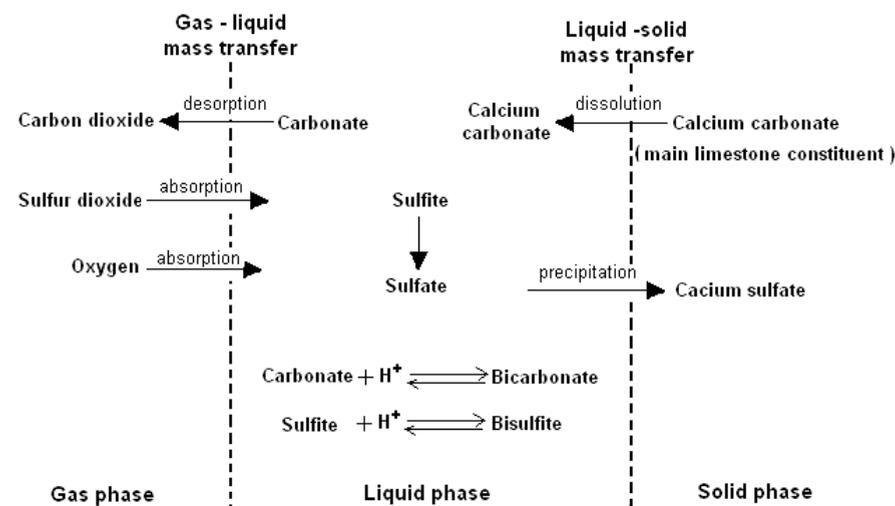

Figure 1. Schematic illustration of mass transfer and reaction steps for sulfur dioxide absorption in calcium carbonate slurry

Regarding the SO_2 absorption mechanism into calcium carbonate slurry, in the oxygen presence, the following processes can be considered [1, 3]:

144

– Transfer of SO_2 trough the gas-film near the gas-liquid interface:

$$N_{SO2} = k_g(p_{SO2} - p^*_{SO2})\qquad(2)$$

– SO_2 absorption in the liquid phase:

$$SO_{2[g]} \leftrightarrow SO_{2[aq]}\qquad(3)$$

$$SO_{2[aq]} + H_2O \leftrightarrow H_2SO_3\qquad(4)$$

$$H_2SO_3 \leftrightarrow H^+ + HSO_3^-\qquad(5)$$
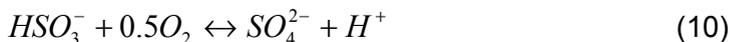
$$HSO_3^- \leftrightarrow H^+ + SO_3^{2-}\qquad(6)$$

A number of chemical reactions take place in the liquid phase. SO_2 is absorbed in the water and forms sulfite and sulfate ions.

– Calcium carbonate dissolution:

$$CaCO_{3[s]} \leftrightarrow CaCO_{3[aq]}\qquad(7)$$

$$CaCO_{3[aq]} \leftrightarrow Ca^{2+} + CO_3^{2-}\qquad(8)$$

$$CO_3^{2-} + H^+ \leftrightarrow HCO_3^-\qquad(9)$$

Limestone dissolves into the slurry to form carbonate and bicarbonate species. The carbonate ion can react with the hydroxyl ion to increase the liquid pH.

– Oxidation:

$$HSO_3^- + 0.5O_2 \leftrightarrow SO_4^{2-} + H^+\qquad(10)$$

– Precipitation:

$$Ca^{2+} + SO_4^{2-} + 2H_2O \leftrightarrow CaSO_4 \cdot 2H_2O\qquad(11)$$

$$Ca^{2+} + SO_3^{2-} + 0.5H_2O \leftrightarrow CaSO_3 \cdot 1/2H_2O\qquad(12)$$

where: g is the gas phase, s - the solid phase, aq - the aqueous phase, HSO_3^- - the bisulfite ion, SO_3^{2-} - the sulfite ion, SO_4^{2-} - the sulfate ion, O_2 - oxygen, H^+ - the hydrogen ion and SO_2 - sulfur dioxide.

The dissolved calcium ions are free to react with the sulfite and sulfate ions to produce calcium sulfite and calcium sulfate. These materials begin to precipitate out of solution when they exceed their solubility limits.

The main factors influencing the dissolution of the calcium carbonate are: the size and origin of the limestone, the pH of liquid phase and the sulfite ions concentration in the suspension. Flue gas desulphurization process is dependent on the solid used in the preparation of absorbent suspension. It is very important to know how natural materials can interact with sulfur dioxide dissolved in suspension.

Chemical composition of the limestone used in the present study was determined by classical analytical methods and presented in table 1.

Experimental kinetic curves obtained at the sulfur dioxide absorption in calcium carbonate slurries with different ratio solid/liquid are shown in figures 2-9.

Table 1. Composition of limestone

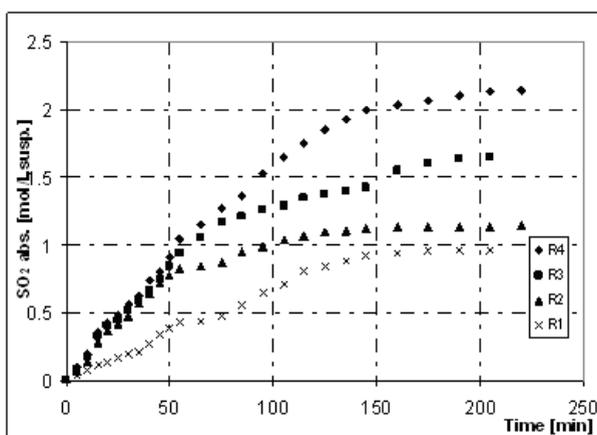| Carbonate source	Composition			
	$CaCO_3$ [%]	Fe_2O_3 [%]	Al_2O_3 [%]	SiO_2 [%]
Limestone Sănduleşti - Turda	97	1,8	0,88	0,3

Figure 2. Kinetic curves of sulfur dioxide absorption in calcium carbonate suspensions with different concentration at T=293 K
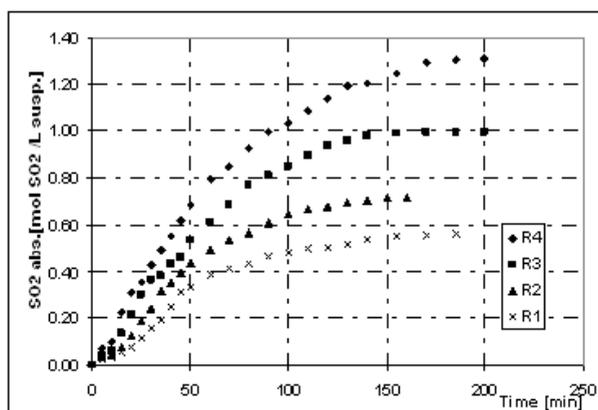

Figure 3. Kinetic curves of sulfur dioxide absorption in calcium carbonate suspensions with different concentration at T=303 K
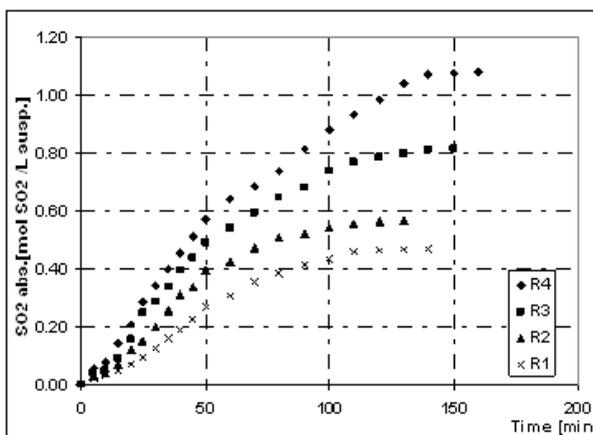
146

Figure 4. Kinetic curves of sulfur dioxide absorption in calcium carbonate suspensions with different concentration at T=313 K

From the plots shown in figures 2-4 it can be observed that the increase of the calcium carbonate content in the suspension, as refereed solid/liquid ration R, increases the sulfur dioxide absorption capacity. Experimental measurements of absorption process were made at four different rations: R: 1/30; 1/15; 1/10; and 1/7.5.
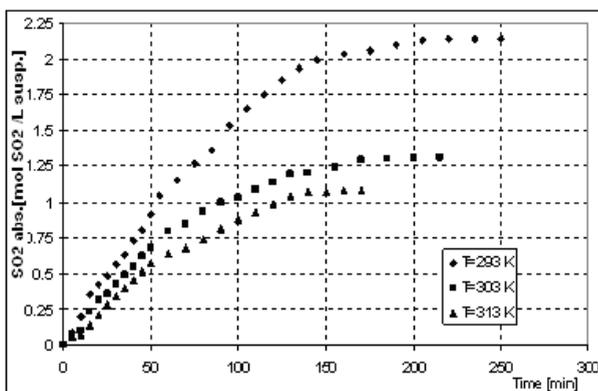

Figure 5. Temperature influence over sulfur dioxide absorption in calcium carbonate suspensions at R4

The absorption capacity increases from 0.9 mol SO_2/L slurry for ratio R1 = 1/30 to 2.14 mol SO_2/L slurry for R4 = 1/7.5, at a constant temperature of 293 K. The increase of absorption capacity with the increase of carbonate slurry content could be explained due to the higher concentration of Ca^{2+} in the slurries that leads to an increase in the internal Ca/S ratio and in the solid-liquid interface area.
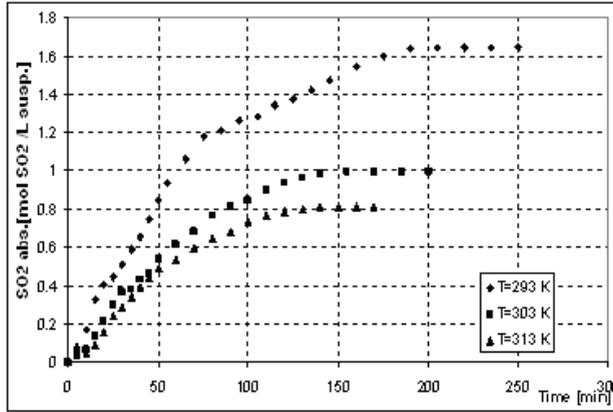
147

Figure 6. Temperature influence over sulfur dioxide absorption in
calcium carbonate suspensions at R3

From figures 5-8 it can be observed that the influence of temperature is significantly on the total absorption capacity. With the increase of temperature, the solubility of SO_2 in water decreases, and as result the absorption capacity decreases. In the same time the solubility of $CaCO_3$ increase only slightly with the temperature increase.
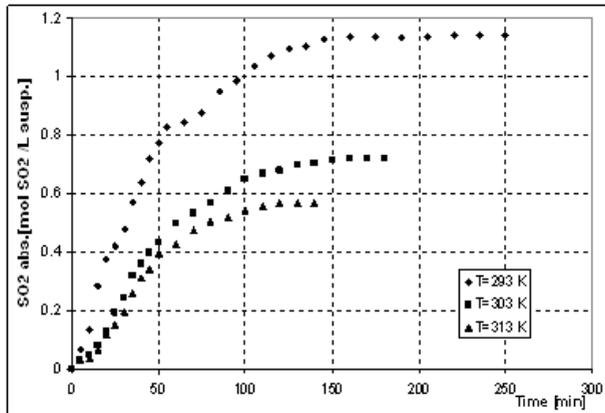

Figure 7. Temperature influence over sulfur dioxide absorption in
calcium carbonate suspensions at R2

Thus, at the highest content of carbonate slurry, R4 = 1/7. 5, the total absorption capacity is reduced from 2.14 mol SO_2/L slurry, at a temperature of 293 K, to 1.1 mol SO_2/L slurry, at 313 K.
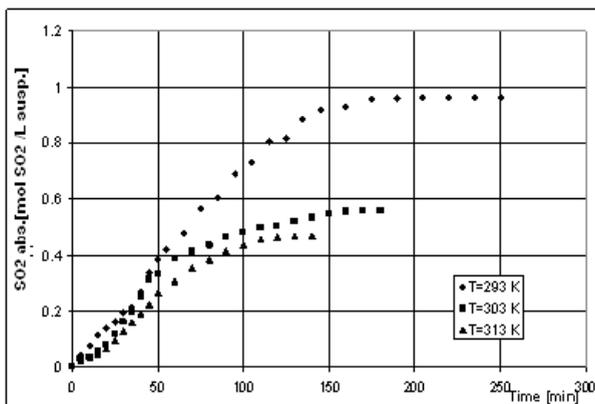
Figure 8. Temperature influence over sulfur dioxide absorption in calcium carbonate suspensions at R1

By diluted suspensions, R1 = 1/30, the absorption capacity reduces from 0.9 mol SO_2/L slurry, at 293 K, to 0.46 mol SO_2/L suspension, at 313 K.
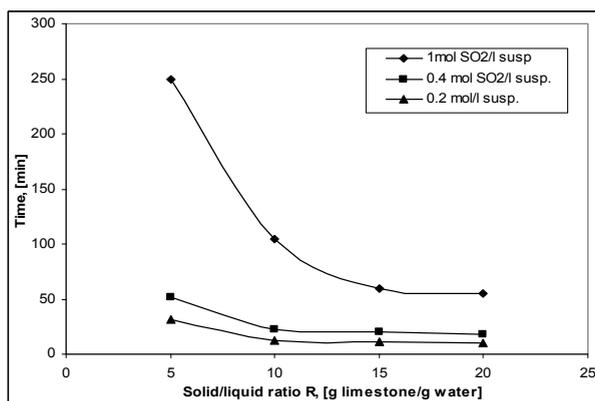
Figure 9. Influence of the solid/liquid ratio over the time necessary to achieve the sulfur dioxide concentration in reaction mass at T=273 K

From the figure 9 it can be observed that the increase of solid/liquid ration in the suspension, diminishes substantially the time needed to achieve the same concentration of sulfur dioxide in the reaction mass.

The differences between the total absorption capacities, considering the slurry content or/and temperature, imposes the setting of the macrokinetic mechanism and the developing of the mathematical model witch can describe the sulfur dioxide absorption process in calcium carbonate slurries.

EXPERIMENTAL SETUP

The experiments were carried out on a laboratory equipment. A schematic diagram of the experimental setup is shown in figure 2, with the essential element the absorber, a 0.75 L glass reactor with mechanical stirring. The supply system for sulfur dioxide and final gas neutralization system complet the experimentally setup.

To eliminate the possibility that the sulfur dioxide transfer through the gas phase becomes a limitative step of rate in the overall process, experimental measurements were made with pure sulfur dioxide from SO_2 cylinder. Stirring the suspension was adjusted so that the separating contact surface between aqueous suspension carbonate and gas phase was smooth, without waves generated by the moving slurry. Interface surface remained flat and steady. The gas which was not absorbed was continuously exhausted and neutralized in the hydroxide solution. The temperature has been controlled using an ultrathermostat. The absorption experiments have been performed at 293, 303 and 313 K with a constant rotation of the mechanical stirring (100 rot/min).
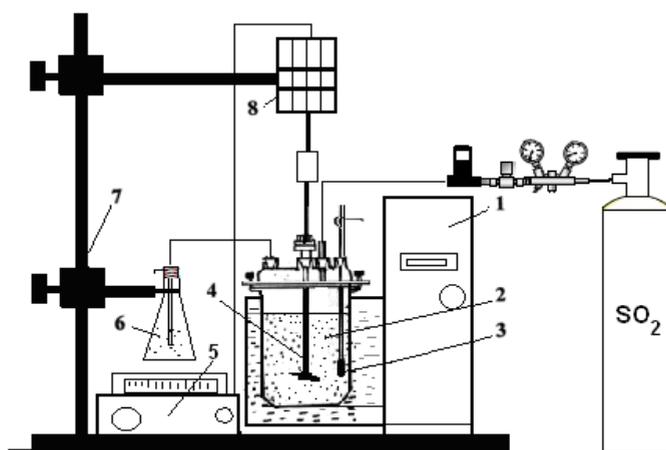
Figure 10. Schematic diagram of the experimental set-up
1 - ultrathermostat, 2 - absorber reactor with stirring, 3 - thermometer, 4 - stirrer,
5 - tachometer, 6 - vessel gas neutralization final, 7 - fixing support, 8 - mixer motor

Calcium carbonate powder with particle size $d_p<0.25$ mm was mixed in distilled water: 5, 10, 15 and 20 g $CaCO_3$/150 g water which corresponds to the ratio: $R_1=1/30$; $R_2= 1/15$; $R_3=1/10$ and $R_4= 1/7.5$.

The evolution of absorption process has been expressed by variation of the content of sulfur dioxide absorbed into the reaction volume, using iodometrical method.

CONCLUSIONS

New experimental data were obtained for the total absorption capacity of SO_2 in four limestone suspensions with different consistency.

The present study has been performed with limestone having a content of 97% $CaCO_3$, chemical reactivity being the main parameter to validate or not the use of the suspension carbonate in this process.

The experimental results demonstrate that the absorption capacity is influenced strongly by the slurry consistency. The total absorption capacity increases from 0.9 mol SO_2 /L slurry for ratio R1 = 1/30 to 2.14 mol SO_2 /L slurry for R4 = 1/7.5, at a temperature of 293 K.

The total absorption capacity is significantly influenced by temperature. With increase of temperature from 293 K to 313 K, the solubility of SO_2 decreases and the final absorption capacity in suspension is reduced to half.

The experimental research shows that the natural limestone having more than 97% $CaCO_3$ can be successfully used in the FGD processes.

REFERENCES

1. Kohl, A.L., Nielsen, R.B., "Gas Purification", Gulf Publishing Company, Houston, **1997**, chapter 7.

2. Astarita, G., Savage, D.W., Bisio, A., "Gas Treating with Chemical Solvents", Wiley, New York, **1983**, chapter 12.

3. Bravo, R.V., Camacho, R.F., Moya, V.M., Garcia, L.A.I., *Chemical Engineering Science*, **2002**, *57*, 2047.

4. Liu Shengyu, Xiao Wende, Liu Pei, Ye Zhixiang, *Clean*, **2008**, *36*, 482.

5. Pellner, P., Khandl, V., *Chem. Papers*, **2002**, *53*, 238.

6. Hongliang Gao, Caiting Li, Gaungming Zeng, Wei Zhang, Lin Shi, Shanhong Li, Yanan Zeng, Xiaopeng Fan, Qingho Wen and Xin Shu, *Energy Fuels*, **2010**, *24*, 4944.

7. Hongliang Gao, Caiting Li, Gaungming Zeng, Wei Zhang, Lin Shi, Shanhong Li, Yanan Zeng, Xiaopeng Fan, Qingho Wen, Xin Shu, *Separation and Purification Technology*, **2011**, *76*, 253.

SYNTHESIS OF SOME NEW DIALDEHYDES AND DIMETHANOLS INCORPORATING PHENOTHIAZINE UNITS

CRISTIAN VICTOR REŢE[a], ISTVAN-ZSOLT KOCSIS[a], ALEXANDRA FODOR[a], RALUCA TURDEAN[a], ION GROSU[a,*]

ABSTRACT. The synthesis of some new dialdehydes with 10*H*-phenothiazine units and of their corresponding dimethanols is reported. NMR investigations fully supported the assigned structures.

Keywords: *phenothiazine, dialdehydes, dialcohols, Suzuki cross-coupling reactions*

INTRODUCTION

Phenothiazine is an important electron rich nitrogen-sulphur heterocyclic motif with a broad pharmacological activity, the phenothiazine core being found in tranquilizers, antipyretics, antihelmitics, antituberculotics or antihistamines [1]. Phenothiazines possess good donor abilities, hence a low oxidation potential, forming easily radical cations [2]. Thus, the "butterfly" dynamic structure of the tricyclic phenothiazine skeleton becomes, upon oxidation to the radical cation, a rigid planar one [3].

In the recent years, due to its interesting electronic properties phenothiazine became intensively used as a redox active unit in material sciences [4], biology and biochemistry and as a marker for biochemical systems such as proteins or DNA [5]. Müller *et al* investigated and incorporated phenothiazine units in various systems like cruciform fluorophores [6], phenothiazophanes [7], molecular wires [8] and ligands for surface modification [9].

In previous works, we studied phenothiazine compounds possessing thioacetate or mercapto groups as adsorbates on gold surfaces [10]. Their behavior as ligands for SAMs formation was also investigated using computational methods [11].

We report herein the synthesis and structural assignment of some new dialdehydes and of their corresponding dimethanols incorporating phenothiazine units.

* Babeş-Bolyai University, Faculty of Chemistry and Chemical Engineering, 11 Arany Janos str., RO-400028 Cluj-Napoca, Romania
 * *igrosu@chem.ubbcluj.ro*

RESULTS AND DISCUSSIONS

Dialdehyde **2** was obtained starting from dibromophenothiazine **1** which first reacted in a lithium-bromine interchange, followed by the trapping of the dilithiated form of **1** with dimethylformamide as electrophile [12] (Scheme 1).
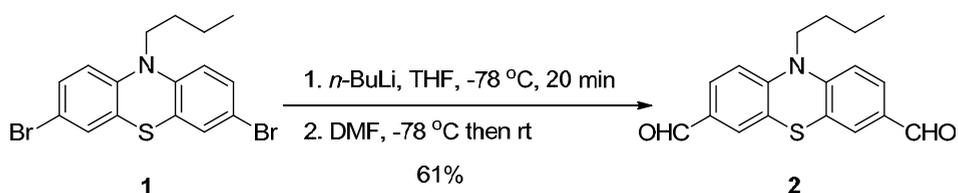
Scheme 1

The synthesis of dialdehydes **5** and **6** was accomplished by Suzuki cross-coupling reactions. Therefore, suitable phenothiazine pinacolyl boronic esters (**3** and **4**) [10, 13b] reacted with appropriate commercially available halogenated formyl derivatives under Suzuki cross-coupling conditions (potassium carbonate as a base, tetrakis(triphenylphosphine) palladium as the catalyst [13], and a mixture of dimethoxyethane and water as solvent) and gave dialdehydes **5** and **6** in fair to good yields (Scheme 2).
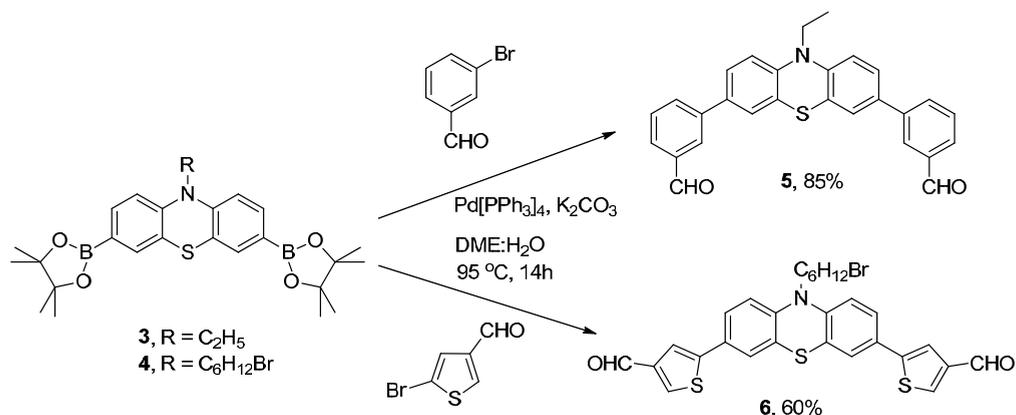
Scheme 2

The synthesized dialdehydes are suitable starting materials for the synthesis of dialcohols. By reducing the dialdehydes **2**, **5** and **6** with sodium borohydride in tetrahydrofurane, following a procedure adapted form the literature [14], the corresponding dimethanols **7**-**9** were obtained in good yields (Scheme 3).

154

NMR analyses fully confirmed the structure of targeted compounds **2**, **5**-**9**. Besides the normally expected signals of the phenothiazine core, the typical ^1H and ^{13}C resonances of formyl and hydroxymethyl groups were found throughout in the discussed series. These NMR data are collecterd in Table 1.
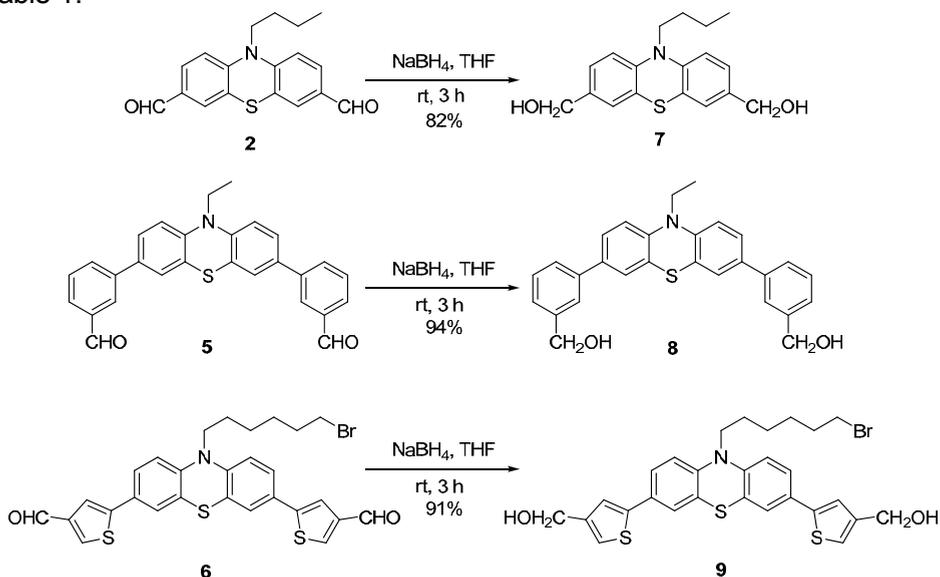
Scheme 3

Table 1. Relevant NMR data (DMSO-d_6, δ, ppm) for compounds **2** and **5-9**.

Compd.	^{1}H			^{13}C	
	C*H*O	C*H*$_2$OH	CH$_2$O*H*	CHO	CH$_2$OH
2	9.80	-	-	190.6	-
5	10.08	-	-	193.2	-
6	9.84	-	-	186.0	-
7	-	4.37	5.10	-	62.1
8	-	4.56	5.25	-	62.8
9	-	4.45	5.16	-	59.0

Upon reduction of the aldehydes with the formation of the corresponding dialcohols, the essential difference in the NMR spectra is the appearance of the signals corresponding to the alcohol group. The methylenic protons appear as dublet signals at 4.37 for **7**, 4.56 for **8** and 4.45 for **9** while the hydroxylic protons appear as triplet signals at 5.10, 5.25 and 5.16 respectively. The ^{13}C-NMR spectra of the alcohols exhibit also the characteristic shifts for the carbon atom in alcohol newly formed (62.1 for **7**, 62.8 for **8** and 59.0 for **9**).

CONCLUSIONS

New dialdehydes (**2**, **5** and **6**) with phenothiazine units were obtained in good yields (60-85 %) either by Suzuki cross-coupling reactions (**5** and **6**) or by DMF trapping by the corresponding dilithiated phenothiazine (**2**). The sodium borohydride reduction of the dialdehydes (**2**, **5** and **6**) furnished in good yields (82-94 %) the corresponding dimethanol derivatives (**7**-**9**).

EXPERIMENTAL SECTION

General

^{1}H NMR (300 or 400 MHz) and ^{13}C NMR (75 or 100 MHz) spectra were recorded in DMSO-d_6 on Bruker spectrometers. ESI MS were recorded on Agilent 6320 ion trap spectrometer in positive mode. Melting points were measured with Kleinfeld Apotec melting point apparatus and they are uncorrected. Thin layer chromatography (TLC) was carried out on aluminium sheets coated with silica gel 60 F_{254} using UV visualization.

Synthesis of derivative 2

A solution of 3,7-dibromo-10-*n*-buthyl-10*H*-phenothiazine (4 mmol) in dry tetrahydrofurane (50 mL) was cooled to -78 °C. Then *n*-BuLi (solution 2.5 M in hexane, 12.8 mmol) was added dropwise for 20 minutes. The reaction mixture was stirred 30 minutes at -78 °C and then dry dimethylfomamide (10 mmol) was added dropwise. After electrophile addition, the cooling bath was removed and the reaction mixture was let to reach the room temperature. Water (50 mL) and diethyl ether (100 mL) were added and the organic layer was separated. The aqueous phase was washed three times with small portions of diethyl ether (3x20 mL) and the combined organic layers were dried over sodium sulphate. After filtering, the solvents were removed in vacuo and the residue was chromatographed on silica gel (dichloromethane / pentane = 4 / 1) to yield 0.76 g (2.46 mmol, 61%) of **2** as an orange solid.

10-n-buthyl-3,7-diformyl-10H-phenothiazine 2. Orange solid, m.p. = 92.4 – 93.2 ºC, yield 61%. Calculated for $C_{18}H_{17}NO_2S$ (311.10): C, 69.43; H, 5.50; N, 4.50; S, 10.30. Found: C, 69.57; H, 5.41; N, 4.66; S, 10.42. ^{1}H NMR (300 MHz, DMSO-d_6, δ ppm): 0.87 (3H, t, *J* = 7.2 Hz), 1.40 (2H, m), 1.67 (2H, m), 3.99 (2H, t, *J* = 6.9 Hz), 7.22 (2H, d, J = 8.4 Hz), 7.60 (2H, d, *J* = 1.5 Hz), 7.73 (2H, dd, *J* = 8.4 Hz, *J* = 1.8 Hz), 9.80 (2H, s). ^{13}C NMR (75 MHz, DMSO-d$_6$, δ ppm): 13.4 (CH$_3$), 19.1 (CH$_2$), 28.0 (CH$_2$), 47.0 (CH$_2$), 116.3 (CH), 122.8 (C$_{quat.}$), 127.8 (CH), 130.1 (CH), 131.6 (C$_{quat.}$), 148.2 (C$_{quat.}$), 190.6 (CH).
MS (ESI) m/z = 312.3 [M+H]$^+$.

General procedure for synthesis of derivatives 5 and 6

Into a mixture of phenothiazine diboronic-diester (**3** or **4**, 2 mmol), potassium carbonate (20 mmol), the appropriate bromoaldehyde (*m*-bromo-benzaldehyde or 3-formyl-5-bromo-thiophene, 4.4 mmol) and solvents [dimethoxy-ethane / distilled water (2 : 1; 90 mL)] argon was purged for 20 minutes. Then, the catalyst tetrakis[triphenylphosphine] palladium (0.2 mmol) was added. The reaction mixture was refluxed for 14 hours. After cooling at room temperature, dichloromethane (200 mL), water (50 mL) and Na_2SO_3 oversaturated solution (50 mL) were added to the reaction mixture and the organic phase was separated. The aqueous layer was extracted three times with small amounts of dichloromethane (3x20 mL). The combined organic layers were dried over sodium sulphate, the solvents were removed in vacuo and the residue was chromatographied on silica gel (dichloromethane / pentane.= 4 / 1)

10-ethyl-3,7-bis(3'-formylphenyl)-10H-phenothiazine 5. Yellow solid, m.p. = 123.8-125.0 ºC, yield 85%. Calculated for $C_{28}H_{21}NO_2S$ (435.13): C, 77.21; H, 4.86; N, 3.22; S, 7.36. Found: C, 77.03; H, 4.75; N, 3.40; S, 7.48. ^{1}H NMR (400 MHz, DMSO-d_6, δ ppm): 1.36 (3H, t, *J* = 6.8 Hz), 4.01 (2H, q), 7.15 (2H, d, *J* = 8.4 Hz), 7.56 (2H, s), 7.60 (2H, d, *J* = 8.4 Hz), 7.66 (2H, t, *J* = 7.6 Hz), 7.84 (2H, d, *J* = 7.2 Hz), 8.00 (2H, d, *J* = 7.6 Hz), 8.19 (2H, s), 10.08 (2H, s). ^{13}C NMR (100 MHz, DMSO-d_6, δ ppm): 12.4 (CH$_3$), 41.2 (CH$_2$), 115.6 (CH), 122.9 (C$_{quat.}$), 124.9 (CH), 126.0 (CH), 127.3 (CH), 127.5 (CH), 129.7 (CH), 131.8 (CH), 132.9 (C$_{quat.}$), 136.7 (C$_{quat.}$), 139.5 (C$_{quat.}$), 143.5 (C$_{quat.}$), 193.2 (CH).
MS (ESI) m/z = 436.2 [M+H]$^+$.

10-(6'-bromohexyl)-3,7-bis(4''-formyl-thiophen-2''-yl)-10H-phenothiazine **6.** Yellow solid, m.p. = 49.1 – 51.0 ºC, yield 60%. Calculated for $C_{28}H_{24}BrNO_2S_3$ (581.02): C, 57.72; H, 4.15; N, 2.40; Br, 13.72; S, 16.51. Found: C, 57.61; H, 4.33; N, 2.27; Br, 13.88; S, 16.51. ^{1}H NMR (300 MHz, DMSO-d_6, δ ppm): 1.39 (4H, overlapped peaks), 1.67-1.77 (2H, overlapped peaks), 3.47 (2H, t, *J* = 6.6 Hz), 3.89 (2H, t, *J* = 6.6 Hz), 7.03-7.06 (2H, m), 7.51-7.53 (4H, overlapped peaks), 7.76 (2H, s), 8.53 (2H, s), 9.84 (2H, s). ^{13}C NMR (75 MHz, DMSO-d_6, δ ppm): 25.1 (CH$_2$), 25.8 (CH$_2$), 27.0 (CH$_2$), 32.0 (CH$_2$), 34.9 (CH$_2$), 46.5 (CH$_2$), 116.1 (CH), 119.4 (CH), 123.6 (C$_{quat.}$), 124.0 (CH), 125.2 (CH), 127.2 (C$_{quat.}$), 137.7 (CH), 143.4 (C$_{quat.}$), 143.9 (C$_{quat.}$), 144.3 (C$_{quat.}$), 186.0 (CH).
MS (ESI) m/z = 582.2 [M+H]$^+$.

General procedure for synthesis of derivatives 7-9

A solution of dialdehyde (**2**, **5** or **6**; 1 mmol) in 40 ml THF was added dropwise to a suspension of NaBH$_4$ (7 mmol) in water (20 mL). The reaction mixture was stirred for 3h at room temperature and then poured in a 1 / 1 mixture of water and ethyl acetate (200 mL). The organic layer was separated and the aqueous phase was extracted three times more with small portions

of ethyl acetate (3x20mL). The combined organic layers were dried over MgSO$_4$. The solvents were evaporated *in vacuo* and the residue was purified by column chromatography (ethyl acetate / pentane = 1 / 2).

10-n-buthyl-3,7-bis(hydroxymethyl)-10H-phenothiazine **7.** Yellow solid, m.p. = 92.4-93.2ºC, yield 82 %. Calculated for C$_{18}$H$_{21}$NO$_2$S (315.13): C, 68.54; H, 6.71; N, 4.44; S, 10.17. Found: C, 68.39; H, 6.54; N, 4.31; S, 10.02. ^{1}H NMR (300 MHz, DMSO-d$_6$, δ ppm): 0.85 (3H, t, *J* = 7.5 Hz), 1.56 (2H, m), 1.63 (2H, m), 3.83 (2H, t, *J* = 6.6 Hz), 4.37 (4H, d, *J* = 5.7 Hz), 5.1 (2H, t, J = 5.7 Hz), 6.93-6.95 (2H, overlapped peaks), 7.06-7.12 (4H, overlapped peaks). ^{13}C NMR (75 MHz, DMSO-d$_6$, δ ppm): 13.6 (CH$_3$), 19.3 (CH$_2$), 28.3 (CH$_2$), 46.0 (CH$_2$), 62.1 (CH$_2$), 115.2 (CH), 123.1 (C$_{quat.}$), 125.2 (CH), 125.8 (CH), 136.5 (C$_{quat.}$), 143.4 (C$_{quat.}$).

MS (ESI) m/z = 316.1 [M+H]$^+$.

10-ethyl-3,7-bis(3'-hydroxymethylphenyl)-10H-phenothiazine **8.** White solid, m.p. = 149.6- 151.5 ºC, yield 94 %. Calculated for C$_{28}$H$_{25}$NO$_2$S (439.16): C, 76.51; H, 5.73; N, 3.19; S, 7.29. Found: C, 76.68; H, 5.52; N, 3.02; S, 7.44. ^{1}H NMR (400 MHz, DMSO-*d$_6$*, δ ppm): 1.36 (3H, t, *J* = 6.4 Hz), 3.95 (2H, q), 4.56 (4H, d, *J* = 5.6 Hz), 5.25 (2H, t, J = 5.6 Hz), 7.07 (2H, d, *J* = 8.4 Hz), 7.27 (2H, d, *J* = 7.2 Hz), 7.37 (2H, t, *J* = 7.0 Hz), 7.43 (2H, s), 7.48 (4H, d, *J* = 8.4 Hz), 7.57 (2H, s). ^{13}C NMR (75 MHz, DMSO-*d$_6$*, δ ppm): 12.5 (CH$_3$), 41.1 (CH$_2$), 62.8 (CH$_2$), 115.5 (CH), 122.8 (C$_{quat.}$), 123.9 (CH), 124.2 (CH), 124.7 (CH), 125.1 (CH), 125.7 (CH), 128.6 (CH), 134.3 (C$_{quat.}$), 138.5 (C$_{quat.}$), 143.16 (C$_{quat.}$), 143.19 (C$_{quat.}$).
MS (ESI) *m/z* = 440.3 [M+H]$^+$

10-(6'-bromohexyl)-3,7-bis(4''-hydroxymethyl-thiophene-2''yl)-10H-phe-nothiazine **9.** Green solid, m.p.=110.9-112.5 ºC, yield 91%. Calculated for C$_{28}$H$_{28}$BrNO$_2$S$_3$ (585.05): C, 57.33; H, 4.81; N, 2.39; Br, 13.62; S, 16.40. Found: C, 57.51; H, 4.69; N, 2.26; Br, 13.48; S, 16.51. ^{1}H NMR (300 MHz, DMSO-*d$_6$*, δ ppm): 1.39-1.40 (4H, overlapped peaks), 1.68-1.77 (2H, overlapped peaks), 3.47 (2H, t, *J* = 6.6 Hz), 3.86 (2H, t, *J* = 6.6 Hz), 4.45 (4H, d, *J* = 5.7 Hz), 5.16 (2H, t, *J* = 5.7 Hz), 7.02 (2H, d, *J* = 8.4 Hz), 7.21 (2H, s), 7.33 (2H, s), 7.38-7.43 (4H, overlapped peaks), 7.76 (2H, s), 8.53 (2H, s), 9.84 (2H, s). ^{13}C NMR (75 MHz, DMSO-*d$_6$*, δ ppm): 25.1 (CH$_2$), 25.8 (CH$_2$), 27.0 (CH$_2$), 32.1 (CH$_2$), 34.9 (CH$_2$), 46.4 (CH$_2$), 59.0 (CH$_2$), 116.0 (CH), 119.8 (CH), 122.6 (CH), 123.4 (CH), 123.5 (C$_{quat.}$), 124.5 (CH), 128.5 (C$_{quat.}$), 142.1 (C$_{quat.}$), 143.3 (C$_{quat.}$), 145.6 (C$_{quat.}$).
MS (ESI) *m/z* = 586.1 [M+H]$^+$

ACKNOWLEDGEMENTS

158

REFERENCES

[1]. (a) F. Mietzsch, *Angew. Chem.,* **1954**, *66*, 363. (b) C. Bodea, I. Silberg, *Adv. Heterocycl. Chem.,* **1968**, *9*, 321.

[2]. L.A. Tinker, A.J. Bard, *J. Am. Chem. Soc.,* **1979**, *101*, 2316.

[3]. J.D. Dell, J.F. Blount, O.V. Briscoe, H.C. Freeman, *Chem. Commun.,* **1968**, 1656.

[4]. S.K. Kim, J.-H. Lee, D.-H. Hwang, *Synthetic Metals,* **2005**, *152*, 201.

[5]. C. Wagner, H.-A. Wagenknecht, *Chem. Eur. J.,* **2005**, *22*, 1871.

[6]. M. Hauck, J. Schönhaber, A.J. Zucchero, K.I. Hardcastle, T.J.J. Müller, U.H.F. Bunz, *J. Org. Chem.,* **2007**, *72*, 6714.

[7]. (a) P. Rajakumar, R. Kanagalatha, *Tetrahedron Lett.,* **2007**, *48*, 8496. (b) K. Memminger, T. Oeser, T.J.J. Müller, *Org. Lett.,* **2008**, *10*, 2797.

[8]. M. Sailer, A.W. Franz, T.J.J. Müller, *Chem. Eur. J.,* **2008**, *14*, 2602.

[9]. A.W. Franz, S. Stoycheva, M. Himmelhaus, T.J.J. Müller, *Beilstein J. Org. Chem.,* **2010**, *6*,1.

[10]. R. Turdean, E. Bogdan, A. Terec, A. Petran, L. Vlase, I. Turcu, I. Grosu, *Centr. Eur. J. Chem.,* **2009**, *7*, 111.

[11]. A. Bende, I. Grosu, I. Turcu, *J. Phys. Chem. A,* **2010**, *114*, 12479.

[12]. S. Ebdrup, *Synthesis,* **1998**, *8*, 1107.

[13]. (a) N. Miyaura, A. Suzuki, *Chem. Rev.,* **1995**, *95*, 2457. (b) M. Sailer, R.-A. Gropeanu, T.J.J. Müller, *J. Org. Chem.,* **2003**, *68*, 7509.

[14]. (a) K. Thakkar, R.L. Geahlen, M. Cushman, *J. Med. Chem.,* **1993**, *36*, 2950. (b) R.A. Gropeanu, PhD Thesis, Babes-Bolyai University, Cluj-Napoca, Romania, **2005**.

CARBON PASTE ELECTRODE INCORPORATING A SYNTHETIC ZEOLITE EXCHANGED WITH Fe(III) FOR AMPEROMETRIC DETECTION OF ASCORBIC ACID

ALYNE LEBORGNE[a], LIANA MARIA MUREŞAN[b,*]

ABSTRACT. A new modified electrode was obtained by incorporating a synthetic zeolite exchanged with Fe(III) in carbon paste. The electrochemical behavior of the modified electrode (Fe13X-CPE) was investigated using cyclic voltammetry. The modified electrode was successfully tested for electrocatalytic oxidation of ascorbic acid (AA) in phosphate buffer (pH 7.0), at an applied potential of +0,15 V *vs.* Ag/AgCl/KCl$_{sat}$. The amperometric sensor for ascorbic acid was characterized by a linear concentration range of 0,05 mM to 0,4 mM AA The theoretical detection limit, calculated from the slope of the regression equation and standard deviation of the calibration curve, was $5.8 \cdot 10^{-5}$ M.

Keywords: ascorbic acid, electrocatalytic oxidation; Fe-exchanged zeolite; modified carbon paste electrode.

INTRODUCTION

One of the most flexible ways to obtain chemically modified electrodes with zeolites is their incorporation in carbon paste [1]. Carbon paste electrodes (CPEs) are popular because they are easily obtainable at minimal costs and are especially suitable for preparing an electrode material modified with admixtures of various compounds, thus giving the electrode certain pre-determined properties. Other advantages of CPEs are low background current, wide potential window and versatility.

Zeolite-modified carbon paste electrodes (ZME-CPEs) keep all these advantages, and in addition, they exhibit a number of chemical, physical and structural characteristics of high interest in the design of electroanalytical systems: shape, size and charge selectivity, physical and chemical stability, high ion-exchange capacity and hydrophilic character due to the presence of zeolites [2,3].

---

[a] IUT Rouen, France
[b] "Babes-Bolyai" University, Department of Physical Chemistry, 11, Arany J. St., 400028 Cluj-Napoca, Romania
[*] Corresponding author: *limur@chem.ubbcluj.ro*

Among the chemical species that can be determined by using ZME-CPEs, ascorbic acid (AA), known also as Vitamin C, is of particular interest, due to the fact that it is playing a key role in living bodies, being an antioxidant that protects cells against damage by free radicals, which are reactive by-products of normal cell activity. This is the reason why L-Ascorbic acid is widely used as a dietary supplement and is also added to manufacture foods as an antioxidant for preservation [4]. Consequently, measuring ascorbic acid content is very important for assessing food product quality.

Electrochemical methods for AA determination are based on different amperometric [5-9] potentiometric [10,11], and voltammetric [12-14] sensors, or on the use of biosensors [15-21]. Among these methods, those based on the utilization of zeolite modified electrodes have attracted much of attention, due to the fact that several mediators can be easily immobilized in the zeolitic matrix. For example, carbon paste electrodes incorporating synthetic zeolites modified with Methylene blue [22] and sensors in which a Fe(III) exchanged zeolite Y is dispersed on the surface of glassy carbon were successfully used for AA detection [23].

In this context, a new sensor incorporating a synthetic mesoporous zeolite (13X, Aldrich) exchanged with Fe ions embedded in a carbon paste matrix was designed and tested for ascorbic acid amperometric detection. The proposed AA sensor possesses high sensitivity and operational stability due to the strong affinity between zeolite and iron(III) and to the efficient immobilization technique.

RESULTS AND DISCUSSIONS

Electrochemical characteristics of Fe13X-CPEs

The presence of Fe(III) ions in the matrix of the carbon paste electrodes was put on evidence by cyclic voltammetry in the potential range from -200 at +1000 mV $vs.$ Ag|AgCl/KCl$_{sat}$ (Figure 1).

As can be seen, in the case of Fe13X-CPE, a well-defined peak pair was observed on the cyclic voltammograms, with the formal standard potential ($E^{0'}$) at about 100 mV. The peak pair was attributed to the reduction / oxidation of Fe(III) ions embedded in the zeolitic matrix.

The peak separation, ΔE_p, was found to be 45 mV at a scan rate of 50 mV/s, and increases with the scan rate (results not shown) indicating a quasi-reversible redox process. This is an indication that the kinetic of electron transfer on the electrode surface is not very fast, as consequence of the nature of the matrix, whose resistance is considerable [5].
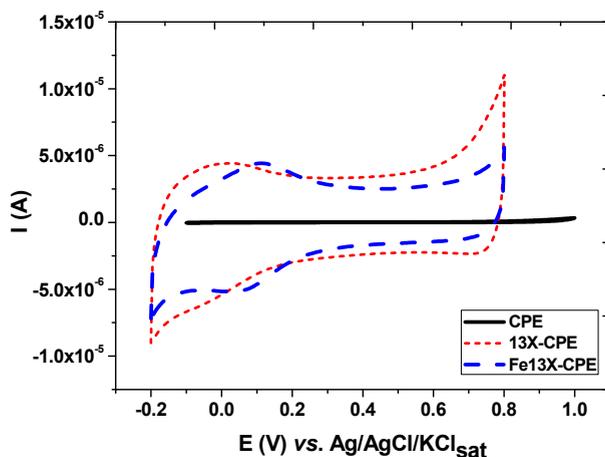
Figure 1. Cyclic voltammograms forFe13X-CPE. Experimental conditions: potential scan rate, 10 mV s^{-1}; supporting electrolyte, 0.1 M phosphate buffer, pH 7.0.

The cyclic voltammograms, recorded in a wide range of potential scan rates (0.01–1.6Vs^{-1}) for two pH values presented a linear dependence of peak current intensities (I_p) on scan rate (v). The slopes of log I *vs.* log v dependencies were close to the theoretical value 1, confirming the immobilization of the redox species generating the electrode response, (the Fe ions) on the electrode surface (Figure 2). As expected, the pH does not influence the electrochemical response of the Fe(III) / Fe(II) redox couple.
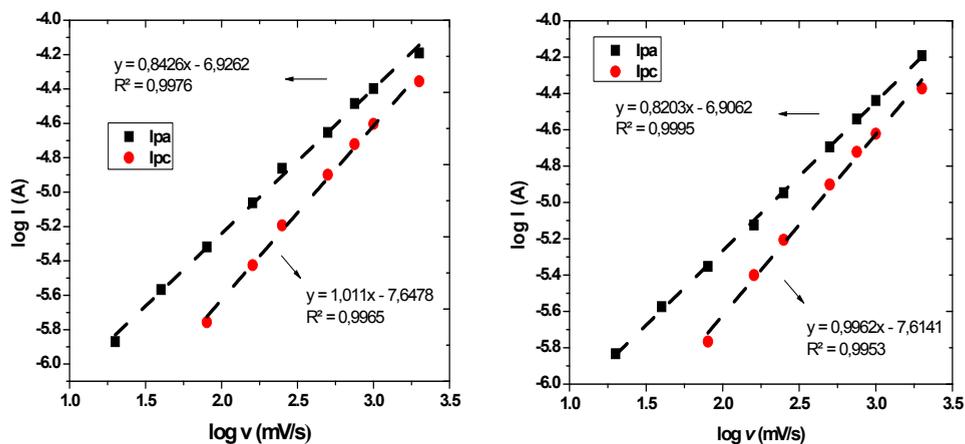

Figure 2. LogI *vs.* log v dependencies for Fe13X-CPE. Experimental conditions: supporting electrolyte, 0.1 M phosphate buffer, pH 7 (left) and pH 3 (right).

Electrocatalytic oxidation of ascorbic acid

The cyclic voltammograms recorded in 0.1 M phosphate buffer pH 7 at Fe13X-CPE in the presence of different concentrations of AA are depicted in Figure 3. As it can be observed, when AA is present, the anodic current strongly increases and the oxidation potential of peak 1 (corresponding to the catalytic oxidation of AA on the Fe-exchanged zeolite) is much lower than peak 2 corresponding to AA oxidation on unmodified carbon paste (Figure 3b), indicating the existence of an electrocatalytic effect. The reason is a chemical interaction between AA and iron(III) loaded in the zeolite.
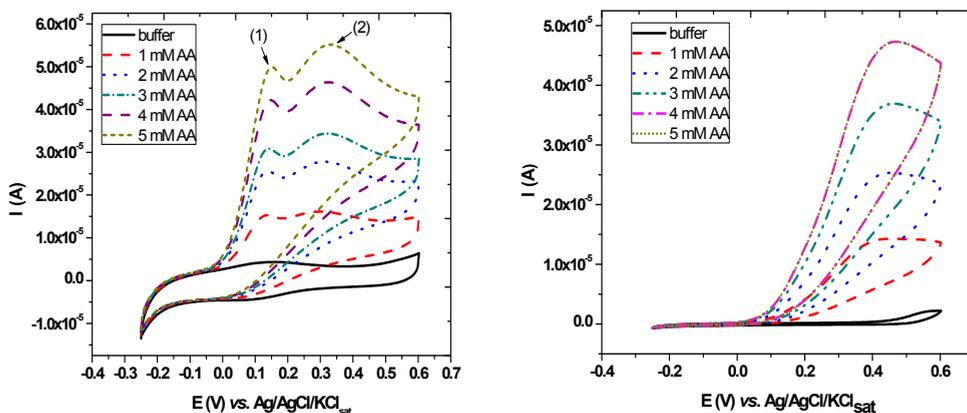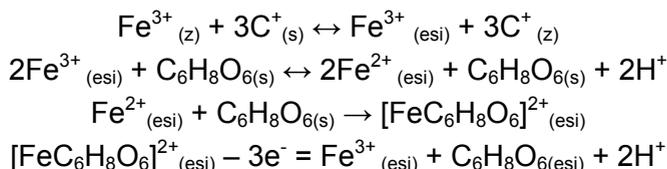

Figure 3. Cyclic voltammograms obtained at Fe13X-CPE in the absence and in the presence of different concentrations of AA on Fe13X-CPE (a) and on unmodified CPE (b). Experimental conditions: potential scan rate, 50 mVs^{-1}; starting potential, -250 mV vs. Ag|AgCl/KCl$_{sat}$; supporting electrolyte, 0.1 M phosphate buffer, pH 7.0.

For peak 1, the reaction taking place at the electrode-solution interface (esi) and into the zeolite modified electrode (z) can be written as follows [23]:

$$Fe^{3+}_{(z)} + 3C^+_{(s)} \leftrightarrow Fe^{3+}_{(esi)} + 3C^+_{(z)}$$
$$2Fe^{3+}_{(esi)} + C_6H_8O_{6(s)} \leftrightarrow 2Fe^{2+}_{(esi)} + C_6H_8O_{6(s)} + 2H^+$$
$$Fe^{2+}_{(esi)} + C_6H_8O_{6(s)} \rightarrow [FeC_6H_8O_6]^{2+}_{(esi)}$$
$$[FeC_6H_8O_6]^{2+}_{(esi)} - 3e^- = Fe^{3+}_{(esi)} + C_6H_8O_{6(esi)} + 2H^+$$

where C stands for a cation present in the buffer solution (s) and H$^+$ is originating from the zeolite matrix.

Batch amperometric measurements at constant applied potential (+0,15 V vs. Ag|AgCl/KCl$_{sat}$.) proved that Fe13X-CPE works well as amperometric sensor for AA. The reproducibility of the electrocatalytic effect of Fe13X-CPE

164

was confirmed by repetitive amperometric measurements (~ 3 measurements). A typical example of stable and fast amperometric response to successive injections of 500 µL 10^{-4} M AA is presented in Figure 4A and the resulting calibration curve, in Figure 4B.

The response time of the sensor is relatively short (~ 25s). As can be observed, the relationship between the steady-state current and the concentration of AA was linear in the range from 0.05 mM and 0.4 mM and the sensitivity, calculated as the slope of the calibration curve, was $6,9.10^{-3}$ A / M. The detection limit, calculated from the slope of the linear portion of the calibration curve (b) and the standard deviation (σ) with the formula (3σ/b) was $5,8.10^{-5}$ M. The analytical parameters of the Fe(III)-zeolite modified carbon paste electrodes are similar to those of other AA sensors reported in the literature [23].
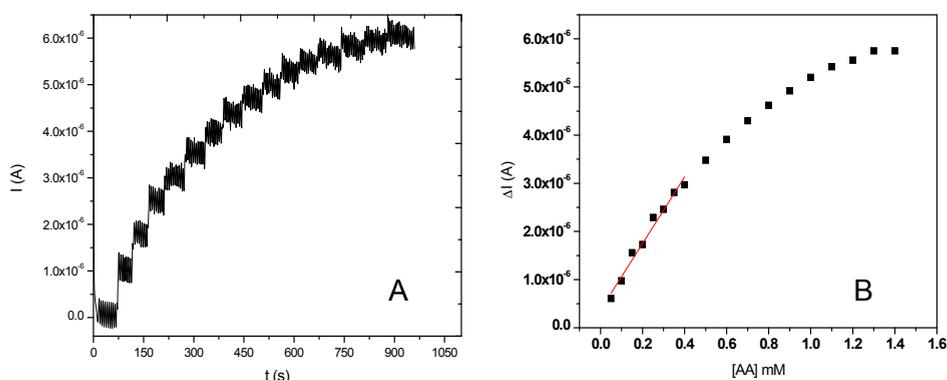

Figure 4. Amperometric response to successive increments of 500 µL 10^{-4} M AA (A) and the calibration curve for AA (B) at Fe13X-CPEs. Experimental conditions: applied potential, +0,15 V *vs.* Ag|AgCl/KCl$_{sat.}$; supporting electrolyte, 0.1 M phosphate buffer, (pH 7.0), dearated solution; magnetic stirring.

In a next step, by using Fe13X-CPE, AA was determined in a real sample, by using the standard addition method (Figure 5).

For this purpose, one tablet (0.5846 g) of a pharmaceutical product (Propolis C) was dissolved in 20 ml distilled water. Three successive additions of 500 µl solution containing Propolis C, followed by three additions of 500 µl standard solution 5.10^{-3}M AA were performed in 10 ml phosphate buffer (pH 7) and the resulting current was recorded using Fe13X-CPE (Figure 5 A) at a constant potential value (+0.15 V *vs.* Ag/AgCl/ AgCl$_{sat}$).

From the I = f(c$_{AA}$) dependence, the unknown concentration of AA in the sample was determined by extrapolation (c$_{AA}$ =4.3 10^{-3} M). Taking into account the dilution factor, 100.97 mg AA were found in a tablet, which is a very satisfactory result if compared to the content declared by the producer (100 mg AA / tablet).
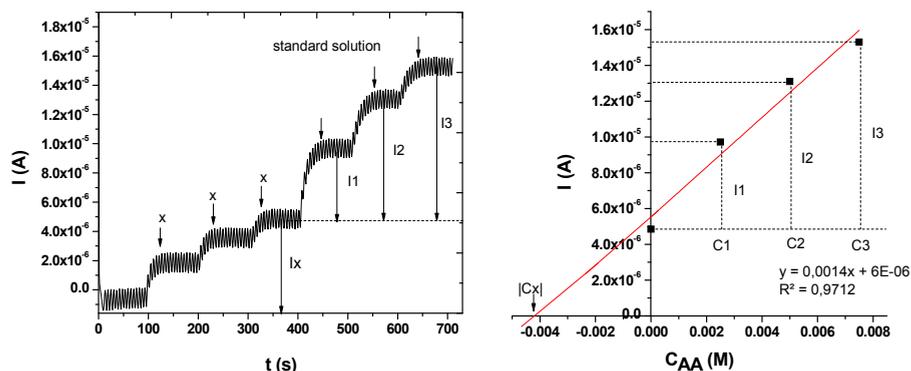
Figure 5. Standard addition method applied for determining AA concentration in a real sample (Propolis C). Experimental conditions: see Fig.4

CONCLUSION

A new electrode based on synthetic mesoporous zeolite modified with Fe(III) incorporated in carbon paste was obtained and characterized. The modified electrodes presented good electrocatalytic effect toward ascorbic acid oxidation in neutral aqueous solution, at an overpotential with more than 500 mV lower than that observed on unmodified electrodes. The Fe13X-CPEs offer the advantages of easy fabrication and cleaning, fast response time, high sensitivity, a low background current and detection limit, which are suitable for routine determinations.

EXPERIMENTAL SECTION

Chemicals

The 13X type zeolite, $1Na_2O:1Al_2O_3:2.8\pm0.2\ SiO_2 \times H_2O$ (particle size, 3-5μ; pore diameter, 10 Å; specific surface area 548.69 m^2/g; bulk density 480.55 kg/m^3; Si/Al ratio 1.5) was purchased from Aldrich (Germany).

Ascorbic acid (AA) was purchased from Sigma (SUA), $K_2HPO_4 \cdot 2H_2O$ and $KH_2PO_4 \cdot H_2O$ were purchased from Merck (Darmstadt, Germany). All other reagents were of analytical grade and used as received.

The supporting electrolyte was a 0.1 M phosphate buffer solution. The pH was adjusted in the interval 3-7 using appropriate H_3PO_4 or NaOH solutions.

Electrode preparation

The carbon paste was prepared by thoroughly mixing of 50 mg graphite powder with 60 μl paraffin oil (Fluka) until homogenization.

166

In parallel, a 0.01M $FeCl_3$ aqueous solution was purged with N_2 for 30 minutes. 1 g of NaY zeolite was lightly ground and immersed to 250 mL 0.01M $FeCl_3$ solution for 24 h. The modified zeolite was filtered, carefully washed with pH 2 HCl to remove occluded material and surface-adherent salt, and then washed with doubly distilled water till free of Cl^- ions. Finally, the Fe(III) exchanged zeolite was dried in air.

For the preparation of the carbon paste electrode incorporating the modified zeolite (Fe13X-CPEs), 25 mg of the modified zeolite were mixed with 25 mg carbon paste and then incorporated in a cylindrical tube (3 mm inner diameter and 5 cm length). The electrode surface was finally polished on paper.

The preparation of Fe13X-CPEs was reproducible when the experimental conditions and variables were maintained constant during the preparation period. The current response of the electrodes did not change significantly by storing them in air for several days.

Electrochemical measurements

Electrochemical experiments were carried out using a typical three-electrode electrochemical cell. The modified carbon paste electrode was used as working electrode, a platinum ring as counter electrode and an $Ag|AgCl/KCl_{sat}$ as reference electrode.

Cyclic voltammetry experiments were performed on a PC-controlled electrochemical analyzer (Autolab-PGSTAT 10, EcoChemie, Utrecht, The Netherlands).

Batch amperometric measurements at different AA concentrations were carried out at an applied potential of 0.15 V *vs.* $Ag|AgCl/KCl_{sat}$, under magnetic stirring, using 0.1 M phosphate buffer solution (pH 7) as supporting electrolyte. The current-time data were collected using the above-mentioned electrochemical analyzer.

REFERENCES

1. A. Walcarius*, Analytica Chimica Acta* **1999**, *384*, 1-8.

2. D.R. Rolison, R.J. Nowak, T.A. Welsh, C.G. Murray, *Talanta,* **1991**, *38*, 27-35.

3. J. Lipkowski, P. Ross, "The Electrochemistry of Novel Materials", VCH Publishers Inc., New York, **1994**.

4. J.C. Bauernfeind, D.M. Pinkert, "Ascorbic Acid as an Added Nutrient to Beverage", Hoffmann-La Roche, Basel, **1970**, 24-28.

5. M. Arvand, Sh. Sohrabnezhad, M.F. Mousavi, *Analytica Chimica Acta,* **2003**, *491*, 193-201.

6. Y. Sha, L. Qian, Y. Ma, H. Bai, X. Yang, *Talanta,* **2006**, *70,* 556-560.

7. I. Jureviciute, K. Brazdziuviene, L. Bernotaite, B. Salkus, A. Malinauskas, *Sensors & Actuators B,* **2005**, *107*, 716-721.

8. T.R.L.C. Paixao, D. Lowinsohn, M. Bertotti, *Journal of Agricultural and Food Chemistry,* **2006**, *54*, 3072-3077.

9. J. Wu, J. Suls, W. Sansen, *Electrochemistry Communications,* **2000**, *2*, 90-93.

10. K. Wang, J.J. Xu, K.S. Tang, H.Y. Chen, *Talanta,* **2005**, *67*, 798-805.

11. J.C.B. Fernandes, L. Rover jr., L.T. Kubota, G. de Oliveira Neto, *Journal of the Brazilian Chemical Society*, **2000**, *11(2),* 182-186.

12. M. Petersson, *Analytica Chimica Acta,* **1986**, *187*, 333-338.

13. V.S. Iijeri, P.V. Jaiswal, A.K. Srivastava, *Analytica Chimica Acta,* **2001**, *439,* 291-297.

14. P.F. Huang, L. Wang, J.Y. Bai, H.J. Wang, Y.Q. Zhao, S.D. Fan, *Microchimica Acta,* **2007**, *157*, 41-47.

15. R. Kirk, R. Sawyer, Pearson's "Composition and Analysis of Food", 9th ed. Longman, Harlow, UK, **1991**.

16. S.P. Sood, L.E. Sartori, D.P. Wittmer, W.G. Haney, *Analytica Chimica Acta,* **1976***, 48(6)*), 796-798.

17. B. Tang, Y. Wang, M. Du, J. Ge, Z. Chen, *Journal of Agricultural and Food Chemistry,* **2003**, *51,* 4198-4201.

18. A.J. MacLeod, *"*Instrumental Methods of Food Analysis", Elek Science, London*,* **1973***, 247*, 374.

19. H. Dai, X.P. Wu, Y.M. Wang, W.C. Yhou, G.N. Chen, *Electrochimica Acta,* **2008***, 53(16),* 5113-5117.

20. E. Akyilmaz, E. Dinckaya, *Talanta*, **1999**, *50*, 87-93.

21. I.N. Tomita, A. Manzoli, F.L. Fertonani, H. Yamanaka, *Eclética Química,* **2005**, *30*, 37-43.

22. C. Varodi, D. Gligor, L.M. Muresan, *Studia UBB Chemia*, **2007**, *52*(1), 109-118.

23. Y. Jiang, M. Zou, K. Yuan, H. Xu, *Electroanalysis,* **1999**, *11(4)*, 254-259.

NUMERICALLY MODELLING THE O$_3$/UV ADVANCED OXIDATION REACTORS BY USING THE COMPUTATIONAL FLUID DYNAMICS METHOD

SORIN CLAUDIU ULINICI[a,*], GRIGORE VLAD[a], BOGDAN HUMOREANU[a], SIMION AŞTILEAN[b]

ABSTRACT. The O$_3$/UV advanced oxidation processes constitute physical-chemical processes recently used as efficient processes of degrading the organic substances and for disinfection purposes within the water treatment and purging technologies. Technically speaking, the O$_3$/UV advanced oxidation systems involve two kinds of distinct processes: the gas/liquid (O$_3$/aqueous solution) transfer, which is a distinct physical step, and the transfer of the ultra-violet radiation photons transfer (λ<310 nm) into the solution and the initiation of a chain of reactions leading both to direct photodegradation processes and to highly reactive OH^o radicals species generation processes. This work suggests the elaboration of a numerical template for the advanced oxidation reactors (O$_3$/UV) based on the CFD (Computational Fluid Dynamics) method, by using the FEM (Finite Element Method) for numerically solving the differential equations systems. This template may constitute both the basis for the elaboration of designing methods in the field of water treatment equipment engineering and the modelling basis for studying more complex advanced oxidation systems, which include heterogeneous photocatalysis processes.

Keywords: *Computational Fluid Dynamics, advanced oxidation, numerical modeling, ozone photolysis*

INTRODUCTION

The classical procedures of removing micro-pollutants from water, and the disinfection processes involve the utilisation of certain oxidising agents or of certain physical agents that generate the degradation of theses pollutants. It is about processes that use the chlorine freed by various compounds thereof, by the ozone or peroxide oxidation or by the UV radiation action. All these procedures, applied separately, have disadvantages linked to slow degradation (or to the absence of degradation) in case of certain compounds, or to the generation of certain secondary reaction compounds (such as the trihalomethanes – in case of the chlorine utilisation). It is in this

[a] S.C. ICPE Bistrita S.A., Str. Parcului, Nr.7, RO-420035 Bistrita, Romania, *sorin_ulinici@icpebn.ro*
[b] Babes-Bolyai University, Faculty of Physics, Institute for Interdisciplinary Research in Bioanoscience, Nanobiophotonics Center, T. Laurian 42, 400271 Cluj-Napoca, Romania

context that the necessity of developing new highly yielded and highly efficient degradation and mineralisation (in case of the organic substances) unselective physical-chemical processes have appeared [1]. The advanced oxidation processes (AOP) fall into this category, as they have been intensively studied and investigated this last decade [11].

The advanced oxidation processes are deemed to be those processes that lead to the oxidative, unselective and energetic degradation of the organic and inorganic substances in the presence of the highly reactive OH^o radical species. These processes are physical-chemical ones, which include both the OH^o radicals generation stage and the reaction products reaction and removal steps. There is a whole diversity of physical and chemical processes that lead to the generation of the OH^o free radicals in an aqueous environment. We can talk about the action of the low temperature plasmas (cold plasmas), about processes of decomposing the O_3 in an aqueous environment, catalytic ozonisation processes [3], advanced oxidation processes in O_3/UV (the ozone photolysis) [7], H_2O_2/UV, H_2O_2/O_3, $H_2O_2/O_3/UV$ systems, about Fenton processes, heterogeneous photocatalysis processes, about the electro-hydraulic cavitation and sonolysis, about processes of super-critically oxidising water, about the action of the γ radiation and of the cathode beams. The use of the advanced oxidation processes for water treatment involve both scientifically knowing the involved phenomena and mechanisms and the capability of designing and implementing such processes at a real scale. In this context, this work here approaches, from the theoretical standpoint and from the numerical modelling one, the O_3/UV advanced oxidation processes in photolysis reactors, this approach being a continuation of certain previous steps related to the modelling of the O_3/UV advanced oxidation systems by using numerical templates elaborated in conformity with certain software environments strictly dedicated to the hydraulic systems, by using experimental data obtained by the exploitation of a pilot station [16]. The numerical modelling involved the use of concepts and methods taken from Computational Fluid Dynamics (**CFD)**, by using the Navier-Stokes equation systems, combined with physical and chemical templates linked to processes of energetically transferring the UV radiation, to convection, diffusion and reaction [17]. The finite element method (FEM) was used for solving the equation systems with partial differentials and limit conditions [15], with an aim to depict the physical and chemical phenomena involved, by using the **Comsol Multiphysics 3.5** software environment [5] .

RESULTS AND DISCUSSION

The physical and numerical template of the advanced oxidation (O_3/UV) reactor

The use of the UV reactors within the O_3/UV advanced oxidation processes involve knowing and exploiting their characteristics, so that maximum yields may be reached under reasonsable energetic consumptions. The use

of the O₃/UV reaction systems for water treatment involves two categories of processes: photo-chemical degradation and photolysis processes and direct disinfection processes.

If the disinfection processes involve the maintenance of a certain contact time between the water flow subjected to the process and the UV radiation field (the provision of a minimum energetic dose, expressed in J/m^2), in case of the photo-chemical degradation processes, what is relevant is the intensity of the radiation field and the profile of the concentrations in the initial condition and in the equilibrium condition, with the help of the reactor, of the chemical species that are of interest, in our case of ozone. A high rate of ozone photolysis involves reaching a high level of the instantaneous concentrations of OH^o radicals. The global reaction rate for the ozone photolysis process is pro rata the product between the quantic yield of the photolysis reaction and the energy of the UV radiation absorbed in the time unit and in the volume unit, according to the following relation [2], [14]:

$$\frac{d[O_3]}{dt} = -\Phi_{O_3} \cdot W_\lambda$$

(1)

where

$[O_3]$ – the concentration of the dissolved oxygen [mol/m^3]

Φ_{O3} – the quantic yield of the photolysis process [mol/J]

W_λ – the volume density of the absorbed power for the wavelength radiation λ [W/m^3]

The volume density of the absorbed power can be put down as :

$$W_\lambda = \mu I_\lambda = 2.303 \cdot \left(\varepsilon_{O_3} C_{O_3} + \sum_i \varepsilon_i C_i \right) \cdot I_\lambda$$

(2)

where : μ – the attenuation coefficient [1/m]; ε_i – the coefficient of absorbing the i species to the λ wavelength (mol^{-1}. m^{-1}); I_λ – the energetic intensity of the radiation in that respective point, at the λ wavelength [W/m^2].

Equation (2) characterises the density of the power absorbed by all the chemical species present in the solution that have absorption band to the λ wavelength. If we strictly refer to the ozone photolysis process, we may introduce the fraction of the density of power absorbed by the ozone, by using the following expression :

$$F_{O_3} = \frac{\varepsilon_{O_3} C_{O_3}}{\sum_i \varepsilon_i C_i}$$

(3)

The ozone photolysis process rate can be written down as :

$$\frac{d[O_3]}{dt} = -\Phi_{O_3} \cdot F_{O_3} . I_\lambda$$

(4)

The numerical modelling of the photolysis process involves knowing the spatial distribution of the radiation's energetic intensity. The great majority of the industrial UV reactors have a coaxial configuration, with the UV lamp placed inside a quartz cylindrical casing, acording to Figure 1 (the annular reactor).
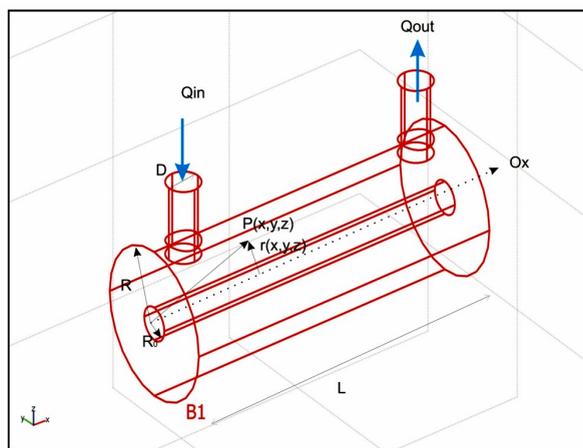

Figure 1. The typical configuration of an O_3/UV annular reactor

There are three basic mathematical templates that describe the spatial distribution of the energetic intensity sent out by the cylindrically shaped lamp [5], [10], [12-13]: the LL template – based on the Lambert law, the PSSE (Point Source with Spheric Emission) template, where the UV lamp is shaped by means of a series of co-linear points, which release an energy spherical spatial distribution, and the LSPP (Linear Source with emission in Parallel Planes) template, according to which the lamp sends out equal energetic intensities in planes that are parallel to the lamp axis. The classic methods of modelling the UV reactors are based on the use of certain global parameters, on the reaction configuration (the effective path of radiation), and on particulars of the geometrical system and of the UV source irradiance characteristics, generally determined by actinometric experimental methods. The main disadvantages of the classic approach relate to the impossibility of extending the templates for more complex geometrical configurations, the global treatment of the reaction system, the impossibility of modelling dynamic regimes. The template presented in this work wipes off the aforesaid disadvantages, constituting the premise of the theoretical and practical approach of complex configurations for the O_3/UV reaction systems.

<u>The template hypotheses</u>:

1. The modelling of the energetic intensity's spatial distribution was made according to the LSSP template, because of its simplicity and of the possibility

of the numerical implementation. According to this template, the radiation energetic implementation is described by the following equation [2], [10]:

$$I = I_0 \frac{r_0}{r(x,y,z)} e^{-(r(x,y,z)-r_0)}$$

(5)

where :

r_0 – the interior radius of the UV reactor (the radius of the quartz casing)
$r(x,y,z)$ – the distance from the lamp to the P point (x,y,z)
I_0 – the irradiance (the energetic intensity) sent out by the lamp [W/m^2]

2. The fluid flow is the flow of an incompressible fluid, so that the Navier-Stokes equations for incompressible fluids (ρ_m= constant) stand valid for the flowing area of the reactor, according to the system of equations written for the 3 axes of coordinates [4] :

$$\rho_m \frac{du_i}{dt} = -\frac{\partial p}{\partial x_i} + \mu \nabla^2 u_i + \rho_m g_i \quad i = 1 \ldots 3$$

(6)

where ρ_m is the mixture density, u_i is the field of speeds in the fluid, g_i represents the components on the three axes of the gravitational acceleration and μ is the volume dynamic viscosity.

2. The reaction kinetics is governed by the two basic equations : the reaction rate equation (4) and the mass transport equation (the non-conservative convection-diffusion equation), the reaction rate being the one specified above (Eq.4) :

$$\frac{\partial c_{O_3}}{\partial t} + \nabla \cdot (-D\nabla c_{O_3}) = R - \nabla \cdot (c_{O_3} \vec{u})$$

(7)

where c_{O_3} is the concentration of the ozone dissolved in water in each point of the volume field taken into consideration and D is the turbulent diffusion coefficient of the ozone solubilised in the fluid environment.

3. The water flow upon the entrance in the reactor is constant, having a constant value of the dissolved ozone concentration.

4. The fluid flow is attached a template of turbulent flow k-ε [5], [9].

The geometry of the O_3/UV advanced oxidation reactor

One has selected two particular geometries, which correspond one to another in practice from the viewpoint of the geometrical characteristics, of the flow parameters and of the functional parameters of the UV radiation source. In case of the template of the reactor with a longitudinal flow with one UV radiation coaxial source (Figure.1), the basic parameters taken into consideration are presented in Table 1.

Table 1. The value of the basic parameters for the longitudinal reactor

The geometrical/functional parameter	Value
The active length of the generator L [m]	0.50
The exterior radius of the reactor R [m]	0.10
The interior radius of the reactor R_0 [m]	0.0225
The diameter of the entrance/exit joint D [m]	0.05
The water flow rate Qin [m^3/h]	10
The irradiance of the UV lamp in the 254 nm line [mW/cm^2] (at the level of the quartz casing)	68.00
The concentration, upon the entrance in the reactor, of the dissolved ozone [g/m^3]	1.00

Figure 2 presents the configuration of the reactor with crosswise circulation and 2 sources of UV radiation that are parallel to the reactor axis. The main parameters of the template are displayed in Table 2.
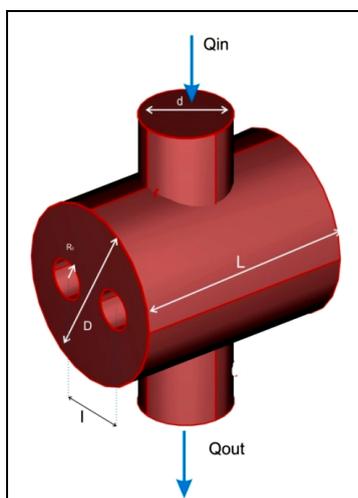

Figure 2. The geometry of the O_3/UV reactor in a crosswise configuration

Table 2. The value of the basic parameters for the crosswise reactor

The geometrical/functional parameter	Value
The active length of the generator L[m]	0.250
The exterior radius of the reactor R [m]	0.100
The interior radius of the reactor R_0 [m]	0.0225
The distance between the radiation sources axes l(m)	0.080
The water flow rate Qin [m^3/h]	100
The irradiance of the UV lamp in the 254 nm line [mW/cm^2]	269
The concentration, upon the entrance in the reactor, of the dissolved ozone [g/m^3]	1.00

The modelling of the advanced oxidation reactors was performed by using the finite elements method (FEM), in the Comsol Multiphysics 3.5. software environment.

The values of the physical constants taken into account for both configurations are displayed in Table 3.

Table 3. The constants of the CFD template

Constant / Characteristic	Value
The fluid temperature [K]	293
The molar absorbance of ozone in water ε [m^2/mol]	330
The quantic yield at 254 nm Φ_{254} [m^2/mol]	$0.1322 \cdot 10^{-5}$
The molar mass of O_3 [g/mol]	47.98
The coefficient of diffusion of ozone in water D [m^2/s]	$2.29 \cdot 10^{-9}$
The water dynamic viscosity η [Pa·s]	10^{-3}
The water absorption coefficient at 254 nm α [m^{-1}]	10

The results analysis and interpretation

The numerical modelling mainly aimed at assessing the ozone photolysis reaction rate in the reactor and at assessing the concentrations of dissolved ozone in various points of the reactor's volume and upon the exit therefrom. The parametrical assessment of the reaction rate and of the dissolved ozone concentration, if the ozone flow rate and concentration are constant upon entrance, was made subject to the values of the UV lamps irradiance I_0[mW/cm^2].

<u>The reactor with a longitudinal circulation</u>. Figure 3 presents the modelling results for the longitudinal distributions of the fluid velocity in the reactor. We find that the values of the velocity components on the y and z axes at the given time are both positive and negative, with fluctuations along the longitudinal axis at the level of the quartz casing. The velocity component on the x axis is positive throughout the whole range and negative values are only recorded at the frontier of axis Ox of the reactor, due to the 'reflexion' to the wall thereof, which brings forth a quasi-stationary area. As compared to the velocities recorded in the reactor's admission and evacuation area (> 1.5 m/s), the fluid's running speed in the quartz casing area is relatively low.

The profile of the reaction rate in various radial sections of the reactor (z = 3;5;8;10 cm), depending on the x quota, shows a dramatic diminishment of the same and an increase of the radial distance to the quartz casing, the value of the reaction rate having a decreasing evolution along the Ox axis, which is mainly due to the diminishment of the dissolved ozone concentration (Figure 4).
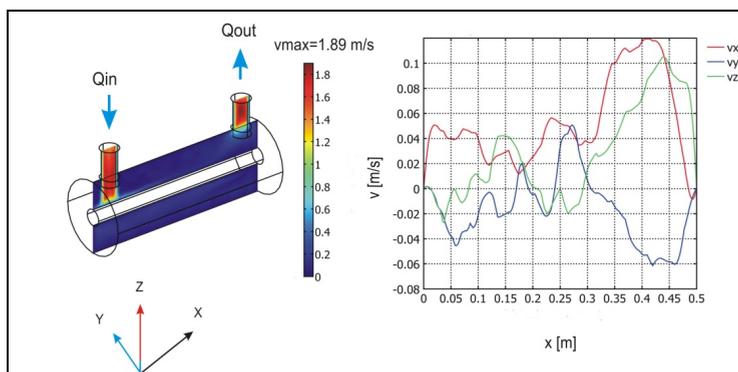
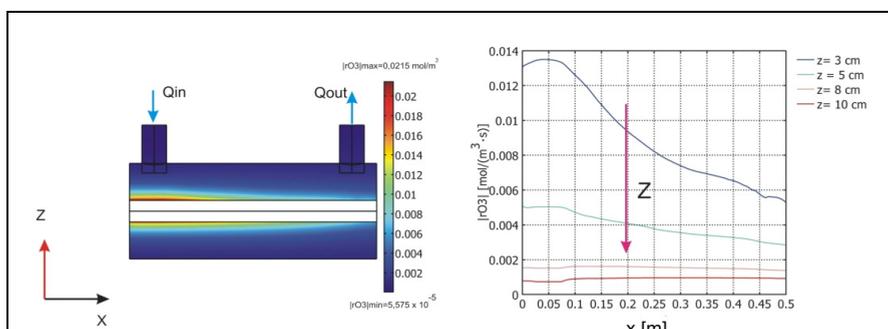**Figure 3.** The longitudinal velocity distribution

Figure 4. The longitudinal profile of the reaction rate

The variation in the longitudinal plane of the dissolved ozone concentrations is rendered in Figure 5, for various z quotas. The parametrical dependance on the value of the I_0 radiance of the UV lamp for the mean reaction volume rate and the ozone concentration upon the exit from the reactor is given in Figure 6. The analysis of the concentration profiles shows an abrupt drop on the x coordinate, with a maximum peak for positive values of z (due to the entrance joint), and a smoother evolution for the negative values of z.
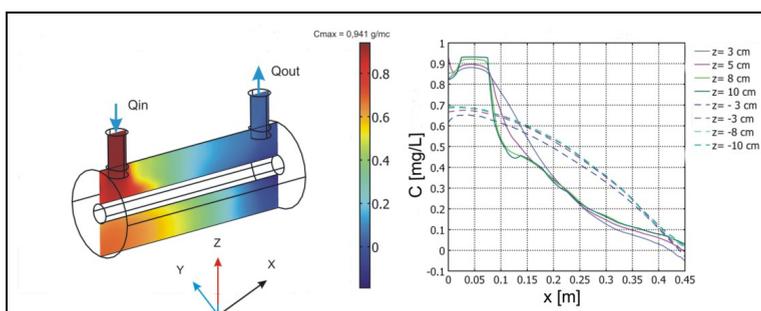

Figure 5. The distribution of the ozone concentrations on the longitudinal axis

Even though the theoretical ozone concentration upon entrance is $1 g O_3/m^3$, because of the 'flow'-type frontier condition ($g O_3/m^2 \cdot s$), the maximum value of the concentration is $0.941 \ g O_3/m^3$, which is due to the extension of the reaction field including at the level of the reactor entrance joint.

The parametrical analysis depending on the lamp irradiance value $[I_0 (mW/cm^2)]$ is displayed in Figure 6 and Figure 7. The reaction rate increases at the same time with the enhancement of the irradiance value, the O_3 concentration dropping at the same time with this increase.
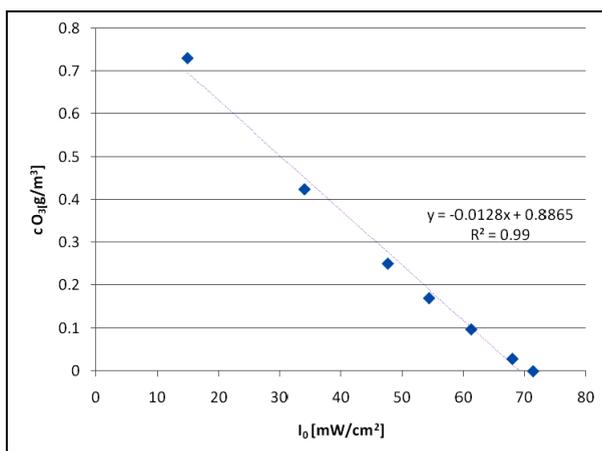
Figure 6. The parametrical variation of the ozone concentration upon the exit from the reactor
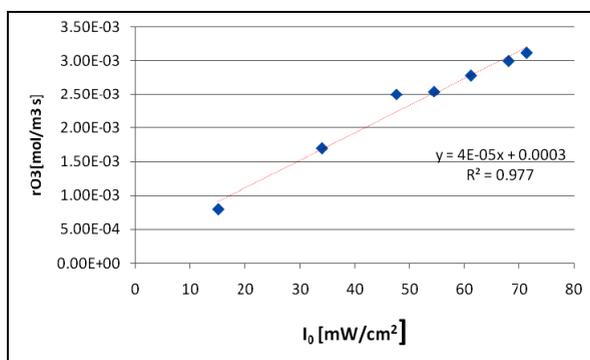
Figure 7. The parametrical variation of the average volume reaction rate

In case of the constructive crosswise-type reactor, the module enables the approach of fluid flow rates upon the entrance in the system that are considerably higher than in case of the longitudinal-type reactor. The distribution of the speeds in the system enables the appearance of 'stagnant' areas, with a reduced fluid speed at the longitudinal extremities and at the reactor's external radius quota. One notices (Figure 8) high values of the fluid velocity

recorded in the median area located between the two quartz tubes. The reaction rate, r_{O3}, is tightly correlated to the intensity of the UV radiation and to the field of speeds in the reactor, showing a minimum value in the central area, with high values of the speeds and maximum values in the other areas. The longitudinal profile of the O_3 concentrations shows a maximum value in the central areas and a lower efficiency of the photolysis process in these regions (Figure 9a).

Upon the exit from the system, the maximum value decreases and the curve profile narrows. The concentrations profile can be best noticed in case of the central section, the maximum area becoming increasingly narrow upon the exit from the reactor (Figure 9b). The blue colour corresponds to areas with a maximum efficiency of the photolysis process. The longitudinal profiles of ozone concentrations are depicted in Figure 10.

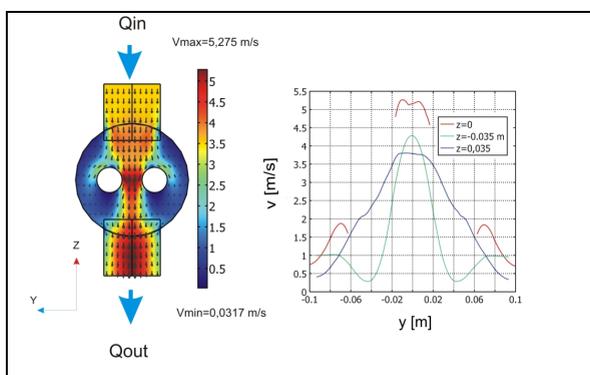**Figure 8.** The velocity distribution in the crosswise section
for the crosswise-type 2- lamped reactor

a.   b.
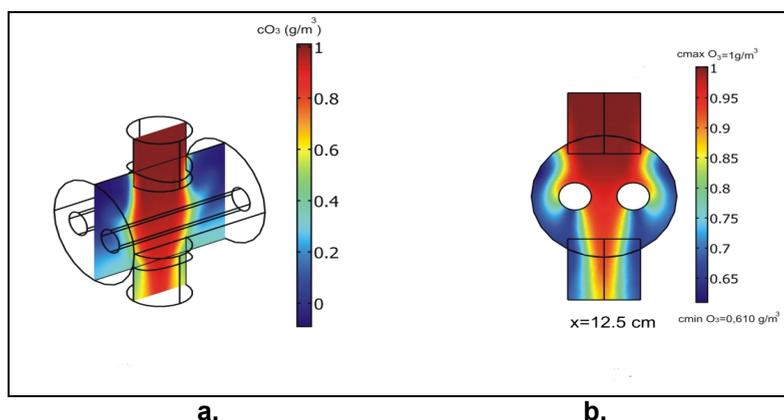
Figure 9. The ozone concentrations distribution: a) In the longitudinal plane;
b) In the crosswise plane
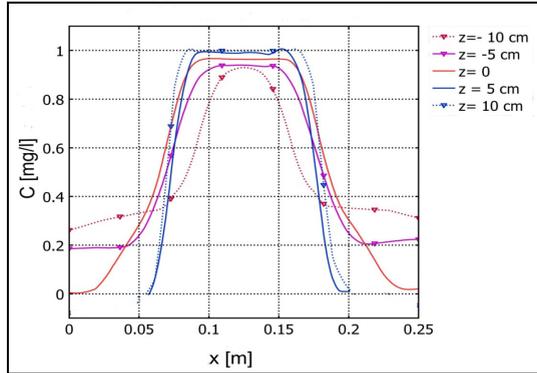
Figure 10. The longitudinal profile of the ozone concentrations

The parametrical analysis depending on the UV radiance of a lamp shows, like in case of the longitudinal template, a quasi-linear dependance of the concentrations upon the exit from the reactor (Fig. 11), a similar dependance being also recorded in case of the average volume reaction rate.
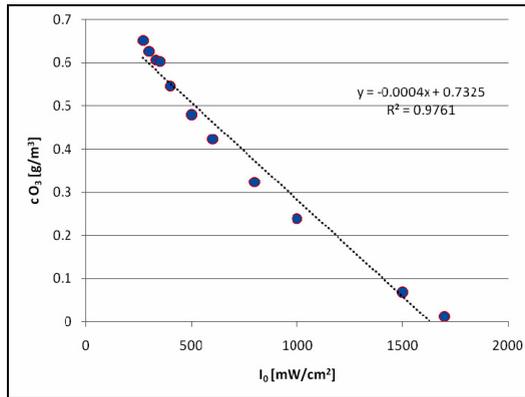
Figure. 11. The parametrical variation of the ozone concentration upon the exit from the reactor depending on the lamp irradiance

CONCLUSIONS

The modelling of the O_3/UV advanced oxidation reactors by using the CFD method brings along higher strictness in the rigorous approach of the ozone photolysis step. If systems of differential equations with partial Navier-Stokes derivates and convection-diffusion ones in the geometrical field of the reactor, combined with a template of distribution of the UV radiation intensity in its volume are used, highly accurate predictions on the photolysis reaction rates and the ozone concentrations from and upon the exit from the reactor can be obtained.

In case of each point of the reactor, the possibility of reaching the basic sizes involved (the speeds components, the radiation intensity, the reaction rate, the ozone concentration) and the possibility of reaching mediated global values for the reaction rates, concentrations and the fluid residence time enable the elaboration of extremely efficient engineering design instruments.

From the standpoint of the research activities, the use of this method for modelling the O_3/UV advanced oxidation reactors enables the extension of the template for various geometries of reactors, with the possibility of including new components and physical and chemical mechanisms in the system, linked to photocatalysis, catalytic ozonisation, sonolysis and electro-chemical separation.

ACKNOWLEDGMENTS

REFERENCES

1. R. Andreozzi, V. Caprio, A. Insola, R. Marrota, *Catalysis Today*, **1999**, *53:1,* 51.
2. F.J. Beltrán, *Ozone: Science & Engineering*, **1997**, *19:1*, 13.
3. F.J. Beltrán, „Ozone Reaction Kinetics for Water and Wastewater Systems", Lewis Publishers, London, N.Y, **2004**.
4. J. Blazek, "Computational Fluid Dynamics: Principles and Applications, Elsevier Science Ltd., **2001**.
5. Comsol Inc., "Chemical Engineering Module User's Guide", Comsol AB, **2008**.
6. A.S. Cuevas, C.A. Arancibia-Bulnes, B. Serrano, *International Journal of Chemical Reactor Engineering*, **2007**, *5,* A58.
7. Ch. Gottschalk, J.A. Libra, A. Saupe, "Ozonation of Water and Waste Water"- 2nd edition, Wiley-VCH Verlag GmbH, Weinheim, **2010**.
8. W.H. Glaze,Y. Lay, J.W. Kang, *Ind. Eng. Chem. Res.*,**1995**, *34*, 2314.
9. K.A. Hoffmann, S.T. Chiang, "Computational Fluid Dynamics", vol **3**, 4th edition, Engineering Education System, Wichita, Kansas, USA, **2000**.
10. P.R. Harris, J.S. Dranoff, *AIChE Journal*, **1965**, *11*, 497.
11. K. Ikehata, M.G. El-Din, *Ozone: Science & Engineering*, **2004**, *26:4,* 327**.**
12. S.M. Jacob, J.S. Dranoff, *Chem. Eng. Prog. Symp. Ser.*, 1**966**, *62*, 47.
13. S.M. Jacob, J.S. Dranoff, *Chem. Eng. Prog. Symp. Ser.*, **1968**, *64*, 54.
14. Leifer A., "The Kinetics of Environmental Aquatic Photochemistry: Theory and Practice", American Chemical Society, New York, **1998**.
15. R.W. Lewis, P. Nithiarasu, K.N. Seetharamu, "Fundamentals of the Finite Element Method for Heat and Fluid Flow", John Wiley & Sons, Ltd, Chichester, UK, **2005**.
16. S. Ulinici, G. Vlad, L. Suciu, *Environmental Engineering and Management Journal*, **2010**, *9:5*, 637.
17. B.A. Wols, J.A.M.H. Hofman, E.F. Beerendonk, W.J.S. Uijtewaal, J.C. Van Dijk, *AicHE Journal*, **2010,** *57:1*, 193.

PLASMA FOR THERAPEUTIC DRUG MONITORING

LAURIAN VLASE[a], SZENDE VANCEA[b, *], CONSTANTIN MIRCIOIU[c], CATALINA ELENA LUPUSORU[d], DANIELA MARCHIDAN[c], CRISTINA MIHAELA GHICIUC[d]

ABSTRACT. A rapid and sensitive liquid chromatography coupled with tandem mass spectrometry (LC/MS/MS) method for the quantification of ethambutol in human plasma was developed and validated. The separation was performed on a Gemini C18 column under isocratic conditions using a mixture of methanol and 0.1% ammonia 65:35 (v/v) as mobile phase, at 40 ºC with a flow rate of 0.6 mL/min. The detection of ethambutol was performed in multiple reaction monitoring mode using an ion trap mass spectrometer with atmospheric pressure chemical ionization, operating in positive MS/MS mode. The human plasma samples (0.1 mL) were deproteinized with methanol and aliquots of 2 µL from supernatants obtained after centrifugation were directly injected into the chromatographic system. The method shows a good linearity (r > 0.994), precision (CV < 8.8%) and accuracy (bias < 12.3%) over the range of 0.36-17.18 µg/mL plasma. The lower limit of quantification (LLOQ) was 0.36 µg/mL and the recovery was between 93-111%. The developed and validated method is simple, rapid and specific for the determination of ethambutol in human plasma and was successfully applied in therapeutic drug monitoring of ethambutol in patients with tuberculosis.

Keywords: ethambutol, LC/MS/MS, human plasma

INTRODUCTION

Ethambutol, d-N,N'-bis (1-hydroxymethylpropyl) ethylenediamine (Fig. 1) is a synthetic oral antibiotic derivative of ethylenediamine which is used for the treatment of tuberculosis in conjunction with at least one other antituberculosis drug.

[a] Department of Pharmaceutical Technology and Biopharmacy, Faculty of Pharmacy, University of Medicine and Pharmacy "Iuliu Haţieganu", Cluj-Napoca, 8 Victor Babeş, 400012, Cluj-Napoca, Romania
[b] Department of Physical Chemistry, Faculty of Pharmacy, University of Medicine and Pharmacy Târgu Mureş, 38 Gheorghe Marinescu, 540139, Târgu Mureş, Romania
[c] Department of Pharmaceutical Technology and Biopharmacy, Faculty of Pharmacy, "Carol Davila" University of Medicine and Pharmacy, Bucharest, 7 Traian Vuia Str, Sector 1, 020955 Bucharest, Romania
[d] Department of Pharmacology, Faculty of Medicine, "Gr.T. Popa", University of Medicine and Pharmacy of Iasi, 16 Universitatii Str., Iasi, 700115, Romania
* corresponding author: *szende_17@yahoo.com*

Although the majority of tuberculosis patients respond to a standardized short course of therapy, it has been shown that among a small group of patients with a poor response to therapy, some have low serum drug concentrations, suggesting that these low concentrations may contribute to the 2–5% of patients with adverse outcomes such as clinical failure or relapse. Most of the patients who had low drug concentrations did not respond to standard therapy but they were successfully treated by dose adjustment after drug monitoring. These findings demonstrate the need for an efficient means of measuring standard antituberculosis drug concentrations to facilitate early screening of therapeutic failure [1].
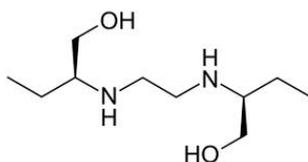
Figure 1. Chemical structure of ethambutol

Several methods involving high-performance liquid-chromatography (HPLC) with fluorescence (FL) [2] or with mass spectrometry (MS) [1, 3-6] detection have been reported for determination of ethambutol in biological matrix.

The HPLC-FL method requires derivatization of ethambutol after liquid-liquid extraction (LLE) in order to transform it in a fluorescent molecule [2]. However, both extraction and derivatization are time-consuming steps, increasing the cost of assay and can affect the recovery. The LC/MS or LC/MS/MS methods offer considerable advantages by their powerful performances: speed, selectivity, sensitivity and robustness. However, the sample preparation procedure by liquid–liquid extraction [4], precipitation-evaporation [3] or double precipitation [1] may complicate the analysis in terms of speed and recovery.

The aim of this work was to develop and validate a new rapid, simple, specific and efficient LC/MS/MS assay for the quantification of ethambutol in human plasma for application in therapeutic drug monitoring.

RESULTS AND DISCUSSION

Sample preparation

In LC/MS assays the sensitivity depends on MS detection mode, but the method involved in sample preparation may also influence the chromatographic background level and can generate matrix suppression effects. Usually an extraction step of analyte from matrix prior to analysis (SPE or LLE) has two main advantages: sample purification and sample pre-concentration. As stated before, the extraction step (either SPE or LLE) is laborious, time consuming

and usually needs an internal standard to compensate the extraction variability. The protein precipitation (PP) as sample processing method is desirable when one needs a high-throughput analysis and low sample-to-sample extraction variability. However, the two main advantage of SPE or LLE extraction mentioned before becomes drawbacks in case of PP: first - the sample is not really purified so matrix interferences or high background noise may appear; and second - the sample is physically diluted during precipitation, lowering the method sensitivity. Thus, the working parameters in developing an analytical method are related to the performance needed: the sample preparation time and costs, the method speed and sensitivity (Table 1).

Table 1. Analytical characteristics of reported LC/MS and LC/MS/MS methods for the determination of ethambutol in biological matrix:

Matrix	Pre-treatment/ extraction[a]	Mobile phase constituents[b]	Detection mode[c]	LOQ[d] (ng/mL)	Run time (min)	Reference
Human plasma	Double PP	Formic acid in MeOH and water	ESI+MS/MS, MRM (m/z 205→116)	50	4	**1**
Human plasma	PP-evaporation	TFA in MeOH and water	APCI+MS/MS MRM (m/z 205→116)	10	3.8	**3**
Human plasma	LLE	MeOH- water-formic acid	APCI+MS/MS, SRM (m/z 205→116)	10	3	**4**
Human plasma	PP	N/A	MS/MS	50	2.8	**5**
Human plasma	PP	N/A	MS/MS	200	N/A	**6**
Human plasma	PP	MeOH-ammonia in water	APCI+MS/MS MRM (m/z 205→116)	360	2	**Current report**

[a]LLE, liquid–liquid extraction, PP, protein precipitation; [b]ACN, acetonitrile; MeOH, methanol, TFA, trifluoracetic acid; [c]ESI, electrospray ionization; APCI, atmospheric pressure chemical ionization; SIM, selected ion monitoring; SRM, selected reaction monitoring, MRM, multiple reaction monitoring; [d]LOQ, limit of quantification, N/A not available

Following a single oral dose of 25 mg/kg of body weight, ethambutol attains a serum level of 2 to 5 µg/mL after 2 to 4 hours from administration [2,4]. Therefore the calibration curve range was adapted to the concentration range of the analyzed samples, namely 0.36-17.18 µg/mL. Because the current assay does not require a high sensitivity as in human pharmacokinetic studies, the PP extraction method becomes an attracting alternative to SPE or LLE due to the high speed and to the high reproducibility of the extraction.

In this method there were analyzed volumes of only 0.1 mL plasma by PP with methanol (0.3 mL) and direct injection into the chromatographic system from supernatant after centrifugation. A good sensitivity (LLOQ of 0.36 µg/mL) and absolute recoveries between 93-111% were obtained corresponding to the needs.

LC-MS assay

The analyte detection was optimized in order to achieve maximum sensitivity and specificity, by tuning the mass spectrometer in order to improve the ion transmission, stabilization and fragmentation in the ion trap. The ethambutol is ionized in APCI source by proton addition, giving a pseudo-molecular ion with m/z 205. After fragmentation, the protonated ethambutol is converted to ion with m/z 116 (Fig. 2).
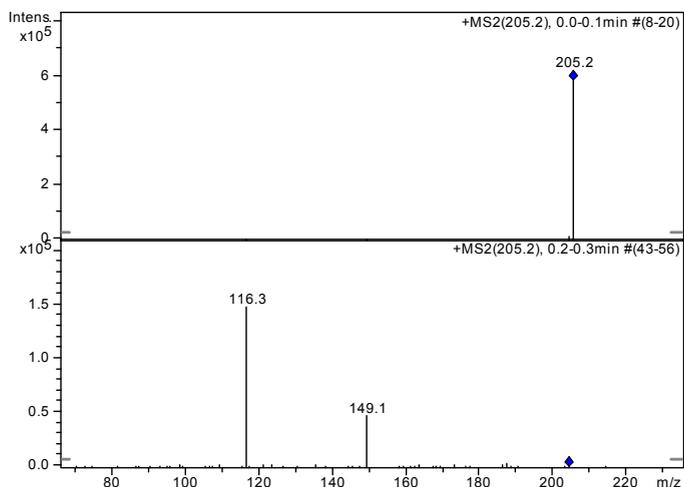
Figure 2. MS spectra of ethambutol – MS spectra (upper image),
MS/MS spectra (lower image)

In order to obtain the needed specificity of analysis and a maximum signal-to-noise ratio (S/N) of analyte, we used the capability of Ion Trap mass spectrometer to do multiple stages isolation-fragmentation processes, that means MS^n analysis. This feature is specific to Ion Trap MS analyzers; other MS systems (single quadrupole, triple quadrupole, time of flight) do not have that capability. Thus, in the MS/MS stage, the m/z 205 ion obtained in the first MS was further fragmented and the obtained mass spectra was recorded (Fig. 2). The obtained m/z 116 ion is specific to ethambutol and was used for quantification. By using MS/MS detection mode, due to high specificity, the overall method sensitivity is increased significantly in comparison with MS detection.

The detection of ethambutol was carried out in multiple reaction monitoring (MRM). The extracted ion chromatogram (EIC) of m/z 116 from m/z 205 was analyzed. In the selected chromatographic conditions the retention time of ethambutol was 1.2 min.

Assay validation

The method was validated in accordance with international guidelines regarding bio-analytical method validation procedure [7,8,11]. A representative chromatogram of a blank sample, a human plasma spiked with ethambutol at LLOQ and a plasma sample from a patient treated with 1600 mg ethambutol/daily for 7 days, sampled after 2h from administration is shown in Fig. 3. No interfering peaks from the endogenous plasma components were observed at the retention time of ethambutol.
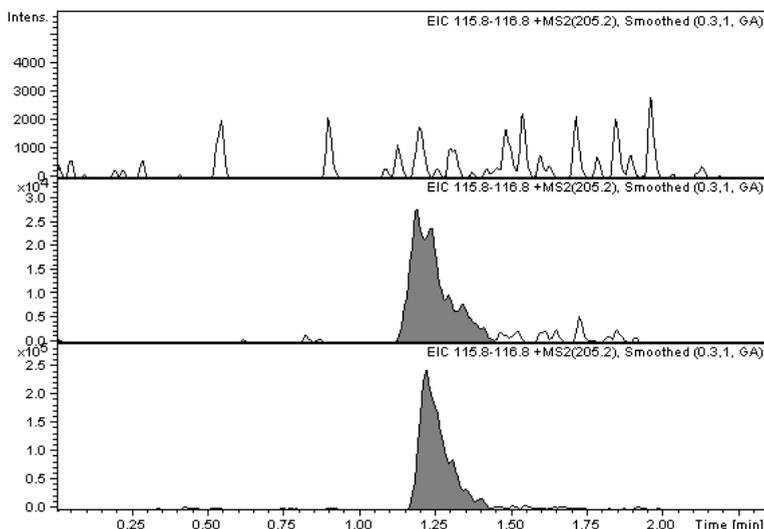
Figure 3. Representative chromatograms of a blank plasma (upper image); plasma spiked with ethambutol (R_T = 1.2 min) at lower limit of quantification (0.36 μg/mL), (middle image); and a plasma sample from a patient treated with ethambutol (lower image).

The calibration curves were linear over the concentration range of 0.36 –17.18 μg/mL in human plasma, with a good correlation coefficient (0.994). The LLOQ was 0.36 μg/mL. The obtained values for intra-day, inter-day precision and accuracy are shown in Tables 2 and 3, respectively. All values for accuracy and precision were within guidelines recommended limits (<15%) [7,8]. The absolute recovery values were between 93-111%.

Table 2. Intra-day precision, accuracy and recovery (n = 5) for ethambutol

$c_{nominal}$ µg/mL	Mean c_{found} µg/mL (± S.D.)	CV %	Bias %	Recovery % (± S.D.)
0.36	0.34±0.01	4.0	-4.2	110.4±4.9
1.07	1.02±0.07	6.6	-5.4	105.7±4.0
2.15	1.88±0.12	6.3	-12.3	111.2±7.1
7.16	7.01±0.44	6.3	-2.1	98.8±6.2

Table 3. Inter-day precision, accuracy and recovery (n = 5) for ethambutol

$c_{nominal}$ µg/mL	Mean c_{found} µg/mL (± S.D.)	CV %	Bias %	Recovery % (± S.D.)
0.36	0.38±0.03	8.8	6.4	104.0±15.7
1.07	1.00±0.02	1.8	-7.0	101.5±7.9
2.15	1.95±0.14	7.4	-9.3	99.2±3.9
7.16	7.12±0.56	7.9	-0.6	93.1±3.8

Method application

The validated method for determination of ethambutol in human plasma was successfully applied in therapeutic drug monitoring of ethambutol in patients with tuberculosis. Overlapping plasma profiles of ethambutol are presented in Fig. 4 (spaghetti plot representation). Although the dosing regimen was similar between patients, one can observe a great inter-individual variability of ethambutol plasma levels, this being the main reason for the necessity of therapeutic drug monitoring and pharmacokinetic studies for this drug.
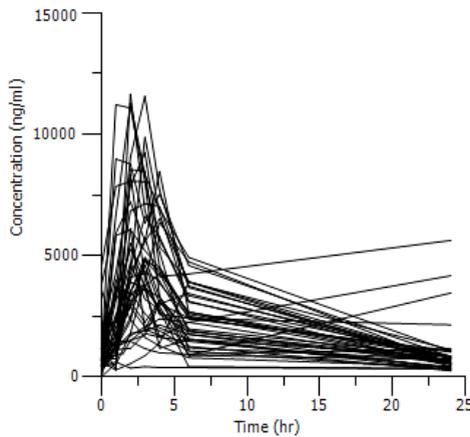

Figure 4. Overlapped plasma profiles of ethambutol administrated to patients with tuberculosis

CONCLUSION

Antimicrobial therapeutic drug monitoring could be an important tool in clinical practice if compliance is poor. Therefore, quantification of drug in plasma is an important issue in clinical practice to enhance efficacy and to reduce toxicity.

The developed LC/MS/MS assay is specific, accurate and not expensive. In terms of analysis time (throughput), this is fastest analytical method published to the date for analysis of ethambutol in biological matrix using a simple protein precipitation as plasma processing method. This new fast and specific method was successfully applied in therapeutic drug monitoring of ethambutol in patients with tuberculosis.

EXPERIMENTAL SECTION

Reagents

Ethambutol was reference standard from USP (Rockville, MD, USA). Methanol of gradient grade for liquid chromatography and 30% ammonia solution of analytical-reagent grade were purchased from Merck KGaA (Darmstadt, Germany). Bidistilled, deionised water pro injections was purchased from Infusion Solution Laboratory of University of Medicine and Pharmacy Cluj-Napoca (Romania). The human blank plasma was from healthy volunteers.

Apparatus

The following apparatus were used: 204 Sigma Centrifuge (Osterode am Harz, Germany); Analytical Plus and Precision Standard Balance (Mettler-Toledo, Switzerland); Vortex Genie 2 mixer (Scientific Industries, New York, USA); Ultrasonic bath Elma Transsonic 700/H (Singen, Germany). The HPLC system used was an 1100 series Agilent Technologies model (Darmstadt, Germany) consisting of one G1312A binary pump, an in-line G1379A degasser, an G1329A autosampler, a G1316A column oven and an Agilent Ion Trap Detector 1100 SL.

Chromatographic and spectrometric conditions

Chromatographic separation was performed on a Gemini (100 mm x 3.0 mm i.d., 3.0 μm) column (Phenomenex) under isocratic conditions using a mixture of methanol and 0.1% ammonia in water, 65:35 (v/v) as mobile phase at 40 °C with a flow rate of 0.6 mL/min. In order to maintain the ESI source clean, the column effluent was diverted to waste for the first 0.8 minutes after injection. The detection of ethambutol was performed in multiple reaction monitoring (MRM) mode using an ion trap mass spectrometer with atmospheric pressure chemical ionization (APCI) source, positive ionization

(capillary 4000 V, nebulizer 50 psi (nitrogen), heater 400 ºC, dry gas nitrogen at 7 L/min, dry gas temperature 350ºC). The extracted ion chromatogram (EIC) of m/z 116 from m/z 205 was analyzed (MS/MS mode).

Standard solutions

A stock solution of ethambutol (1.193 mg/mL) was prepared by dissolving an appropriate quantity of ethambutol in methanol. A working solution (35.79 µg/mL) was prepared by appropriate dilution in human blank plasma. This solution was used to prepare seven plasma calibration standards with the concentrations between 0.36 and 17.18 µg/mL, respectively. Quality control (QC) samples of 1.07 µg/mL (lower), 2.15 µg/mL (medium) and 7.16 µg/mL (higher) were prepared by adding the appropriate volumes of working solutions to human blank plasma.

Sample preparation

Standards and plasma samples (0.1 mL) were deproteinized with methanol (0.3 mL). After vortex-mixture (10 s) and centrifugation (3 min at 12000 rpm), the supernatants (0.15 mL) were transferred in autosampler vials and 2 µL were injected into the HPLC system.

Method validation

The specificity of the method was evaluated by comparing the chromatograms obtained from the plasma samples containing ethambutol with those obtained from plasma blank samples.

The concentration of ethambutol was determined automatically by the instrument data system using peak areas and the external standard method. The calibration curve model was determined by the least squares analysis: $y = b + ax$, weighted ($1/y^2$) linear regression, where y - peak area of the analyte and x - concentration of the analyte (µg/mL).

The intra-day precision (expressed as coefficient of variation, CV %) and accuracy (expressed as relative difference between obtained and theoretical concentration, bias %) were determined by analysis of five different samples (n = 5) from each QC standards (at lower, medium and higher levels) on the same day. The inter-day precision and accuracy were determined by analysis on five different days (n = 5) of one sample from each QC standards (at lower, medium and higher levels). The lower limit of quantification (LLOQ) was established as the lowest calibration standard concentration with an accuracy and precision less than 20%. The relative recoveries (at LLOQ, lower, medium and higher levels) were determined by comparing the response of the spiked plasma with the response of standard solutions with the same concentration of ethambutol as plasma (n = 5) [7-10].

ACKNOWLEDGMENTS

REFERENCES

1. S.H. Song, S.H. Jun, K.U. Park, Y. Yoon, J.H. Lee, J.Q. Kim, J. Song, *Rapid Commun Mass Spectrom*, **2007**, *21*,1331.

2. M. Breda, P. Marrari, E. Pianezzola, M. Strolin Benedetti, *J Chromatogr A*, **1996**, *729*, 301.

3. Z. Gong, Y. Basir, D. Chu, M. McCort-Tipton, *J Chromatogr B Analyt Technol Biomed Life Sci*, **2009**, *877(16-17)*, 1698.

4. X. Chen, B. Song, H. Jiang, K. Yu, D. Zhong, *Rapid Commun Mass Spectrom*, **2005**, *19(18)*, 2591.

5. J.E. Jr. Conte, E. Lin, Y. Zhao, E. Zurlinden, *J Chromatogr Sci*, **2002**, *40(2)*, 113.

6. H. Kim, J-L. Kim, S.K. Bae, K-H. Liu, J-G. Shin, *9th International ISSX Meeting, Istanbul, Turkey*, **2010**.

7. Guidance for Industry, Bioanalytical Method Validation. U.S. Department of Health and Human Services, Food and Drug Administration. Federal Register, **2001**, 66.

8. Guidance on the Investigation of Bioavailability and Bioequivalence. The European Agency for the Evaluation of Medicinal Products, Committee for Proprietary Medicinal Products, **2001**, CPMP/EWP/QWP/1401/98.

9. D. Mihu, L. Vlase, S. Imre, C.M. Mihu, M. Achim, D.L. Muntean, *Studia UBB Chemia*, **2009**, *54(3)*, 151.

10. M. Achim, D. Muntean, L. Vlase, I. Bâldea, D. Mihu, S.E. Leucuţa, *Studia UBB Chemia*, **2009**, *54(3)*, 7.

11. Guideline on bioanalytical method validation, European Medicines Agency, 21 July 2011 EMEA/CHMP/EWP/192217/2009

SYNTHESIS, CHARACTERIZATION AND COMPLEXATION STUDY OF NEW 4-(DIPHENYLPHOSPHINO)-PHENOTHIAZINES

TAMAS LOVASZ[a,*], EMESE GALA[a], CASTELIA CRISTEA[a], LUMINIŢA SILAGHI-DUMITRESCU[a]

ABSTRACT. The synthesis of new 4-(diphenylphosphino)-phenothiazine derivatives was achieved by a regioselective lithiation of the thio-aryl structural unit of the phenothiazine precursor, followed by *in situ* reaction of the intermediate with chloro-diphenylphosphine. Symmetrical 4,6-*bis*(diphenylphosphino)-phenothiazine was obtained by similar functionalization of the isolated 4-(diphenylphosphino)-phenothiazine. These air stable aryl-phosphines were purified by column chromatography and characterized by MS, FT-IR, ^{1}H-, ^{13}C- and ^{31}P-NMR spectroscopy. Coordination of 10-alkyl-4-(diphenyl-phosphino)-phenothiazines to Pd(II) was confirmed by means of ^{31}P-NMR spectroscopy which indicated a strong deshielding effect upon P atoms.

Keywords: *Phenothiazine, Heteroaryl-diphenylphosphine, Pd(II) complex, ^{31}P-NMR*

INTRODUCTION

Triarylphosphine derivatives attracted considerable interest in the last years, especially due to their reactivity and utilization as ligands for efficient transition metals catalyzed syntheses [1-3]. A wide variety of aryl-diphenyl-phosphines were described in the scientific literature, and their properties such as air stability, redox properties and supramolecular assemblies were thoroughly investigated [4, 5]. The phenothiazine deriva-tives are tricyclic compounds well known for their rich electron structure and redox active character [6, 7]. Moreover, the supramolecular associations of molecules containing folded phenothiazine units may play an important role in the control of conformation, geometry and aggregation of such derivatives. 10-Alkyl-10*H*phenothiazines contain folded structures, characterized by a boat conformation of the central 1,4-thiazine ring; substituents such as methyl,

---

[a] Babeş-Bolyai University, Faculty of Chemistry and Chemical Engineering, Kogălniceanu str., No.1, RO-400028 Cluj-Napoca, România

* *tlovasz@chem.ubbcluj.ro*

ethyl, *iso*-propyl prefer a quasi-equatorial position (when there are no other groups to C(1) or C(9) neighboring positions). As determined by XRD method, the folding angles tend to become smaller when the size of the alkyl substituent becomes larger, since the alkyl chain extends to the convex side of the phenothiazine ring [8-10].

For many palladium catalyzed reactions, an essential step appears to be the reduction of Pd(II) to Pd(0) species right at the beginning of the catalytic cycle [11]. In certain classical phosphine-assisted protocols the oxidation of the phosphine may contribute to the reduction of Pd(II) to Pd(0) but, the resulted phosphine-oxides can no longer participate to the catalytic cycle and thus larger loads of ligand are required. Based on the well recognized low oxidation potential of phenothiazine derivatives, we suggest that in a phenothiazinyl-phosphine ligand, the redox-active phenothiazine unit can overtake the reductive role of the phosphine and under these circumstances, the reduction of Pd(II) to Pd(0) would proceed without the loose of its catalytical activity.

We believe that the structural features of alkyl-phenothiazines may be conveniently exploited in the design of new *tris*-aryl-phosphine type ligands for transition metals complexes with catalytic activity. Continuing our interest in the synthesis and characterization of (diphenylphosphino)-phenothiazine derivatives [12], in this work we add supplementary data regarding the preparation new 10-ethyl- and 10-isopropyl-4-(diphenylphosphino)-phenothiazines and we also describe the formation of complexes between 4-(diphenylphosphino)-phenothiazines and PdCl$_2$.

The applicability of the new 10-alkyl-4-(diphenylphosphino)-phenothiazine palladium complexes in traditional catalytic reactions is to be tested.

RESULTS AND DISCUTION

N-alkyl-phenothiazines were often employed as substrates in the preparation of higher substituted-phenothiazine derivatives. The regioselective preparation of 4-substituted-phenothiazines was achieved using a strategy which involved lithiated phenothiazine intermediates, taking benefit of the enhanced reactivity of this electron rich heterocycle coupled with the *orto* directing capacity of the sulphur atom in its arylthio structural unit [13, 14]. We successfully applied this synthetic route for the preparation of 4-(diphenyl-phosphino)-10-methyl-10*H*-phenothiazine, as previously reported [12]. In this work we add supplementary data regarding the preparation of new 10-ethyl- and 10-isopropyl-4-(diphenylphosphino)-phenothiazine **2b,c** as shown in scheme 1. The preparative protocol involved two reaction steps: i) lithiation of alkyl-phenothiazine substrate **1a-c** followed by ii) reaction of the lithiated intermediate with one equivalent of chloro-diphenylphosphine.
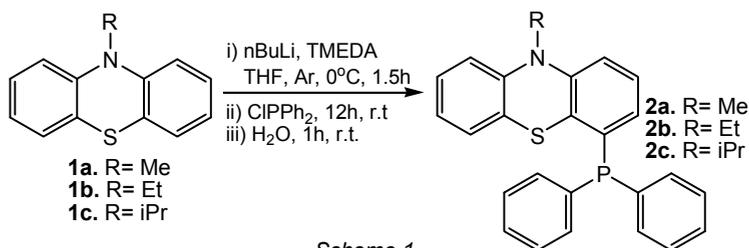
Scheme 1

GC-MS analysis of the reaction mixtures indicated the formation of 4-(diphenylphosphino)-10-alkyl-10*H*-phenothiazines (**2a** m/z=397, **2b** m/z= 411 and **2c** m/z=425 *a.m.u* respectively), accompanied by small amounts of the corresponding *bis*-(diphenylphosphine)-phenothiazines (M+185), phosphinoxides (M+16) and alkyl-phenothiazines. Moderate yields of 4-(diphenylphosphino)-10-alkyl-10*H*-phenothiazines **2a-c** were isolated by column chromatography.

In order to obtain higher amounts of the new 4,6-*bis*(diphenylphosphino)-10-methyl-10H-phenothiazine **3**, **2a** was subjected to lithiation and then, the orange solution thus obtained was further treated with one equiv. of chlorodiphenylphosphine (Scheme 2). The oily product isolated by column chromatography slowly solidified in time.
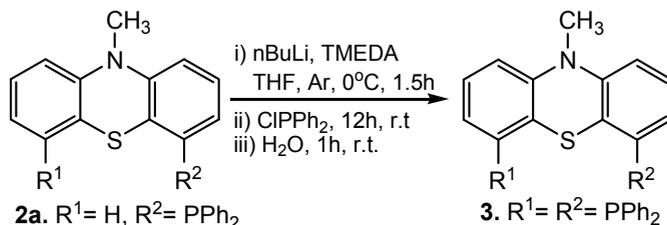
Scheme 2

The structures of the new compounds were unambiguously assigned based on their recorded MS, FT-IR, ^{1}H-, ^{13}C- and ^{31}P-NMR spectra.

The new phenothiazinyl-phosphines **2b** and **3** as well as the previously described **2a** and 4-[(3-sodiumbenzensulfonato)-phenyl-phosphino]-10-methyl-10*H*-phenothiazine **4** [12], were independently used as ligands for complexation of palladium chloride in dichloromethane solution, under inert atmosphere, based on a modified literature procedure [15]. The reaction mixtures were stirred for 12h at room temperature and during this time, the colorless solutions of the reagents slowly turned to orange. Finally, after removing the solvent, the products were thoroughly washed with hexane and diethyl-ether. The insoluble complexes (scheme 3) were examined without other further purification.

$$nL + PdCl_2 \xrightarrow[\text{Ar, r.t}]{CH_2Cl_2} L_nPdCl_2$$

L= **2a**, **2b**, **3**, **4**   **5**
n= 1, 2
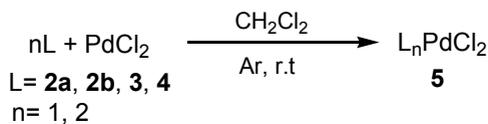
Scheme 3

^{31}P-NMR spectroscopy proved to be an efficient tool for studying the P atom complexes, as well as for the observation of some intermediates in catalytic reactions [16, 17]. The coordination of the phosphorous atom in phosphines produces a strong deshielding effect and consequently the corresponding chemical shift values appear shifted by 50-70 ppm [18]. A similar deshielding effect was detected in the case of each palladium complex **5,** when compared to the parent 4-(diphenylphosphino)-10-alkyl-10*H*-phenothiazine ligand, as it can be seen from the chemical shift values listed in table 1.

Table 1. 121.44 MHz ^{31}P-NMR Chemical shift values (ppm) for 4-(diphenylphosphino)-10-alkyl-10*H*-phenothiazines free ligands and their corresponding palladium complexes.

^{31}P NMR δ(ppm)	**2a**	**2b**	**3**	**4**
Free ligand	-13.4	-13.2	-16.1	-13.4[a]
Pd complex	59.7	59.6	59.7	27.3[b]

[a] recorded in $CDCl_3$
[b] recorded in d^6-DMSO

In the ^{31}P-NMR spectra of ligands **2a**, **2b**, **3** and **4** respectively, an intense signal situated at negative chemical shift values corresponds to a shielded P(III) structure. The compounds separated after the complexation of Pd(II) gave a ^{31}P-NMR signal considerably shifted downfield, thus supporting the formation of Pd-P bonds. The Pd complex of water soluble ligand **4** was not soluble in $CDCl_3$; its ^{31}P NMR spectrum was recorded in DMSO-d_6 and thus, the intermolecular associations with this polar solvent dramatically modified the observed chemical shift value, but still the shielding effect of complexation remains distinctly observable.

CONCLUSIONS

The two step reaction strategy involving the lithiation of an alkyl-phenothiazine substrate followed by the reaction of the lithium-organic intermediate with chlorodiphenylphosphine was successfully applied in the preparation of the new 10-ethyl- and 10-isopropyl-4-(diphenylphosphino)-phenothiazine as well as for the preparation of symmetrical 4,6-*bis*(diphenyl-phosphino)-10-methyl-10H-phenothiazine. The phenothiazinyl-diphenyl-phosphines are air stable compounds which can be purified by column chromatography. Coordination of 10-alkyl-4-(diphenylphosphino)-phenothiazines to Pd(II) was confirmed by means of ^{31}P-NMR spectroscopy which indicated a strong deshielding effect upon P atoms.

EXPERIMENTAL SECTION

All chemicals and solvents were dried and purified by usual methods. Compounds **1a-c** and **2a** were prepared according to described procedures [12, 19, 20]. All reactions as well as column chromatography were followed by TLC using Merck pre-coated silica gel 60 F_{254} aluminium sheets. Column chromatography was performed using Merck silica gel 60 (63- 200 mesh) and flash chromatography with RediSep^{TM} Silica column with a Teledyne Isco CombiFlash$^{TM}R_f$ apparatus. Melting points were determined with an Electro-thermal IA 9200 digital melting point apparatus and are uncorrected. The mass spectra were recorded by a GC-MS (EI, CI) Shimadzu mass spectrometer. IR spectra were recorded on a Bruker Vector 22 FT-IR spectrometer fitted with a Golden Gate ATR accessory. ^{1}H and ^{13}C-NMR spectra were recorded in CDCl$_3$ in 5 mm tubes at RT, on Bruker Avance 300 MHz spectrometer, using TMS as internal reference with the deuterium signal of the solvent as the lock. The spectral data are listed in the experimental part.

General procedure for synthesis of 4-(diphenylphosphino)-10-alkyl-10*H*-phenothiazines

To a stirred solution of 10-alkyl-10*H*-phenothiazine (9.4 mmol) in dry THF (40 cm^3) was added TMEDA (3.0 cm^3, 20 mmol), followed by dropwise addition of *n*-BuLi (20 mmol, 12.5 cm^3 of a 1.6 M solution in hexane) at 0 ºC under Ar. The mixture was stirred at 0 ºC for 1.5 h and Ph$_2$PCl (4.41 g, 20 mmol) was then added. After 12 h stirring at r.t., the reaction mixture was treated with 10 cm^3 of H$_2$O. The organic phase was separated and the aqueous phase was extracted with Et$_2$O (3x25 cm^3). The combined organic phases were dried over Na$_2$SO$_4$. After removal of the solvent *in vacuo*, the residue was separated by column chromatography on silicagel with heptane/Et$_3$N (30:1) as eluent and then recrystallized from Et$_2$O.

4-(diphenylphosphino)-10-methyl-10*H*-phenothiazine 2a

The product was purified by column chromatography and recrystallized from Et$_2$O to give white crystals m.p.: 189 ºC (1.5 g, 40%) lit. m.p.= 189-191 ºC [12] MS (EI$^+$) m/z: 397 (M$^+$, 100%), 382, 286, 273, 242, 212, 183, 77.

4-(diphenylphosphino)-10-ethyl-10*H*-phenothiazine 2b

Phosphination of 10-ethyl-10H-phenothiazine (**1b**) was carried out according general procedure presented above. The product was purified by column chromatography and recrystallized from Et$_2$O to give white crystals, m.p.= 151-152ºC (1.26, 33%), IR (ATR) ν [cm^{-1}]: 694, 746, 758, 1136, 1196, 1254, 1281, 1327, 1364, 1409, 1444, 1477, 1557, 1589, 2983, 3011. ^{31}P NMR (121.5 MHz, CDCl$_3$) δ (ppm): -13.2. ^{1}H NMR (300 MHz, CDCl$_3$) δ (ppm): 1.42 (t, 3H, $^3J_{HH}$= 7.2 Hz, CH$_3$), 3.94 (q, 2H, $^3J_{HH}$= 7.2 Hz, *N*-CH$_2$), 6.39 (dd, 1H, $^3J_{HH}$= 7.2 Hz, $^3J_{PH}$=3.3

Hz, H3), 6.86 (d, 2H, $^3J_{HH}$= 7.8 Hz, H1,9), 6.88 (t, 1H, $^3J_{HH}$= 7.2 Hz, $^3J_{HH}$= 7.8 Hz H2), 7.05 (t, 1H, $^3J_{HH}$= 7.7 Hz, $^3J_{HH}$= 8.6 Hz, H7), 7.09 (d, 1H, $^3J_{HH}$= 8.6 Hz, H6); 7.13 (1H, t, $^3J_{HH}$= 7.7 Hz, $^3J_{HH}$= 7.8 Hz, H8), 7.30-7.35 (10H, m, H_{Ph}). ^{13}C NMR (75 MHz, CDCl$_3$): 13.2, 42.1, 115.1, 115.5, 122.5, 124.7, 126.9, 127.4, 128.7, 128.8, 130.0, 134.1, 134.3, 135.6, 136.2, 138.0, 143.5, 145.3 MS (EI$^+$) m/z: 411 (M$^+$, 100%), 396, 382, 272, 183, 77.

4-(diphenylphosphino)-10-isopropyl-10*H*-phenothiazine 2c

Phosphination of 10-isopropyl-10H-phenothiazine (**1c**) was carried out according general procedure presented above. The product was purified by column chromatography and recrystallized from Et$_2$O to give white crystals, m.p.= 146-147 °C (1.1g, 27%), IR (ATR) ν [cm^{-1}]: 687, 726, 916, 1126, 1246, 1290, 1304, 1400, 1446, 1478, 1555, 1589, 2976, 3078. ^{31}P NMR (121.5 MHz, CDCl$_3$) δ (ppm): -13.1. ^{1}H NMR (300 MHz, CDCl$_3$) δ (ppm): 1.65 (d, 6H, $^3J_{HH}$= 6.8 Hz CH$_3$), 4.32 (h, 1H, $^3J_{HH}$= 6.8 Hz, *N*-CH), 6.43 (dd, 1H, $^3J_{HH}$= 6.5 Hz, $^3J_{PH}$=3.0 Hz, H3), 6.89 (t, 1H, $^3J_{HH}$= 7.8 Hz, H2), 7.05-7.10 (m, 4H, H1,6,7,9), 7.13 (1H, t, H8), 7.33-7.38 (10H, m, H_{Ph}). ^{13}C NMR (75 MHz, CDCl$_3$): 31.6, 53.4, 117.6, 117.9, 122.3, 126.2, 126.7, 127.4, 128.2, 128.3, 128.5, 133.0, 133.6, 133.8, 135.7, 135.9, 144.9, 145.4. MS (EI$^+$) m/z: 425 (M$^+$), 382(100%), 304, 274, 197, 183, 77.

4,6-bis(diphenylphosphino)-10-methyl-10H-phenothiazine 3

To a stirred solution of 4-(diphenylphosphino)-10-methyl-10*H*-phenothiazine **2a** (0.4 g, 1 mmol) in dry THF (50 cm^3) was added TMEDA (0.3 cm^3, 2 mmol), followed by dropwise addition of *n*-BuLi (2 mmol, 1.25 cm^3 of a 1.6 M solution in hexane) at 0 °C under Ar. The mixture was stirred at 0 °C for 2 h and Ph$_2$PCl (0.44 g, 2 mmol) was then added. After 12 h stirring at r.t., the reaction mixture was treated with 25 cm^3 of H$_2$O. The organic phase was separated and the aqueous phase was extracted with ethyl acetate (3x25 cm^3). The combined organic phases were dried over Na$_2$SO$_4$. After removal of the solvent *in vacuum*, the residue was separated by column chromatography on silica gel with heptane/Et$_3$N (30:1) as eluent. The resulting colorless oil slowly solidify resulting a white precipitate m.p.= 190-192 °C (0.21 g, 36%). IR (ATR) ν [cm^{-1}]: 686, 727, 772, 1037, 1099, 1192, 1244, 1288, 1331, 1446, 1474, 1555, 1587, 2863, 2965. ^{31}P NMR (121.5 MHz, CDCl$_3$) δ (ppm): -16.1. ^{1}H NMR (300 MHz, CDCl$_3$) δ (ppm): 3.42 (s, 3H, *N*-CH$_3$), 6.88 (d, 2H, $^3J_{HH}$= 8.3 Hz, H1), 6.92 (dd, 1H, $^3J_{HH}$= 8.3 Hz, $^3J_{PH}$= 2.6 Hz, H3), 7.13 (t, 2H, $^3J_{HH}$= 8.0 Hz, H2), 7.36-7.45 (20H, m, H_{Ph}). ^{13}C NMR (75 MHz, CDCl$_3$): 35.7, 114.2, 122.6, 125.4, 127.3, 128.7, 129.0, 132.7, 136.2, 139.3, 145.9. MS (EI$^+$) m/z: 411 (M$^+$, 100%), 396, 382, 272, 183, 77.

4-[(3-sodiumbenzensulfonato)-phenyl-phosphino]-10-methyl-10*H*-phenothiazine 4

Sulfonation of 4-(diphenylphosphino)-10-methyl-10*H*-phenothiazine (0.2 g, 0.5 mmol) was performed according literature procedure [12]. The

product was isolated by extraction with ethyl acetate and evaporation of the solvent as a green-white solid (0.2 g, 80%) m.p. 199 °C decomposition. ^{31}P NMR (121.5 MHz, CDCl$_3$) δ (ppm): -13.4.

ACKNOWLEDGEMENT

REFERENCES

1. Y. Guo, H. Fu, H. Chen, X. Li, *Cat. Commun.*, **2008**, 9, 1842.

2. J.R. Briggs, H. Hagen, S. Julka, J.T. Patton, *J. Organomet. Chem.*, **2011**, *696*(8), 1677.

3. P. Pongrácz, Gy. Petöcz, M. Shaw, D. Bradley, G. Williams, L. Kollár, *J. Organomet. Chem.*, **2010**, *695*(22), 2381.

4. H. Shimizu, I. Nagasaki, T. Saito, *Tetrahedron*, **2005**, *61*, 5405.

5. P.W.N.M. van Leeuwen, ”Homogeneous Catalysis. Understanding tha Art”, Kluwer Academic Publishers, Dodrecht, **2004**, chapter 1.5.

6. J.B. Christensen, M.F. Nielsen, J.A.E.H. Van Haare, M.W.P.L. Baars, R.A.J. Janssen, E.W. Meijer, *Eur. J. Org. Chem.*, **2001**, *11*, 2123.

7. M. Hauck, R. Turdean, K. Memminger, J. Schönhaber, F. Romingers, T.J.J. Müller, *J. Org. Chem.*, **2010**, *75*(24), 8591

8. S.S.C. Chu, D. Van der Helm, *Acta Cryst.*, **1974**, *B30*, 2489.

9. S.S.C. Chu, D. van der Helm, *Acta Cryst.*, **1975**, *B31*, 1179.

10. S.S.C. Chu, D. van der Helm, *Acta Cryst.*, **1976**, *B32*, 1012.

11. S. Aizawa, M. Kondo, R. Miyatake, M. Tamai, *Inorg. Chim. Acta*, **2007**, *360*, 2809.

12. T. Lovasz, E. Gal, L. Gaina, I. Sas, C. Cristea, L. Silaghi-Dumitrescu, *Studia UBB Chemia*, **2010**, *55*(3), 249.

13. S. Ebdrup, *Synthesis*, **1998**, *8*, 1107.

14. S. Ebdrup, *J. Chem. Soc. Perkin Trans I.*, **1998**, 1147.

15. T.R. Krishna, N. Jayaraman, *Tetrahedron*, **2004**, *60*(45), 10325.

16. Gy. Petöcz, Z. Berente, T. Kégl, L. Kollár, *J. Organomet. Chem.*, **2004**, *689*(7), 1188.

17. D.S. Glueck, *Coord. Chem. Rev.*, **2008**, *252*, 2171.

18. V.A. Stepanova, V.V. Dunina, I.P. Smoliakova, *J. Organomet. Chem.*, **2011**, *696*(4), 871.

19. L. Gaina, T. Dallos, C. Cristea, *Studia UBB Chemia*, **2010**, *55*(1), 97

20. H. Gilman, R. D. Nelson, J. F. Champaigne, *J. Am. Chem. Soc.*, **1952**, *74*, 4205.

ELECTROCHEMICAL BEHAVIOR OF CELLOBIOSE DEHYDROGENASE FROM *NEUROSPORA CRASSA* IMMOBILIZED ON GRAPHITE AND Au-4-MERCAPTOPHENOL MODIFIED ELECTRODES

GÁBOR KOVÁCS[a], IONEL CĂTĂLIN POPESCU[a,*]

ABSTRACT. The amperometric responses of G/CDH and Au-4-mercaptophenol/CDH modified electrodes to lactose were comparatively recorded under flow injection and cyclic voltammetry operating modes, respectively. The differences noticed between the characteristic parameters of the two investigated bioelectrodes were explained in terms of the influences exerted by the given experimental conditions on direct electron transfer process, existing between cellobiose dehydrogenase (CDH) and the investigated electrode materials.

Keywords: amperometric biosensors, cellobiose dehydrogenase, direct electron transfer, self-assembled monolayer, Au and graphite modified electrodes.

INTRODUCTION

Modification of different electrode surfaces with enzymes is the main idea of amperometric biosensor construction. The basic requirements for amperometric biosensors are: (i) an enzyme which reacts on its substrate, reducing or oxidizing it at the surface of a suitable electrode; (ii) a method for immobilizing the enzyme in close proximity to the electrode, which retains the activity of the enzyme and is offering a suitable electron transfer pathway toward the electrode; (iii) an electronic system capable of controlling (and registering) the potential of the electrode and measuring the current produced by the redox process [1].

The enzyme used for our research was cellobiose dehydrogenase (CDH) from *Neurospora crassa.* CDH (EC 1.1.99.18) is an extracellular enzyme produced by a variety of different fungi. Around 30 species of fungi have shown to produce CDH. All CDHs belong to two related subgroups: class I, produced only by basidiomycetes (filamentous fungi) and class II, with longer and more complex structure, produced by ascomycetes (sac fungi). The most common and well-known CDH's are those produced by wood-degrading

---

[a] Universitatea Babeş-Bolyai, Facultatea de Chimie şi Inginerie Chimică, Str. Kogălniceanu, Nr. 1, RO-400084 Cluj-Napoca, Romania

* cpopescu@chem.ubbcluj.ro

and plant pathogen fungi [2-4]. The interest related to CDH is due to its ability to show efficient direct electron transfer (DET) properties at various electrode materials (different type of graphite [5-10], carbon nanotubes [11] and gold [12-14]), towards various substrates (e.g. cellobiose [15, 16], glucose [17, 18], lactose [9, 19]). Thus, CDH is considered very promising for applications in the field of biosensors and biofuel cells.

The enzyme immobilization and the construction variant allowing the DET between its active center and the electrode surface can be made by various methods. One easy way is the immobilization of the enzyme through simple chemo-physical adsorption on the surface of the electrode (Figure 1). This method is used to modify different graphite electrode surfaces (e.g. spectroscopic [8, 20], screen printed [21-24]), due to good reproducibility rates, high porosity of the electrode materials (thus they can adsorb the enzymes with high efficiency), and the low cost of the electrode material.

Another method used for assuring the electrical connection for efficient DET consists in the modification of the electrode surface with self-assembled monolayers (SAMs) [25-27]. In the case of metal electrodes, especially Au, the modification of the electrode surface with thiols, having various end-group functionalities, represents a good solution to overcome the difficulties met with DET [12, 14, 28, 29]. A SAM of thiols can provide a well-ordered structure onto electrode surface and hence, the enzyme maintains a precise distance from the electrode surface and a particular orientation of the enzyme, which favors an efficient DET, and assures high currents for less enzyme consumption.
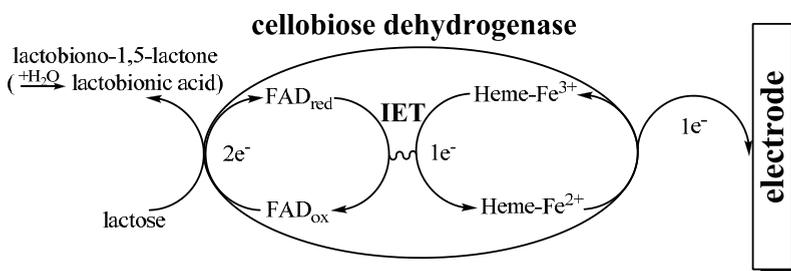
Figure 1. Schematic diagram of the process of direct electron transfer between the adsorbed CDH enzyme and the graphite or Au electrode modified with a self-assembled monolayer of 4-mercaptophenol.

When CDH is immobilized properly on the electrode surface (either on graphite or Au), in presence of substrate (e.g. lactose) the enzyme will oxidize it by the FAD cofactor to lactone and the electrons produced from this reaction will be transferred one-by-one at the electrode surface *via* the heme domain: the process is called internal electron transfer (IET) (Figure 1).

In the present study, in order to obtain more information about the DET efficiency for immobilized CDH, its electrochemical behavior was comparatively investigated by amperometry, performed either by flow injection measurements at a CDH-modified graphite electrode or by cyclic voltammetry at a CDH-modified Au electrode, which was previously covered with a SAM made of 4-mercaptophenol (SPh-OH). For this purpose, the responses to lactose, under DET operation mode, for both above-mentioned modified electrodes were monitored in different experimental conditions (pH and substrate concentration). The collected data served to establish the optimal constructive variant of the bioelectrodes incorporating CDH.

RESULTS AND DISCUSSION

Immobilization of CDH on different electrode materials

In the work presented here, spectroscopic graphite and gold electrodes modified with SAM were used as supporting materials for immobilization by simple adsorption of CDH isolated from *Neurospora crassa*. From the previous works [14] it is known that the favorable orientation of the enzyme, which is determinant for obtaining an efficient DET, is strongly affected by both the electrode material and the method used for enzyme immobilization.

Immobilization of CDH on graphite electrode involves a simple chemo-physical adsorption onto the surface of the polished graphite rod. Consequently, the optimal enzyme orientation on the surface of the electrode is not guaranteed, as the enzymes molecules are adsorbed randomly. Some adsorbed molecules will be able to participate in catalysis and electron transfer, but some other are immobilized in such a way that either the heme domain is not oriented in order to assures the transfer of the electrons produced during the catalytic process at FAD domain, or the orientation of catalytic center is unable to load the substrate from solution (Figure 2A). Often, a different construction is used for the electron transfer pathway. This requires the modification of the electrode surface (gold) with thiols, assembling a monolayer, and attaching the enzyme in an ordered layer. Theoretically, this approach supposes that all the adsorbed enzyme molecules are involved in catalysis and electron transfer (Figure 2B).

In this context, it was interesting to compare the electrocatalytic efficiency of the two construction variants described above. For this purpose, two different CDH-modified electrodes (G/CDH and Au-SPh-OH/CDH) were prepared and their electrocatalytic behavior was investigated towards the same substrate (lactose).
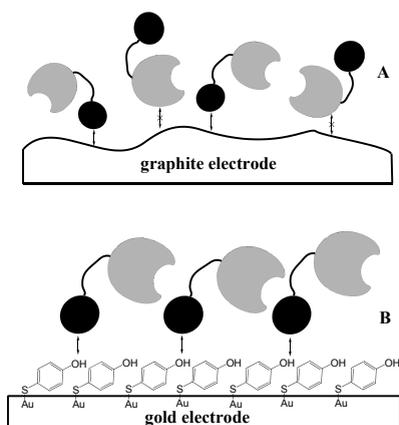
Figure 2. Schematic diagram showing the adsorption/orientation of the CDH enzyme (FAD domain – grey; heme domain – black; linker – black line) on graphite (A) and Au electrode modified with a self-assembled monolayer of 4-mercaptophenol (B).

pH influence

The relative amperometric responses of G/CDH and Au-SPh-OH/CDH electrodes to 5 mM lactose at different pH values, recorded under flow conditions (G/CDH) or in cyclic voltammetry (Au-SPh-OH/CDH) are shown in Figure 3. As can be seen, for both electrodes, the optimum working pH is placed around 5.5. The difference between the pH profiles, observed in the case of investigated electrodes, should be explained in terms of the interaction between the pH induced conformation changes of the immobilized CDH molecule and their effect on the electron transfer process, occurring at different electrode surfaces. At the same time, the more organized structure, characteristic to Au-SPh-OH/CDH modified electrode, should be considered, too. Thus, it can be supposed that, within certain limits, the surface properties of the graphite and Au-SPh-OH electrodes are not significantly affected by the pH variation. Contrarily, the DET and IET processes, involved in the electron transfer between the CDH molecules and the electrode surfaces, are strongly influenced by the conformational changes of the enzyme molecules, which are induced by the variation of the distance between the two functional domains occurring when the pH changes. Concluding, the sharp maximum noticed on the pH profile of Au-SPh-OH/CDH electrode response certainly reflects the high sensitivity of an ordered structure for small conformational changes occurring around the optimal pH value. In this context, it is worth to mention that the catalytic activity observed at Au-SPh-OH/CDH modified electrode decreases with more than 50% of its maximum value, for a pH change of 0.5 units (Figure 3).
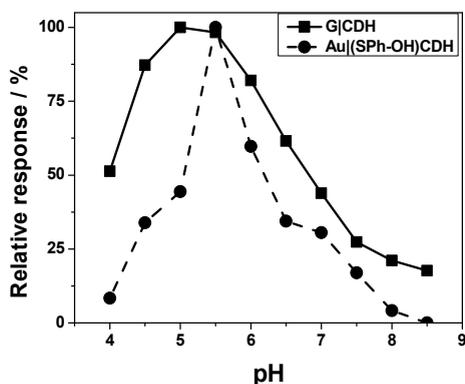
Figure 3. pH influence on the relative amperometric responses of **G/CDH** (■, ——) and **Au-SPh-OH/CDH** (●,— —) modified electrodes. Experimental conditions for **G/CDH**: flow injection mode, injections of 5 mM lactose, volume of injected sample, 50 µL; flow rate, 0.5 mL / min; applied potential, +300 mV *vs.* Ag|AgCl, 0.1M KCl; for **Au-SPh-OH/CDH**, cyclic voltammetry mode, starting potential, -300 mV *vs.* SCE, v=10 mV/s; supporting electrolyte 50 mM acetate buffer (pH 4 to 6) and 50 mM phosphate buffer (pH 6.5 to 8.5).

Electrocatalytic efficiency

The amperometric responses of the modified electrodes were recorded at two different pH values: the optimum value (pH 5.5) and a value of practical interest for biotechnological applications (pH 7.0).

The calibration curves obtained for G/CDH modified electrode against lactose are shown in Figure 4. As expected, the bioelectrode gives a well-shaped Michaelis-Menten behavior at both pH values. The highest efficiency was observed in slightly acidic media. The value of the apparent Michaelis-Menten constant (K_m^{app}) decreases to its half at neutral pH compared to the value estimated for optimum pH: from 488 µM to 225 µM lactose. The maximum current (I_{max}) shows a similar behavior, decreasing from 2.03 µA (pH 5.5) to 0.8 µA (pH 7.0). Consequently, the bioelectrode sensitivity is slightly affected by the pH changes, decreasing with less than 15%, from 57.5 (pH 5.5) to 49.1 (pH 7.0) µA*mM^{-1}cm^{-2}. It should be mentioned that both values are slightly higher than those recently reported for a similar system [23].

The electrochemistry of CDH and its voltammetric response at Au-SPh-OH/CDH modified electrode was studied in absence and in presence of lactose, at pH 5.5 and at pH 7.0. In absence of the substrate, the response due to the redox-couple $Fe^{2+/3+}$ from heme domain was observed. At pH 5.5 the formal standard potential ($E^{0'}$) was found +150 mV *vs.* SCE, while at pH 7.0 $E^{0'}$ was +160 mV *vs.* SCE (Figure 5). Irrespective of the surrounding pH, in presence of the substrate (lactose) a clear catalytic current was observed. As it was suggested for a similar CDH [14], the thiols with alcohol end-group immobilized on the Au surface, induce the enzyme molecule orientation in a

favorable position at the surface of the modified electrodes. Thus, the biocatalytic process is enhanced, resulting in an active and selective bioelectrode. The current decrease noticed at neutral pH can be attributed to the decrease of DET efficiency, due to weaker (Au-SPh-OH) - CDH interactions, followed either by the decrease of the CDH adsorption rate or by unfavorable conformational changes occurring within the enzyme molecule. Consequently, the electron transfer becomes less efficient and the bioelectrode response decreases.
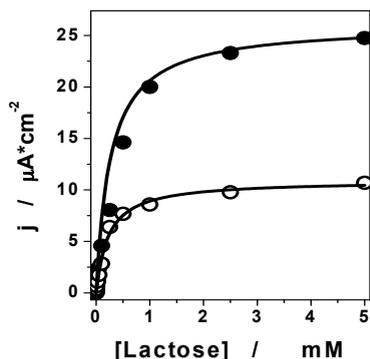
Figure 4. Calibration curves of G/CDH modified electrode towards lactose, recorded at two different pH values. Experimental conditions: applied potential, +300 mV vs. Ag|AgCl, 0.1M KCl; volume of injected sample, 50 µL; flow rate, 0.5 mL/min; flow carriers, 50 mM acetate (pH 5.5) or 50 mM phosphate buffer (pH 7.0); filled symbols were used for pH 5.5 and open symbols for pH 7.0. The solid lines correspond to Michaelis-Menten non-linear fittings.
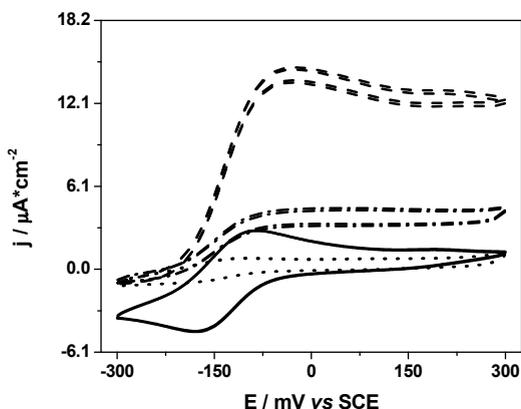
Figure 5. Voltammetric response of **Au-SPh-OH/CDH** modified electrode in absence [pH 5.5 (——); pH 7.0 (·····)] and in presence [pH 5.5(- -); pH 7.0 (- · -)] of 5 mM lactose. Experimental conditions: starting potential, -300 mV *vs.* SCE; potential scan rate, 10 mV/s; 50 mM acetate (pH 5.5) or 50 mM phosphate buffer (pH 7.0).

The values estimating the catalytic efficiency for the two investigated electrodes are shown Table 1. The I_0 value is referring to the current measured in absence of the substrate, while the $I_{peak, S}$ value stands for the peak current measured in presence of the substrate. It can be noticed that the values of efficiency corresponding to the G/CDH modified electrode are much higher than those estimated for the Au-SPh-OH/CDH modified electrode. This behavior is obviously due to a higher enzyme loading in the case of the first bioelectrode. Indeed, a surface characterized by a high roughness factor (graphite) and allowing an unconstrained distribution of the CDH molecules will exhibit a higher enzyme activity than a surface with a lower roughness factor (Au-SPh-OH) and exerting size constraints for CDH molecules.

Table 1. Electrocatalytic efficiency of the CDH modified electrodes for 5 mM lactose (for experimental conditions see Figure 5 for Au-SPh-OH/CDH and Figure 4 for G/CDH).

Electrode	Electrocatalytic efficiency ($I_{peak, S}/I_0$)	
	pH 5.5	pH 7.0
G/CDH	72	30
Au-SPh-OH/CDH	9.76	3.84

Additionally, the sensitivity (expressed as the ratio between of the electrocatalytic efficiencies estimated at pH 5.5 and pH 7.0) of the second bioelectrode to pH changes (2.54) is slightly higher than that estimated for the first one (2.40). This behavior supports the results reported above, confirming once again that an ordered structure is more sensitive to small conformational changes of the enzyme molecules, occurring around the optimal pH value.

CONCLUSIONS

During the half century of biosensors history various electrode materials and electron transfer pathways were investigated aiming at possible applications in medicine and biotechnology. In the presented work the similarities and differences of DET at two different CDH modified graphite electrodes were investigated.

Both approaches have their advantages and drawbacks. The CDH immobilization by "simple adsorption" on the graphite surface provides a rapid and cost effective way towards future applications for biosensors and/or biofuel cells construction. The weakness of this method consists in a random adsorption of the enzyme, resulting in a smaller reproducibility of the prepared bioelectrodes. The "SAM" approach, illustrated by Au electrodes modified with 4-mercaptophenol, offers the advantage of a huge versatility, due to the high number of thiocompounds which can be involved in this approach. Another "pro" for the "SAM" approach is the presence of a quasi-ordered structure,

including the enzyme, built on the electrode surface, which facilitates a reproducible preparation of the bioelectrodes. Its main disadvantage refers to the low enzymatic activity of the electrode surface coupled with the relative instability of the monolayer.

Besides these, the present work points out that in the case of CDH, an enzyme able to sustain DET at different electrode materials, the "SAM" approach exhibits a higher vulnerability to pH changes than the "simple adsorption" one. This behavior was explained taking into consideration the conformational changes of the CDH molecules, which, in the case of a better organized interface, exert a stronger influence on the bioelectrode activity.

EXPERIMENTAL SECTION

Reagents

All chemicals used were of analytical grade. Citric acid-1 hydrate, β-lactose and 4-mercaptophenol (SPh-OH) were purchased from Sigma-Aldrich (Sigma-Aldrich Chemicals, Steinheim, Germany). Sodium hydrogen phosphate monohydrate and sodium hydroxide were obtained from VWR (VWR International, Darmstadt, Germany), while hydrochloric acid was purchased from Fluka (Fluka, Buchs, Switzerland).

Cellobiose dehydrogenase from Neurospora crassa (CDH) was a kind gift received from Dr. Roland Ludwig, Department of Food Sciences and Technology, BOKU-University of Natural Resources and Applied Life Sciences, Vienna. It was obtained and purified as previously described [30]. The protein concentration was estimated using Bradford assay as 13.9 mg/mL. The enzyme activity, at pH 4 and 30°C, was found to be 118.73 U/ml and 63.6 U/ml by using DCIP assay and Cyt C assay respectively.

The buffer solutions used in all experiments were prepared using either a 50 mM citric acid solution (for pHs ranging from 4.0 to 6.5) or a 50 mM sodium hydrogen phosphate (for pHs placed in the 6.0 to 8.5 interval). The desired pH value was adjusted with 4 M NaOH or 5 M HCl. Before use, the buffer and the substrate solutions were carefully degassed.

All solutions were prepared using deionized water (18 MΩ) purified with a Milli-Q system (Millipore, Bedford, MA, USA). All measurements were performed at room temperature (22 °C).

Flow injection electrochemical setup

A flow-through wall jet cell was used as amperometric detector [31], connected on-line to a single line flow injection (FI) system (Figure 6). The carrier flow was maintained at a constant flow rate of 0.5 mL/min by using a peristaltic pump (Gilson, Villier-le-Bel, France). The injector was an electrically controlled six-port valve (Rheodyne, Cotati, CA, USA), provided with an injection loop of 50 µL volume.
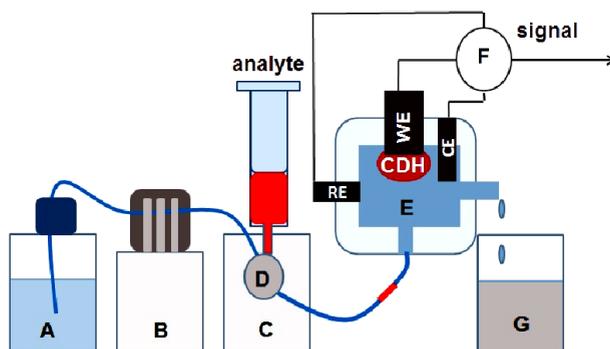
Figure 6. The experimental FI setup with carrier/buffer solution (A), peristaltic pump (B), injector (C), valve (D), flow-through cell (E), potentiostat (F) and waste collector (G).

The electrochemical cell consisted of a conventional three electrode system, where the working electrode (WE) was the CDH-modified graphite, the reference (RE) was a Ag|AgCl, 0.1 M KCl electrode and the counter electrode (CE) was a Pt wire. The CDH modified electrode was press-fitted into a Teflon holder, inserted into the wall-jet cell and kept at a constant distance (~1 mm) from the inlet nozzle.

The electrochemical cell was connected to a low current potentiostat (Zäta Elektronik, Lund, Sweden) and the response currents were recorded on a strip chart recorder (Kipp&Zonen, Delft, The Netherlands).

Cyclic voltammetry measurements

Cyclic voltammetry (CV) experiments were performed under anaerobic conditions (assured by a previous degassing of the solutions and by using a flow of pure argon gas over the working solution) with a BAS 100W Electrochemical Analyzer (Bioanalytical Systems, West Lafayette, IN, USA). A three electrode cell was used with the working electrode, a saturated calomel electrode (SCE) as the reference electrode and a Pt wire as the auxiliary electrode. The scan rate of 300 mV/s was used for the electrochemical cleaning procedure or 10 mV/s for the regular measurements.

Preparation of CDH-modified graphite electrodes

The graphite electrodes were prepared using spectroscopic graphite rods (OD 3.05 mm; Ringsdorff-Werke GmbH, Bonn, Germany). A rod of adequate length was cut and polished on wet emery paper (Tufbak, Durite, P1200); afterwards, it was carefully rinsed with deionized water and dried. The CDH was immobilized through simple chemo-physical adsorption onto the surface of the polished graphite rod by using the following procedure: 5 µL

of CDH solution was spread onto the entire active surface of the electrode (0.0731 cm^2). The CDH modified graphite electrode (G/CDH) was dried at room temperature for approximately 20 minutes and then stored overnight at 4ºC. Before use, the G/CDH electrode was thoroughly rinsed with Milli-Q water in order to remove any weakly adsorbed enzyme. Afterwards, the G/CDH electrode was placed into the wall jet cell filled with the buffer solution, the required potential was applied and the output current was recorded. Before performing any substrate injection into the flow system, the carrier buffer solution was continuously pumped until a stable background current was obtained.

Preparation of Au-SPh-OH/CDH modified electrodes

The cleaning of the disc Au electrode (CH-Instruments, Cordova, TN, USA, Ø 2 mm, area of 0.033 cm^2) started by dipping the Au electrode in "piranha" solution (3:1 v/v H_2SO_4:H_2O_2) for 5 min. Then, the electrode was mirror-like polished with aqueous alumina FF slurry (1 and 0.1 μm, Stuers, Denmark) deposited on Microcloth (Buehler). Furthermore, the electrodes were carefully rinsed with water, ultrasonicated for 5 min in Milli-Q water, and electrochemically cleaned in 0.5 M H_2SO_4, by performing 20 cycles with a scan rate of 300 mV/s between −100 and 1700 mV *vs.* SCE. Finally, they were rinsed again with Milli-Q water.

The preparation of CDH-thiol-modified electrodes started by the immersion of the clean Au electrodes in a 1mM solution of thiol dissolved in ethanol for 60 min. This treatment results in the formation of the self-assembled monolayer of thiol on the electrode surface. Before the exposure to CDH, they were carefully rinsed with ethanol in order to remove the weakly absorbed thiols and dried with Ar. CDH deposition on the Au-SAM modified electrodes was made by spreading of 2 μL of enzyme solution onto the thiol-modified Au surface. The enzyme drop was allowed to gently dry in order to avoid the spread of the enzyme drop outside of the electrode area. A dialysis membrane (molecular weight cut off 6000–8000), pre-soaked in the buffer solution, was applied onto the electrode and fitted tightly to the electrode surface with a rubber O-ring. For three equivalently prepared electrodes the enzymatic activities was found reproducible in the limits of 5%. Between measurements, the Au-SPh-OH/CDH modified electrodes were stored at 4 ^{0}C in a water saturated atmosphere.

REFERENCES

[1]. G.W.J. Harwood, C.W. Pouton, *Advanced Drug Delivery Reviews*, **1996**, *18*, 163.

[2]. G. Henriksson, G. Johansson, G. Pettersson, *Journal of Biotechnology*, **2000**, *78*, 93.

[3]. M. Zamocky, R. Ludwig, C. Peterbauer, B.M. Hallberg, C. Divne, P. Nicholls, D. Haltrich, *Current Protein & Peptide Science*, **2006**, *7*, 255.

[4]. R. Ludwig, W. Harreither, F. Tasca, L. Gorton, *ChemPhysChem*, **2010**, *11*, 2674.

[5]. T. Larsson, M. Elmgren, S.-E. Lindquist, M. Tessema, L. Gorton, M. Tessema, G. Henriksson, *Analytica Chimica Acta*, **1996**, *331*, 207.

[6]. T. Larsson, A. Lindgren, T. Ruzgas, S.E. Lindquist, L. Gorton, *Journal of Electro-analytical Chemistry*, **2000**, *482*, 1.

[7]. A. Lindgren, L. Gorton, T. Ruzgas, U. Baminger, D. Haltrich, M. Schulein, *Journal of Electroanalytical Chemistry*, **2001**, *496*, 76.

[8]. W. Harreither, V. Coman, R. Ludwig, D. Haltrich, L. Gorton, *Electroanalysis*, **2007**, *19*, 172.

[9]. L. Stoica, R. Ludwig, D. Haltrich, L. Gorton, *Analytical Chemistry*, **2006**, *78*, 393.

[10]. L. Stoica, T. Ruzgas, R. Ludwig, D. Haltrich, L. Gorton, *Langmuir*, **2006**, *22*, 10801.

[11]. F. Tasca, M.N. Zafar, W. Harreither, G. Noll, R. Ludwig, L. Gorton, *Analyst*, **2011**, *136*, 2033.

[12]. A. Lindgren, T. Larsson, T. Ruzgas, L. Gorton, *Journal of Electroanalytical Chemistry*, **2000**, *494*, 105.

[13]. A. Lindgren, L. Gorton, T. Ruzgas, U. Baminger, D. Haltrich, M. Schülein, *Journal of Electroanalytical Chemistry*, **2001**, *496*, 76.

[14]. L. Stoica, N. Dimcheva, D. Haltrich, T. Ruzgas, L. Gorton, *Biosensors and Bioelectronics*, **2005**, *20*, 2010.

[15]. M. Nordling, M. Elmgren, J. Stahlberg, G. Pettersson, S.E. Lindquist, *Analytical Biochemistry*, **1993**, *214*, 389.

[16]. M. Tessema, T. Larsson, T. Buttler, E. Csöregi, T. Ruzgas, M. Nordling, S.-E. Lindquist, G. Pettersson, L. Gorton, *Analytica Chimica Acta*, **1997**, *349*, 179.

[17]. F. Tasca, L. Gorton, M. Kujawa, I. Patel, W. Harreither, C.K. Peterbauer, R. Ludwig, G. Nöll, *Biosensors and Bioelectronics*, **2010**, *25*, 1710.

[18]. C. Sygmund, W. Harreither, D. Haltrich, L. Gorton, R. Ludwig, *New Biotechnology*, **2009**, *25, Supplement*, S115.

[19]. G. Safina, R. Ludwig, L. Gorton, *Electrochimica Acta*, **2010**, *55*, 7690.

[20]. S. Shleev, A. El Kasmi, T. Ruzgas, L. Gorton, *Electrochemistry Communications*, **2004**, *6*, 934.

[21]. S. Ledru, N. Ruillé, M. Boujtita, *Biosensors and Bioelectronics*, **2006**, *21*, 1591.

[22]. S. Shleev, J. Tkac, A. Christenson, T. Ruzgas, A.I. Yaropolov, J.W. Whittaker, L. Gorton, *Biosensors and Bioelectronics*, **2005**, *20*, 2517.

[23]. S.A. Trashin, D. Haltrich, R. Ludwig, L. Gorton, A.A. Karyakin, *Bioelectrochemistry*, **2009**, *76*, 87.

[24]. O.D. Renedo, M.A. Alonso-Lomillo, M.J.A. Martínez, *Talanta*, **2007**, *73*, 202.

[25]. J.J. Gooding, D.B. Hibbert, *TrAC Trends in Analytical Chemistry*, **1999**, *18*, 525.

[26]. N.K. Chaki, K. Vijayamohanan, *Biosensors and Bioelectronics*, **2002**, *17*, 1.

[27]. A.L. Eckermann, D.J. Feld, J.A. Shaw, T.J. Meade, *Coordination Chemistry Reviews*, **2010**, *254*, 1769.

[28]. E.E. Ferapontova, L. Gorton, *Bioelectrochemistry*, **2005**, *66*, 55.

[29]. D. Sarauli, R. Ludwig, D. Haltrich, L. Gorton, F. Lisdat, *Bioelectrochemistry*.

[30]. W. Harreither, C. Sygmund, M. Augustin, M. Narciso, L. Rabinovich Mikhail, L. Gorton, D. Haltrich, R. Ludwig, *Applied and environmental microbiology*, **2011**, *77*, 1804.

[31]. R. Appelqvist, G. Marko-Varga, L. Gorton, A. Torstensson, G. Johansson, *Analytica Chimica Acta*, **1985**, *169*, 237.

ELECTROCHEMICAL BEHAVIOUR OF METALLIC TITANIUM IN MnO$_2$ ELECTROSYNTHESIS FROM SYNTHETIC SOLUTIONS SIMULATING SPENT BATTERY LEACH LIQUORS

ROMEO RACZ[a], ADRIANA MANCIULEA[a], PETRU ILEA[a, *]

ABSTRACT. Electrochemical power cells with MnO$_2$ cathode represent an important waste group. After discharge, trough leaching and anodic electrosynthesis, this oxide can be recovered. Pure titanium represents an interesting substrate for this process both economically and environmentally.

In H$_2$SO$_4$ electrolytes titanium exhibits active corrosion, active–passive transition and passive voltage regions. At higher polarization, dielectric breakdown of the passive layer occurs, resulting in oxygen evolution. In the presence of Mn^{2+} ions the titanium active corrosion is inhibited and at higher potentials oxidation of the manganese ions occurs. Anodic surface modification by potentiostatic sweeping is proposed in presence of Mn^{2+} ions. During MnO$_2$ electrosynthesis tests on the modified electrode, no passivation was observed, which is not in agreement with the literature. Our measurements prove the feasibility of titanium usage as an anode in the electrolytic recovery route of MnO$_2$ from spent household Zn-Mn battery leach liquors.

Keywords: *titanium; corrosion; passivation; EMD; spent battery leach liquors*

INTRODUCTION

Latest European Environmental Agency's waste management indicators show, despite existing regulations, that waste quantity generated per capita did not drop in the last 11 years and might increase in the near future [1]. When discarded improperly, spent batteries represent 12% (%w/w) of the household waste, resulting an important pollution source in terms of heavy metal content [2].

Our interest is to find an advantageous technology for manganese recovery from spent Zn - Mn batteries trough sustainable process intensification and environmentally friendly process development. The conversion of the reacted manganese from spent household batteries to manganese dioxide through an electrochemical route represents an attractive opportunity both environmentally and economically.

---

[a] Department of Physical Chemistry, "Babes-Bolyai" University, 1, M. Kogalniceanu St., 400084 Cluj-Napoca, Romania

* pilea@chem.ubbcluj.ro

In recent years main interest has been focused on the development of new processes for recycling discarded materials; particularly on the possibility of high value metal recovery from spent batteries [3]. Numerous studies have been published regarding pyrometallurgical and hydrometallurgical routes for heavy metal recovery from low-grade ores and may be feasible for their recovery from spent batteries as well [4,5].

As earlier reported by different authors, the production of electro-synthetic MnO_2 (EMD) is carried out through the electrolysis of hot $MnSO_4$ and sulphuric acid solutions. Prior to the synthesis process, metals are leached away from their oxides with acid or alkali solutions or reacted in presence of an oxidizing or reducing agent [6,7] in order to completely or partially extract them from the solid to the liquid phase. Resulted liquors can be subjected to purification or can be processed as they are for MnO_2 electrowinning through anodic oxidation of Mn^{2+} ions present in the solution.

Choosing the adequate anodic material for the MnO_2 electrowinning process is essential. Large overpotential for the oxygen evolution reaction (OER), structural compatibility with the electrocrystallized material, chemical and electrochemical stability, ease of maintenance and cost-effectiveness are attributes of the appropriate substrate.

Literature reports a series of tested materials such as graphite [8], carbon nanotubes [9], lead and it's alloys with Sn, Sb, Ag [10] and lately titanium as anodic substrate because electrocrystallized EMD is of higher purity than one obtained on other substrates [11].

In the galvanic series of metals, titanium has a standard potential of −1.63 V which is close to aluminium. Therefore, titanium cannot be considered as being intrinsically noble. Yet, the excellent resistance of titanium to general corrosion in most environments is well known. This is the result of a stable protective surface film, which consists basically of TiO_2. This thin oxide film passivates titanium as long as the integrity of the film is maintained.

In electrochemical processes, when used as anodic material, the titanium's passivation is unwanted because of the low electric conductivity resulting in high-energy consumption. Nevertheless, in order to control this phenomenon several surface modification and passivation control techniques have been reported; literature lists as follows: surface coating with (3–5 μm) platinum film [12], heated platinum plated Ti anode [13], RuO_2 and IrO_2 coatings [14], anodic substrate activation through thermal-diffusion coating [15] β-PbO_2 coating and mixture of melted metallic titanium with graphite [11]. By surface modification with the previously listed techniques, a film can be developed which improves MnO_2 electrosynthesis on titanium.

When immersed in H_2SO_4, the dissolution of metallic titanium in the active state can be described by the presence of the following reactions [16]:

$$Ti \rightarrow Ti^{2+} + 2e^- \qquad \varepsilon^0 = -1.63 \text{ V/NHE} \qquad (1)$$

$$Ti \rightarrow Ti^{3+} + 3e^- \qquad \varepsilon^0 = -1.37 \text{ V/NHE} \qquad (2)$$
$$Ti \rightarrow Ti^{4+} + 4e^- \qquad \varepsilon^0 = -0.91 \text{ V/NHE} \qquad (3)$$
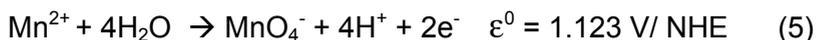
Since the lower valence titanium oxides are not stable in H_2SO_4 media [17], and no direct passivation can take place, reactions 1 and 2 have the highest probability to occur. Ma and Perré [18] suggest that metallic titanium corrosion in sulphuric acid (concentration range 0.1M – 1M) is due to the formation of the anion $[Ti(SO_4)_{2x}]^{-2x}$. With increasing acid concentration the formation of $[TiO_2(SO_4)_x]^{-2x}$ mainly occurs. These anions supposed to break down resulting in TiO_2.

According to M. Metikos et al. [19] the composition of the anodic film on titanium changes with increasing polarization resulting the following types of oxides:

$$TiH_x \rightarrow TiO \rightarrow Ti_2O_3 \cdot TiO_2 \rightarrow Ti_5O_9 \rightarrow Ti_6O_{11} \rightarrow Ti_3O_5 \rightarrow TiO_2 \quad (4)$$

Information about the manufacturing parameters of the titanium substrate becomes of interest because the substrate's crystal orientation highly promotes or retards the targeted oxide crystal formation [20] during MnO_2 electrosynthesis on Ti substrate with the following possible reactions [14]:

$$Mn^{2+} + 4H_2O \rightarrow MnO_4^- + 4H^+ + 2e^- \quad \varepsilon^0 = 1.123 \text{ V/ NHE} \quad (5)$$
$$2H_2O \rightarrow O_2 + 4H^+ + 4e^- \qquad\qquad \varepsilon^0 = 1.229 \text{ V/ NHE} \quad (6)$$
$$Mn^{2+} + 4H_2O \rightarrow MnO_4^- + 8H^+ + 5e^- \qquad \varepsilon^0 = 1.51 \text{ V/ NHE} \quad (7)$$
$$MnO_2 + 2H_2O \rightarrow MnO_4^- + 4H^+ + 3e^- \qquad \varepsilon^0 = 1.625 \text{ V/ NHE} \quad (8)$$

Titanium represents an efficient substrate for MnO_2 electrosynthesis from spent battery leach liquors, resulting in higher purity deposits and maintenance benefits by chemical and mechanical stability.

The aim of this study was to investigate the electrochemical behaviour of polarized metallic titanium in solutions similar in composition with one resulted from spent battery lixiviation, with application in MnO_2 electrosynthesis from the above solutions.

RESULTS AND DISSCUSIONS

Electrochemical corrosion measurements

Metallic titanium open circuit potential's (OCP) evolution was observed and registered, after immersion in 1M H_2SO_4 solutions in absence and presence of several Mn^{2+} concentrations (Figure 1).

A shift of the OCP values towards more positive potentials is observed in cases when different concentration of Mn^{2+} are present in the solution, as compared to metallic titanium in sulphuric acid solutions without additives, suggesting an interaction of Mn^{2+} with the anodic reaction of the corrosion process.
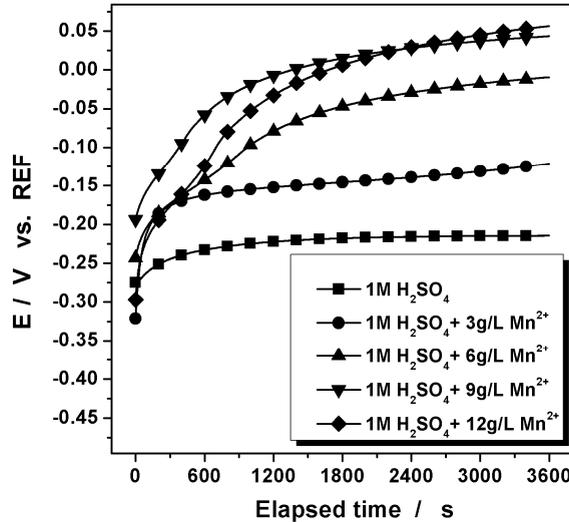
Figure 1. Titanium OCP evolution; Electrolyte: 1M H_2SO_4 in presence of several Mn^{2+} ion concentration [3 - 12g/L] Measurement duration: 1 h

The observed positivation of titanium OCP values with increasing Mn^{2+} concentration expresses an important decrease of the solutions corrosive effect on the titanium surface.

Polarization curves

Polarization measurements (Figure 2) were carried out in order to characterize the corrosion behaviour of the metallic titanium surface by applying the Stern - Geary theory [21], and by using Tafel interpretation.

According to the Stern-Geary theory, in the close vicinity of the open-circuit corrosion potential, the current density i is expressed by the following equation:

$$i = i_{corr}\, e^{[b_a(E-E_{corr})]} - e^{[b_c(E-E_{corr})]}$$

(9)

where b_a and b_c are the anodic and catodic activation coefficients.

Following the intricate active – passive behaviour of pure titanium in highly acidic sulphate solutions, the obtained polarization curves do not exhibit typical Tafel behaviour, and consequently an accurate evaluation of the corrosion parameters is not possible. However, the values of ε_{corr} and the corrosion current density, i_{corr}, were estimated near zero-overall current on the potential range of

±250 mV vs. OCP with a sweeping rate of 0.166 mVs^{-1}. Graphical representation of the polarisation curves is not shown. Evaluated parameters for the corrosion process are presented in Table 1.

Table 1. Parameters of the metallic titanium corrosion process

Solution	ε_{corr} (mV vs. REF)	i_{corr} (µA/cm^2)	$-b_c^*$ (mV^{-1})	b_a^* (mV^{-1})
1M H$_2$SO$_4$	-0.2	19	89	218
1M H$_2$SO$_4$+ 3g/L Mn^{2+}	-0.1	17	155	161
1M H$_2$SO$_4$+ 6g/L Mn^{2+}	0	15	98	139
1M H$_2$SO$_4$+ 9g/L Mn^{2+}	0.05	12	103	110
1M H$_2$SO$_4$+ 12g/L Mn^{2+}	0.04	10	86	118

*b_a and b_c are the Tafel anodic and cathodic activation coefficients

From the data presented in Table 1, positivation of the titanium's corrosion potential (ε_{corr}) and a slight diminishing of the corrosion current density can be noted, which corresponds to active corrosion inhibition of the metallic surface.

Voltammetry measurements

Linear voltammetry curves (LVC), presented in Figure 3, reveal four voltage regions: (i) active corrosion, (ii) active-passive transition, (iii) passivity and (iv) the voltage beyond which the dielectric breakdown of the passive film occurs. These observations are in good agreement with the cited literature [16, 22]. Each region from the polarization curve corresponds to different reactions, which occur with potential positivation.

Concurrent reactions [16] increase the number of geometrical faults in the formed TiO$_2$ layer and help the current passage.

The recorded polarization curves, with the addition of Mn^{2+} are presented in the inset of Figure 3, showing a clear dependence of the peak current with increasing Mn^{2+} concentration.

It is also notable that the presence of Mn^{2+} ions modifies the polarization curve's profile in region (iv), resulting in the breakdown of the insulating layer by the oxidation of manganese ions at ε_{ox}=~ 1.4 V/REF

MnO$_2$ electrocrystalization on metallic titanium in H$_2$SO$_4$ media occurs by the following global reaction:

$$Mn^{2+} + 2H_2O \rightarrow MnO_2 + 2e^- + 4H^+ \qquad \varepsilon^0 = 1.4 \text{ V/ NHE} \qquad (10)$$
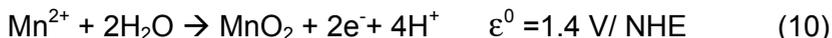
EMD crystal structures have been observed on the titanium surface by scanning electron microscope (see section 4).

Occurrence of these manganese oxides on the anodic surface leads to structural faults in the TiO_2 film, which leads to the breakdown of the so formed titanium oxide thin film and allows the oxidative electrosynthesis to occur [17].
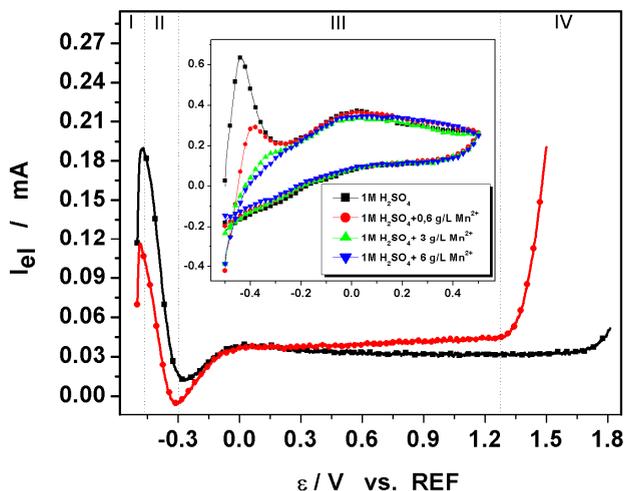

Figure 3. Metallic titanium polarization curves in the absence (■) and presence of Mn^{2+} ions (•). Inset: Titanium oxidation peak current evolution with the addition of different Mn^{2+} concentration

Activation of Ti electrode

Surface modification was required in order to use metallic titanium as a substrate for MnO_2 electrosynthesis. Several activation measurements have been performed in 1M H_2SO_4 and different concentrations of Mn^{2+}. By visual examination, an increasing number of MnO_2 germination centres on titanium have been noted with increasing manganese(II) ion concentration and have been considered for the further applied surface activation protocol.

Under potentiostatic control the previously cleaned (as described in the experimental section), metallic titanium (Figure 5a) was subjected to polarization in a solution with Mn^{2+} concentration similar with one resulted from spent battery lixiviation. During this process electrolytic manganese dioxide crystals developed as shown in Figure 5b.

The electrode surface modification was achieved in two steps and represents the surface activation protocol.

Metallic titanium has been immersed in a solution containing 6g/L Mn^{2+}. In the first step (S1) the potential was modified with 2 mVs^{-1} in the range from 0 to 1.5V/ REF. During the second step (S2) the potential was modified in the range from 1.5 to 1.7V/ REF with 2mVs^{-1}.

Preparation of the electrode by polarization technique in the first (S1) potential domain leads to the formation of a mixed TiO$_x$ and MnO$_x$ oxide film which protects the surface from passivation. During the second step (S2), by visual examination, the number of germination centres formed during S1 did not increase; growth of the existing crystalline formations has been noted. The switch from S1 to S2 was made by current interruption for 1 second and was considered responsible for the crystal growth instead of germination centre multiplication.

The potential value was varied below MnO$_4^-$ formation and oxygen evolution reaction at the electrochemical conditions.

Manganese dioxide electrosynthesis tests

The activated titanium electrode was inserted in a divided cell setup, composed by a modified titanium electrode (MTE), platinum counter electrode (PCE), Ag||AgCl/KCl$_{sat}$ reference electrode and a porous ceramic material for MTE separation from PCE.

During 4 hours of continuous electrolysis the MTE did not exhibit passivation or critical behaviour (Figure 4).

Under continuous stirring and constant temperature (22°C) a film of MnO$_2$ was deposited (Figure 5c) on the modified titanium surface from acidic spent battery leach liquor with an average concentration of 6 g/L Mn^{2+}.
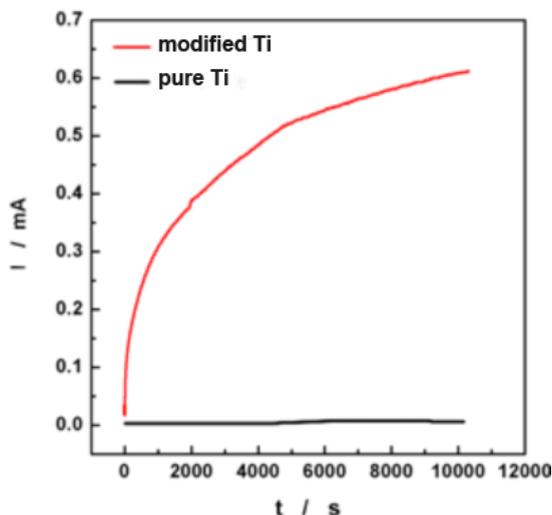

Figure 4. Current evolution on the pure and modified titanium electrode during potentiostatic electrolysis; working anodic potential ε = +1.7V/REF; Electrolyte: 1M H$_2$SO$_4$ (pH=0.5); Mn^{2+} 6g/L; w = 500 rpm

Surface and composition characterization of MTE

The electrode surface has been characterized by imaging techniques. After chemical treatment the titanium shows pitting corrosion morphologies (Figure. 5a), which underlines the treatment's efficiency regarding existing oxide removal as shown in Table 2. After electrolysis the manganese dioxide was observed as a compact crystalline formation localized on the metallic surface.

The deposit morphology has been determined by scanning electron microscopy (SEM) (Quanta 3D FEG). EDAX X-ray dispersive energy analyser attached to the SEM has been used to determine the chemical composition of the electrodeposited MnO_2. Results are shown in Table 3.

Table 2. EDAX analysis for metallic titanium surface

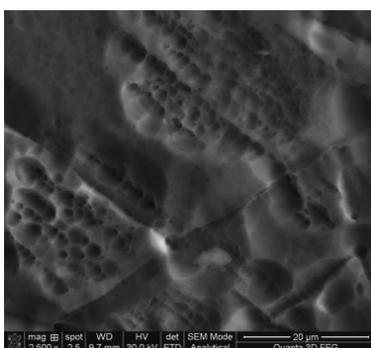| Element	Wt %	At %
N/A	1.72	0.37
Ti	98.28	99.63

Figure 5a. Pure metallic titanium surface before activation protocol;

Figure 5b. Manganese dioxide germination on Ti–after S2 step;
Electrolyte: 1M H_2SO_4 + 6g/L Mn^{2+}, pH=~0.5, sweep rate 2mVs^{-1}
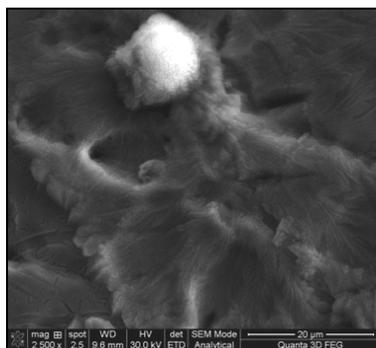
Figure 5c. Electrolytic manganese dioxide deposit after 3 hours electrosynthesis; Electrolyte: spent battery leach liquors, pH=~0.5, 6g/L Mn^{2+}, 1M H$_2$SO$_4$

In Figure 5b, electrolytic germination of manganese dioxide obtained after activation procedure S2 can be observed. Figure 5c. represents SEM imaging of the obtained MnO$_2$ deposit by potentiostatic electrolysis. The resulted crystal structure does not resemble specific manganese crystallization morphology but similar features with the electroactive γ - MnO$_2$ form can be observed.

Table 3. EDAX analysis for deposited MnO$_2$ (EMD)

on the modified titanium surface

Element	Wt %	At %
Mn	21.71	10.47
S	25.68	21.23
O	37.32	61.83
Ti	1.84	1.02
N/A	13.45	5.45

CONCLUSIONS

The influence of manganese (II) inclusion was studied on the electrochemical behaviour of commercially pure titanium in acidic electrolytes through open circuit potential measurements.

The presence of Mn^{2+} ions in the acidic electrolyte maintains good electric conductivity caused by formation of a mixed oxide film on the electrode surface. Based on these assumptions, a titanium surface activation technique was developed which allows MnO$_2$ electrosynthesis.

MnO_2 deposited during anodic polarization on the titanium surface, act as nucleation centre for the latter developing EMD film.

Commercially pure titanium anode surface modification prior to MnO_2 electrodeposition from spent battery leach liquors is essential.

By surface modification, titanium passivation has been delayed during anodic polarisation, from several tents of minutes as described in the literature, to several hundred minutes in our experimental conditions.

EXPERIMENTAL PART

Electrode preparation

The working electrode used in our experiments consisted of a 1 cm^2 titanium cylinder (ϕ = 2 mm). Before each measurement, in order to remove any pre-existing oxide film, the titanium surface was immersed for 33 seconds in a mixture composed of 25% HF and 75% HNO_3, washed with double distilled water, patted dry with a lint-free cloth then immersed in the electrolyte within the electrochemical cell.

Electrochemical cell and electrolytes

The cell used in this study consisted of a graded glass flask, in which the titanium working electrode and platinum counter electrode was immersed. In all measurements Ag||AgCl/KCl$_{sat}$ reference electrode (REF) was used. Before every experiment a magnetic stirrer was used for oxygen and hydrogen bubbles removal.

Solutions were prepared from *Merck* 98% H_2SO_4, *J.T. Baker* $MnSO_4$ (mono-hydrate) and double distilled water, without further purification.

Spent Zn-Mn batteries have been manually dismantled by removing external casing followed by the removal of the metal caps and plastic grommets. Remaining Zn anode and MnO_2 cathode were carefully separated and weighted. The resulted black powder was leached with 1M H_2SO_4 for 1 hour at room temperature.

Used equipment and software

For solid and liquid analysis Avanta PM GBC atomic absorption spectrophotometer was used. For surface characterization a scanning electron microscope (SEM) (Quanta 3D FEG) was used. For surface chemical analysis EDAX X-ray dispersive energy analyser attached to the SEM was applied.

Liquid and solid phases obtained during this study have been analysed by atomic absorption (AAS) technique for composition determination.

Electrochemical measurements have been done with PC controlled PARSTAT 2273 and Daltronix Electrochemical System, composed by DXC 238 potentiostat connected to a PC trough National Instruments (NI) DAQ hardware. Software packages used have been developed in our laboratory in NI Labview environment.

ACKNOWLEDGMENTS

REFERENCES

1. European Commission, Eurostat, Publications Office of the European Union, **2010**, 148-149.
2. I. De Michelis, F. Ferella, E. Karakaya, F. Beolchini, F. Veglio, *Journal of Power Sources*, **2007**, *172*, 975.
3. E. Sayilgan, T. Kukrer, G. Civelekoglu, F. Ferella, A. Akcil, F. Veglio, M. Kitis, *Hydrometallurgy*, **2009**, *97*, 158.
4. Wensheng Zhang, Chu Yong Cheng, *Hydrometallurgy*, **2007**, *89*, 137.
5. A.A. Baba, A.F. Adekola, R.B. Bale, *Journal of Hazardous Materials*, **2009**, *171*, 838.
6. E. Sayilgan, T. Kukrer, F. Ferella, A. Akcil, F. Veglio, M. Kitis, *Hydrometallurgy*, **2009**, *97*, 73.
7. Shun Myung Shin, Gamini Senanayake, Jeong-sooSohn, Jin-gu Kang, Dong-hyo Yang, Tae-hyun Kim, *Hydrometallurgy*, **2009**, *96*, 349.
8. Keqiang Ding, *International Journal of Electrochemical Science,* **2010**, *5*, 668 .
9. Yaohui Wang, Hao Liu, Xueliang Sun, Igor Zhitomirsky, *Scripta Materialia*, **2009**, *61*, 1079.
10. P. Ilea, I.-C. Popescu, M. Urda, L. Oniciu, *Hydrometallurgy*, **1997**, *46*, 149.
11. P. Ilea, "Electrosinteze anorganice", Casa Cărții de Știință, **2005**, 167.
12. A.G. Kholmogorov, A.M. Zyzhaev, U.S. Kononov, G.A. Moiseeva, G.L. Pashkov, *Hydrometallurgy*, **2001**, *56*, 1.

13. Yu. S. Kononov, G.L. Pashkov, V.V. Patrushev, A.G. Kholmogorov, V.P. Plekhanov, *Zhurnal Prikladnoi Khimii*, **2007**, *80*, 339.

14. Qifeng Wei, Xiulian Ren, Jie Du, Sijie Wei, SuRong Hu, *Minerals Engineering*, **2010**, *23*, 578.

15. S.V. Skopov, S.S. Naboichenko, L.I. Galkova, *Tsvetnaya Metallurgiya*, **2009**, *1*, 25.

16. W.B. Utomo, S.W. Donne, *Electrochimica Acta*, **2006**, *51*, 3338.

17. Z. Abdel Hady, J. Pagetti, *Journal of Applied Electrochemistry*, **1976**, *6*, 333.

18. Chuk-Ching Ma, Ernest M. Peres, *Industrial and Engineering Chemistry*, **1951**, *43*, 675.

19. M. Metikos-Hukovic, *Surface Technology*, **1985**, *24*, 273.

20. Gerd Lütjering, James C. Williams, *Engineering Materials and processes - Titanium – 2nd edition*, Springer, **2007**.

21. M. Stern, A.L. Geary, *Journal of Electrochemical Society*, **1957**, *104*, 56.

22. S.M.A. Hosseini, V.B. Sigh, *Materials Chemistry and Physics,* **1993**, *33*, 63.

COMPARATIVE STUDY OF SOLUBILIZATION METHODS FOR ZINC AND MANGANESE RECOVERY FROM SPENT BATTERIES

MIHAELA ANTON[a], ADRIANA MANCIULEA[a], PETRU ILEA[a, *]

ABSTRACT. The solubilization of used batteries components is of great scientific and economic interest, on account of recycling requirement of these wastes and recovery of valuable materials. In this paper, the recovery of zinc and manganese from Zn-$ZnCl_2$-MnO_2 (Zn-carbon) spent batteries was studied through chemical and electrochemical acid leaching experiments. Experimental parameters, such as acid concentration, solid: liquid ratio (S: L), temperature, time and current intensity were studied related to the dissolution of the black powder of the Zn-MnO_2 batteries. Leaching tests were carried out using H_2SO_4, in order to maximize zinc extraction and minimize Mn and Fe extraction. The best conditions for acid leaching (98 % of Zn, 24 % of Mn and 18 % of Fe) were obtained with 2 M H_2SO_4, S: L= 1:5, room temperature and 1 hour leaching time. The results of electrochemical experiments showed selective leaching of Zn, together with a good recovery of metallic Zn (99.99% purity) at the cathode.

Keywords: environmental protection, recycling, Zn–carbon batteries, chemical /electrochemical leaching.

INTRODUCTION

The zinc–carbon and Zn–MnO_2 alkaline batteries are included as non-rechargeable batteries (primary cells), which are designed to be fully discharged only once, and then discarded [1].

Zn–$ZnCl_2$-MnO_2 (Zn-C) used batteries, that account for almost 90% of waste batteries, are mainly composed of Zn, MnO_2, Fe and discharge yields such as ZnO, Mn_2O_3 [2]. The presence of iron is due to the dismantling mode and the electrochemical manufacture of MnO_2.

Currently, these spent electrochemical power sources are treated as wastes and dumped in landfills or incinerated, representing a serious pollutant in terms of metals content when discarded in an inappropriate way. While

---

[a] "Babes Bolyai" University, Faculty of Chemistry and Chemical Engineering, Kogălniceanu, No. 1, RO- 400084 Cluj- Napoca, Romania

* pilea@chem.ubbcluj.ro

the recycling and further reuse of metals from spent batteries are becoming essential due to environmental concerns, it is also important that these processes should be practical and cost-effective. The recycling of these wastes must be imperative and would offer economic benefits through the recovery of the valuable materials, as well as, the conservation of raw materials in the interest of the sustainable development. Recovered materials can be reused in battery production or other industries and would reduce the energy consumption and prevents pollution.

Several processes, as pyrometallurgical and hydrometallurgical, have been studied and developed to recover metals (Zn, Mn, Fe) and recycle batteries [3-8].

Depending on what follows in the recycling process, Zn and Mn recovery can be done in different ways, by means of acid and acid-reductive solubilization of black powder.

The use of different reducing agent in acidic leaching appears to be effective for solubilization of 80-90% Mn from spent batteries [4, 5]. Acid-reductive solubilization allows solubilization of large amounts of manganese, which will negatively influence the further recovery of zinc by electrodeposition [9-12].

To prevent electrode corrosion and to ensure high zinc purity, electrolytes must fulfil some minimum requirements related to metallic impurities concentrations. One of the most important metallic impurities is iron, because it is one of the major impurities. The maximum iron concentration tolerated in the electrolytic liquor is 10 mg/L [13]. As a result of this restriction, the liquor obtained in the leaching stage must be treated to remove most of this iron. Therefore it is necessary a separation of zinc, manganese and iron ions by precipitation from the leaching solution. The oxidative precipitation of manganese as insoluble manganese oxides, mainly MnO_2, has found a wide application for removal of manganese impurity from Zn, Co, and Ni electrowinning process. Various oxidants for Mn(II) have been studied and applied to the practical processes, including ozone, SO_2 /O_2 oxidizing mixture, Caro's acid, peroxydisulphuric acid, hypochlorite and chlorate [11, 14]. Additional manganese dioxide or potassium permanganate is usually introduced to the zinc sulphate electrolyte from the leaching process in order to oxidize iron impurities [15, 16].

By applying electrochemical processes to the black powder of spent batteries Mn^{2+} ions in the electrolyte is oxidized to MnO^{4-} which react immediately with Mn^{2+} to form Mn^{3+} and finally MnO_2 [17]. Therefore generation of MnO^{4-} ions determines the precipitation of MnO_2 and $Fe(OH)_3$, lowering Mn^{2+} and Fe^{2+} concentration in the leaching solution.

In this study, selective acid leaching of Zn from spent Zn–C batteries was investigated by chemical and combined chemical/electrochemical methods. Under these circumstances, the black powder (BP) was used as obtained from the batteries. The effect of various conditions of solubilization was investigated

such as sulphuric acid concentration, time, temperature, solid: liquid ratio and current intensity. Electrochemical experiments using low concentration of H_2SO_4 were performed in order to evaluate the improvement of Zn extraction compared to chemical solubilization.

RESULTS AND DISCUSSION

Metallic components of black powder from spent batteries

Black powder was divided in 5 granulometric classes and then solubilized using *aqua regia*. Metallic components concentrations measured by AAS method are presented in Table 1. Concerning the metals content, no relevant differences between different granulometric classes were observed. Therefore the experiments were carried out in the homogeneous mass of the material, without dividing it in granulometric classes. Metals content in black powder is in the range of those reported in the literature depending on the degree of discharge of the battery [7, 18].

Table 1. Metal content in the black powder (*)

Granulation (mm)	Zn %	Mn %	Fe %
3.15	16.7	25.0	0.42
2	22.4	30.6	0.80
1	22.7	30.0	0.78
0.5	20.5	31.0	0.97
<0.5	18.3	32.6	0.82

(*) percentages calculated in relation to the mass of solid taken for analysis; others miscellaneous parts (graphite and oxygen) represent the difference up to 100%.

Chemical solubilization

Acid concentration and solid-liquid ratio effects

The extraction degrees of Zn, Mn and Fe as a function of solid : liquid ratios (g/mL) at different concentrations of H_2SO_4 are shown in Figure 1.

At higher concentrations of H_2SO_4, for example 97% H_2SO_4 (data not shown), the extraction yield for Zn (6.84%) and Mn (7.13 %) were very low. Under these conditions, the leaching experiments were conducted with 0.5 M, 1 M and 2 M H_2SO_4.

As seen in Figure 1, in all cases, the leaching degree of Zn is much higher than for Mn and Fe.

Lower acid concentrations, 0.05 M H_2SO_4, provide a poor extraction degree, even with large S:L (Zn 51%, Mn 14%, 0.05 M H_2SO_4, S:L= 1:60, 1h, 25º C), while with increasing H_2SO_4 concentration, the extraction of metals increases.
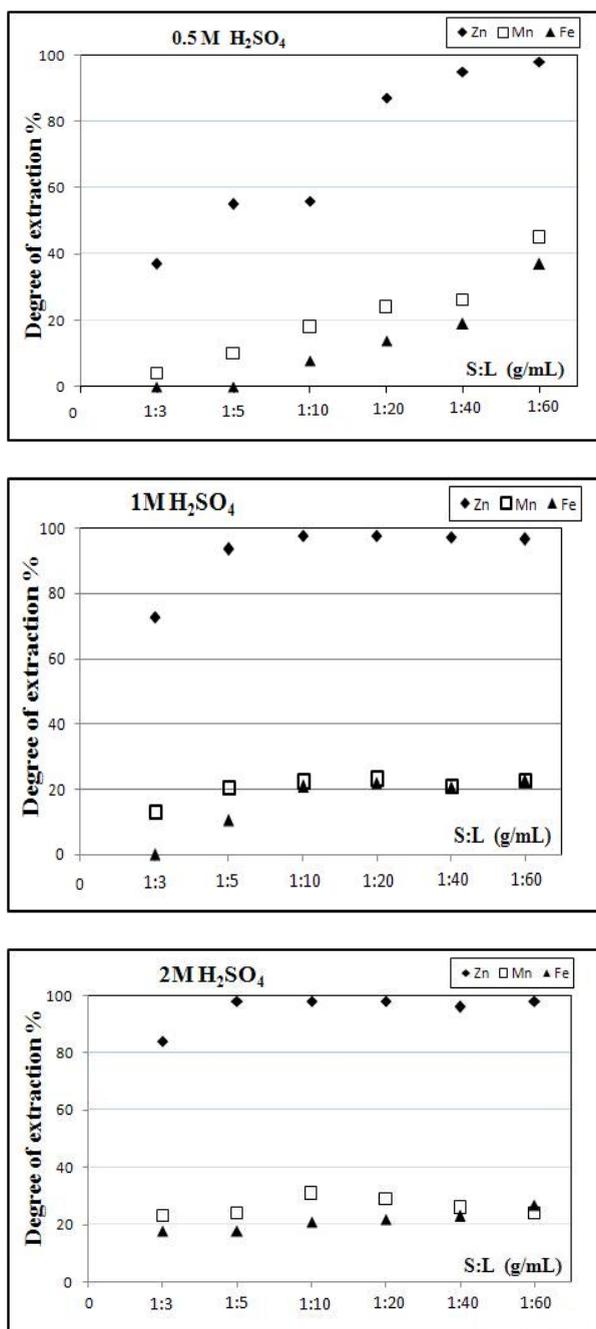
Figure 1. Influence of S:L ratio on the leaching degree of Zn, Mn and Fe after 1 hour, for different concentration of H_2SO_4, 25° C

Our aim was to have high extraction degree of zinc and minimum extraction degree for iron and manganese. For this reason, 2 M H_2SO_4 was considered sufficient, with a good leaching efficiency for S:L ratio of only 1:5. Figure 1 also shows that lower mixing ratios lead to an increase in the metals extraction degree. There are no relevant differences regarding the extraction yields between S:L of 1:5 and 1:40 or 1:60. Considering also that handling large volumes is difficult, the following experiments were carried out at S:L ratio of 1:5.

Effect of the solubilization time

Figure 2 shows the influence of time on the leaching of Zn, Mn and Fe in 1 M and 2 M H_2SO_4.
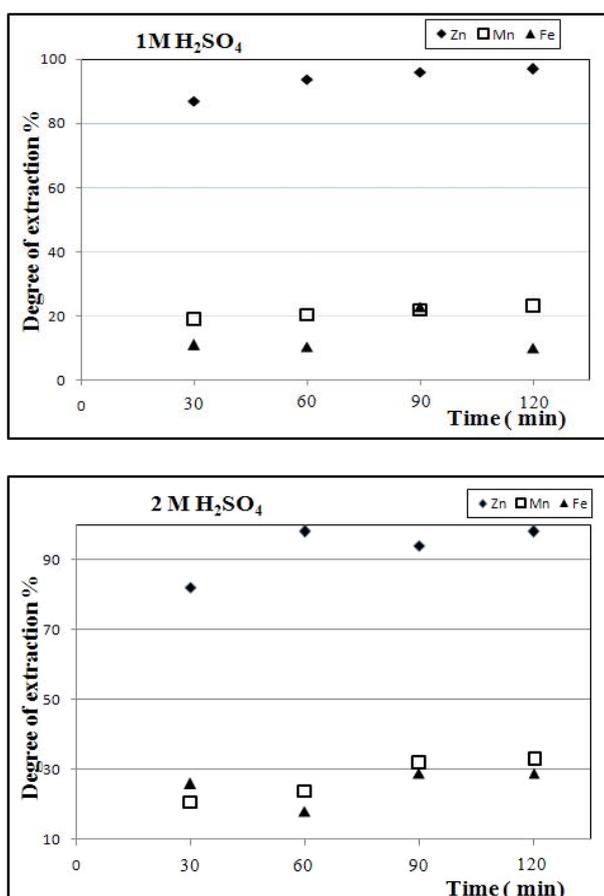
Figure 2. Influence of time on the extraction degree of Zn, Mn and Fe in 1 M and 2 M H_2SO_4 at 25°C

Given the low extraction degree of Zn during 1 h experiments, at S:L = 1:5 (55% Zn, 10% Mn), the time evaluation for 0.5 M H_2SO_4 was not considered necessary.

The extraction degree for Zn in 2 M H_2SO_4 had a 16% increase in time, from 30 to 60 minutes, whilst for Mn there is slight effect (3% increase). In 1 M H_2SO_4, the increase in metal extraction is not so great (7 % Zn, 2 % Mn from 30 to 60 minutes).

Increasing solubilization time from 30 to 120 minutes does not influence greatly the extraction degree of Zn and Mn.

Temperature effect

Figure 3 shows that the temperature has no major effect on the leaching of Zn in the range 25–80°C. At temperatures between 25 and 80 °C almost all the Zn is leached with 1 M and 2 M H_2SO_4. There is an increasing of Mn and Fe extraction degree with 2 M H_2SO_4 with the temperature increase. For Fe extraction with 1 M H_2SO_4 a decrease with temperature increase was observed.

Favorable impact of temperature increase will be analyzed in the following sections in conjunction with the others parameters.
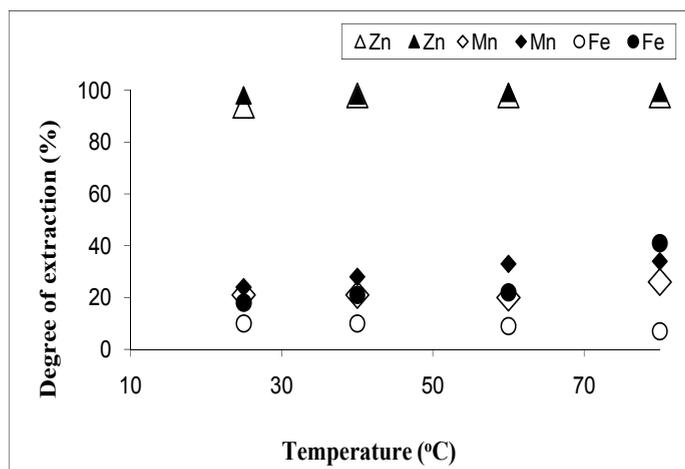
Figure 3. Influence of temperature on the leaching of Zn, Mn and Fe at different concentration of H_2SO_4, (Δ, ◊, o for 1 M and ▲, ♦, ● for 2 M H_2SO_4)

Comparative analysis of experimental data for chemical solubilization

Regarding the performance of chemical solubilization process reported to previous studies presented in literature the following comparisons can be made. Based on the study of Senanayake and co-workers [19], the best

228

leaching conditions for spent Zn–C batteries were: 1 M H_2SO_4, S: L= 1:10, 30-32 ^{o}C and 1 hour when the extraction efficiency obtained were 98% Zn and 35% Mn. Our experiments showed that the most favourable conditions for the extraction of zinc from BP are: 2 M H_2SO_4, S: L = 1:5, 25 ^{o}C and 1 hour. These conditions ensure the extraction of 98% Zn, 24% Mn and 18% Fe. In comparison with data reported by Senanayake and co-workers, the lower manganese leaching from our experiments is more convenient for the next step of Zn electroextraction process from leaching liquid. In other study carried out by El-Naidi *et al.* [18], the Zn and Mn efficiency extraction were lower (87% Zn and 7% Mn) than our results with the same H_2SO_4 concentration but higher temperature (50 ^{o}C) and longer time (2 hours).

Chemical/electrochemical solubilization of the black powder

To improve the performance of the solubilization process mixed solubilization tests (chemical and electrochemical) were carried out.

Table 2 shows the comparative results between the chemical extraction (C) and a mixed chemical/electrochemical (CE) extraction. Using these methods the degree of extraction in 0.5 and 2 M H_2SO_4, S:L = 1:10 and 1 hour of leaching time was evaluated. The CE method used an electrochemical reactor, operated galvanostatically at 0.2, 0.4 and 0.6 A, respectively. The Zn deposit was obtained on an Al cathode, with a purity of 99.99%, iron being the only impurity in the deposit.

As can be seen in Table 2, for 0.5 M H_2SO_4, by using electrochemical method the Zn solubilization was increased up to more then 80%, the Mn content decreased to 2-3% and the Fe solubilization decreased slightly.

Table 2. Degree of extraction for Zn, Mn and Fe by chemical and chemical/electrochemical solubilization in H_2SO_4 at 25ºC

Extraction methods	I(A)	H_2SO_4 concentration, M					
		0.5			2		
		Zn	Mn	Fe	Zn	Mn	Fe
		Extraction degree, %					
C	-	56	18	8	98	24	18
CE	0.2	90	3	7	96	27	23
	0.4	83	2	4	98	25	28
	0.6	91	3	5	96	17	20

For 2 M H_2SO_4, an attempt was made in order to assess the content of metals in relation to the applied current intensity. The results for the experiments at four current intensities (0.1, 0.2, 0.4, 0.6 A), S:L= 1:10 are shown in Figure 4.

It can be seen a decrease of the extraction degree for Mn and Fe with increasing the current intensities. The concentration level for Zn decreases due to the process of electrodeposition.
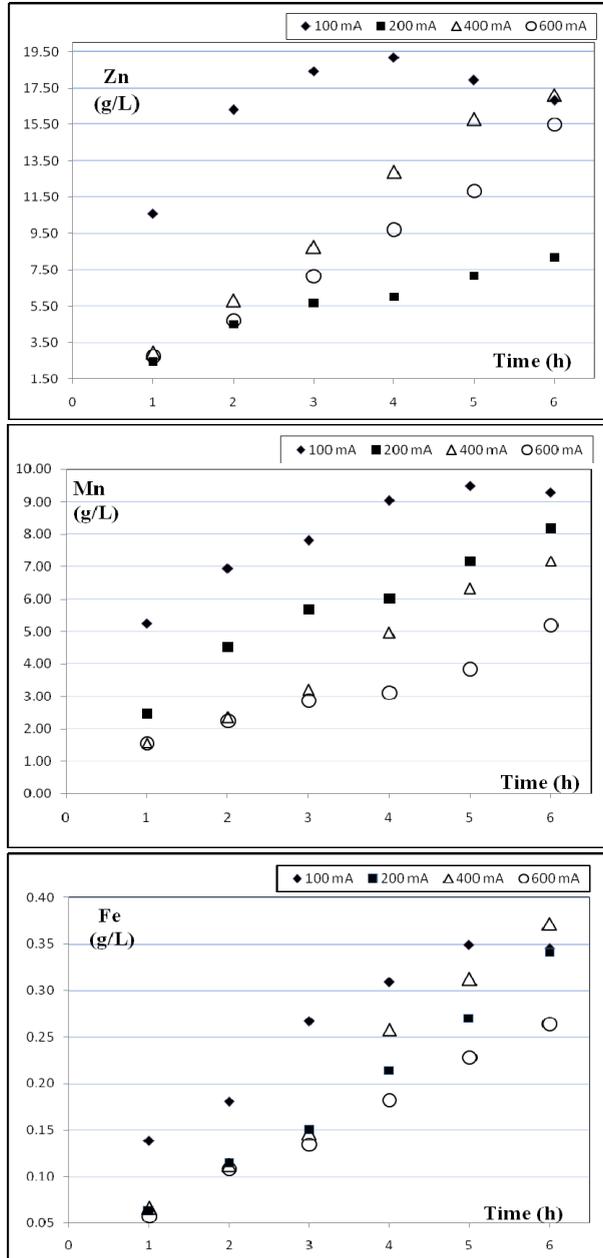

Figure 4. Variation of Zn, Mn and Fe concentration with time at different current intensities (0.1, 0.2, 0.4 and 0.6 A) with 2 M H_2SO_4, S: L= 1:10.

In the electrochemical experiments with 0.5 M H_2SO_4, the low degree of extraction for Mn and Fe can be explained by the oxidative precipitation of manganese and iron as insoluble compounds, mainly MnO_2 and $Fe(OH)_3$. During the anodic solubilization process, the electrolyte solution had pink coloration specific to MnO_4^- ions, which oxidized Mn(II) and Fe(II) to higher valence oxides.

CONCLUSIONS

The appropriate leaching conditions of BP Zn-C spent batteries, by using chemical and electrochemical methods, were investigated in order to obtain a high extraction of zinc and to minimize the iron and manganese solubilization. Chemical solubilization was evaluated taking into consideration the influence of different parameters such as acid concentration, solid-liquid mixing ratio, solubilization time and temperature. The results showed that the increasing of acid concentration leads to an increase in the degree of extraction. For a mixing ratio S: L = 1:5, provided a degree of extraction of 94-98% Zn, 21-24% Mn and 10-18% Fe in 1 M or 2 M H_2SO_4, in 1 hour.

The combined chemical and electrochemical solubilization using diluted H_2SO_4 allowed efficient manganese and iron removal at room temperature, by oxidative precipitation, avoiding high temperature alternative processes and addition of other reagents.

When the current intensity increases from 0.2 A to 0.6 A, the combined solubilization in 2 M H_2SO_4 showed a decrease in Mn and Fe concentrations with approximately 60%, respectively 70%, due to the oxidative precipitation without supplementary addition of reagents. Under these circumstances, the subsequent electroextraction of pure Zn is simpler and more efficient than in presence of higher concentrations of Mn and Fe.

EXPERIMENTAL SECTION

The reagents used were of analytical reagent (AR) grade. The leaching solutions consisted of aqua regia (3:1 HCl: HNO_3 ratio), H_2SO_4 solutions at specified concentrations.

Spent Zn-carbon batteries, collected from waste yard and used during this study were R20 size. These cells were manually cut into halves along with their longitudinal axes using a saw blade. The active paste inside the cell has been removed and its weight represented 71% of the total weight of the spent batteries. Black powder, a mixture of MnO_2, ZnO, $ZnCl_2$, FeO and coal, was crushed after being disassembled and divided into granulometric classes <0.5 mm, 0.5 mm, 1 mm, 2 mm, 3.15 mm. Metal content was determined by atomic absorption spectroscopy (AAS) for each grain size class in part by solubilization in aqua regia for 2 hours, 1:10 ratio (Table 1).

Chemical leaching was performed under constant stirring, using H_2SO_4 (concentration: 0.5 M, 1 M, 2 M), different solid: liquid ratios (1:3, 1:5, 1:10, 1:20, 1:40, 1:60), time (30, 60, 90, 120 minutes).

The electrochemical experiments were performed using a DXC240 computer controlled bipotentiostat. Anodic solubilization tests were carried out in 0.5 M and 2 M H_2SO_4, in a volume of 100 mL. The current intensity values were from 0.1 A to 0.6 A, in order to investigate the degree of extraction of metals from black powder. Working electrodes used were aluminium plate (4.8 cm^2) as a cathode and lead (16.8 cm^2) as current collector. Lead plate was inserted in a nylon bag, which contained the black powder of batteries and then immersed in electrolyte solution.

ACKNOWLEDGEMENTS

REFERENCES

1. C.C. Bueno Martha de Souza, D. Corrêa de Oliveira, J.A. Soares Tenório, *Journal of Power Sources*, **2001**, *103*, 120.

2. S.M. Shin, G. Senanayake, J. Sohn, J. Kang, D. Yang, T. Kim, *Hydrometallurgy*, **2009**, *96*, 349.

3. A.M. Bernardes, D.C.R. Espinosa, J.A.S. Tenório, *Journal of Power Sources*, **2004**, *130*, 291.

4. E. Sayilgan, T. Kukrer, N.O. Yigit, G. Civelekoglu, M. Kitis, *Journal of Hazardous Materials,* **2009**, *173*, 137.

5. E. Sayilgan T. Kukrer, F. Ferella, A. Akcil, F. Veglio, M. Kitis, *Hydrometallurgy,* **2009**, *97*, 73.

6. C.C. Bueno Martha de Souza, J.A.S. Tenório, *Journal of Power Sources*, **2004**, *136*, 191.

7. L.R.S. Veloso, L.E. Oliveira Carmo Rodrigues, D.A. Ferreira, F.S. Magalhães, M.B. Mansur, *Journal of Power Sources*, **2005**, *152*, 295.

8. A.A. Baba, A.F. Adekola, R.B. Baleb, *Journal of Hazardous Materials*, **2009**, *171*, 838.

9. Q.B. Zhang, Y. Hua, *Hydrometallurgy*, **2009**, *99*, 249.

10. I. Ivanov, Y. Stefanov, *Hydrometallurgy*, **2002**, *64*, 181.

11. W. Zhang, C.Y. Cheng*, Hydrometallurgy*, **2007**, *89*, 178.

12. L. Muresan, G. Maurin, L. Oniciu, D. Gaga, *Hydrometallurgy*, **1996**, *43*, 345.

13. P.E. Tsakiridis, P. Oustadakis, A. Katsiapi, S. Agatzini-Leonardou, *Journal of Hazardaous Materials*, **2010**, *179*, 8.

14. J. Avraamides, G. Senanayake, R. Clegg, *Journal of Power Sources*, **2006**,*159*, 1488.

15. D. Filippou, *Mineral Processing and Extractive Metallurgy Review*, **2004**, *25*, 205.

16. D. Herrero, P.L. Arias, J.F. Cambra, N. Antuñano, *Hydrometallurgy*, **2011**, *105*, 370.

17. P. Yu, T.J. O'Keefe*, Journal of the Electrochemical Society*, **2002**, *149*, A558.

18. Y.A. El-Nadi, J.A. Daoud, H.F. Aly, *Journal of Hazardous Materials*, **2007**, *143*, 328.

19. G. Senayake, S.M. Shin, A. Senaputra, A. Winn, D. Pugaev, J. Avraamides, J.S. Sohn, D.J. Kim, *Hydrometallurgy,* **2010**, *105*, 36.

ETHANOL DETERMINATION IN SUGAR BEET FERMENTATION LIQUID BY FULL EVAPORATION HEADSPACE GAS CHROMATOGRAPHIC METHOD

ADRIANA GOG[a, *], LACRAMIOARA SENILA[a], SIMONA BARSAN[a], ANCUTA PUSCAS[a], EMIL LUCA[b]

ABSTRACT. This paper reports a full evaporation (FE) headspace gas chromatographic (HS-GC) method for rapid determination of ethanol in sugar beet fermentation liquid. In this method, a very small volume,10 µL of sugar beet fermentation liquid sample is introduced into a headspace sample vial and heated up to a temperature of 105 ºC, when a full evaporation can be achieved within 3 min. The ethanol in the headspace of the vial is then measured by GC-FID. The full evaporation technique showed a good reproducibility, with a relative standard deviation less than 2.54% for six measurements. The method was verified by using spiked fermentation samples with different volumes of standard ethanol solution when ethanol concentrations were determined together with their corresponding confidence intervals, the relative standard deviations and the recovery degrees. The relative standard deviations ranged from 1.18% to 2.59% and the recovery degrees ranged from 88.7% to 92.6%. The present method is simple, rapid and requires no sample pretreatment.

Keywords: ethanol, sugar beet fermentation liquid, full evaporation headspace

INTRODUCTION

Bioethanol can be a suitable alternative to replace fossil fuels and represents one of the key for reducing pressure on the levels of atmospheric carbon. Bioethanol can be produced from fermentation of corn grain (wheat, barley and rye), sugar beet, sugar cane and vegetable residues [1, 2]. Today, bioethanol produced from cereals and biodiesel from rape seed are the two biofuels obtained from agriculture in Europe.

The bioconversion of sugar beet to bioethanol contains three steps: extraction of sugars from sugar beet chips (hydrolysis), fermentation of sugars and bioethanol distillation/analysis [3].

---

[a] INCDO-INOE 2000 Research Institute for Analytical Instrumentation - ICIA, 67 Donath St. 400293 Cluj-Napoca, Romania, *adriana.gog@icia.ro*
[b] University of Agricultural Sciences and Veterinary Medicine Cluj-Napoca, Faculty of Horticulture, 3 Calea Manastur St., 400372 Cluj-Napoca, Romania

Ethanol can be produced either from molasses, which is a by-product after the sugar is extracted, or directly obtained from sherbet.

In present work, sugar beet was converted to bioethanol production by direct fermentation (without previous hydrolysis) of its sugars (sucrose) by solid state fermentation (SSF) [4].

The quantification of ethanol during the fermentation process plays an important role in food industry researches. Many methods are used for ethanol determination from the fermentation liquids like colorimetry [5,6] enzymatic methods [7,8], dichromate oxidation [9], high performance liquid chromatography [10,11] and gas chromatography [12,13].

The fermentation liquids have a very complex composition, thus, together with the suspended yeast they contain many non-volatile compounds such as sugars, colored substances etc. Therefore laborious and time-consuming pretreatment procedures are necessary to remove the compounds that interfere in the ethanol quantification. For this reason it is necessary to develop simple and accurate methods for ethanol quantification during the fermentation processes.

Headspace gas chromatography (HS-GC) proved an effective technique for measuring volatile species in samples with complex matrices [14,15]. The advantage of the headspace sampling is that direct liquid or solid probing is avoided and complex sample matrix in a liquid or solid sample can be simplified or even eliminated in its vapor phase. The full evaporation (FE) technique was one of the early headspace - gas chromatographic techniques. It utilizes the headspace sampler as an evaporator rather than an enclosed static vapor-liquid equilibrium space to achieve quantitative analysis of volatile species in samples. The technique was initially developed by Markelov and Guzowski [16] in 1993. A very small sample size was used in a sample vial to achieve a near-complete evaporation or transfer of analytes from a condensed matrix into a vapor phase in the headspace of the sample vial in a very short period of time; therefore sample pretreatments are not required. The method is based on the near-complete transfer of the analyte into the vapor phase and then the measurement of the volatile species in the headspace by GC [17]. This method has been successfully used in several studies reported in the literature [18-20].

The objective of the present study was to develop a simple full evaporation headspace GC method for the rapid determination of ethanol from sugar beet fermentation liquid samples. The method has been developed using a (5%-phenyl)-methylpolysiloxane column, a non-polar capillary column with greater thermal stability and with a wide range of applications, including the analysis of alcohols [21]. After the fermentation process was finished the ethanol formed was separated from the fermentation liquid using a fractionated distillation process. The ethanol thus obtained was further analyzed using the same full evaporation headspace GC technique for the identification of methanol and C3-C5 higher saturated alcohols. In order to have a good

separation of C3-C5 higher saturated alcohols the non-polar column was replaced with a polar column, with a polyethylene glycol stationary phase. Although for this column damage occurs at lower temperatures and lower oxygen levels, its separation characteristics proved useful in the case of C3-C5 higher saturated alcohols.

RESULTS AND DISCUSSION

Analysis of sugar beet fermentation sample using FE-HS-GC-FID method

The GC chromatogram of a sugar-beet fermentation sample analyzed using FE headspace analysis is shown in Fig.1. It can be seen that the ethanol, the major component present in the sample gave the highest peak in the chromatogram at the retention time of 4.430 min, and is clearly separated from methanol, another volatile compound identified in the fermentation sample.
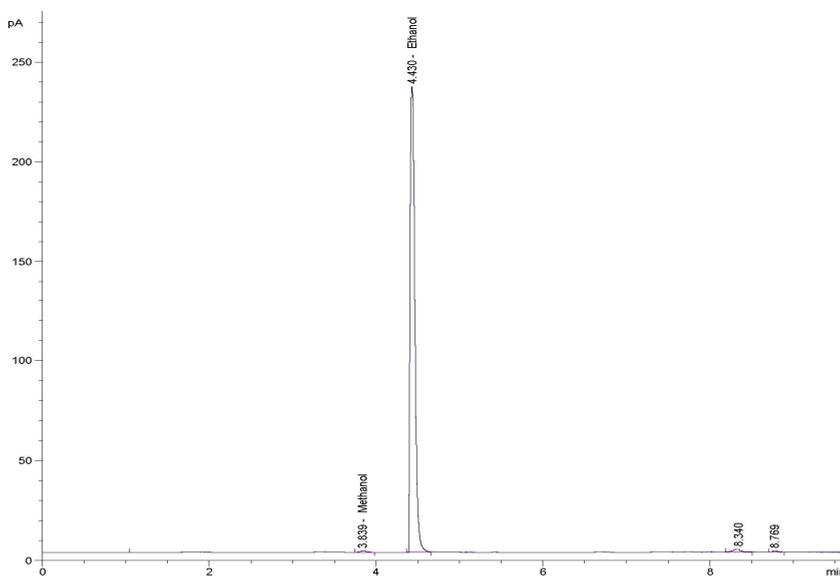
Figure 1. Chromatogram of a sugar-beet fermentation sample analyzed using FE-HS-GC method

Method validation

In the present study an external standard calibration was used for the ethanol quantification by full evaporation headspace method using a standard ethanol solution of 10 g/L. The calibration was realized by adding different volumes (5, 10, 15, 20, 25, 50 µl) of the standard ethanol solution into a set of headspace vials followed by immediate capping of headspace

vials, sample incubation in the headspace oven and gas chromatographic analysis. After the GC analysis of the standard solutions used for calibration, the following calibration curve was obtained:

$$y = 3.32(\pm 0.06) \times m + 309(\pm 16.4)$$

where y represents the gas chromatographic response (ethanol area) and m represents the absolute amount (in µg) of ethanol from the sample analyzed. The method was linear between 50 and 500 µg, with a regression coefficient of 0.9994 (n=6). The 95% confidence intervals ($\alpha = 0.05$, 4 degrees of freedom) for the slope and y-intercept of the calibration curve were 3.32±0.17 and 309±45.5 respectively. The full evaporation technique showed a good reproducibility, with a relative standard deviation less than 2.54% for six measurements.

The present method was verified by using spiked fermentation samples with ethanol. The sugar beet fermentation liquid used as reference was analyzed by FE-HS-GC in order to determine the initial content of ethanol (before adding ethanol). The initial concentration of ethanol in the sugar beet fermentation sample was 3260 mg/L. A volume of 500 µL fermentation sample was spiked with the following volumes of 10 g/L standard ethanol solution: 5, 10, 15, 20, 25 µL. Thus, the recovery grade of full evaporation method could be determined by comparing the theoretical values of ethanol from the spiked samples with the measured values using this technique. The variation of the methodology was expressed as confidence intervals (95%) of the ethanol concentrations measured. Table 1 shows ethanol concentrations, the relative standard deviations and the recovery degrees for the determination of ethanol concentration from the spiked sugar beet fermentation samples.

Table 1. Verification of the FE-HS-GC method using spiked fermentation samples with different volumes of standard ethanol solution. Theoretical and measured concentrations (mean ± confidence interval), relative standard deviations (RSDs) and recovery degrees in the analyses of spiked fermentation samples (n=3)

Spiked sample no.	Initial ethanol concentration of fermentation sample (mg/L)	Added volume of standard ethanol solution (µL)	Ethanol concentration of spiked samples (mg/L)		RSD[b] (%)	Recovery degree[d] (%)
			Theoretical values	Measured values[a]		
1	3260	5	8260	7360±474	2.59	89.1
2	3260	10	13260	11762±418	1.43	88.7
3	3260	15	18260	16872±494	1.18	92.4
4	3260	20	23260	21050±675	1.29	90.5
5	3260	25	28260	26169±765	1.18	92.6

[a] Mean ± confidence interval (n=3, confidence level: 95%)
[b] Relative standard deviation
[d] Mean value (n=3)

The results obtained are similar with those reported by Li et al. [18].

Identification of methanol and higher alcohols in distilled ethanol sample using FE-HS-GC-FID method

Ethanol formed during sugar beet fermentation process was separated from the fermentation liquid by fractionate distillation. The FE-HS-GC method was also used to identify methanol and higher alcohols that are present in distilled ethanol resulted from the sugar beet fermentation process. The headspace operating conditions used were the same as for ethanol quantification but for the separation process, a polar capillary column has been used, in order to separate the alcohols. The chromatogram obtained for the distilled ethanol sample is shown in Fig.2.
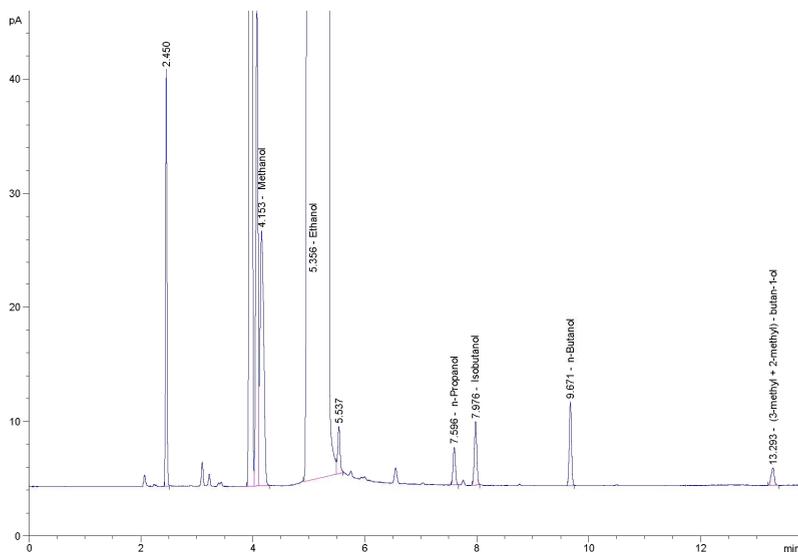
Figure 2. Chromatogram of a distilled ethanol sample analyzed using FE-HS-GC method

It can be seen that these alcohols are clearly separated with the exception of 3-methyl and 2-methyl-butan-1-ol, that being isomers are very difficult to be separated. The alcohols identified and their corresponding retention times are shown in Table 2.

Table 2. Identified alcohols in distilled ethanol using FE-HS-GC method

	Retention time RT (min)	Alcohol
1	4.153	Methanol
2	7.596	n-Propanol
3	7.976	Isobutanol
4	9.671	n-Butanol
5	13.293	(3-methyl+2-methyl)-butan-1-ol

Thus, the FE-HS-GC method could be successfully used for the identification of methanol and higher alcohols. Further studies are necessary in order to determine if this method is suitable for the quantification of methanol and higher alcohols from distilled ethanol.

CONCLUSIONS

A full evaporation headspace gas chromatographic method has been used to determine the ethanol in sugar beet fermentation liquid. The present method is simple, rapid, and accurate and can be successfully used to monitor ethanol formation during fermentation processes. It also can be used to identify higher alcohols that are present in distilled ethanol.

EXPERIMENTAL PART

Materials and methods

All chemicals used in this study were of analytical reagent-grade. Absolute ethanol, methanol, n-propanol, isobutanol, 3-methyl-isobutanol and 2-methyl-isobuthanol were purchased from Merck (Darmstadt, Germany). A standard ethanol solution of 10 g/L in water was used for external standard calibration. The analyzed sample was obtained from a sugar-beet fermentation process in a lab fermentation system. Headspace vials for the autosampler, magnetic caps with PTFE/silicone septa were purchased from Agilent Technologies (Palo Alto, CA, USA).

Gas chromatographic analysis

All measurements were carried out using an Agilent 7890A gas chromatograph (Agilent Technologies, Palo Alto, CA, USA) equipped with a CTC Combi PAL autosampler (CTC Analytics AG, Zwingen, Switzerland) and a flame ionization detector (FID). The GC operating conditions used for ethanol quantification were the following: HP-5 capillary column (J&W Scientific 19091J-413, length 30 m, inner diameter 320 μm and film thickness 250 μm); temperature program: 35 °C held for 10 min; helium carrier gas 1.2 ml/min, inlet temperature 250°C; detector temperature 250°C; the hydrogen and air flow rates 40 and 400 ml/min, respectively; helium makeup flow 30 ml/min. The GC operating conditions used for the identification of higher saturated alcohols were the following: DB-WAX capillary column (J&W Scientific 123-7032, length 30 m, inner diameter 320 μm and film thickness 250 μm); temperature program: 35 °C (5 min hold) to 150 °C at 5 °C/min then to 250 °C (2 min hold) at 20 °C/min; inlet temperature 220 °C; detector temperature 280 °C; helium carrier gas 1.5 ml/min; hydrogen and air flow rates 40 and 400 ml/min, respectively; helium makeup flow 30 ml/min.

The optimal parameters of the sample preparation and headspace operating conditions used in this study were selected according to other studies [17] in order to have complete ethanol evaporation. A volume of 10 μl

240

of sample solution was introduced into a 20 ml headspace vial followed by immediate capping of the headspace vial. The vial was placed in the headspace oven of the CTC Combi Pal autosampler and a 2.5 ml gastight headspace syringe was used to extract 1 ml of the gas phase in the headspace vials and inject into the GC.

Headspace operating conditions used for ethanol quantification and also for the identification of higher saturated alcohols were as follows: incubation time 5 min, incubation temperature 105 °C, agitation speed 750 rpm, syringe temperature 110°C, syringe flushing time 1 min.

REFERENCES

1. L.A. Rodríguez, M.E. Toro, F. Vazquez, M.L. Correa-Daneri, S.C. Gouiric, M.D. Vallejo, *International Journal of Hydrogen Energy*, **2010**, *35*, 5914.
2. E. İçöz, K.M. Tuğrul, A. Saral, E. İçöz, *Biomass and Bioenergy*, **2009**, *33*, 1.
3. B. Śantek, G. Gwehenberger, M.I. Śantek, M. Narodoslawsky, P. Horvat, *Resources, Conservation and Recycling*, **2010**, *54*, 872.
4. D. Krajnic, P. Glavič, *Chemical Engineering Research and Design*, **2009**, *87*, 1217.
5. J.P. Zanon, M.F.S. Peres, E.A.L. Gattas, *Enzyme and Microbial Technology*, **2007**, *40,* 466.
6. O.W. Lau, S.F. Luk, *International Journal of Food Science & Technology*, **1994**, *29*, 469.
7. M.V. Gonchar, M.M. Maidan, H.M. Pavlishko, A.A. Sibirny, *Food Technology and Biotechnology*, **2001**, *39*, 37.
8. J.E. Atwater, J.R. Akse, J. DeHart, R.R. Wheeler Jr., *Analytical Letters,* **1997**, *30*, 1445.
9. W. Hormitz, Official Methods of Analysis of the Association of Official Analytical Chemists, 12th ed., Association of Official Analytical Chemists, Washington, DC, **1980**.
10. F. Tagliaro, R. Dorizzi, S. Ghielmi, *Journal of chromatography. B, Biomedical applications*, **1991**, *566*, 333.
11. D. Lefebvre, V. Gabriel, Y. Vayssier, C. Fontagne-Faucher, *Lebensmittel-Wissenschaft und-Technologie*, **2002**, *35*, 407.
12. G.K. Buckee, A.P. Mundy, *Journal of the Institute of Brewing*, **1993**, *99*, 381.
13. D.G. McLachlan, P.D. Wheeler, G.G. Sims, *Journal of Agricultural and Food Chemistry*, **1999**, *47*, 217.
14. C. Ubeda, R.M. Callejón, C. Hidalgo, M.J. Torija, A. Mas, A.M. Troncoso, M.L. Morales, *Food Research International*, **2011**, *44*, 259.
15. J. Somuramasami, Y.-C. Wei, E.F. Soliman, A. M. Rustum, *Journal of Pharmaceutical and Biomedical Analysis*, **2011**, *54*, 242.

16. M. Markelov, J.P. Guzowski, *Analytica Chimica Acta*, 1993, *276*, 235.

17. B. Kolb, L.S. Ettre, "Static Headspace Gas Chromatography—Theory and Practice", Wiley-VCH, New York, **1997**.

18. H. Li, X.-S. Chai, Y. Deng, H. Zhan, S. Fu, *Journal of Chromatography A*, **2009**, *1216*, 169.

19. H. Li, X.-S. Chai, Y. Deng, H. Zhan, S. Fu, *Journal of Chromatography A*, **2010**, *1217*, 7616.

20. H.-C. Hu, X.-S. Chai, *Journal of Chromatography A*, **2012**, *1222*, 1.

21. http://www.labplus.co.kr/catalog/detailed_pages/Hp1n5.pdf.

ADHESIVE FRACTURE IN DOUBLE-LAP ADHESIVE ASSEMBLIES

O. NEMEŞ[a], A.M. CHIPER[a], A.R. RUS[a], O. TATARU[a], B.M. SOPORAN[a], P. BERE[a]

ABSTRACT. A comparative analysis of various double-lap assembly configurations was realized using a refined analytical model for the stress distribution. All the components of the stress field were defined function of the $\sigma_{xx}^{(1)}(x)$ stress in the first element and then introduced into the potential energy formulation. Using this analysis method allow to establish a Tsai-Hill type failure criterion.

Keywords: adhesives, double-lap joints, fracture criterion

INTRODUCTION

Starting with the work of Volkersen [1], other authors [2 - 12] have developed various models for single lap or double lap adhesive bonded joints. Some complex studies about various analytical models are compared by daSilva et al. [13]. By including the shearing strains, neglected until there, Tsai and Oplinger [14] were developed the existing models. Mortensen and Thomsen [15, 16] refined the approach for the analysis and design of various joints adhesively bonded by taking into account the influence of the interface effects between the adherents.

Performing a three-dimensional stress analysis on double-lap adhesive bonded joints under uniaxial tension, Bogdanovich and Kizhakkethara [17], have been determined the stress variation in the joint structure with a comprehensive three-dimensional numerical study, considering adhesive layers as 3-D elastic entities.

The model developed by Diaz Diaz et al. [18] assumed that the adhesive thickness is small compared to that of the adherents and the stresses to be uniform through the adhesive thickness. This model was validated by comparing the model results with those of a finite element calculation.

Minimizing the potential energy associated with the stress field and applying a variational method with some simplifying assumptions, the authors [19-21] developed and validated a new analytical model for a fast adhesive assembly analysis.

---

[a] Universitatea Tehnică din Cluj-Napoca

This work use a technique based on the minimization of the potential energy applied on various assembly configurations. After results analysis we can establish an adhesive failure criterion of Tsai-Hill type depending on the adhesive nature and properties.

RESULTS AND DISCUSSION

The analytical model developed by minimizing the potential energy [20] associated with the stress field will be used in the present study to analyze the influence of various parameters affecting the intensity and distribution of the stresses in double-lap adhesive assemblies. This analysis will be reduced to a study of the influence of materials type, adhesive type and thickness and overlap length. The adhesive thickness in the assembly is showed in figure 1 and the assembly parameters are presented in Table 1. The adhesive used in all those configurations is an epoxy adhesive, multipurpose, one component, heat curing thixotropic paste adhesive of high strength and toughness (Araldite AV 119) with the properties showed in Table 1.

e_c = 0,229 mm   e_c = 0,189 mm

e_c = 0,262 mm   e_c = 0,214 mm
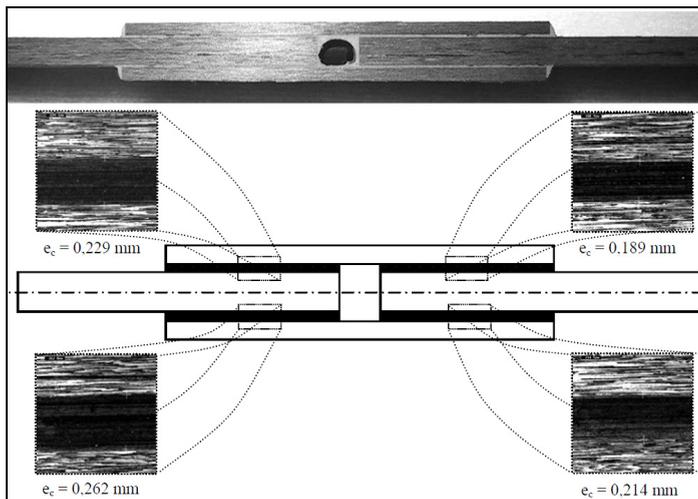
Figure 1. Adhesive thickness in double-lap adhesive bonded joint assemblies.

The stress distributions in the adhesive (Figure 2), for the analyzed configurations, shows the distributions of the peeling and shear stresses for the configurations showed in Table 1. We notice that for σ_{yy}, the maximum values are obtained on the free edges (z = 0, z = L) (Figure 2a) and they are localized at the edges. The balance between the maximum values are function of materials configuration and for τ_{xy}, we observe (Figure 2b) two peaks of stresses

250

Table 1. Double-lap adhesive assemblies configuration.

N°.	Substrate 1	Adhesive	substrate 2	e_1 [mm]	e_c [mm]	e_2 [mm]	L [mm]	F [N/mm]
1.	Titanium TA 6V E = 105000 MPa G = 40385 MPa υ = 0.3		Titanium TA 6V E = 105000 MPa G = 40385 MPa υ = 0.3	2	0.1	2	100	1
2.	Aluminium AU 4G E = 75000 MPa G = 28846 MPa υ = 0.3	Araldite AV 119 E_c = 2700 MPa G_c = 1000 MPa $υ_c$ = 0.35	Aluminium AU 4G E = 75000 MPa G = 28846 MPa υ = 0.3	2	0.1	2	100	1
3.	Glass/Epoxy ±45° E_x = 14470 MPa E_y = 14470 MPa G_{xy} = 12140 MPa υ = 0.508		Glass/Epoxy ±45° E_x = 14470 MPa E_y = 14470 MPa G_{xy} = 12140 MPa υ = 0.508	2	0.1	2	100	1

located at equal distances from the two free edges. The maximum value is varying function of assembly configuration and it is between 1 and 10 % of the applied force. The peaks do not have the same intensity because of the difference of rigidities of the two bonded adherents.
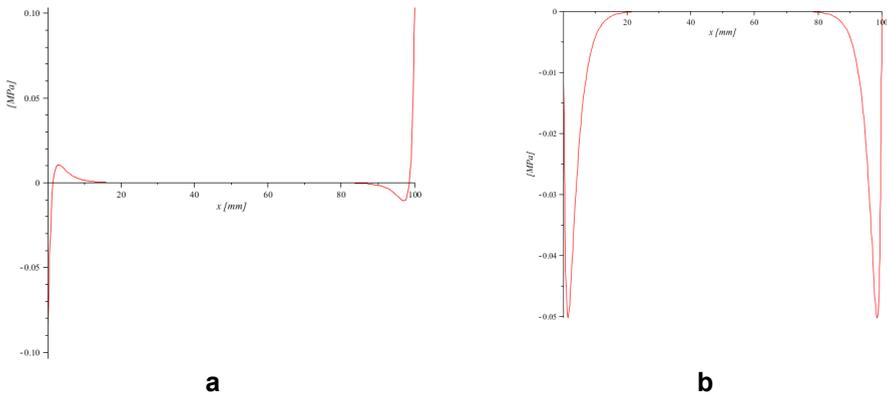

a   b

Figure 2. Stress distributions in the adhesive: a) Peeling stress (σ_{yy}); b) Shear stress (τ_{xy}). Config 3. (Table 1).

We note that the peeling stresses are greater than the shear stresses. The use of a fracture criterion for the adhesive bonded joint must take into account not only the shear stress τ_{xy} but also the peeling stress σ_{yy}. We can establish a failure criterion of the Hill-Tsai type as follows:

$$K_T = \underbrace{\left(\frac{\sigma_{yy}^{(c)}}{\sigma_R^{(c)}}\right)^2}_{K_\sigma} + \underbrace{\left(\frac{\tau_{xy}^{(c)}}{\tau_R^{(c)}}\right)^2}_{K_\tau} \qquad (1)$$

$$K_T \rightarrow \begin{cases} \geq 1 \text{ - failure} \\ < 1 \text{ - no failure} \end{cases} \qquad (2)$$

As showed in Figure 2 it should be noted that taking the peeling stresses into account is of primary importance.

The influence of adhesive thickness (e_c = 0.05; 0.1; 0.3; 0.5; 1 mm) on the intensity and distribution of shear and peeling stresses is shown in Figures 3 and 4. We observe that as the thickness of adhesive increases, the values of the stresses decrease at the free edges. The distribution tends to become uniform.
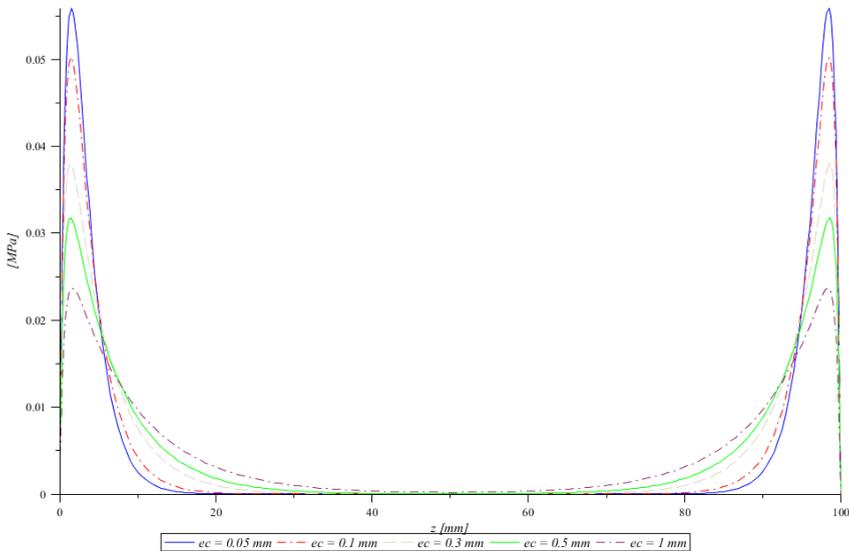
Figure 3. Shear stress (τ_{xy}) variation according to adhesive thickness length for config. 3 (Table 1).
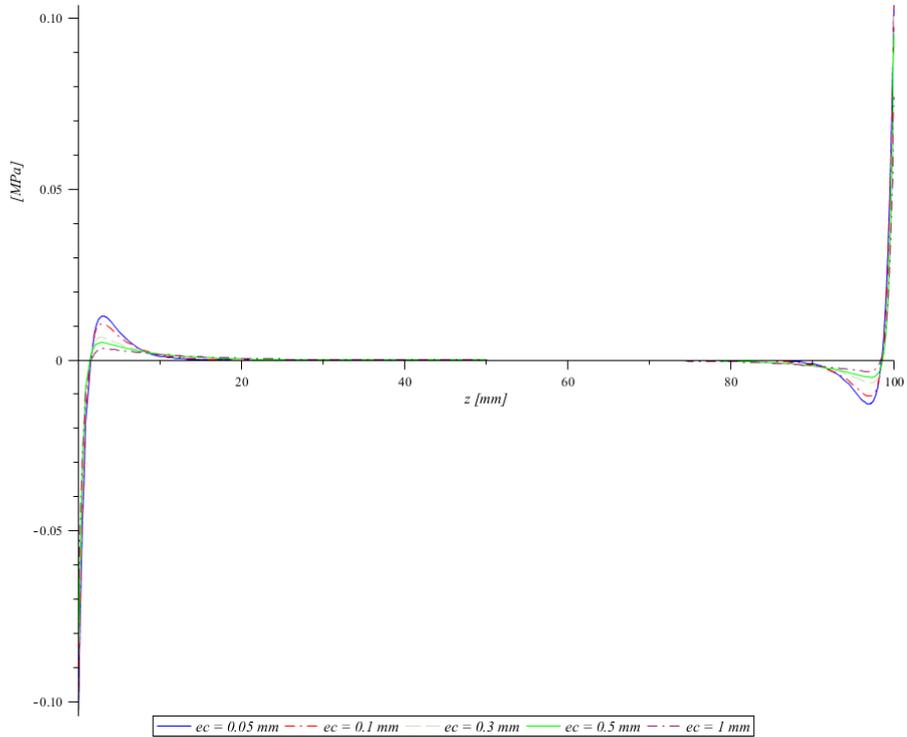
Figure 4. Peeling stress (σ_{yy}) variation according to adhesive thickness length for config. 3 (Table 1).

After the analysis of the suggested configuration and the influence of geometrical and physical parameters on the stress field we can observe that bonded composite assemblies have the same behaviour as metal adhesive-bonded joints.

CONCLUSIONS

Adhesive joining is a simple method of assembly where the adhesive properties define the performance of the adhesive bonded joints. The latest generations of adhesives, delivered in the form of film, make it possible to minimize the number of operations and increase the mechanical behaviour.

This analysis was carried out on the stress distribution in the substrates and the adhesive joint. The stress distribution in the adhesive remained very close to the solution given by finite elements performed by our research group [22]. This model is reliable and allows a fast analysis of double-lap adhesive joints assemblies.

253

ACKNOWLEDGEMENTS

REFERENCES

[1] O. Volkersen, *Die Luftfahrtforschung*, **1938**, *15*, 41.

[2] M. Goland, N.Y. Buffalo, E. Reissner, *Journal of Applied Mechanics*, **1944**, *66,* A17.

[3] L.J. Hart-Smith, NASA-CR-112236, **1973**.

[4] W.J. Renton, J.K. Vinson, *Journal of Applied Mechanics*, **1977**, 101.

[5] I.U. Ojalvo, H.L. Eidinoff, *AIAA Journal*, **1978**, *16,* 204.

[6] D.A. Bigwood, A.D. Crocombe, *Int. J. Adhes. Adhes.*, **1989**, *9,* 229.

[7] D.J. Allman, *Journal of Mechanical Applied Mathematics*, **1977**, *30,* 415.

[8] O. Volkersen, *Construction métallique*, **1965**, *4,* 3.

[9] Y. Gilibert, A. Rigolot, *Mécanique des solides*, **1979**, *288*, 287.

[10] Y. Gilibert, A. Rigolot, *Mécanique des solides*, **1979**, *288*, 287.

[11] Y. Gilibert, *Matériaux et techniques*, **1991**, 5.

[12] L. Tong, *International Journal of Solids Structures*, **1994**, *31*, 2919.

[13] L.F.M. da Silva, P.J.C. das Neves, R.D. Adams, J.K. Spelt, *Int. J. Adhes. Adhes.* **2009**, *29*, 319.

[14] M.Y. Tsai, D.W. Oplinger, J. Morton, *Int. J. Solid Structures,* **1998**, *35*, 1163-1185.

[15] F. Mortensen, O.T. Thomsen, *Composite Structures*, **2002**, *56*, 165.

[16] F. Mortensen, O.T. Thomsen, *Composite Science and Technology*, **2002**, *62*, 1011.

[17] A.E. Bogdanovich, I. Kizhakkethara, *Composites B*, **1999**, 30, 537.

[18] A. Diaz Diaz, R. Hadj-Ahmed, G. Foret, A. Ehrlacher, *Int. J. Adhes. Adhes,* **2009**, *29*, 67.

[19] O. Nemes, *Studia UBB Chemia*, **2007**, *52*, 175.

[20] O. Nemes, F. Lachaud, *Int. J. Adhes. Adhes*., **2010**, *30*, 288.

[21] O. Nemes, *Studia UBB Chemia*, **2010**, *55*, 389.

[22] O. Nemes, F. Lachaud, A. Mojtabi, M. Borzan, St. Grigoras, *Mater. Plast*., **2008**, *45*, 390.

NADH OXIDATION AT MELDOLA BLUE MODIFIED GLASSY CARBON ELECTRODES. A COMPARATIVE STUDY

CARMEN IOANA FORŢ[a, *], IONEL CĂTĂLIN POPESCU[b]

ABSTRACT. Three types of modified electrodes based on glassy carbon (powder and rod) and Meldola Blue (MB) were used for NADH electrocatalytic oxidation. MB was immobilized by simple adsorption on two different phosphates materials, crystalline zirconium phosphate (α-ZP) and crystalline titanium phosphate (α-TP), as well as on carbon aerogel (CA). The phosphate materials were incorporated in carbon paste, while CA was immobilized on a glassy carbon rod using a chitosan matrix. The basic electrochemistry of adsorbed MB and its ability to catalyze NADH electrooxidation have been investigated by cyclic voltammetry, performed in different experimental conditions (pH, potential scan rate, NADH concentration). The electroanalytical parameters of the investigated modified electrodes showed that: (i) irrespective the material, the formal standard potential of the immobilized MB was found pH dependent; (ii) the best electrocatalytic response was obtained for MB-αTP modified electrode.

Keywords: electrocatalysis, NADH electrooxidation, glassy carbon electrode, redox dyes

INTRODUCTION

Dehydrogenases represent the majority of redox enzymes. They require for the operation the presence $NAD(P)^+$ / NAD(P)H coenzyme. Consequently, the electrochemical regeneration of this coenzyme - in fact the oxidation of the reduced form, NAD(P)H - is an important issue. Indeed, for many years the electrochemical oxidation of NADH was studied, and it was concluded that in order to achieve this process at different conventional electrode materials relatively high overpotentials are required [1, 2] or is necessary the presence of a suitable redox mediator [3]. It is worth to add, that the direct electrochemical oxidation of NADH is accompanied by the electrode fouling, which is due to the NAD^+ adsorption on the electrode surface or to the side reactions involving the radicals generated during the coenzyme oxidation.

[a] "Babes-Bolyai" University, Laboratory of Electrochemical Research and Nonconventional Materials, 11, Arany J. St., 400028 Cluj-Napoca, Romania
[b] "Babes-Bolyai" University, Department of Physical Chemistry, 11, Arany J. St., 400028 Cluj-Napoca, Romania
[*] Corresponding author: iladiu@chem.ubbcluj.ro

One of the best mediators for NADH catalytic oxidation is Meldola Blue (MB), a phenoxazine compound involving two electrons and two protons [4, 5].

Excepting the water solubility of the MB, another reason for its immobilization onto different type of support materials is the shift of its formal standard potential (E°') towards more positive potentials, at a value allowing the operation of the modified electrode within the potential window essentially free of interfering reactions [6]. Previous studies showed that, when MB was directly adsorbed onto pyrolytic graphite, its E°' value was –175 mV *vs.* Ag|AgCl (at pH 7) [4], which is outside of the optimum window for amperometric detection [7]. Additionally, an increase of this E°' value will indirectly induce an increase of the rate constant for NADH electrocatalytic oxidation, which, actually, is large enough to be limited by the mass transport process [8, 9].

Due to their peculiar properties crystalline phosphates were used in many research areas as catalysts, ion exchangers, molecular sieves, and electrode materials [10]. Thus, because of their negatively charged phosphate groups, crystalline phosphates are good ion conductors and good ion exchangers (strong acidic materials). Additionally, they are layered materials, which present two important features: (i) the interlayer spaces can be adjusted to accommodate guests of different size; (ii) they have the control over the orientation, aggregation and distribution of the adsorbed guests [11].

Recently, carbon aerogels (CAs) were used as support material for the immobilization of different chemical species with catalytic properties [12]. CAs have interesting properties, such as high specific surface area, porosity, and electrical conductivity, associated with a good chemical stability. Therefore, CAs are attractive materials for different applications such as electrode materials in supercapacitors and rechargeable batteries, catalyst supports, adsorbent materials and thermal insulators [13].

In the present work carbon aerogel (CA), a high mesoporous material, was compared with crystalline zirconium phosphate (α-ZP) and crystalline titanium phosphate (α-TP) when all were used as support material for MB immobilization. The resulting modified materials, MB-αTP, MB-αZP and MB-CA, were deposited on two types of glassy carbon, Sigradur K powder (SK) or glassy carbon rod (GC) in order to obtain two MB modified carbon paste electrodes, (MB-αTP-SK-CPE) and MB-αZP-SK-CPE, and MB modified glassy carbon electrodes (MB-CA/GCEs). Aiming to estimate and compare their electroanalytical parameters, the electrochemical behavior of the obtained modified electrodes and their ability to catalyze the electrooxidation of NADH have been investigated by cyclic voltammetry, performed in different experimental conditions (pH, potential scan rate, NADH concentration).

RESULTS AND DISCUSSIONS

Electrochemical behavior of the MB modified GC electrodes

A comparison between the cyclic voltammograms (CVs) recorded at MB modified electrodes with similar measurements performed at electrodes without immobilized MB lead to observe that, as expected, no redox process occurred at electrodes in the absence of MB, while MB-αTP-SK-CPE (Sigradur K : MB-αTP = 19:1; w/w), MB-αZP-SK-CPE (Sigradur K : MB-αZP = 19:1; w/w), and MB-CA/GCE present one voltammetric peaks pair, which is due to the oxido-reduction process involving the mediator redox couple (Figure 1).
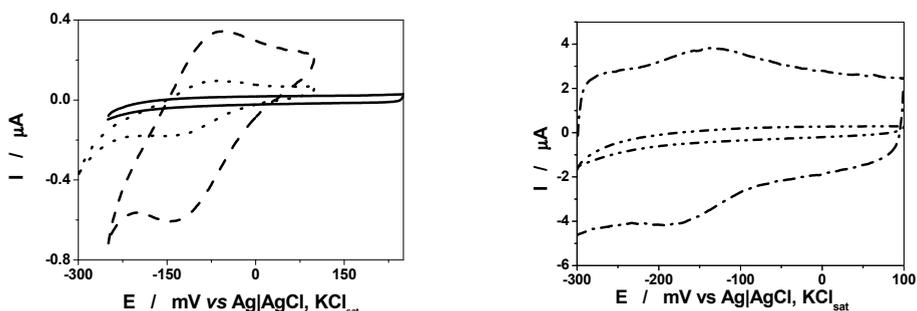
Figure 1. Cyclic voltammogram recorded at MB-αTP-SK-CPE (····), MB-αZP-SK-CPE (----), SK-CPE (—), MB-CA/GCE (-··-) and GCE (-···-). Experimental conditions: scan rate, 20 mV/s, supporting electrolyte Tris buffer, 0.1 M, pH 7.

The background current observed on the recorded CVs was higher for all MB modified electrodes than that evidenced for the corresponding unmodified electrodes (SK-CPE or GCE) (Figure 1). A plausible explanation of this fact should take into consideration that all support material used for mediator immobilization (α-TP, α-ZP, and CA), have high specific surface area, conferring a high electrochemical active surface to the modified electrodes. Indeed, the highest background current among the compared modified electrodes was observed in the case of the electrode modified with CA, which is a high mesoporous material (Figure 1) [14].

The electrochemical parameters of the MB modified GCEs are summarized in Table 1. In all cases, the peak separation values (ΔE_p), the width at half maximum current intensity ($W_{1/2}$) and the ratio between the intensity of the cathodic and anodic peaks (I_{pa}/I_{pc}) point to a quasi-reversible redox process [15].

The values of the formal standard potential ($E^{\circ\prime}$) for all MB modified GCEs (Table 1) are in the optimal potential range for electroanalytical applications [7], and assure an efficient production of enzyme active NAD^+ [6, 8]. Among the prepared modified electrodes, the MB-αZP-SK-CPE and MB-αTP-SK-CPE exhibit identical values of ($E^{\circ\prime}$) for MB redox couple, which are slight lower than that corresponding to MB-CA/GCE.

Table 1. Electrochemical parameters of the investigated GC modified electrodes.

Electrode	$E^{o'}$ (mV)	ΔE_p (mV)	$W_{1/2}$ (mV)		I_{pa}/I_{pc}
			anodic	catodic	
MB-CA/GCE	-140	40	110	100	1.1
MB-αZP-SK-CPE	-100	65	120	100	1.07
MB-αTP-SK-CPE	-100	60	100	90	0.87

$\Delta E_p = E_{pa} - E_{pc}$, where E_{pa} and E_{pc} are the cathodic and anodic peak potentials.

The short-term stability of the modified electrodes was estimated by continuous voltammetric cycling within the potential window of practical interest. The time evolution of the recorded CVs revealed that the peak current and the peak potential corresponding to the MB redox wave show a good stability. Thus, by using the relation $\frac{\left(I_{pa}\right)_{100^{th}\,cycles}}{\left(I_{pa}\right)_{1^{st}\,cycle}} \times 100\%$, the current stability was found as follows: ~80% for MB-αTP-SK-CPE; ~101% for MB-αZP-SK-CPE was; and ~105% for MB-CA/GCE. These results show a low decrease or even an increase of the electrode activity due to its activation induced by the continuous potential cycling. Consequently, the simple adsorption of MB on the α-TP, α-ZP or CA support materials, followed by the incorporation MB / support material in the electrodes composition, lead to stable and functional modified electrodes.

For all prepared modified electrodes based on MB-αTP, MB-αZP and MB-CA the $E^{o'}$ value depends on the pH in the same manner as that reported for MB dissolved in aqueous solution [16], MB adsorbed on spectrographic graphite [4] or on α-ZP [17]. In good agreement with previously published results [4], the $E^{o'}$ vs. pH dependence shows two linear regions: one with the slope of ~60 mV/pH, and the second having the slope of ~30 mV/pH unit (Figure 2). This behavior indicates that, irrespective of the support material, the pK_a value for the adsorbed MB is around 4 [4]. Indeed, all experimental data were well fitted to the following nonlinear regression equation: $E = E^{0'} - 0.059 * pH + 0.029 * \log(1 + 10^{pH - pK_a})$. The calculated pK_a values for MB-αTP-SK-CPE, MB-αZP-SK-CPE and MB-CA/GCE are presented in Table 2. These pK_a values are lower than that reported for MB adsorbed on spectrographic graphite (pK_a = 5) [4]. This difference suggests that, due to the interactions with the support materials the MB immobilized onto α-ZP, α-TP or CA becomes more acidic than when adsorbed onto graphite.

The cyclic voltammograms recorded at pH 7, in a wide range of potential scan rates (0.001 – 18 Vs^{-1}), showed a linear dependence of the peak currents (I_{pa}) on the scan rate (v). Thus, the slopes of $\log(I_{pa})$ vs. $\log(v)$

dependencies (Figure 3) were close to the theoretical value (1), confirming the immobilization of the redox mediator MB on the support material (α-ZP, α-TP or CA) (Table 3).
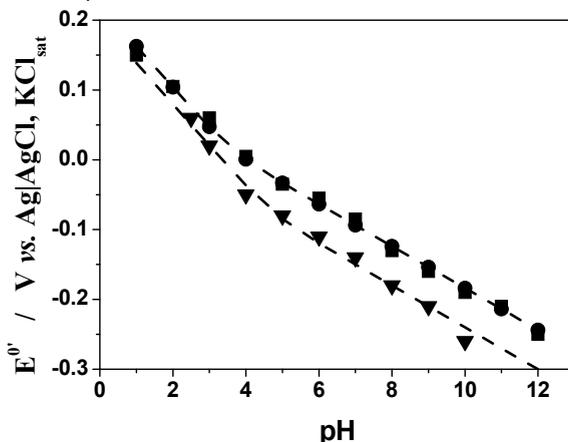
Figure 2. pH influence on the $E^{\circ'}$ value of MB adsorbed on: α-ZP [SK : MB-αZP = 19:1 (w/w)] (●) [18]; α-TP [SK : MB-αTP = 19:1 (w/w)] (■) and CA (▼).

Table 2. pK_a calculated values for MB-αTP-SK-CPE, MB-αZP-SK-CPE, and MB-CA/GCE.

Electrode	pK_a	chi^2	R^2	N
MB-αZP-SK-CPE	4.3 ± 0.4	0.0002	0.9866	11
MB-αTP-SK-CPE	3.6 ± 0.2	0.00007	0.9963	12
MB-CA/GCE	4.7 ± 0.3	0.0001	0.9899	9
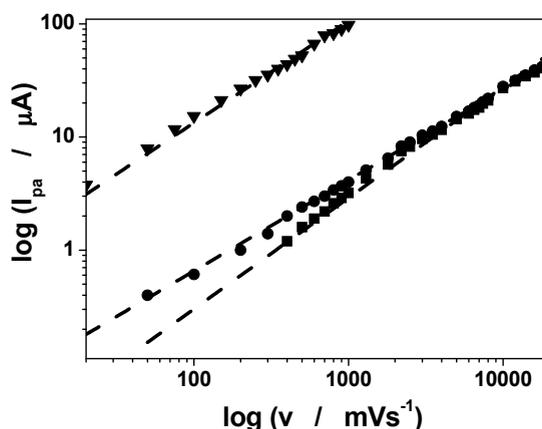
Figure 3. Influence of the potential scan rate on the anodic peak current recorded at MB-αTP-SK-CPE (■), MB-αZP-SK-CPE (●), and MB-CA/GCE (▼). Experimental conditions: supporting electrolyte, 0.1 M Tris buffer (pH 7).

Table 3. The slopes of the log(I_{pa}) *vs.* log(v) for MB-αZP-SK-CPE, MB-αZP-SK-CPE and MB-CA/GCE modified electrodes.

Electrode	Slope	R	N
MB-CA/GCE	0.90 ± 0.02	0.994	19
MB-αZP-SK-CPE	0.80 ± 0.01	0.997	32
MB-αTP-SK-CPE	0.98 ± 0.01	0.994	26

Electrocatalytic NADH oxidation at MB modified GC electrodes

MB-αZP-SK-CPE, MB-αTP-SK-CPE and MB-CA/GCE showed clear electrocatalytic activity for NADH oxidation. Thus, the cyclic voltammograms recorded at these electrodes in the presence of NADH (Figure 4, solid lines) present all the features of an electrocatalytic process: the oxidation peak is drastically increased, simultaneously with the disappearance of the reduction peak.
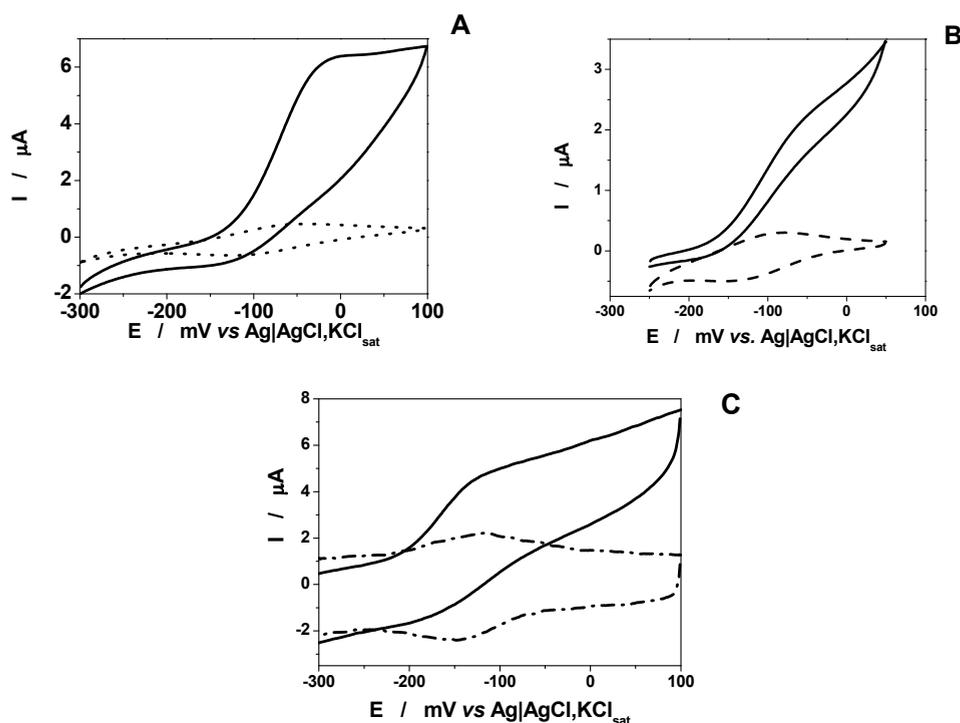
Figure 4. Electrocatalytic oxidation of NADH at MB-αTP-SK-CPE (A), MB-αZP-SK-CPE (B) and MB-CA/GCE (C) in the absence and in the presence of 5 mM NADH. Experimental conditions: scan rate, 20 mV/sec; supporting electrolyte, 0.1 M Tris buffer, (pH 7).

The efficiency (*Eff*) of the electrocatalytic oxidation of NADH at the investigated modified electrodes (MB-αTP-SK-CPE, MB-αZP-SK-CPE and MB-CA/GCE) was calculated according to the following relation: $\mathbf{Eff = (I_{cat} - I_0)/I_0}$, where I_{cat} is the oxidation current intensity in presence of 5 mM NADH and I_0 is the oxidation current intensity observed in its absence. Among the calculated electrocatalytic efficiencies, the highest value was obtained for MB-αTP-SK-CPE, and decrease in the following sequence: $Eff_{MB-αTP-SK-CPE} > Eff_{MB-αZP-SK-CPE} > Eff_{MB-CA/GCE}$ (Table 4).

The surface coverage (Γ) was estimated by using the equation $\mathbf{\Gamma = Q/nFA}$, where Q is the electric charge obtained by integrating the anodic peak, corrected for the background current; *n*, *F* and *A* are the number of electrons transferred in redox reaction, Faraday's constant and the electrode geometric area, respectively.

Table 4. Electrocatalytic efficiencies for NADH oxidation
at modified GC electrodes.

Electrode	Eff	Γ 10^{10} mol cm^{-2}
MB-CA/GCE	2.2	1.85
MB-αZP-SK-CPE	7.5	0.32
MB-αTP-SK-CPE	19.4	0.08

Surprisingly, the MB coverage value for MB-αTP-SK-CPE was the lowest, comparing with those obtained for MB-αZP-SK-CPE or MB-CA/GCE, but is associated with the highest electrocatalytic efficiency. A plausible explanation for this behavior could due to the differences existing between the structure of the support material used for mediator immobilization. Therefore, when CA, a high mesoporous material, was used as support material the free access of NADH to the immobilized MB was more difficult due to some steric hindrances.

CONCLUSIONS

Two different types of glassy carbon (powder and rod) and three types of support materials have been successfully used for the preparation of MB-αZP-SK-CPE, MB-αTP-SK-CPE and MB-CA/GCE modified electrodes. The electrochemical parameters of the modified electrodes point out the presence of the immobilized MB species on the electrode surface. All E°' values are placed in the optimal potential range for the amperometric

detection. The pH dependence of E°', for all investigated modified electrodes, was fitted using a nonlinear model, allowing the estimation of the pK_a value for the immobilized MB. The electrochemical and electroanalytical parameters of the investigated electrodes recommend them as stable and reproducible sensors for NADH. Among them MB-αTP-SK-CPE presents the best electrocatalytic response for NADH electrooxidation.

EXPERIMENTAL SECTION

Synthesis of CA. CA was prepared using a mixture of resorcinol (98% purity, Aldrich), formaldehyde (37% solution, Aldrich), Na_2CO_3 (99.9% purity, Aldrich), and deionized water, according to a previously reported sol-gel method [14].

Synthesis of acidic alpha- zirconium phosphate (α-ZP) and alpha-titanium phosphate (α-TP). α-ZP and α-TP were prepared according to a previously reported method [17], and [19], respectively.

Immobilisation of the organic dye (Meldola Blue) on the support material surfaces. The immobilization process was carried out using an aqueous solution of the organic dye (Meldola Blue, MB; Sigma, St. Louis, MO, USA) in a concentration of 0.001% (w/v). The procedure of immobilization was as follows: 50 mg of support material (α-ZP, α-TP and CA) was added to 50 ml of dye solution and the mixture was shaken for 1 h. The precipitate (MB-αZP, MB-αTP and MB-CA) was filtered, washed with de-ionized water and dried at room temperature.

Preparation of the modified glassy carbon electrode. The carbon paste electrodes were prepared by thoroughly mixing glassy carbon powder (Sigradur K, HTW, Hochtemperatur-Werkstoffe GmbH, Bonn, Germany) and MB-αZP or MB-αTP with paraffin oil (Fluka, Buchs, Switzerland) in an agate mortar. For 20 mg of carbon powder and MB-αZP or MB-αTP mixture, with a ratio of glassy carbon powder to MB-αZP or MB-αTP of 19:1 (w/w), 5 μL of paraffin oil were added. The size of the spherical glassy carbon particles was 0.4 – 1.2 μm. The obtained pastes were put into the cavity of a Teflon holder, in the bottom of which a piece of pyrolytic graphite was used for electric contact. The Teflon holder then was screwed onto a rotating disc electrode device (EG-G PAR, model 616, Princeton, USA) and was used as working electrode for cyclic voltammetry.

The home made glassy carbon rod electrodes were prepared by introducing glassy carbon rod into a Teflon holder, then was screwed onto a rotating disc electrode device (Radiometer Analytical, France) and was used as working electrode for cyclic voltammetry. The glassy carbon rod was thoroughly polished on alumina (1 μm Stuers, Copenhagen, Denmark),

then rinsed with Milli-Q water. Chitosan solution was prepared by adding 10 mg chitosan (Sigma-Aldrich) to 10 mL of acetic acid (glacial acetic acid, Sigma) 0.1 M. Then a suspension of 1 g/L MB-CA in this solution was prepared. 5 μL from this suspension were placed onto clean GC electrode surface, and let to dry at room temperature.

The geometrical area of the prepared modified electrodes was 0.049 cm^2.

Electrochemical measurements. The measurements were performed using a BAS 100 W Electrochemical Analyzer (Bioanalytical Systems, West Lafayette, IN, USA), which was connected to a PC microcomputer for potential control and data acquisition. The modified GCEs were used as working electrode, a platinum ring as the counter electrode, and Ag|AgCl,KCl$_{sat}$ as reference electrode. Cyclic voltammetry was carried out in 0.1 M solution of Tris (Sigma). The pH of the electrolyte solutions was adjusted to the desired values by adding HCl or KOH (Merck).

All experiments were performed in deoxygenated electrolytes by bubbling argon for 20 min before each measurement. Al reagents were used as received.

For each prepared modified glassy carbon, the surface coverage (Γ, mol cm^{-2}) was estimated through integration of the area of the wave registered with cyclic voltammetry.

NADH electro-oxidation study. The electrocatalytic oxidation of NADH using MB adsorbed onto MB-αZP, MB-αTP or CA modified glassy carbon electrodes were investigated through addition of freshly prepared NADH (Sigma) solution to the electrolyte solution. Investigations on the electrocatalytic oxidation of NADH were performed using cyclic voltammetry. For cyclic voltammetry measurements, the initial potential was -300 mV *versus* Ag|AgCl,KCl$_{sat}$ for MB-αTP and MB-CA and -250 mV *versus* Ag|AgCl,KCl$_{sat}$ for MB-αZP. The experiments were performed in the potential range: -300 to 100 mV *versus* Ag|AgCl,KCl$_{sat}$ for MB-αTP and MB-CA and -250 to 100 mV *versus* Ag|AgCl,KCl$_{sat}$ for MB-αZP.

REFERENCES

1. W.J. Blaedel, R.A. Jenkins, *Analytical Chemistry,* **1975**, *47*, 1337.

2. J. Moiroux, P.J. Elving, *Analytical Chemistry,* **1978**, *50*, 1056.

3. C.I. Ladiu, I.C. Popescu, L. Gorton, *Journal of Solid State Electrochemistry,* **2005**, *9*, 296.

4. L. Gorton, A. Torstensson, A. Jaegfeldt, G. Johansson, *Journal of Electroanalytical Chemistry,* **1984**, *161*, 103.

5. L. Gorton, *Journal of the Chemical Society, Faraday Transaction* **1986**, *1*, 1245.

6. C. Trobajo, S.A. Khainakov, A. Espina, J.R. Garcia, *Chemistry of Materials*, **2000**, *12*, 1787.

7. C.V. Kumar, A. Chaudgari, *Microporous and Mesoporous Materials,* **2000**, *41*, 307.

8. Y. Ando, K. Sasaki, R. Adzic, *Electrochemistry Communication*, **2009**, *11*, 1135.

9. Y. Zhang, D. Kang, M. Aindow, C. Erkey, *Journal of Physical Chemistry B*, **2005**, *109*, 2617.

10. L. Gorton, E. Csoregi, E. Dominguez, J. Emmeus, G. Jonsson-Pettersson, G. Marko-Varga, B. Persson, *Analytica Chimica Acta,* **1991**, *250*, 203.

11. L. Gorton, *Electroanalysis,* **1995**, *7*, 23.

12. L. Gorton, E. Dominguez, *Reviews in Molecular Biotechnology,* **2002**, *82*, 371.

13. L. Gorton, E. Dominguez, in G.S. Wilson (Ed.), *Encyclopedia of Electrochemistry*, Wiley, New York **2002**, *9*, 11.

14. L.C. Cotet, A. Roig, I.C. Popescu, V. Cosoveanu, E. Molins, V. Danciu, *Revue Roumaine de Chimie,* **2007**, *52*, 1077.

15. M.J. Honeychurch, G.A. Rechnitz, *Electroanalysis,* **1998**, *10*, 285.

16. L.T. Kubota, F. Munteanu, A. Roddick-Lanzilotta, A.J. McQuillan, L. Gorton, *Quimica Analitica,* **2000**, *19*, 15.

17. C.I. Ladiu, I.C. Popescu, R. Garcia, L. Gorton, *Revue Roumaine de Chimie,* **2007**, *52*, 67.

18. C.I. Ladiu, R. Garcia, I.C. Popescu, L. Gorton, *Chemical Bulletin of "Politehnica" University of Timisoara,* **2004**, *49*, 51.

19. C.I. Ladiu, R. Garcia, I.C. Popescu, L. Gorton, *Revista de Chimie (Bucuresti)*, **2007**, *58*, 465.

APPLICATION OF COLORIMETRY AS AN ANALYTICAL TOOL*

NATALIYA NIKITINA[a,*], ELENA RESHETNYAK[a],
VALERIY SHEVCHENKO[b], YANA ZHITNYAKOVSKAYA[a]

ABSTRACT. Colorimetry method was applied for estimation the precision of the measurement results of chromaticity characteristics of colored sorbates on paper, polyurethane foam and silica gel using a portable photometer-reflectometer. The relative standard deviation of measurement results is not exceed 1.0%; the trueness and precision of results of determination with the photometer-reflectometer are not worse than results obtained using a scanner or a spectrophotometer with an attachment for diffuse reflectance. A two-parameter colorimetry was allied to study the possibility of the determination separately of two metals in a mixture with the reagent indicator papers and gelatin films. It was established that application of two-parameter colorimetry has significant limitations; the relative standard deviation of the results of separately two-colorimetric determination may exceed 50%. Colorimetry method and statistics of observations were used for the chromaticity evaluation of uniformity of color scales prepared using transparent gelatin films, polyurethane foams and indicator papers. For choosing an optimal scale for visually test determinations should be given the preference to the visual method – statistics of observations.

Keywords: colorimetry, chromaticity coordinates, test-system, sorbent

INTRODUCTION

Colorimetry method is widely used in solid-phase spectroscopy and test analysis. The quantitative expression of color coordinates and chromaticity characteristics are used for optimization of the conditions of reagent immobilization on the sorbent phase, investigation of the acid-base and complexing properties of the immobilized reagents, prediction of the increase in the selectivity of analytical reactions involving solid-phase reagents [1, 2]. By combining the sorption processes with concentration and selecting the most sensitive chromaticity functions, the detection limit of analytes is reduced

---

* This paper was presented at the "17th International Symposium on Separation Sciences. News and Beauty in Separation Sciences, Cluj-Napoca, Romania, September 5-9, 2011".
[a] Department of Chemical Metrology, Kharkiv V.N. Karazin National University, Svoboda sq., 4, Kharkiv 61022, Ukraine, * nikitina@univer.kharkov.ua
[b] Scientific-expert Criminalistic Centre of Ministry of Home Affairs in Kharkov Region, Mayakovskiy str., 22, Kharkiv, Ukraine

on 1.5-2 orders [2, 3]. The colorimetry method [4, 5] is applied in the visual analysis to test uniform chromaticity of color scales, prepared by using the non-transparent sorbents (silicas, silica gels, paper, ion-exchange resins) [2, 6, 7]. The chromatic characteristics of L, a, b, and total color difference ΔE in the CIELAB system is calculated on the basis of the color coordinates received from diffuse reflectance spectra (in the study of non-transparent media) or the transmission spectra (in the case of transparent matrix) [4, 5, 8].

The fast, objective and automated method of estimating the chromaticity characteristics of colored samples in the RGB system has appeared with the prevalence of digital photography, scanners, and computer image processing software [3, 9-16]. Advances in miniaturization of optical transducers allowed to create new optical elements - color sensor based on light-emitting diodes to detect the signal from colored solid surfaces [17-21].

The colorimetry method as «analytical tool» was applied in this paper as follow: for the precision estimation of results from the chromaticity characteristics measurements of colored sorbents using a portable photometer-reflectometer; for the investigation of a possibility of using of sorption-colorimetry two-component analysis of metal ions with reagent indicator papers; for evaluation of chromaticity uniformity of color scales prepared using sorbents of different nature.

RESULTS AND DISCUSSION

The portable photometer application. The design of the device measuring system includes four light-emitting diodes (LEDs), which are located on the four sides of the color sensor and sent to the sample angularly 45º [21] (Figure 1). This makes a possibility to scan colored solid samples of different porosity, including powdered sorbents.
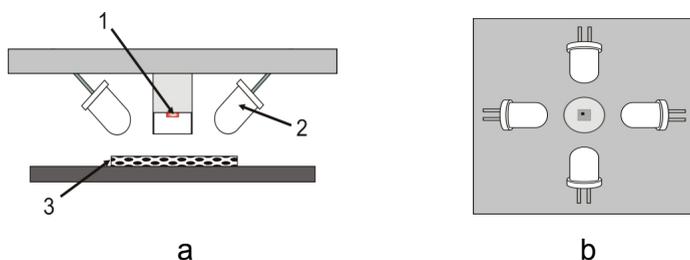
Figure 1. Arrangement of a portable photometer:
a - side view (1 – sensor, 2 – LED, 3 - specimen), b - bottom view.

The porous polyurethane foam (PUF), the dense reagent paper (RIP) and the silica gel were chosen to study the dependence of the precision of results of chromaticity measurements from the density of the sorbent and sorbate colors. Many-coloured products of known heterophase reactions (Table 9, the test-systems 1, 2, 5, 12, 13) [11, 22, 23] were chosen. The diffuse

reflectance spectra of the sorbates are overlapped almost the entire visible wavelengths range. The absorption maxima were: 622 nm and 488 nm for the thiocyanate complexes of the Co^{2+} ions and Fe^{3+} adsorbed on PUF; 558 nm for the immobilized complex of Cu^{2+} ions with formazans on paper; 540 and 595 nm for the cationic forms of Neutral Red (NR) and Malachite Green (MG) adsorbed on silica gel.

The dependence of brightness of R-, G-, B-channels from the analyte concentration in solution (Figure 2) was obtained as a result of scanning of the stained samples of PUF, RIP and silica with a photometer. For each system was chosen the channel whose brightness decreased most sharply with increasing of the analyte concentration: for the complexes of Co(II) and Cu(II) and MG - this channel is R, for the complexes of Fe(III) and indicator NR - channel G.
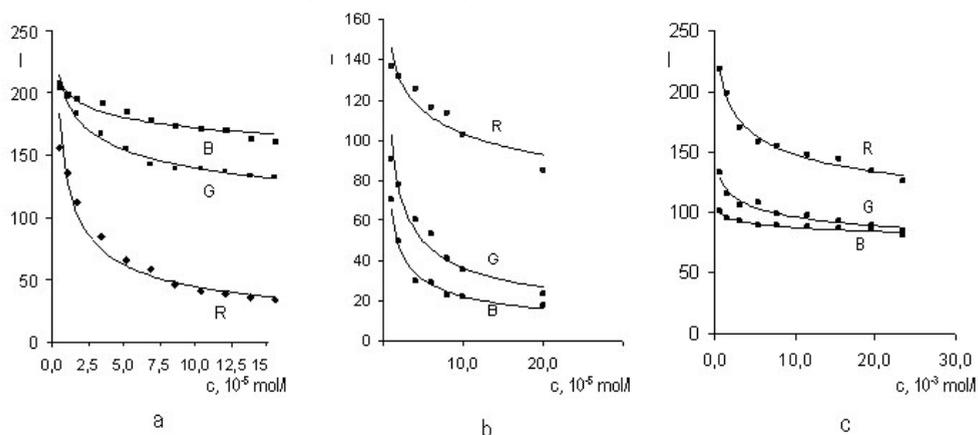
Figure 2. Dependence of brightness of R-, G-, B-channels from the analyte concentration in solution for: a – thiocyanate complexes of Co^{2+} ions adsorbed on PUF; b – indicator Neutral Red absorbed on silica; c – complexes of Cu^{2+} ions with formazans on paper.

All experimental curves describe a decreasing power function according to eq. 1:

$$I (R, G, B) = a \cdot c^{-t} \tag{1}$$

where: a, t - curve equation parameters; c - analyte concentration (Table 1).

Table 1. The meanings of the parameters of graduation curve (eq. 1)

Test system	Color channel	Concentration range, mol/l	Parameters		R^2
			a	t	
RIP-Cu-Test	R	$(0.8–12) \cdot 10^{-3}$	48.3±0.200	0.15±0.02	0.972
Co^{2+}-SCN-PUF	R	$(0.5–15) \cdot 10^{-6}$	0.610±0.009	0.48±0.07	0.964
Fe^{3+}-SCN-PUF	G	$(0.4–15) \cdot 10^{-6}$	0.850±0.006	0.36±0.02	0.984
NR-Silica	G	$(0.1–1) \cdot 10^{-5}$	0.206±0.003	0.47±0.04	0.969
MG-Silica	R	$(0.1–1) \cdot 10^{-5}$	0.191±0.002	0.67±0.03	0.989

The precision of chromaticity characteristics measurement results was studied in conditions of repeatability. The characteristic of precision by "repeatability" was evaluated for the same test samples by five-times measuring of the selected color channel brightness. In the case of evaluation of intermediate precision, the results of parallelly measurements (R, G) were the average of nine identical samples prepared for 10-12 concentrations of the working range.

The data from Table 2 show that the precision characteristics for colored PUF are slightly worse than that for RIP and silica. The largest scatter of the results was observed during the brightness measuring of the red channel for the system Co^{2+}-SCN-PUF. For all systems the value of relative standard deviation of measurement of R-, G- and B-components of the color of sorbates remained practically unchanged over the entire concentration range.

Table 2. The precision characteristics of the R-, G-, B-color components measurement results of different nature sorbents

Sorbent	Repeatability, s_r% (n=5)	Intermediate precision, s_r% (n=9)
PUF	0.10-0.6	0.1-0.7
Paper	0.08-0.3	0.1-0.3
Silica	0.06-0.4	0.1-0.4

The trueness of analysis results were tested using the standard solutions (Table 3, last column). The results are in good agreement with each other, there is no systematic error. The accuracy of our data is not worse than the results obtained using an office scanner or using a spectrophotometer with an attachment for diffuse reflectance [11, 24].

Table 3. The results of trueness checking using standard solutions

Test-system	Concen-tration	$c(M^{z+})$, mg/l			
		Recovery (n=3, P=0.95)			
		Diffuse reflectance		RGB	
		SF-2000 [24]	Spectron [11]	Scanner [11]	Photometer
Cu^{2+}-RIP	125	125±1 (s_r,%=0.2)	-	-	126±1 (s_r, %=0.2)
Co^{2+}-PUF	0.45	0.44±0.05 (s_r,%=3)	-	-	0.46±0.01 (s_r, %=0.5)
	0.40	-	0.40±0.03 (s_r,%=3)	0.50±0.10 (s_r,%=9)	-
Fe^{3+}-PUF	0.15	0.14±0.01 (s_r,%=2)	-	-	0.16±0.01 (s_r,%=1.5)

The relative error of the Fe(III) determination with a portable photometer (Table 3) was lower than using a portable spectrophotometer equipped with a microcell and emitting in the wavelength range 440-640 nm. The content of Fe(III) was controlled in the range of 0-0.2 mg/l with an error of ~2.4% [17].

With microspectrophotometer [18] and reflective sensor [19], the content of Fe(III) in aqueous media was measured with a relative standard deviation about 5%.

Thus, a portable photometer [21] on its characteristics is not worse than laboratory spectrophotometers (measurement of diffuse reflectance) and allows to measure the chromaticity characteristics of colored sorbents of different nature with relative standard deviation which is not exceed 1.0%.

Sorption-colorimetry determination of metal ions in their mixture using reagent indicator paper. The majority of analytical reagents used in photometry and visual colorimetry for metals control in aqueous media are not selective. Developers of test systems, for instance, indicate: "test system is designed for total content of metal ions estimation" [22, 25-30]. However, analysts are often interested in the separate determination of metals; in this case we have to talk about how to increase the selectivity of reactions, reagents, test systems and processes. Selectivity of analytical reactions can be improved by varying the determination conditions (pH, temperature) or by adding of masking agents.

The various parameters so called coefficients or factors of selectivity are used to the quantitative expression of the selectivity. They are equals to a ratio of some parameters of interfering component to the same parameter of the target component. There is the ratio of ion concentrations in potentiometry, the distribution coefficients in separation methods, ion mobility in migration methods, the molar absorption coefficients in spectrophotometry [31].

The authors of [2, 32-36] have suggested to use a two-parameter colorimetry to improve the selectivity of the metal ions determination, which form a similar color products of heterophase reactions. The colored metal complexes were adsorbed on the modified silica and from the diffuse reflectance spectroscopy data color coordinates of A and B were calculated to implement the method of separate colorimetric determination of analytes. The dependences of changing of color coordinates A from B varying the concentration of metal ions in solution were obtained. The conclusion about the possibility of separate determination of metals was made on the basis of the separation factor α, which was calculated by the equations:

$$\alpha = |arctg\ k_{M1} - arctg\ k_{M2}|, \text{ if } |arctg\ k_{M1} - arctg\ k_{M2}| < 90°;$$
$$\alpha = 180° - |arctg\ k_{M1} - arctg\ k_{M2}|, \text{ if } |arctg\ k_{M1} - arctg\ k_{M2}| \geq 90°, \quad (2)$$

k_{M1}, k_{M2} - the slope of the graphic dependences of changing of color coordinates A from B at different concentrations of M_1 and M_2 respectively.

The separate determination of metals is possible if $\alpha \geq 25°$ [2] in the case of diffuse reflectance measurements on a colorimeter "Spektroton" (or other spectrophotometer with the same class of accuracy, for example, SF-2000).

The content of metals was found by solution of the system, composed as a vector sum of analytical signals according to the equations:

$$\Delta L_\Sigma^2 = (a_{11} + b_{11}x_1)^2 + (a_{12} + b_{12}x_2)^2,$$
$$\Delta S_\Sigma^2 = (a_{21} + b_{21}x_1)^2 + (a_{22} + b_{22}x_2)^2, \qquad (3)$$

where x_1, x_2 - the unknown concentrations of metal ions M_1 and M_2 in solution; a_{ij} and b_{ij} ($i, j = 1, 2$) - the equation parameters of dependences of the color differences in brightness (ΔL) or saturation (ΔS) from x_1 and x_2 [2].

The two-parameter colorimetry was applied to study the possibility of separate determination of two metals, immobilized in the form of colored complexes on paper or in a gelatin film. The non-selective reagents - formazan (Figure 3), 4-(2-pyridylazo)-resorcin (PAR) and 1-(2-pyridylazo)-2-naphtol (PAN) (test systems 6, 8 and 11 from Table 9) were used.
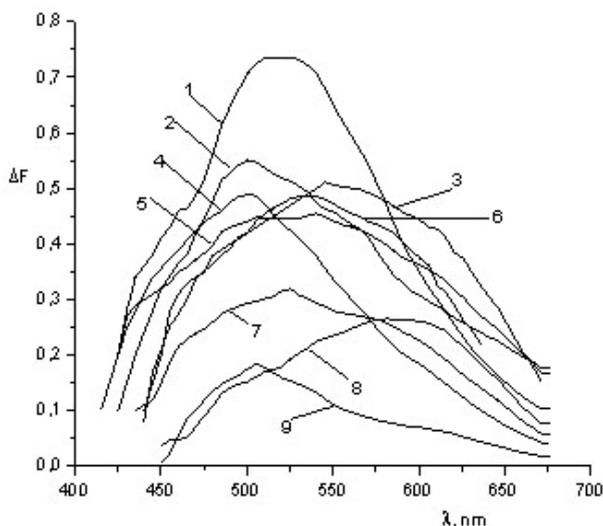
Figure 3. The absorption spectra of the sorbed complexes of metal ions with formazans on indicator paper RIP-Metal-test: 1 – Cu^{2+}, 2 – Co^{2+}, 3 – Mn^{2+}, 4 – Ni^{2+}, 5 – Fe^{3+}, 6 – $\sum M^{n+}$, 7 – Zn^{2+}, 8 – Cd^{2+}, 9 – Pb^{2+} (in solutions $c(M^{n+}) = c(\sum M^{n+}) = 8.0 \cdot 10^{-3}$ mol/l, pH 5).

For all immobilized metal complexes were calculated chromaticity characteristics and the dependences B from A were ploted on the basis of the absorption or reflection spectra (Figure 4, for RIP-Metal-test the similar dependences in the range of concentrations of M^{n+} from 0.5 to 8.0 mmol/l) were ploted.

As it can be seen from Figure 4a none of the pair of metal ions in their total presence in solution can not be separately identified by reaction with PAR in a gelatin film; all the graphics are almost parallel. In the case of

270

reaction M^{2+} with PAN on paper (Figure 4b), the angle between the graphic dependences was more than 25° for couples: Co^{2+} ion - either M^{2+} that is cobalt falls out of the total amount of metal in spectroscopic measurements and it can be determined separately. In the visual colorimetric measurements in the case of close concentration of metal ions the green color of the cobalt (III) complex with PAN is not visible on the background of the red complexes of other metals.
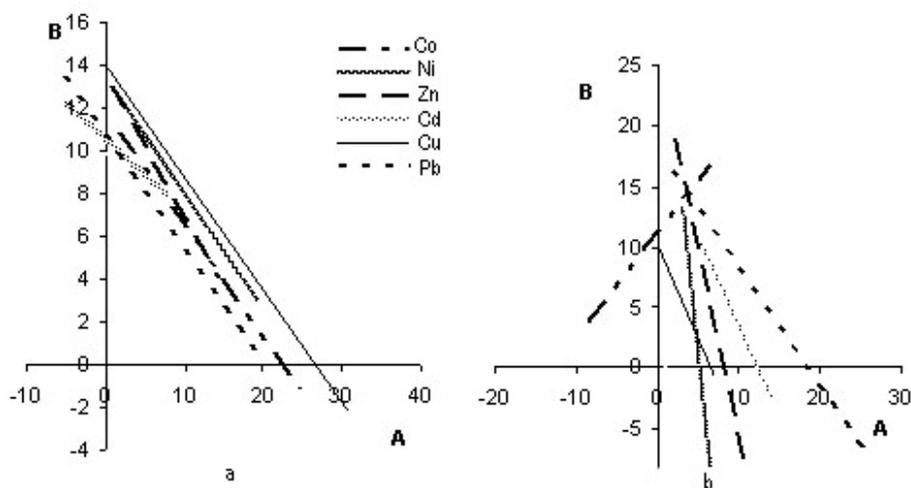
Figure 4. The change of color coordinates of immobilized complexes from metal ions concentration in a solution (from $1 \cdot 10^{-5}$ to $3.2 \cdot 10^{-4}$ mol/l):
a) metal ion complexes with PAR in gelatin film;
b) metal ion complexes with PAN on RIP.

The separation factor values for all pairs of metal ions adsorbed on the RIP-metal-test are shown in Table 4. According to the data for some pairs of α>25°, they can be separately determined.

Table 4. The separation factor values for pairs of metal ion complexes adsorbed on the RIP-metal-test

	Cu^{2+}	Pb^{2+}	Zn^{2+}	Cd^{2+}	Ni^{2+}	Co^{2+}	Mn^{2+}	Fe^{3+}
Cu^{2+}	—	69.3°	52.6°	52.5°	37.7°	2.2°	48.3°	51.0°
Pb^{2+}	69.3°	—	16.7°	16.8°	31.6°	71.5°	21.1°	18.3°
Zn^{2+}	52.6°	16.7°	—	0.1°	15.0°	54.8°	4.4°	1.7°
Cd^{2+}	52.5°	16.8°	0.1°	—	14.9°	54.7°	4.3°	1.5°
Ni^{2+}	37.7°	31.6°	15.0°	14.9°	—	39.9°	10.6°	13.3°
Co^{2+}	2.2°	71.5°	54.8°	54.7°	39.9°	—	50.5°	53.2°
Mn^{2+}	48.3°	21.1°	4.4°	4.3°	10.6°	50.5°	—	2.6°
Fe^{3+}	51.0°	18.3°	1.7°	1.5°	13.3°	53.2°	2.6°	—

The examples of the single results of two-component determination of metal ions in model solutions with indicator papers are presented in table 5. For selected pairs the colored test samples were obtained, diffuse reflectance was measured, color coordinates were calculated and the system of the equations (3) was solved using the program Mathcad 2001. The system of the equations of fourth degree has four roots, two of which are often negative. However, the four positive roots or three negative and one positive root can satisfy of equations solution. We are faced with this situation (Table 5) and in this case the analysis is meaningless. For more good examples the difference between the concentration values of injected and found metal ions varied from 2 to 50%. Thus, the application of two-parameter colorimetry has significant limitations.

Table 5. The results of two-component colorimetry determination
of metal ions in model solutions with indicator paper

RIP			Concentration in model solution		Recovery, %	
	M_1	M_2	$c(M_1)$, µmol/l	$c(M_2)$, µmol/l	M_1	M_2
RIP-PAN	Co	Zn	6.0	6.0	123	103
			4.0	4.0	103	negative
		Ni	4.0	4.0	147	102
			2.0	2.0	70	154
		Pb	2.0	2.0	65	80
			8.0	8.0	4 positive results	
RIP	M_1	M_2	$c(M_1)$, mmol/l	$c(M_2)$, mmol/l	M_1	M_2
RIP-Metal-Test	Cu	Ni	$1.7 \cdot 10^{-3}$	$3.8 \cdot 10^{-3}$	135	126
			$4.2 \cdot 10^{-3}$	$1.7 \cdot 10^{-3}$	114	129
		Zn	$4.2 \cdot 10^{-3}$	$1.5 \cdot 10^{-3}$	93	107
			$1.5 \cdot 10^{-3}$	$1.5 \cdot 10^{-3}$	93	135
			$3.9 \cdot 10^{-3}$	$3.8 \cdot 10^{-3}$	28	100

The color scales construction. The comparison color scale is applied to quantitative estimation of the analyte content in the objects of analysis. Scales are a set of test samples (standards) corresponding exactly to known analyte content [1, 22]. Concentration of the determined component on the color scale increases in geometric progression. This deals with a human perception of color and exponential dependency of color characteristics from the analyte concentration. The coefficient of geometric progression, which is the ratio of adjacent concentrations on the scale ($q=c_{n+1}/c_n$), is chosen equal two or three. There are also other recommendations, for example, in the work [37] was proposed to build scale in accordance with the Fibonacci number, in this case every subsequent concentration on a scale equals the sum of the two previous concentrations, progression approaches asymptotically to a geometric with q=1.618.

The scale should be with uniform chromaticity and well perceived by the human eye. This is a basic requirement for the color scale for visual colorimetry. The color scale uniform chromaticity prepared by using non-transparent sorbents (silica, paper, ion-exchange resin) is checked using a colorimetry method [2, 6]. The general color discrimination ΔE is selected as main analytical parameter to record the change in color of modified sorbents. On the basis of ΔE experimental dependency from the analyte concentration the color scale with a constant step ΔE=10 is built. It is considered that the error of test technique is minimized and the scale will be distinguished by eye of any person [2, 7].

However, the criterion ΔE ≥ 10 was not strictly enough to visual discrimination of color differences of adjacent scale standards. The total color difference varied on 5-7 reference units [26] in case of Al (III) determination with chromazurol S immobilized on a cellulose chromatography paper using color scale with q=2. The authors [37] affirm that the value of ΔE=5 is the natural border of eye color perception if the scale is constructed in accordance with a Fibonacci series.

Thus there is no general consensus about how to build a color scale and how to estimate its quality; it is not clear what criterion corresponds to the boundary color discrimination; no recommendations for testing uniform chromaticity scale, prepared using transparent sorbent.

To study these problems seven test systems were chosen: Co^{2+}-SCN-PUF, Fe^{3+}-SCN-PUF, NO_2^--PUF, RIP-Co-Test, Co^{2+}-NRS-gelatin film, Al^{3+}-EChC-gelatin film and ΣM^{n+}-PAR- gelatin film (Table 9). The four color scales with the coefficients q=1.5, q=2, q=3 and q≈1.618 (Fibonacci series) were prepared three times for all test systems.

On the basis of colorimetry measurements for all sorbents were obtained the values of total color difference ΔE and for each concentration range on a scale the difference according to eq. (4) was calculated:

$$\Delta E^* = \Delta E_{n+1} - \Delta E_n. \tag{4}$$

It was found which of the scales were constructed more correctly using the value of color discrimination step on the scale (ΔE*).

Along with the colorimetry method for estimation of quality of prepared color scales, statistics of observations was applied. The scales were placed on a sheet of white paper in order of analyte concentration increasing and compared the color intensity of the adjacent standard samples of the scale. Fifty independent observers were asked: "Do you see any difference between the color of adjacent samples of the scale?" After that the frequency of detection of the color discrimination was calculated:

$$P(c) = n/N \tag{5}$$

where: n - number of positive responses, N - total number of observations.

The scale with P(c) ≥ 0.9 was chosen, that is more than 90% of observers have seen the color difference of adjacent scale standards. This scale should provide high accuracy of test determinations.

The examples of the results of visual and instrumental methods of investigation of the color scales construction correctness for the two test systems based on polyurethane and gelatin film are presented in Tables 6 and 7. In the case of the Fe(III) determination in the form of $Fe(SCN)_4^-$ complexes sorbed on PUF you should choose a scale with coefficient 2 or 3 in the Fe^{3+} concentration range 0.02-0.80 mg/l. In this range on a scale with q=2 color discrimination step ΔE*=4-6, on a scale with q=3 color discrimination step ΔE*=7-8 (Table 6). The intensity of color tablets increased sharply above these concentrations and the value of the difference ΔE* increased too. In the case of the Co(II) determination as blue thiocyanate complexes was observed a similar situation. The uniform chromaticity scale with coefficient 2 was observed in the Co^{2+} concentration range of 0.03-0.5 mg/l (ΔE*≈4); at higher concentrations the value of ΔE* increased dramatically. Scales with coefficients q=1.5 and q=1.618 were invalid at a Co^{2+} concentration less than 0.5 mg/l.

Table 6. The meanings ΔE* and the frequency of detection of the color discrimination of adjacent standards of color scales for test-system Fe^{3+}-SCN-PUF.

Interval Δc(Fe^{3+}), mg/l	P, % (N=50)	ΔE*	Interval Δc(Fe^{3+}), mg/l	P, % (N=50)	ΔE*
q=2			q=3		
0-0.02	100	4	0-0.02	100	4
0.02-0.04	92	4	0.02-0.06	100	8
0.04-0.08	93	4	0.06-0.18	98	7
0.08-0.16	95	6	0.18-0.54	100	8
0.16-0.32	98	4	0.54-1.62	100	16
0.32-0.64	100	6	-	-	-
0.64-1.28	100	14	-	-	-
q=1.5			Fibonacci series		
0-0.02	100	4	0-0.02	100	4
0.02-0.03	68	2.5	0.02-0.03	70	3
0.03-0.05	60	3	0.03-0.05	63	2.5
0.05-0.07	44	2	0.05-0.08	85	3.5
0.07-0.10	72	2	0.08-0.13	89	4
0.10-0.15	94	6	0.13-0.21	86	3
0.15-0.23	96	4	0.21-0.34	87	3
0.23-0.34	90	6	0.34-0.55	85	3
0.34-0.51	89	3	0.55-0.89	91	5
0.51-0.77	88	4	-	-	-

The samples of indicator papers on the scales with coefficients 2 and 3 were more differentiated for a test system based on the indicator paper RIP-Co-Test, the condition P(c)>90% satisfied with $\Delta E^* \geq 4$. The scale with q=1.5 was less reproducible in color test samples perception, on the scale constructed in accordance with Fibonacci series the value of P(c) has not reached 90%. Thus, the value of $\Delta E^*=4$ can be taken as a boundary for visual color discrimination of red and blue colors shades on the PUF, red color shades on a yellow paper and the value of $\Delta E^*=3$ - for color discrimination yellow color shades on the PUF (Table 8). If you follow the recommendations of [2] to create uniform color scales ($\Delta E^*=10$) the concentration of Fe^{3+}, Co^{2+} and NO_2 ions would be increased by more than 3 times, that is unreasonably for practical purposes.

The colorimetry method was not managed to apply for estimation of the color scales quality prepared using transparent gelatin films. The value of the total color difference of Al(III) with Eriochrome Cyanine R (EChC) immobilized complex practically unchanged until the middle of the scale concentration ranges (up to Al^{3+} concentration ~0.5 mg/l), and the difference ΔE^* was equal zero (Table 7).

Table 7. The meanings ΔE^* and the frequency of detection of the color discrimination of adjacent standards of color scales for test-system Al^{3+}-EChC-gelatin film

Interval $\Delta c(Al^{3+})$, mg/l	P, % (N=50)	ΔE^*	Interval $\Delta c(Al^{3+})$, mg/l	P, % (N=50)	ΔE^*
q=2			q=3		
0-0.14	90	1	0-0.14	90	1
0.14-0.27	92	0	0.14-0.41	98	0
0.27-0.54	95	0	0.41-1.23	100	1
0.54-1.08	98	0	1.23-3.69	100	1
1.08-2.16	100	1	-	-	-
q=1.5			Fibonacci series		
0-0.14	90	1	0-0.14	90	0
0.14-0.20	60	0	0.14-0.16	26	0
0.20-0.30	54	0	0.16-0.30	86	0
0.30-0.46	96	0	0.30-0.46	90	0
0.46-0.70	94	1	0.46-0.76	96	0
0.70-1.05	80	1	0.76-1.22	100	2
1.05-1.57	92	0	1.22-1.98	86	1
1.57-2.36	92	1	-	-	-

The difference ΔE^* did not exceed 2 at higher concentration of the complex. Similar results were obtained for the test systems for determination of Co^{2+} ions with the Nitroso-R-salt (NRS) and the sum of metal ions with PAR. The difference ΔE^* exceeded zero value for $c(Co^{2+})\sim1.5$ mg/l and $c(\Sigma M^{2+})\sim1\cdot10^{-5}$ mol/l.

Statistics of observations allowed to choose an optimal color scale. More than 90% of observers distinguish adjacent color reference samples of the scale over the whole concentrations range for the three studied test systems. For optimal color scales have been chosen scales with coefficients $q=2$ and $q=3$.

Thus, it is impossible to formulate common recommendation and common criteria for the construction of color scales using different sorbents. For choosing an optimal scale for visual test determinations should be give preference to the visual method. In each case should choose the geometric progression of the concentration and the background color, which will provid color distinguishing of the adjacent standard samples of the scale more than 90% of a large number of observers (~50).

Table 8. The results of optimal color scale choice

Test-system	ΔE^*	Efficient scale			
		q=2	q=3	q=1.5	q=1.62
Fe^{3+}-SCN-PUF	4	+	+	-	-
Co^{2+}-SCN-PUF	4	+	+	-	-
NO_2^--PUF	3	+	+	-	+
RIP-Co-Test	4	+	+	-	-
Co^{2+}-NRS-gelatin film	-	+	+	-	-
ΣM^{2+}-PAR-gelatin film	-	+	+	-	-
Al^{3+}-EChC-gelatin film	-	+	+	-	-

CONCLUSIONS

A mini photometer-reflectometer [21] allows to measure the chromaticity characteristics of colored sorbents of different nature with relative standard deviation which is not exceed 1.0%.

Application of two-parameter colorimetry has significant limitations; after separation or masking of interfering components in real samples, the relative standard deviation of the results of separate two-colorimetric determination may exceed 50% or this method of analysis might has no solutions.

Colorimetry method is not suitable for estimation of the quality of color scales prepared using transparent gelatin films. For choosing an optimal scale for visual test determinations should be give preference to the visual method.

EXPERIMENTAL SECTION

Four types of sorbents – porous polyurethane foam (PUF), dense reagent paper, silica and gelatin film and products of heterophase reactions with different colors have been chosen for investigations.

Reagents, materials and equipment

All solutions were prepared using distilled water and all chemicals were of reagent grade. The true concentrations of metal ions in initial salt solutions were determined using trilonometric ($Co(NO_3)_2$, $Cd(NO_3)_2$, $Ni(NO_3)_2$, $Zn(NO_3)_2$, $Pb(NO_3)_2$, $FeCl_3$, $Al(NO_3)_3$ [38]) and iodometric titration. Stock solutions of 1 mol/l NaF, 5 mol/l KSCN, 1 mol/l NaCl, 0.01 mol/l $NaNO_2$, 0.8 mol/l $Na_2B_4O_7$, 0.03 mol/l Nitroso-R-salt (NRS), 0.005 mol/l 4-(2-pyridylazo)-resorcin (PAR), 0.001 mol/l Malachite Green (MG), 0.001 mol/l Neutral Red (NR) and 0.5 mol/l Cetylpyridinium Chloride (CPCh) were prepared by dissolution of exactly weighed amounts of reagents in water. The solution of 1-(2-pyridylazo)-2-naphtol (PAN) with mass fraction 0.1% was prepared by dissolution of exactly weighed amounts of reagent in acetone. The solution of Eriochrome Cyanine R (EChC) with mass concentration 0.7 mg/l was prepared according to recommendations [39]. In the case of Ferrum (III) determination the solution of KSCN was purified from Fe^{3+} ions impurity using prepared PUF tablets.

The solutions of strong acids (H_2SO_4, HCl) and buffer solutions (acetic, borax) were used to create the required pH values.

Indicator paper. The specimens of reagent indicator paper on the basis of epoxidized cellulose [22]: RIP-Co-Test with immobilized 1-nitroso-2-naphthol; RIP-Cu-Test with covalently fixed 1,3-biphenyl-5-(6-methyl-4-oxo-3,4-dihydropyrimidine-2-yl)-formazan; RIP-Metal-Test on the basis of 1-(2-carboxyphenyl)-5-(benzoxazolyl-2-yl)-formazonylcellulose; RIP-Metal-Test II on the basis of irregular 1-(2-carboxyphenyl)-5-(4-methyl-6-metoxypyrimidine-2-yl)-formazan-6-cellulose [23] and also prepared by the technique [25] the indicator paper with adsorption fixed of 1-(2-piridilazo)-2-naphthol were used in this work.

Polyurethane foam. Test means for determination Co^{2+} and Fe^{3+} ions with KSCN and chemisorption determination of nitrite was prepared from the polyurethane sheet on the basis of mixed esters (brand 2240) according to the technique described in [1, 3]. The sorbent used in the form of tablets with a diameter of 16 mm, thickness of 7-10 mm, weight 0.03-0.05 g. Tablets of PUF was purified by keeping during 30 min in solutions of 0.1 mol/l H_2SO_4 (for Co^{2+} determination), 0.1 mol/l HCl (for Fe^{3+} determination), 5 mol/l HCl (for NO_2^- determination), then tablets were washed with water to pH 5-6, acetone, squeezed between sheets of filter paper, air dried and stored at room temperature in a darkness.

Gelatin films were used in the role of carrier material for the Co^{2+} determination with Nitroso-R-salt, Al^{3+} with Eriochrome cyanine R and metal ions sum (Zn^{2+}, Pb^{2+}, Cu^{2+}, Co^{2+}, Ni^{2+}, Cd^{2+}) with 4-(2-pyridylazo)-resorcin. Photographic films for offset printing manufactured by AGFA, with thickness of gelatin layer around 20 μm, fixed on the transparent triacetylcellulose support [40] were used for the producing of sensitive elements. The samples used were colorless and transparent with size 2.5×3.5 cm. previously the silver halogenides were completely removed from the films.

The Nitroso-R-salt extraction in a gelatin matrix was carried out from water solution with the NRS concentration of 0.003 mol/l and pH 2 (HCl); Eriochrome cyanine R – from the solution $5 \cdot 10^{-4}$ mol/l EChC, 0.01 mol/l CPCh and pH 5.5; 4-(2-pyridylazo)-resorcin – from the solution of 0.001 mol/l PAR. Samples of the films were immersed in a reagent solution for 30 min in the case of the NRS, for 20 minutes – EChC and for 45 minutes – in the case of the PAR, then the films were removed from the solution with tweezers and air dried in a Petri dish placed edgewise on a filter paper. Samples of the films with immobilized reagents were uniformly colored in yellow (NRS, PAR) and orange (EChC), they were stored at room temperature in a darkness.

We used macroporous *silica* grade L 100/250. Malachite Green and Neutral Red indicators were sorb from solution as cationic forms, creating a pH 9.18 and 3 respectively. Powder with weight of 0.2 g was poured in the indicator solution (25 ml) and the suspension was shaken on a mechanical mixer for 3 minutes in the case of the MG and 90 minutes in case of the NR.

Characteristics of test systems and conditions of testing procedure are shown in Table 9. All observations were carried out in daylight illumination in conditions of diffused light, the value of lighting in the room was 500-600 lux. Comparison of the color intensity of the adjacent reference samples of the scale and color comparison of control samples, which were obtained as a result of testing the control samples or model solutions, with the color scale were carried out by placing the scale and control samples on a sheet of white paper.

Colorimetric measurement. Diffuse reflection of PUF tablets and RIP samples was measured using spectrophotometer SF-2000. Tablets and sample indicator paper were fixed on the attachment; the reflection was measured relative to white purified tablet of PUF or a sample of white dense paper in the wavelength range from 400 to 700 nm. Using the software that is supplemented to the spectrophotometer chromaticity characteristics and the values of total color difference (ΔE) were obtained.

Absorption (transmission) of gelatin films was registered using spectrophotometer Hitachi U 3202. The films were fixed in the holder in a cuvette compartment. Absorption spectra of the films with reagent or complex were measured against reference colourless film. The method of selected coordinates

was chosen to calculate the X, Y, Z color coordinates [4, 5, 8]. Coordinates *L, a, b* and total color difference were calculated by formulas:

$$L = 116(Y/Y_0)^{1/3} - 16, \tag{6}$$
$$a = 500[(X/X_0)^{1/3} - (Y/Y_0)^{1/3}], \tag{7}$$
$$b = 200[(Y/Y_0)^{1/3} - (Z/Z_0)^{1/3}], \tag{8}$$
$$\Delta E = [(L_0 - L)^2 + (a - a_0)^2 + (b - b_0)^2]^{1/2}, \tag{9}$$

L, a, b, *L_0, a_0, b_0* – color coordinates of sample with immobilized complex and sample with reagent respectively.

Color coordinates in the RGB system were obtained using a portable photometer-reflectometer, which has both optical filters in red, blue and green spectral regions (λ_R = 615 nm, λ_G = 540 nm, λ_B = 465 nm) and sensors without filters with a spectral range of sensitivity 400–700 nm [21]. The instrument has a small overall size 70×60×35 mm and a connection to USB, which makes the system suitable for colorimetric measurements of colored non-transparent samples (Figure 1).

Stained samples of silica gel, PUF and RIP were scanned with predetermined calibration of the photometer using white standard. Samples of PUF and RIP were placed at a white substrate and firmly pressed to the device screen. The powder of modified silica with a mass of ~ 0.1 g densely was poured into a white circular teflon cell (10 mm in diameter and 2 mm high), the upper layer of powder was leveled and the measurements were carried out. The brightness of R-, G-, B-channels was performed using computer programs Microsoft Excel and Origin 6.0. Brightness of channels varied in the range of 0-4500 that corresponds to a value range 0-225 in a case of desktop scanner.

LIST OF ABBREVIATIONS

ΔE – total color difference
LEDs – light-emitting diodes
PUF – polyurethane foam
RIP – reagent paper
NR – Neutral Red
MG – Malachite Green
PAR – 4-(2-pyridylazo)-resorcin
PAN – 1-(2-pyridylazo)-2-naphtol
NRS – Nitroso-R-salt
CPCh – Cetylpyridinium Chloride
EChC – Eriochrome Cyanine R

Table 9. The characteristics of the test-systems and testing conditions

№	Analyte	Reagent	Indicator system	Sorbent	Concentration range, mol/l	Time, min	Color changing of a sorbent
1	Co^{2+}	SCN⁻	KSCN, 1.0 mol/l NaF, 0.01 mol/l H_2SO_4, pH 2	PUF	$(0.5-40)\cdot10^{-6}$	30	white – blue
2	Fe^{3+}	SCN⁻	KSCN, 1.0 mol/l H_2SO_4, pH 2	PUF	$(0.4-20)\cdot10^{-6}$	15	white – red
3	NO_2^{-}	–	HCl, pH 0		$(0.15-3.0)\cdot10^{-5}$	25	white – yellow
4	Co^{2+}	Formazan	RIP-Co-Test, pH 6.6		$(1.6-22)\cdot10^{-4}$	5 sec	yellow – red
5	Cu^{2+}	Formazan	RIP-Cu-Test, HCl, pH 3	Paper	$(0.8-12)\cdot10^{-3}$	15	yellow – violet
6*	ΣM^{n+}	Formazan	RIP-Metal-Test		$(0.5-8)\cdot10^{-3}$	3 sec	yellow – dark grey
7*	ΣM^{n+}	Formazan	RIP-Metal-Test II		$(1-8)\cdot10^{-4}$	3 sec	yellow – dark blue
8*	ΣM^{n+}	PAN	$Na_2B_4O_7$, pH 9		$(5-32)\cdot10^{-6}$	15	yellow – red
9	Al^{3+}	EChC	CPCh, $1\cdot10^{-4}$ mol/l acetate buffer, pH 5 NaCl, 0.1 mol/l	Gelatin film	$(0.5-13.0)\cdot10^{-5}$	20	violet – dark blue
10	Co^{2+}	NRS	HCl, pH 2		$(0.5-16)\cdot10^{-5}$	20	yellow – reddish-brown
11*	ΣM^{n+}	PAR	acetate buffer, pH 5		$(0.3-40)\cdot10^{-5}$	15	yellow – red
12	MG	–	borate buffer, pH 9.18	Silica	$(0.1-1)\cdot10^{-5}$	3	white – blue
13	NR	–	HCl, pH 3		$(0.1-1)\cdot10^{-5}$	120	white – crimson

*In the case of the determination of total metal ion concentration in each solution created equal molar concentrations of metals

REFERENCES

1. Yu.A. Zolotov, V.M. Ivanov, V.G. Amelin, "Khimicheskie test-metody analiza", Editorial URSS, Moskow, **2002**.

2. V.M. Ivanov, O.V. Kuznetsova, *Russ. Chem. Rev.*, **2001**, *70*, 357.

3. S.G. Dmitrienko, V.V. Apyari, "Penopoliuretany: sorbtsionnye svoistva i primenenie v khimicheskom analize", KRASAND, Moskow, **2010**.

4. N. Ohta, A. Robertson, "Colorimetry: Fundamentals and Applications", John Wiley & Sons, **2006.**

5. J. Schanda, "Colorimetry: Understanding the CIE System", Wiley-Interscience, **2007**.

6. V.M. Ivanov, S.A. Morozko, S.V. Kachin, *Zhurnal Analiticheskoi Khimii*, **1994**, *49*, 857.

7. O.A. Zaporozhets, L.S. Ivan'ko, L.V. Bykova, N.A. Mostovaya, *J. Anal. Chem.*, **2004**, *59*, 23.

8. E.A. Kirillov, "Tsvetovedenie", Legprombytizdat, Moskow, **1987**.

9. A.V. Gerasimov, *J. Anal. Chem.*, **2004**, *59*, 348.

10. N. Brown, J. Peng, M.R. Jackson, R.M. Parkin, *Optics & Laser Technology*, **2001**, *33*, 103.

11. Yu.L. Shishkin, S.G. Dmitrienko, O.M. Medvedeva, S.A. Badakova, L.N. Pyatkova, *J. Anal. Chem.*, **2004**, *59*, 102.

12. M. Kompany-Zareh, M. Mansourian, F. Ravaee, *Anal. Chim. Acta*, **2002**, *471*, 97.

13. V.V. Apyari, S.G. Dmitrienko, *J. Anal. Chem.*, **2008**, *63*, 530.

14. Ya. Suzuki, M. Endo, J. Jin, K. Iwase, M. Iwatsuki, *Analytical Sciences*, **2006**, *22*, 411.

15. A. Aghanouri, S.H. Amirshahi, F. Agahian, *Analytical Sciences*, **2010**, *26,* 101.

16. V.V. Apyari, S.G. Dmitrienko, V.M. Ostrovskaya, E.K. Anaev, Yu.A. Zolotov, *Anal. Bioanal. Chem.*, **2008**, *391*, 1977.

17. Ya. Shimazaki, Sh. Watamabe, M. Takahashi, M. Iwatsuki, *Analytical Sciences*, **2000**, *16*, 1091.

18. S. Kawakubo, A. Naito, A. Fujihara, M. Iwatsuki, *Analytical Sciences,* **2004**, *20*, 1159.

19. P.K. Yang, J.C. Chen, Y.H. Chang, *Optics Communications*, **2007**, *272*, 320.

20. K. Liang, W. Li, X.L. Liu, W.J. Wang, D.J. Han, *Displays,* **2009**, *30*, 107.

21. D.V. Snizhko, *Radiotekhnika: Vseukr. Mizhvid. Nauk.-tekh. zb.*, **2009**, *156*, 263.

22. V.M. Ostrovskaya, O.A. Zaporozhets, G.K. Budnikov, N.M. Chernavskaya. "Voda. Indikatornye sistemy", FGUP VTII, Moskow, **2002.**

23. V.M. Ostrovskaya, E.A. Reshetnyak, N.A. Nikitina, A.V. Panteleimonov, Yu.V. Kholin, *J. Anal. Chem.*, **2004**, *59*, 995.

24. E.A. Reshetnyak, N.A. Nikitina, D.V. Snizhko, Ya.A. Zhitnyakovskaya, Ya.A. Bondarenko, V.M. Ostrovskaya, *Kharkov University Bulletin*, **2010**, *19(42)*, 208.

25. R.P. Pantaler, N.B. Lebed, L.I. Avramenko, A.B. Blank, *Zhurnal Analiticheskoi Khimii*, **1997**, *52*, 643.

26. V.G. Amelin, *Zhurnal Analiticheskoi Khimii*, **2000**, *55*, 532.

27. N.A. Nikitina, Test-metody khimicheskogo analiza s vizual'noi indiktsiei: metrologacheskoe obespechenie, novye test-sistemy: Avtoref. dis. khand. khim. nayk: 02.00.02, Kharkov, **2006**.

28. O.P. Shvoeva, V.P. Dedkova, A.G. Gitlits, S.B. Savin, *Zhurnal Analiticheskoi Khimii*, **1997**, *52*, 89.

29. S.V. Savin, V.P. Dedkova, O.P. Shvoeva, *Uspekhi khimii*, **2000**, *69*, 203.

30. O. Zaporozhets, O. Gawer, V. Sukhan, *Talanta*, **1998**, *46*, 1387.

31. L.N. Moskvin, I.G. Zenkevich, L.A. Kartsova, *J. Anal. Chem.*, **2004**, *59*, 617.

32. V.M. Ivanov, O.V. Kuznetsova, O.V. Grineva, *Zhurnal Analiticheskoi Khimii*, **1999**, *54*, 263.

33. S.A. Morozko, V.M. Ivanov, *Zhurnal Analiticheskoi Khimii*, **1997**, *52*, 858.

34. V.M. Ivanov, O.V. Kuznetsova, *J. Anal. Chem.*, **2000**, *55*, 899.

35. D.A. Knyazev, V.M. Ivanov, S.G. Samokhvalov, Yu.A. Zolotov, V.M. Markina et al., *J. Anal. Chem.*, **2002**, *57*, 75.

36. D.A. Knyazev, A.V. Zhevnerov, V.M. Ivanov, V.D. Knyazev, *J. Anal. Chem.*, **2006**, *61*, 1149.

37. L.P. Eksperiandova, C.V. Khimchenko, *Metody i ob'tkty khimicheskogo analiza*, **2008**, *3*, 113.

38. F. Umland, A. Jans Sen, D. Thirig, G. Wonsch, "Theorie und Praktishe Anwendung von Komplexbildnern", Akademishe Verlagsgesellschaft, Frankfurt am Main, **1971**.

39. V.I. Ivanov, "Voda pitevaya. Normativnye dokymenty", Spravochnik. NTTS «Leonorm-standart», L'vov, **2001**.

40. T.H. James, "The Theory of the Photographic Process", 4th Edition, Macmillan Publishing Co., New York, **1977**.